

**THE EFFECT OF LFC PROCESS VARIABLES ON  
SOLIDIFICATION AND THERMAL RESPONSE OF  
AZ91E MAGNESIUM ALLOY CASTINGS**

By

**Lukas Bichler, B. Eng., Ryerson University, 2003**

A thesis  
presented to Ryerson University  
in partial fulfillment of the  
requirement for the degree of

Master of Applied Science

in the program of  
Mechanical Engineering

Toronto, Ontario, Canada, 2005

Copyright © Lukas Bichler, 2005

UMI Number: EC53425

### INFORMATION TO USERS

The quality of this reproduction is dependent upon the quality of the copy submitted. Broken or indistinct print, colored or poor quality illustrations and photographs, print bleed-through, substandard margins, and improper alignment can adversely affect reproduction.

In the unlikely event that the author did not send a complete manuscript and there are missing pages, these will be noted. Also, if unauthorized copyright material had to be removed, a note will indicate the deletion.



---

UMI Microform EC53425  
Copyright 2009 by ProQuest LLC  
All rights reserved. This microform edition is protected against  
unauthorized copying under Title 17, United States Code.

---

ProQuest LLC  
789 East Eisenhower Parkway  
P.O. Box 1346  
Ann Arbor, MI 48106-1346

## **Author's Declaration**

I hereby declare that I am the sole author of this thesis.

I authorize Ryerson University to lend this thesis to other institutions or individuals for the purpose of scholarly research.

---

Lukas Bichler

I further authorize Ryerson University to reproduce this thesis by photocopying or by other means, in total or in part, at the request of other institutions or individuals for the purpose of scholarly research.

---

Lukas Bichler

## Borrower's Page

Name	Address	Date



**Abstract**  
**THE EFFECT OF LFC PROCESS VARIABLES ON**  
**SOLIDIFICATION AND THERMAL RESPONSE OF**  
**AZ91E MAGNESIUM ALLOY CASTINGS**

© Lukas Bichler, 2004

Master of Applied Science

In the program of Mechanical Engineering  
Toronto, Ontario, Canada, 2005

Magnesium alloys are gaining in popularity as materials of choice for automotive and aerospace applications. Magnesium alloys have the lowest density of all structural metals, effectively making their specific properties highly attractive. Lost Foam Casting (LFC) is a novel near-net-shape manufacturing process utilizing expanded polystyrene (EPS) as a mold filler. Presence of the EPS in the casting cavity promotes formation of unique casting defects. These include misruns, folds, entrapped polystyrene pyrolysis products and potentially increased levels of gas porosity. There is very little published literature on the feasibility of casting magnesium alloys by the LFC process.

This research was an attempt to evaluate the effect of selected LFC process variables on AZ91E magnesium alloy castings produced by the LFC process. In this work, the effect of melt superheat, casting section thickness, EPS foam properties and the application of vacuum during mold filling were investigated and correlated to the casting quality and molten metal flow behavior. Further, detailed thermal analysis was carried out to determine the solidification history of the castings. The results of the thermal analysis were used to determine the effect of the cooling rate on the development of the casting microstructure. Moreover, the morphology and the mode of second phase ( $\text{Mg}_{17}\text{Al}_{12}$ ) precipitation were studied and quantified.

The results suggest that application of vacuum during the mold filling process increased the metal flow lengths. However, the casting soundness deteriorated due to the applied vacuum. Variations in the density of the vacuum cast horizontal bars were explained through the presence of partially solidified metal. The molten metal flow was further influenced by the foam density and the bead fusion. Greater flow lengths were observed in the high density 1.6 pcf foam castings. In the low density 1.3 pcf foam castings, numerous casting defects were associated with the presence of the liquid-EPS pyrolysis products. In general, the thermal analysis suggested that non-equilibrium alloy solidification promoted the formation of the lamellar non-equilibrium  $\text{Mg}_{17}\text{Al}_{12}$  precipitate, and this was confirmed by optical microscopy.

## Acknowledgements

I would like to express my deepest gratitude to Dr. C. Ravindran for his guidance and support during this project. I thank Dr. Ravindran for his patience in teaching his academic children to walk the path of life.

The author is also indebted to Mr. A. Machin for his advice and knowledge he contributed to this project.

The author wishes to acknowledge the assistance of Dr. Y. Fasoyinu and Dr. M. Sahoo of CANMET-MTL for enabling casting production at their facilities.

Further, the author wishes to thank Mr. C. Cvetnic, Mr. S. Jagoo, Mr. N. Dhingra and Mr. G. Diamantakos for their help and support throughout the project.

The author acknowledges the National Research and Engineering Council of Canada (NSERC) for financial support.

Finally, I would like to thank my family and Margarita for their love, support and patience. Without them, completion of this thesis would not be possible.

# Table of Contents

Author's Declaration.....	ii
Borrower's Page .....	iii
Abstract .....	iv
Acknowledgements.....	v
Table of Contents.....	vi
List of Tables.....	ix
List of Illustrations.....	x
Nomenclature.....	xiv
Chapter 1 – Introduction .....	1
Chapter 2 – Literature Review .....	2
2.1 Lost Foam Casting.....	2
2.2 Mold filling and fluidity .....	4
2.2.1 Effect of vacuum .....	6
2.2.1.1 Effect of vacuum on the metal front profile .....	8
2.2.1.2 Effect of vacuum on the pyrolysis products removal rate.....	9
2.2.1.3 Effect of vacuum on the heat transfer.....	9
2.3 Magnesium alloys.....	10
2.3.1 Effect of aluminum.....	11
2.4 Development of the microstructure.....	13
2.4.1 Equilibrium solidification.....	14
2.4.2 Non-equilibrium solidification .....	15
2.4.3 Mg <sub>17</sub> Al <sub>12</sub> phase morphology .....	16
2.4.3.1 Fully divorced eutectic.....	18
2.4.3.2 Partially divorced eutectic.....	18
2.4.3.3 Morphology of the Mg <sub>17</sub> Al <sub>12</sub> phase .....	19
2.4.3.4 Precipitation of the Mg <sub>17</sub> Al <sub>12</sub> phase.....	21
2.4.3.4.1 Morphology of the continuous precipitate .....	22
2.4.3.4.2 Morphology of the discontinuous precipitate .....	23
2.5 Defect formation.....	25
2.5.1 Porosity .....	25
2.5.1.1 Shrinkage porosity .....	26
2.5.1.2 Gas porosity .....	27
2.5.1.3 Solute segregation and porosity.....	28
2.5.1.4 Adam's Riser Equation .....	28
2.6 AZ91E density.....	29
2.7 Thermal analysis.....	30
2.7.1 Computer Aided Cooling Curve Analysis .....	32
2.7.2 Data smoothing .....	33
2.7.2.1 The method of "Least-Squares" .....	33
Chapter 3 – Experimental Procedure .....	34
3.1 Project structure.....	34
3.2 Pattern assembly .....	36
3.3 Ceramic coating slurry.....	38
3.4 Installation of thermocouples.....	38
3.5 Casting box.....	38
3.5.1 Mold medium .....	39
3.5.2 Mold vibration.....	40
3.6 Melting .....	41

3.7 Treatment of experimental data.....	42
3.8 Casting sectioning.....	43
3.9 Casting density measurements.....	44
3.10 Casting microstructure analysis.....	44
3.10.1 Optical image analysis.....	45
Chapter 4 – Results and Discussion.....	47
4.1 Adam's Riser Equation.....	47
4.2 Overall casting quality.....	49
4.2.1 Casting Condition: 660 °C, 1.3 pcf foam, with vacuum.....	49
4.2.2 Casting Condition: 660 °C, 1.6 pcf foam, with vacuum.....	53
4.2.3 Casting Condition: 660 °C, 1.3 pcf foam, without vacuum.....	57
4.2.4 Casting Condition: 660 °C, 1.6 pcf foam, without vacuum.....	58
4.2.5 Casting Condition: 700 °C, 1.6 pcf foam, with vacuum.....	59
4.2.6 Casting Condition: 700 °C, 1.3 pcf foam, with vacuum.....	62
4.2.7 Casting Condition: 700 °C, 1.6 pcf foam, without vacuum.....	63
4.2.8 Casting Condition: 700 °C, 1.3 pcf foam, without vacuum.....	64
4.2.9 Section summary.....	65
4.3 Casting fill and flow length.....	66
4.3.1 Pouring temperature: 660 °C.....	66
4.3.2 Pouring temperature: 700 °C.....	69
4.3.3 Section summary.....	70
4.4 Casting density and soundness.....	71
4.4.1 Casting Condition: 660 °C, 1.3 pcf foam, with vacuum.....	72
4.4.2 Casting Condition: 660 °C, 1.6 pcf foam, with vacuum.....	74
4.4.3 Casting Condition: 660 °C, 1.3 pcf foam, without vacuum.....	77
4.4.4 Casting Condition: 660 °C, 1.6 pcf foam, without vacuum.....	79
4.4.5 Casting Condition: 700 °C, 1.6 pcf foam, with vacuum.....	81
4.4.6 Casting Condition: 700 °C, 1.3 pcf foam, with vacuum.....	82
4.4.7 Casting Condition: 700 °C, 1.6 pcf foam, without vacuum.....	84
4.4.8 Casting Condition: 700 °C, 1.3 pcf foam, without vacuum.....	84
4.4.9 Statistical analysis.....	86
4.4.10 Section summary.....	90
4.5 Metal velocity.....	91
4.5.1 Casting Condition: 660 °C, 1.3 pcf foam, with vacuum.....	91
4.5.2 Casting Condition: 660 °C, 1.6 pcf foam, with vacuum.....	92
4.5.3 Casting Condition: 660 °C, 1.6 pcf foam, without vacuum.....	93
4.5.4 Casting Condition: 700 °C, 1.6 pcf foam, with vacuum.....	94
4.5.5 Casting Condition: 700 °C, 1.3 pcf foam, with vacuum.....	95
4.5.6 Casting Condition: 700 °C, 1.6 pcf foam, without vacuum.....	96
4.5.7 Casting Condition: 700 °C, 1.3 pcf foam, without vacuum.....	97
4.5.8 Section summary.....	98
4.6 Local solidification time and the cooling rate.....	99
4.6.1 Pouring temperature: 660 °C.....	100
4.6.2 Pouring temperature: 700 °C.....	103
4.6.3 Chvorinov's rule.....	108
4.7 Casting temperature distribution.....	110
4.8 Casting temperature gradient.....	113
4.9 Casting porosity and the criterion functions.....	116
4.9.1 Pouring temperature: 660 °C.....	117
4.9.2 Pouring temperature: 700 °C.....	121
4.9.3 Criterion functions.....	126

4.9.4 Section summary .....	128
4.10 Microstructure of the casting .....	129
4.10.1 Constitutional undercooling in the AZ91E alloy .....	130
4.10.2 Effect of cooling rate on the $Mg_{17}Al_{12}$ precipitate .....	134
4.10.3 Development of the “equilibrium-like” precipitate.....	142
4.10.4 Development of the lamellar “non-equilibrium” precipitate.....	143
4.10.5 Characterization of the $Mg_{17}Al_{12}$ precipitate.....	147
4.10.6 Effect of the $Mg_{17}Al_{12}$ precipitate on the casting density.....	161
4.10.7 Lamellar spacing of the $Mg_{17}Al_{12}$ precipitate .....	162
4.10.8 Section summary .....	166
Chapter 5 – Conclusions .....	167
Chapter 6 – Suggestions for Further Work .....	170
Appendix A – EPS foam decomposition (energy approach).....	171
Appendix B – Statistical analysis.....	172
B.1 - Effect of pouring temperature and vacuum on the casting density for the 1.6 pcf foam castings.....	172
B.2 - Effect of foam density and vacuum on the average casting density in the 660 °C pouring temperature casting trials.....	172
B.3 - Effect of foam density and vacuum on the average casting density in the 700 °C pouring temperature casting trials.....	173
B.4 - Effect of section thickness and pouring temperature on the local solidification time (LST) for gravity cast 1.6 pcf foam trials.....	173
B.5 - Effect of pouring temperature and section thickness on thermal gradients for vacuum cast 1.6 pcf trials.....	174
Appendix C – Minimal lamellar spacing .....	175
References .....	176

## List of Tables

Table 1: Thermal properties of pure Mg and Al. ....	4
Table 2: Chemical composition of AZ91E, in wt%. ....	41
Table 3: Typical casting sequence.....	41
Table 4: Metallographic specimen polishing procedure.....	45
Table 5: Alloy data used in A.R.E model.....	47
Table 6: Casting geometry data.....	47
Table 7: Effect of individual casting trials on the casting density.....	87
Table 8: Effect of pouring temperature and vacuum on the casting density, ANOVA results.....	88
Table 9: Effect of foam density and vacuum on the casting density in the 660 °C pouring temperature trials, ANOVA results. ....	88
Table 10: Effect of foam density and vacuum on the casting density in the 700 °C pouring temperature trials, ANOVA results. ....	89
Table 11: Metal velocities and the velocity standard deviations for different casting conditions.....	97
Table 12: Ranking of casting conditions based on the average metal velocities.....	98
Table 13: Cooling rates and flow lengths in the 1.0 cm thick horizontal bars. ....	99
Table 14: Average cooling rates in the horizontal bars for different casting conditions.....	101
Table 15: Effect of section thickness and pouring temperature on the local solidification time, ANOVA results.....	105
Table 16: Effect of vacuum on the average cooling rates in the horizontal bars.....	106
Table 17: Average casting temperatures for different times after beginning of solidification.....	110
Table 18: Effect of pouring temperature and section thickness on the thermal gradient, ANOVA analysis. ....	114
Table 19: Average casting porosity for the 660 °C pouring temperature casting trials.....	118
Table 20: Average casting porosity for the 700 °C pouring temperature casting trials.....	122
Table 21: Solute redistribution in the AZ91E alloy. ....	130
Table 22: Average Mg <sub>17</sub> Al <sub>12</sub> percent area for different casting conditions.....	159
Table 23: Detailed results of the ANOVA analysis of the effect of pouring temperature and vacuum on the casting density. ....	172
Table 24: Detailed results of the ANOVA analysis of the effect of foam density and vacuum on the casting density for the 660 °C pouring temperature trials. ....	172
Table 25: Detailed results of the ANOVA analysis for the effect of foam density and vacuum on the casting density in the 700 °C pouring temperature trials.....	173
Table 26: Detailed results of the ANOVA analysis of the effect of section thickness and pouring temperature on the LST. ....	173
Table 27: Detailed results of the ANOVA analysis of the effect of pouring temperature and section thickness on the casting thermal gradients. ....	174

## List of Illustrations

Figure 1: Typical casting system.....	3
Figure 2: Effect of vacuum level on the metal flow length. ....	7
Figure 3: Effect of pouring temperature and vacuum degree on the metal flow length.....	7
Figure 4: Metal front profile for a low-vacuum level.....	8
Figure 5: Metal front profile for an intermediate vacuum level. ....	8
Figure 6: Metal front profile for a high-vacuum level.....	8
Figure 7: Binary Mg-Al phase diagram. ....	11
Figure 8: AZ31-3wt% Aluminum, sand cast (x200). ....	12
Figure 9: A8-8wt% Aluminum, sand cast (x200).....	12
Figure 10: Mg-15wt% Aluminum, permanent-mould cast.....	12
Figure 11: Mg-rich end of the Mg-Al binary phase diagram.....	14
Figure 12: Effect of Al content and cooling rate on the $Mg_{17}Al_{12}$ morphology.....	16
Figure 13: Fully divorced eutectic microstructure. ....	18
Figure 14: Partially divorced eutectic microstructure. ....	18
Figure 15: Eutectoid precipitation in the Mg-6wt%Al alloy (x175).....	20
Figure 16: Same as Figure 15; homogenized for 1 hr at 400 °C and slowly cooled (x175).....	20
Figure 17: Eutectoid structure heated for a short period of time at 400 °C (x400, x500). ....	20
Figure 18: Continuous precipitation of $Mg_{17}Al_{12}$ in the Mg-8wt%Al alloy; (a) Optical micrograph (x1000) and (b) Scanning Electron Micrograph. ....	22
Figure 19: Discontinuous precipitation of $Mg_{17}Al_{12}$ in the Mg-8wt%Al alloy; (a) Optical micrograph (x500) and (b) Scanning Electron Micrograph.....	23
Figure 20: Mg-9wt%Al alloy sand cast and quenched (x200). ....	24
Figure 21: Mg-9wt%Al alloy sand cast and slowly cooled (x200).....	24
Figure 22: Effect of Al content on the casting porosity.....	26
Figure 23: Typical shrinkage microporosity in Mg-Al castings. ....	26
Figure 24: Hydrogen gas solubility in molten Al and Mg. ....	27
Figure 25: Effect of casting temperature on the alloy density. ....	29
Figure 26: Typical cooling curve for the AZ91E alloy. ....	30
Figure 27: Experimental plan.....	35
Figure 28: 3D View of the casting foam pattern. ....	36
Figure 29: Dimensions of the pouring biscuit and overall bar dimensions, in cm. ....	36
Figure 30: Poorly fused ARCO T21 foam. ....	37
Figure 31: Well fused ARCO T21 foam. ....	37
Figure 32: Top view of the casting box with instrumented foam pattern. ....	39
Figure 33: Sealing of the casting box with a PVC sheet. ....	40
Figure 34: Raw temperature data. ....	42
Figure 35: Modified temperature data.....	42
Figure 36: Locations of metallographic samples.....	43
Figure 37: Observed $Mg_{17}Al_{12}$ phase. ....	46
Figure 38: Areas included in the $Mg_{17}Al_{12}$ percent area calculation. ....	46
Figure 39: A. R. E. plot.....	48
Figure 40: Casting: 660 °C / 1.3 pcf / with vacuum, bottom side. ....	50
Figure 41: Partially solidified chunks in the frozen metal front. ....	51
Figure 42: Concave metal front profiles of the 1.5cm, 2.0 cm and 2.5 cm thick bars. ....	51
Figure 43: River-like impressions caused by the liquid-EPS residue; 2.0 cm thick bar. ....	52
Figure 44: Surface extension of shrinkage porosity. ....	52
Figure 45: Subsurface shrinkage porosity network. ....	52
Figure 46: Casting: 660 °C / 1.6 pcf / with vacuum, bottom side. ....	53
Figure 47: Casting: 660 °C / 1.6 pcf / with vacuum, top side. ....	53

Figure 48: Sand grains adhering to the bottom side of the casting.....	54
Figure 49: Micrograph of sand grains adhering to the bottom side of the casting. ....	54
Figure 50: Metal front of the 1.0 cm thick bar. ....	54
Figure 51: Burned-on ceramic coating and liquid-EPS channel. ....	55
Figure 52: Enlarged liquid-EPS channel from Figure 51.....	55
Figure 53: Liquid-EPS barrier at the metal-coating interface. ....	55
Figure 54: Liquid-EPS “wet” marks.....	56
Figure 55: Casting: 660 °C / 1.3 pcf / without vacuum, bottom side.....	57
Figure 56: Frozen metal front of the 1.0 cm thick bar.....	57
Figure 57: Convex metal front of the 1.5 cm thick bar. ....	57
Figure 58: Casting: 660 °C / 1.6 pcf / without vacuum, bottom side.....	58
Figure 59: Convex metal front of the 1.0 cm thick bar. ....	58
Figure 60: Fold defect in the 1.0 cm thick bar.....	59
Figure 61: Stereo micrograph of the fold defect in Figure 60.....	59
Figure 62: Casting: 700 °C / 1.6 pcf / with vacuum, bottom side.....	60
Figure 63: Casting: 700 °C / 1.6 pcf / with vacuum, top side.....	60
Figure 64: Adhering sand grains at the bottom side of the casting. ....	60
Figure 65: Sand grains engulfed by the frozen alloy.....	60
Figure 66: End face of the 1.5 cm thick bar. ....	61
Figure 67: Casting: 700 °C / 1.3 pcf / with vacuum, bottom side.....	62
Figure 68: Concave metal front of the 1.5 cm thick bar.....	62
Figure 69: Casting: 700 °C / 1.6 pcf / without vacuum, bottom side.....	63
Figure 70: Convex metal front of the 1.0 cm thick bar. ....	63
Figure 71: River-like impressions on the sides of the 1.5 cm thick bar. ....	63
Figure 72: Casting: 700 °C / 1.3 pcf / without vacuum, bottom side.....	64
Figure 73: Convex metal front of the 1.0 cm thick bar. ....	64
Figure 74: Concave metal front profile and liquid-EPS residue marks of the 2.0 cm thick bar.....	64
Figure 75: Liquid-EPS defect in the 2.5 cm thick bar.....	65
Figure 76: End face of the 2.5 cm thick bar. ....	65
Figure 77: Casting percent fill: 660 °C pouring temperature trials.....	66
Figure 78: Heat affected zones in EPS foams of different bead fusion. ....	68
Figure 79: Poorly fused 1.3 pcf foam.....	68
Figure 80: Well fused 1.6 pcf foam. ....	68
Figure 81: Casting percent fill: 700 °C pouring temperature trials.....	69
Figure 82: Average density distribution for trial: 660 °C / 1.3 pcf / with vacuum.....	72
Figure 83: Sub-surface shrinkage porosity in the 2.0 cm thick bar.....	72
Figure 84: Interdendritic shrinkage porosity in the 2.5 cm thick bar. ....	72
Figure 85: Sectioned 2.5 cm thick horizontal bar.....	73
Figure 86: Average density distribution for trial: 660 °C / 1.6 pcf / with vacuum. ....	74
Figure 87: Solidus velocity for trial: 660 °C / 1.6 pcf / with vacuum.....	74
Figure 88: Sectioned view of the 1.5 cm thick horizontal bar.....	75
Figure 89: Internal cavity in the 1.5 cm thick bar at the 2.5 cm distance from the sprue.....	75
Figure 90: Sectioned view of the 2.0 cm thick bar.....	76
Figure 91: Frozen metal chunks near the flow tip of the 2.0 cm thick bar.....	76
Figure 92: Sectioned view of the 2.5 cm thick bar.....	77
Figure 93: Subsurface cavity in the 2.5 cm thick bar. ....	78
Figure 94: Liquid-EPS residue adhering to the internal cavity walls.....	78
Figure 95: Liquid-EPS residue, enlarged. ....	78
Figure 96: Average density distribution for trial: 660 °C / 1.6 pcf / without vacuum.....	79
Figure 97: Solidus velocity for trial: 660 °C / 1.6 pcf / without vacuum.....	79
Figure 98: Effect of section thickness on the cooling rate and the casting density.....	80



Figure 99: Average density distribution for trial: 700 °C / 1.6 pcf / with vacuum.....	81
Figure 100: Solidus velocity for trial: 700 °C / 1.6 pcf / with vacuum. ....	81
Figure 101: Sand inclusion near the metal-mold interface. ....	81
Figure 102: Detailed view of the sand inclusion in Figure 101 .....	81
Figure 103: Average density distribution for trial: 700 °C / 1.3 pcf / with vacuum. ....	82
Figure 104: Solidus velocity for trial: 700 °C / 1.3 pcf / with vacuum. ....	82
Figure 105: Solidified metal chunks at the metal front of the 1.0 cm thick bar.....	83
Figure 106: Liquid-EPS impressions along the sides of the 1.0 cm thick bar. ....	83
Figure 107: Internal casting cavities in the 1.0 cm thick bar at 8 cm distance from the sprue.....	83
Figure 108: Average density distribution for trial: 700 °C / 1.6 pcf / without vacuum.....	84
Figure 109: Solidus velocity for trial: 700 °C / 1.6 pcf / without vacuum. ....	84
Figure 110: Average density distribution for trial: 700 °C / 1.3 pcf / without vacuum.....	85
Figure 111: Solidus velocity for trial: 700 °C / 1.3 pcf / without vacuum. ....	85
Figure 112: Casting density data for all casting trials. ....	85
Figure 113: Average metal velocity for trial: 660 °C / 1.3 pcf / with vacuum.....	91
Figure 114: Average metal velocity for trial: 660 °C / 1.6 pcf / with vacuum.....	92
Figure 115: Average metal velocity for trial: 660 °C / 1.6 pcf / without vacuum.....	93
Figure 116: Average metal velocity for trial: 700 °C / 1.6 pcf / with vacuum.....	94
Figure 117: Average metal velocity for trial: 700 °C / 1.3 pcf / with vacuum.....	95
Figure 118: Average metal velocity for trial: 700 °C / 1.6 pcf / without vacuum.....	96
Figure 119: Average metal velocity for trial: 700 °C / 1.3 pcf / without vacuum.....	97
Figure 120: LST and CR results for the 660 °C pouring temperature casting trials.....	102
Figure 121: Effect of pouring temperature on the LST of the vacuum cast 1.6 pcf foam castings. ....	103
Figure 122: Effect of pouring temperature on the CR of the vacuum cast 1.6 pcf foam castings.....	104
Figure 123: Effect of vacuum on the CR of the 1.6 pcf foam castings poured at 700 °C. ....	105
Figure 124: LST and CR plots for the 700 °C pouring temperature casting trials. ....	107
Figure 125: Chvorinov's plot for all casting conditions.....	108
Figure 126: Chvorinov's plots for individual casting conditions. ....	109
Figure 127: Temperature profiles in the 1.5 cm thick bar after 15, 30, 60 and 120 seconds. ....	112
Figure 128: Thermal gradients in the 1.5 cm thick bars at 5 cm distance from the sprue.....	113
Figure 129: Cooling curves for trial: 660 °C / 1.6 pcf / with vacuum.....	115
Figure 130: Optical porosity results for the 660 °C pouring temperature trials. ....	117
Figure 131: Entrapped liquid-EPS residue near partially solidified chunks in the casting bar. ....	118
Figure 132: Traces of liquid-EPS residue near a metal chunk.....	118
Figure 133: Shrinkage network in the 2.0 cm thick bar at 5 cm distance from the sprue, 660 °C / 1.3 pcf / with vacuum trial. ....	119
Figure 134: Surface extensions of shrinkage pores in the 660 °C / 1.6 pcf / with vacuum trial.....	119
Figure 135: Microstructure of the 2.5 cm thick bar center location at 5 cm distance from the sprue. ....	120
Figure 136: Optical porosity results for the 700 °C pouring temperature trials. ....	121
Figure 137: Shrinkage porosity in the 2.5 cm thick bar at a 5 cm distance from the sprue, 700 °C / 1.6 pcf / with vacuum trial. ....	122
Figure 138: Microstructure of the 2.5 cm thick bar center location at 5 cm distance from the sprue. ....	123
Figure 139: Liquid-EPS bubble near the casting surface. ....	124
Figure 140: Porosity percent area vs. metal velocity.....	125
Figure 141: Niyama criterion function and optical porosity.....	127
Figure 142: Schematic representation of the solute enriched region ahead of the S-L interface. ....	131
Figure 143: Schematic temperature profiles.....	132
Figure 144: Schematic solute gradient profile for the primary Mg phase. ....	133
Figure 145: Microstructure of the 2.0 cm thick bar at the 7.6 cm distance from the sprue, 700 °C / 1.6 pcf / with vacuum trial. ....	133
Figure 146: Mg <sub>17</sub> Al <sub>12</sub> percent area vs. cooling rate. ....	136

Figure 147: Duration of the eutectic reaction vs. cooling rate. ....	137
Figure 148: Dendrites at the mold wall in the 2.0 cm thick bar at 5 cm distance from the sprue, 660 °C / 1.3 pcf / with vacuum trial.....	138
Figure 149: Microstructure of the 2.0 cm thick bar midsection at 5 cm distance from the sprue, 660 °C / 1.3 pcf / with vacuum trial.....	138
Figure 150: Microstructure development at the 5 cm distance from the sprue. ....	139
Figure 151: Microstructure of the 1.5 cm bar at 7.6 cm distance from the sprue, 700 °C / 1.3 pcf / without vacuum trial.....	140
Figure 152: Microstructure of the 2.5 cm bar at 7.6 cm distance from the sprue, 700 °C / 1.3 pcf / without vacuum trial.....	140
Figure 153: Dispersed $Mg_{17}Al_{12}$ in the 1.5 cm bar at 7.6 cm distance from the sprue, 700 °C / 1.3 pcf / with vacuum trial.....	141
Figure 154: $Mg_{17}Al_{12}$ phase in the 1.5 cm bar at 2.5cm distance from the sprue, 700 °C / 1.3 pcf / without vacuum trial.....	141
Figure 155: $Mg_{17}Al_{12}$ precipitate within the $\alpha$ -Mg grains.....	142
Figure 156: Equilibrium phase generation. ....	143
Figure 157: Effect of cooling rate on the eutectic temperature. ....	144
Figure 158: Generic phase diagram.....	145
Figure 159: Non-equilibrium phase generation.....	146
Figure 160: Lamellar $Mg_{17}Al_{12}$ precipitate.....	146
Figure 161: Casting microstructure: 660 °C / 1.3 pcf / with vacuum trial (500x).....	148
Figure 162: Casting microstructure: 660 °C / 1.6 pcf / with vacuum trial (500x).....	149
Figure 163: Casting microstructure: 660 °C / 1.3 pcf / without vacuum trial (500x).....	150
Figure 164: Casting microstructure: 660 °C / 1.6 pcf / without vacuum trial (500x).....	151
Figure 165: Casting microstructure: 700 °C / 1.6 pcf / with vacuum trial (500x).....	152
Figure 166: Casting microstructure: 700 °C / 1.3 pcf / with vacuum trial (500x).....	153
Figure 167: Casting microstructure: 700 °C / 1.6 pcf / without vacuum trial (500x).....	154
Figure 168: Casting microstructure: 700 °C / 1.3 pcf / without vacuum trial (500x).....	155
Figure 169: Precipitate in the 2.5 cm bar at 5 cm distance from the sprue, 700 °C / 1.6 pcf / with vacuum trial.....	156
Figure 170: Fully divorced eutectic in the 2.5 cm bar at 5 cm distance from the sprue, 660 °C / 1.3 pcf / with vacuum trial.....	156
Figure 171: Partially divorced eutectic in the 1.0 cm bar at 5 cm distance from the sprue, 660 °C / 1.6 pcf / with vacuum trial.....	156
Figure 172: Pyramidal lamellar growth in the 2.5 cm bar at 5 cm distance from the sprue, 660 °C / 1.3 pcf / without vacuum trial.....	157
Figure 173: Growth directions of the lamellar $Mg_{17}Al_{12}$ precipitate.....	157
Figure 174: $Mg_{17}Al_{12}$ percent area vs. distance from the sprue.....	158
Figure 175: Microstructure of the 1.5 cm thick bar at 7.6 cm distance from the sprue, 700 °C / 1.6 pcf / without vacuum trial.....	160
Figure 176: Microstructure of the 1.5 cm bar at 7.6 cm distance from the sprue, 700 °C / 1.3 pcf / without vacuum trial.....	160
Figure 177: Figure 175 enlarged. ....	160
Figure 178: Effect of the $Mg_{17}Al_{12}$ percent area on the casting density. ....	161
Figure 179: Fine and coarse lamellae of the $Mg_{17}Al_{12}$ phase. ....	163
Figure 180: Digitally enhanced Figure 179.....	163
Figure 181: $Mg_{17}Al_{12}$ lamellar spacing vs. distance from sprue. ....	165

## Nomenclature

Symbol	Description	Units
<b><i>Greek</i></b>		
$\beta$	Solidification contraction	
$\gamma_{\alpha/\beta}$	Interfacial energy	
$\lambda$	Lamellar spacing	$\mu\text{m}$
$\mu'$	Theoretical (population) alloy density	$\text{g/cm}^3$
$\mu$	Liquid metal viscosity	$\text{kg/m.s}$
$\nu$	Degrees of freedom	
$\rho_l$	Density of liquid metal	$\text{g/cm}^3$
$\rho_p$	Density of EPS foam	$\text{g/cm}^3$
$\chi^2$	Chi-squared random variable	
$\Delta G$	Change in Gibbs free energy	$\text{J/kg}$
$\Delta H_f$	Change in alloy enthalpy	$\text{J/kg}$
$\Delta T$	Degree of superheat	$^{\circ}\text{C}$
$\Delta T_u$	Thermal undercooling	$^{\circ}\text{C}$
<b><i>English</i></b>		
$a$	Casting section thickness	$\text{cm}$
$c_l$	Specific heat of liquid metal	$\text{J/kg.K}$
$h$	Heat transfer coefficient at the metal-mold interface	$\text{W/m}^2.\text{K}$
$k$	Chvorinov's constant	$\text{s/m}^2$
$k_p$	Partition coefficient	
$m$	Slope of the liquidus line	
$n$	Chvorinov's exponent	
$n'$	Sample size	
$\text{pcf}$	Pounds per cubic foot	$\text{lb/ft}^3$
$s$	Sample standard deviation	
$t$	Time	$\text{s}$
$\bar{t}$	Student t-statistic	
$\bar{x}$	Sample average density	$\text{g/cm}^3$

$A_c$	Casting surface area	$\text{cm}^2$
$C_L$	Solute concentration in liquid phase	wt%
$C_o$	Bulk solute concentration	wt%
$CR, dT/dt$	Cooling rate	$^{\circ}\text{C/s}$
$C_s$	Solute concentration in solid phase	wt%
$D_L$	Diffusivity of solute in liquid	$\text{m}^2/\text{s}$
$F$	Fisher F-statistic	
$G$	Temperature gradient	$^{\circ}\text{C/cm}$
$H$	Latent heat (heat of fusion)	$\text{J/kg}$
$H_E$	Decomposition energy of the EPS foam	$\text{J/kg}$
$L_c$	Characteristic "Chill Zone"	
$L_f$	Flow length	$\text{cm}$
$LST, t_f$	Local solidification time	$\text{s}$
$Re$	Reynold's number	
$T$	Temperature	$^{\circ}\text{C}$
$T_c$	Eutectic temperature	$^{\circ}\text{C}$
$T_M$	Alloy melting temperature	$^{\circ}\text{C}$
$T_o$	Mold temperature	$^{\circ}\text{C}$
$V$	Metal flow velocity	$\text{cm/s}$
$V_c$	Casting volume	$\text{cm}^3$
$V_r$	Riser volume	$\text{cm}^3$
$V_s$	Solidus velocity	$\text{cm/s}$
$V_{S-L}$	Solid-liquid interface growth velocity	$\text{cm/s}$
$W_{air}$	Weight of sample in air	$\text{g}$
$W_{c/w}$	Weight of cup and water	$\text{g}$
$W_{s/w}$	Weight of sample (suspended on a thread in a cup of water), cup and water	$\text{g}$

### ***Elements***

Al	Aluminum
C	Carbon
CO <sub>2</sub>	Carbon Dioxide
Cu	Copper
Fe	Iron
Mg	Magnesium
Mg <sub>17</sub> Al <sub>12</sub>	Second-phase in binary Mg-Al Alloys
Mn	Manganese
Na-SiF	Sodium-Silico-Fluoride
Ni	Nickel
SF <sub>6</sub>	Sulphur-Hexa-Fluoride
Si	Silicon
Zn	Zinc

### ***Abbreviations***

A.R.E.	Adam's Riser Equation
ANOVA	Analysis of variance
BCC	Body Centered Cubic crystal structure
EPS	Expandable Polystyrene
GFN	Grain Fineness Number
HCP	Hexagonal Close Packed crystal structure
LFC	Lost Foam Casting
RPM	Revolutions per minute
SEM	Scanning Electron Microscopy
S-L	Solid-Liquid interface
VAC	With vacuum
No-VAC	Without vacuum

## Chapter 1 – Introduction

Magnesium alloys are increasingly used for innovative applications in the automotive and aerospace industries. Primarily, they are employed with the goal of reducing overall vehicular weight and exhaust emissions, thus enabling more efficient vehicles. Advantages of magnesium alloys stem mainly from their low density. In addition to their specific strength, they have excellent ductility and energy absorption capacity. Casting is the primary manufacturing process for these alloys. However, consistent mold filling and defect-free solidification remain as challenges in the production of magnesium castings.

Lost Foam Casting (LFC) is a novel and innovative casting process enabling production of complex castings. Further, the cost of production of these castings by the LFC process is much less relative to the conventional processes, such as sand casting. Over the past 20 – 25 years, almost 30% of the die cast components have come to be produced by the LFC process. Major strides in the LFC of cast irons and aluminum alloys are attributed to significant research and development endeavors of the automotive industry. Much of these are in the development of new polymers, bead expansion techniques, selection of favorable alloys and parameters. Thus, scientific data related to superheats, heat transfer, flow length, etc. are available to a reasonable extent for LFC of cast irons and aluminum alloys.

The phenomenal growth in LFC of cast irons and aluminum alloys has not resulted in a concomitant growth in the LFC of magnesium alloys. In fact, there is very little published research on foam casting of magnesium alloys. Thus, the process data for LFC of magnesium alloys are yet to be developed. In this research, the AZ91E magnesium alloy was selected due to its overall superior properties – castability, mechanical strength and ductility, relative to other magnesium alloys. The aim of this work was to manipulate superheat, mold pressure, casting geometry and foam properties to ensure production of complete castings of good quality.

In addition, computer aided thermal analysis was carried out for the solidification of magnesium alloy castings produced by the LFC process. The casting section thickness, application of vacuum and melt superheat were correlated to the casting quality, solidification characteristics and ensuing alloy microstructure. Development of the  $Mg_{17}Al_{12}$  precipitate in the casting microstructure was also investigated.

## **Chapter 2 – Literature Review**

In this chapter, there is a general description of the lost foam casting process, followed by an introduction to magnesium alloys and their solidification behavior. Microstructural development and precipitation modes in magnesium alloys are explained. Thermal analysis and numerical methods used to evaluate experimental data are discussed.

### **2.1 Lost Foam Casting**

Lost Foam Casting (LFC) is a full mold casting process with expandable polystyrene (EPS) foam as the mold filler.<sup>1</sup> This novel casting process is a viable alternative to the established casting processes, such as sand casting and high-pressure die casting. Extensive research continues to be carried out with the view to understanding the effect of LFC process parameters on the resulting casting quality.<sup>2</sup> General acceptance of the LFC process by the industry is dependent on the foundry's ability to manufacture high-integrity castings of high quality.

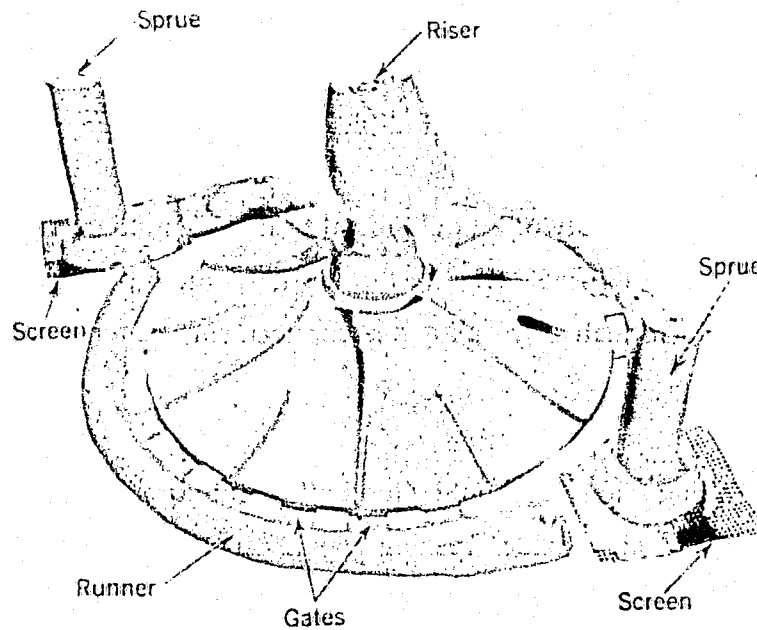
In the LFC process, the foam pattern is an exact replica of the casting to be produced. The foam pattern can be either molded to shape or it can be assembled by cutting foam slabs into pieces and then gluing individual pieces together. In the latter case, hot melt glue is used to join the foam pieces together.

The assembled pattern is coated with a ceramic refractory slurry, which prevents metal penetration to the surrounding sand during mold filling. Further, the ceramic coating also influences the rate of the foam pyrolysis products removal from the casting cavity to the surrounding sand.

After coating, the pattern is placed into a casting flask and loose unbonded sand is poured around it. The mold is then compacted using a vibrating table. The mold vibration is monitored to ensure sand mold integrity for all casting sections.

After compaction of the sand, molten metal is poured directly into the foam pattern, thus initiating pyrolysis of the EPS pattern. Molten metal eventually replaces all of the foam, thus creating a replica of the original foam pattern assembly.

Mold filling and production of internally sound castings are influenced by numerous casting parameters. Foam characteristics, metal pouring temperature, mold medium and coating properties must be controlled to allow proper feeding of the molten metal to the casting cavity. In order to prevent solidification shrinkage, risers may be used. These risers are not a part of the actual casting; however, they are designed to be the last segments of the casting assembly to solidify. Consequently, they provide liquid metal to the adjacent sections of the solidifying casting. Figure 1 shows a typical casting system, including risers, gates and multiple feeding sprues.



*Figure 1: Typical casting system.<sup>3</sup>*

At this point, there is no published research with a unique focus on understanding and optimizing the LFC process for magnesium alloys. Initial research on the LFC of magnesium alloys has been limited to minor modification of the known aluminum LFC process. However, the thermo-physical properties of magnesium alloys are different from those of aluminum alloys. As a result, magnesium alloys were not cast with reasonable success. Ideally, an optimized LFC process for magnesium alloys will enable manufacture of castings with the following qualities:<sup>4</sup>

1. Adequate strength and ductility to compete with other light metal castings for a variety of applications.
2. The best possible mechanical properties for particular high-temperature applications (up to and above the temperature of relatively rapid oxidation of magnesium in air, 400 °C).



3. Minimum macro- and micro-porosity and freedom from hot-cracking, in order to maintain strength and pressure tightness.
4. Satisfactory surface finish.
5. Wide variety of shapes and section sizes.

With respect to the above criteria, magnesium alloys pose a difficult challenge as they tend to solidify rapidly, thus producing incomplete castings. Therefore, a major challenge to successful casting production is the mold filling portion of the casting process.

## 2.2 Mold filling and fluidity

The term fluidity is defined as the ability of a liquid metal to fill the mold cavity.<sup>5</sup> Usually, fluidity,  $L_f$ , is determined by the length of a solidified metal in the casting.<sup>6</sup> Fluidity is a complex property and is affected by a number of variables, such as the alloy's latent heat, surface tension, viscosity and density, as well as the alloy's freezing range.<sup>7</sup>

Alloy fluidity governs the filling rate of the mold. Good alloy fluidity allows filling of the intricate parts of a complex casting. Alloys with a wide freezing range usually have reduced fluidity and have a tendency to deliver partially solidified metal to the casting, whereas pure metals and alloys of eutectic composition are less viscous, flow further than non-eutectic alloys and reproduce details more accurately. In the case of magnesium and its alloys, the variation of enthalpy between the liquid and the solid phase is relatively small. Consequently, less energy needs to be dissipated during solidification of magnesium alloys, which results in their rapid freezing, shorter solidification times and shorter metal flow lengths.<sup>8</sup>

Table 1 compares the enthalpy values for pure Mg and Al metals.

*Table 1: Thermal properties of pure Mg and Al.<sup>9, 10</sup>*

	Enthalpy of fusion [kJ/kg]	Liquid density [kg/m <sup>3</sup> ]	Enthalpy per unit volume [MJ/m <sup>3</sup> ]
Pure Magnesium	368	1610	592
Pure Aluminum	397	2550	1012

Fluidity in the LFC process is affected by the endothermic foam degradation reactions, which occur at the molten metal front.<sup>11</sup> The nature of these reactions may depend on the geometry of the interface between the molten metal front and the region where the solid-EPS degradation occurs.<sup>12</sup>

Further, fluidity is affected by the casting section thickness. It was well established<sup>5, 8, 12</sup> that thinner casting sections promote higher solidification rates. This is due to the fact that the chilling effect of the relatively cold sand mold diminishes with increasing casting modulus. (Casting modulus is defined as the volume to area ratio of the casting,  $V_c/A_c$ .)<sup>5</sup>

The enthalpy of the liquid metal (a function of pouring temperature) is also known to directly affect the alloy fluidity.<sup>8</sup> A superheated metal remains liquid for a longer period of time, thus allowing improved casting fill. (Superheat is defined as the temperature difference between actual pouring temperature and the liquidus temperature of a particular alloy.)

Pan and Liao<sup>13</sup> attempted to synthesize the influence of superheat and other LFC casting variables into one mathematical model, viz.,

$$L_f = \frac{\rho_L a V}{2h(T_M - T_O)} \left( \frac{H}{2} + C_L \Delta T - \frac{L_f \rho_P}{l_c \rho_L} H_E \right) \quad (1)$$

Where:

$V$  = Flow velocity

$a$  = Thickness of the casting

$c_L$  = Specific heat of the liquid metal

$h$  = Heat transfer coefficient at the metal-mold interface

$H$  = Heat of fusion (or latent heat)

$H_E$  = Decomposition energy of the EPS pattern

$l_c$  = Length of the "Characteristic Chill Zone"

$L_f$  = Flow length

$T_M$  = Melting temperature of the metal

$T_O$  = Mold-medium temperature

$\Delta T$  = Degree of superheat

$\rho_L$  = Density of the liquid metal

$\rho_P$  = Density of the EPS pattern

This model was validated for aluminum LFC. However, past research <sup>14</sup> suggests that this model cannot be readily adapted for predicting flow length of magnesium alloys cast by the LFC process. As Equation 1 does not account for the oscillatory nature of the metal flow during mold filling, the calculated results typically overestimated the actual metal flow lengths.

Chvorinov <sup>61</sup> suggested a relationship between the solidification time and the casting geometry:

$$t_f = k \left( \frac{V_c}{A_c} \right)^n \quad (2)$$

Where:

$t_f$  = Local solidification time

$V_c$  = Casting volume

$A_c$  = Casting surface area

$k$  = Chvorinov's constant

$n$  = Chvorinov's exponent

Shivkumar <sup>15</sup> and Okorafor <sup>16</sup> stated that Chvorinov's rule may not be readily applicable to LFC of aluminum alloys, since this model does not account for the energy loss required to degrade the solid-EPS foam. The applicability of this rule for magnesium alloys, however, has never been investigated.

### ***2.2.1 Effect of vacuum***

Often, metal flow in the mold is enhanced by the application of a vacuum (i.e., a negative pressure). However, this is not practical for all manufacturing processes and may lead to undesired casting surface defects, such as mold penetration.

In general, for moderate levels of vacuum, the metal flow length increases with increasing degree of applied vacuum. This can be seen from the work of Liu et. al <sup>17</sup> in Figure 2.

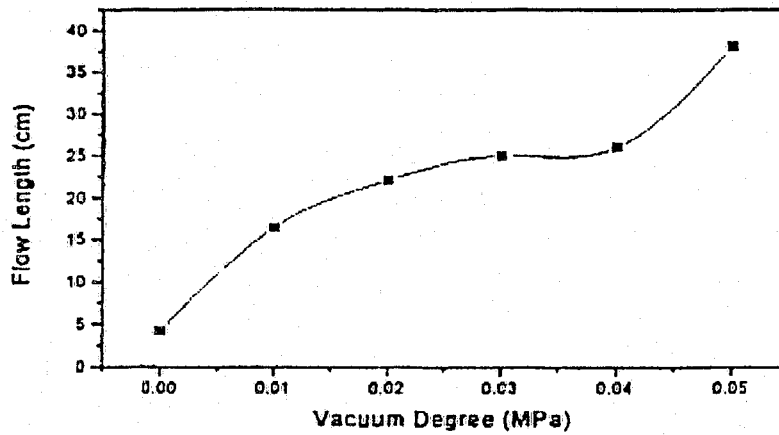


Figure 2: Effect of vacuum level on the metal flow length.<sup>17</sup>

The combined effect of the pouring temperature and the vacuum degree is illustrated in Figure 3 below:

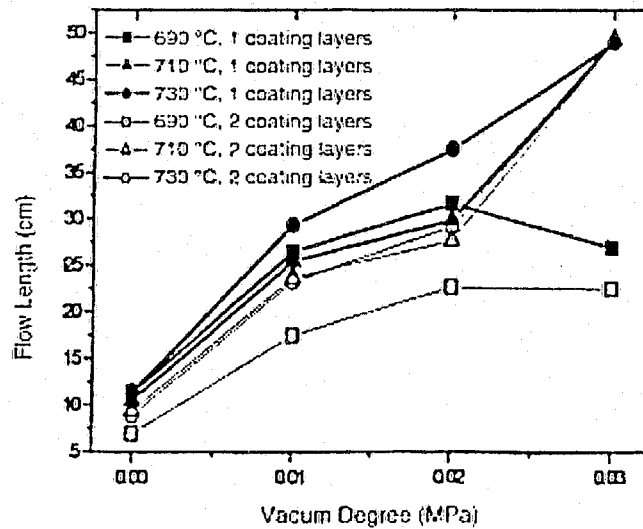
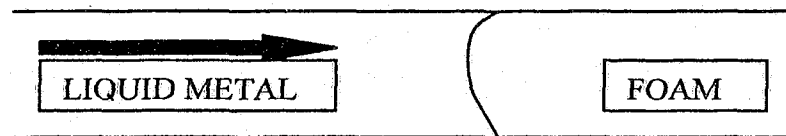


Figure 3: Effect of pouring temperature and vacuum degree on the metal flow length.<sup>17</sup>

Strong interactive effects of vacuum, pouring temperature and the coating thickness were found in Liu's work. Liu et. al. studied the effect of the vacuum gradient on the casting fillability from the points of the metal front profile, the rate of pyrolysis products removal and the heat transfer.

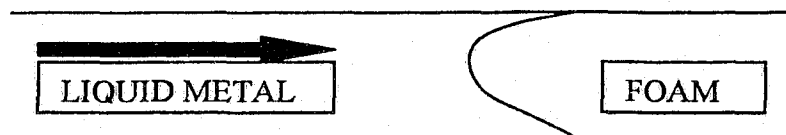
### 2.2.1.1 Effect of vacuum on the metal front profile

Application of a vacuum establishes a pressure gradient from the pattern walls through the coating to the unbonded sand mold.<sup>17</sup> This causes the liquid metal to advance preferentially against the mold walls. The associated change of the metal front profile (from convex to concave) has a great influence on the overall mold filling process. At low vacuum levels, fluidity increases with an increase in the applied vacuum. This is due to the fact that a small pressure gradient changes the curvature of the metal front only slightly (Figure 4). As a result, the foam pattern decomposition products at the metal-foam interface can be effectively and easily removed from the casting cavity.



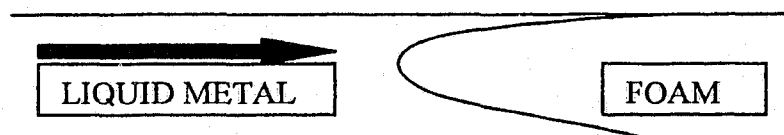
*Figure 4: Metal front profile for a low-vacuum level.*

With a further increase in the degree of vacuum, the metal front at the pattern wall will extend more along the mold walls, as shown in Figure 5. Thus, the decomposition products at the center of the flow channel may get entrapped in the casting. Further, the degradation products will require a longer path to reach the metal-mold interface, consequently hindering the metal flow.



*Figure 5: Metal front profile for an intermediate vacuum level.*

When the vacuum level exceeds a critical value, the metal at the pattern walls will be well ahead of the metal at the channel center, as seen in Figure 6. In this case, the decomposition products accumulated at the center of the casting channel will greatly impede the metal flow. Furthermore, as greater surface area of the liquid metal is exposed to the solid-EPS, higher heat extraction rates from the molten metal are likely to occur. Thus, the molten metal will experience higher cooling rates with attendant rapid solidification.



*Figure 6: Metal front profile for a high-vacuum level.*

#### 2.2.1.2 Effect of vacuum on the pyrolysis products removal rate

Since the typical pouring temperatures of magnesium alloys are relatively low, the EPS pattern decomposition products are primarily liquid.<sup>57</sup> As a result, the gap between the metal front and the receding polystyrene foam may be narrow. Conversely, if the pouring temperature was high, the interface gap would be wider due to the formation of additional gaseous pyrolysis products.

The liquid-EPS products leave the hot metal surface and travel to the relatively cooler coating and much cooler surrounding sand. It is possible<sup>17</sup> that a fraction of the liquid polystyrene begins to harden when the liquid pyrolysis products pass through the refractory coating. Such a phenomenon reduces the coating's permeability and impedes the removal of additional pyrolysis products. Application of vacuum can delay or reduce the possibility of such clogging of the refractory coating pores by assisting the transport of the liquid-EPS products through the coating into the surrounding sand.

#### 2.2.1.3 Effect of vacuum on the heat transfer

Applying vacuum during mold filling influences the overall heat transfer from the molten metal to the surroundings. First, it influences the heat transfer rate. Secondly, it affects the heat transfer mode.<sup>17</sup>

The rate at which EPS pyrolysis products are extracted to the surrounding sand affects the molten metal front chill time. The chill time in turn affects the rate of heat transfer from the molten metal. The chilling occurs due to the contact of the molten metal front with the EPS pyrolysis products. Faster transfer of pyrolysis products from the casting cavity as a result of applied vacuum may reduce the cooling rate experienced by the metal.

In conventional casting processes, heat conduction is the primary mode of heat transfer. However, if vacuum is applied during mold filling, heat transfer due to convection may further contribute to the overall heat transfer rate. Therefore, the solidification rate may increase due to a potential gas flow inside of the mold. Further, the overall heat transfer rate may increase in proportion to the degree of vacuum applied, as higher vacuum levels would draw more gas into the mold.

## 2.3 Magnesium alloys

For many technological applications, magnesium may be suitably alloyed to obtain the required strength, ductility, workability, corrosion resistance and castability.<sup>18</sup>

Solid solubility of one metal in another depends on several factors. Most importantly, both alloying elements should have the same crystal structure. In addition, similarities in atomic size, chemical affinity and electron valency are also imperative to efficient alloying.<sup>19</sup>

Numerous alloying combinations are possible with magnesium alloys to achieve the targeted properties. Zinc is added to improve the room temperature strength and fluidity. Silicon is added to improve creep strength of the alloys by forming  $\text{Mg}_2\text{Si}$  particles on the grain boundaries. Addition of manganese is required to control the corrosion behavior.<sup>20</sup> However, the most commercially used magnesium alloys are those based on the magnesium (Mg) - aluminum (Al) system.

Aluminum is often added to improve castability. This is achieved by a decrease of the freezing range and an increase of the effective superheat. In addition, aluminum improves room temperature tensile properties due to the solid solution strengthening and formation of the  $\text{Mg}_{17}\text{Al}_{12}$  precipitate. However, at temperatures above 150 °C, the beneficial effects of aluminum appear to diminish because of the microstructural instabilities resulting from either coarsening or re-precipitation of the  $\text{Mg}_{17}\text{Al}_{12}$  phase from the supersaturated magnesium grains.<sup>21</sup>

### 2.3.1 Effect of aluminum

Most of the commercial magnesium alloys belong to the binary magnesium-aluminum group (disregarding small amounts of manganese and zinc). The solubility curve of the binary Mg-Al alloys displaces only slightly when either manganese or zinc is added. Thus, for most commercial magnesium alloys, the Mg-Al binary phase diagram, Figure 7, adapted from Beck<sup>22</sup> serves as an accurate means of predicting equilibrium phase development.

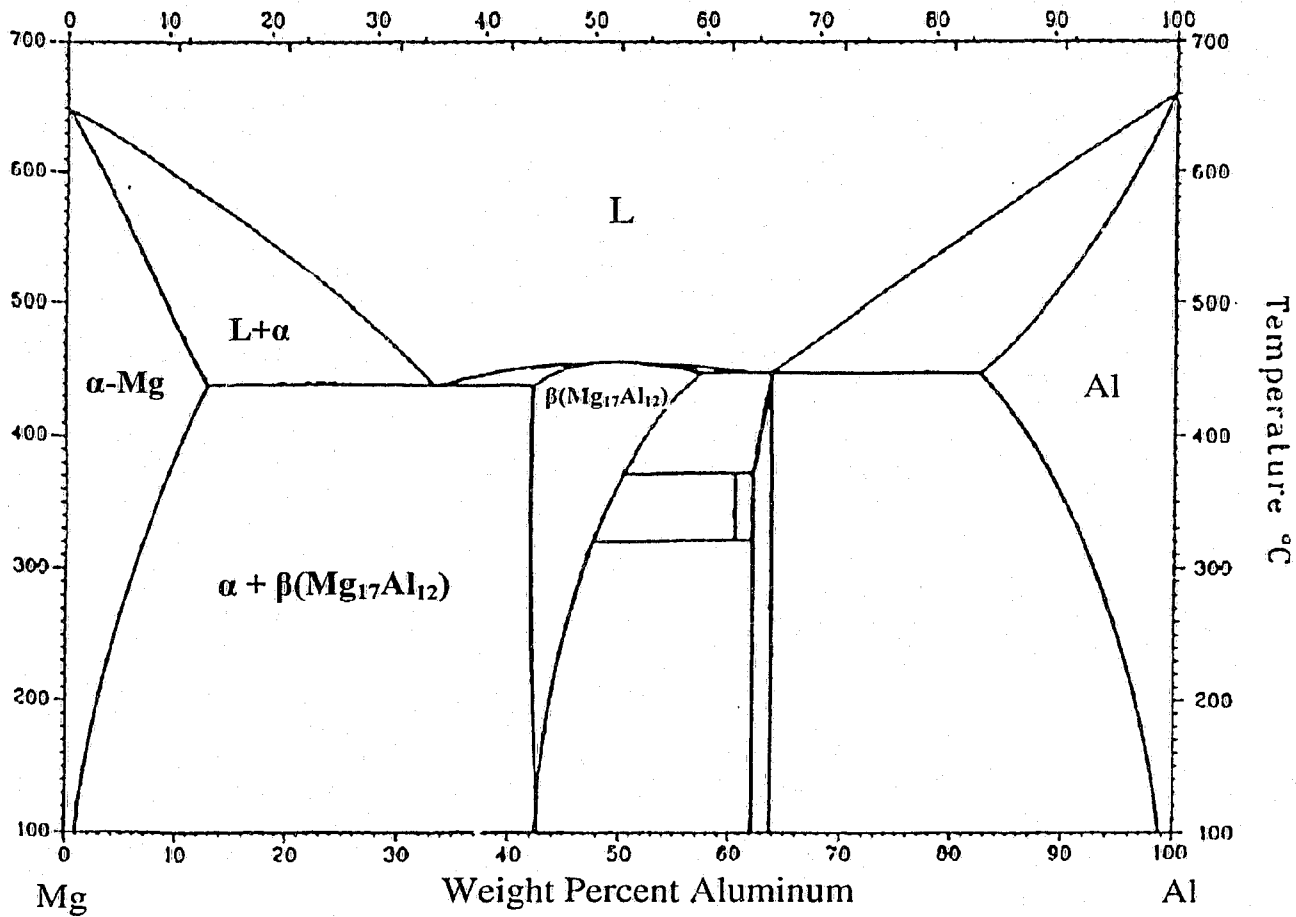


Figure 7: Binary Mg-Al phase diagram.<sup>22</sup>

The morphology of the second phase (Mg<sub>17</sub>Al<sub>12</sub>) depends on the amount of aluminum added. Figure 8, Figure 9 and Figure 10 illustrate the effect of adding aluminum to the magnesium matrix.<sup>20,22</sup> Clearly, the amount of the Mg<sub>17</sub>Al<sub>12</sub> phase on the grain boundaries increases with increasing Al content. In addition, aluminum content in excess of 15 wt% results in the formation of dendritic microstructure.<sup>25</sup> These dendrites nucleate from the primary magnesium grains, while the interdendritic regions are composed of the lamellar eutectic Mg<sub>17</sub>Al<sub>12</sub> phase.



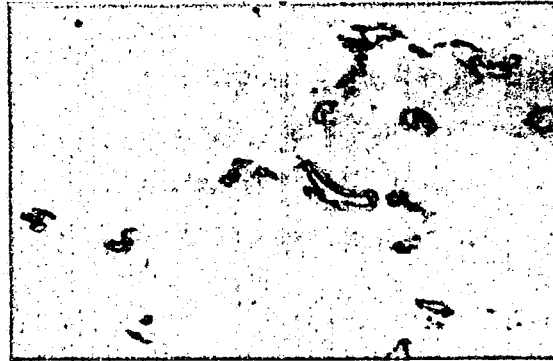


Figure 8: AZ31-3wt% Aluminum, sand cast (x200).<sup>22</sup>

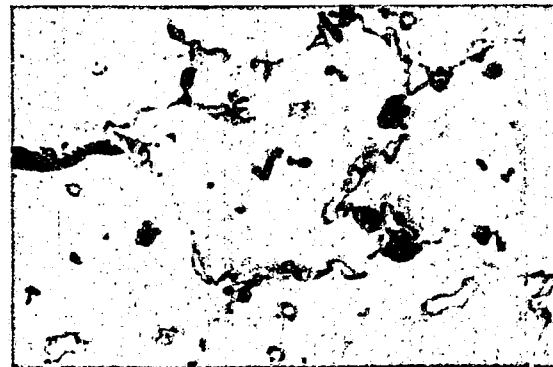


Figure 9: A8-8wt% Aluminum, sand cast (x200).<sup>22</sup>

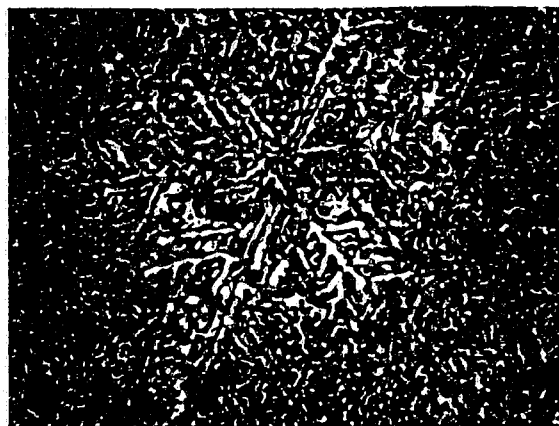


Figure 10: Mg-15wt% Aluminum, permanent-mould cast.<sup>20</sup>

## 2.4 Development of the microstructure

The concept of solidification comprises two basic phenomena: 1) nucleation, and 2) growth of crystals from the liquid melt. By lowering the temperature of the melt below its equilibrium liquidus temperature, the solid phase becomes the thermodynamically stable form of matter, and a transformation from liquid to solid is initiated. The rate of the “liquid  $\rightarrow$  solid” transformation depends on the rate of heat extraction from the system.<sup>23</sup>

During dendritic solidification of castings, several processes take place during alloy's cooling through the semisolid (or mushy) region. These processes include nucleation, crystallization, ripening, interdendritic fluid flow and solid movement. The resulting dendritic structure is greatly affected by the cooling conditions during the early stages of solidification.<sup>24</sup>

Since Mg has a hexagonal-close-packed (HCP) crystal structure, dendrite arms may branch with a six-fold symmetry. Well developed primary  $\alpha$ -Mg dendrites with secondary arms are seen in Figure 10. The growth of the Mg dendrites is sustained by the need to maintain chemical equilibrium in the alloy. In this process, solute is rejected ahead of the growing dendrites.<sup>25</sup>

The maximum solid solubility for aluminum (solute) in magnesium (solvent) at the eutectic temperature is 12.7 wt%Al. A Mg/Mg<sub>17</sub>Al<sub>12</sub> eutectic appears at about 33 wt%Al. The majority of the Mg-Al commercial alloys have Al content below the maximum solid solubility and are hypoeutectic alloys. Ideally, these alloys solidify with a primary  $\alpha$ -Mg phase and a subsequent precipitation of the Mg<sub>17</sub>Al<sub>12</sub> phase from the Mg-Al solid-solution. However, due to non-equilibrium cooling conditions, the Mg<sub>17</sub>Al<sub>12</sub> metastable eutectic develops during solidification and remains in the as-cast microstructure.<sup>20</sup>

### 2.4.1 Equilibrium solidification

The binary Mg-Al diagram can be used to elucidate the equilibrium solidification of the AZ91 alloys. Figure 11 shows the magnesium-rich end of the phase diagram, with a dashed line indicating the composition of the AZ91 alloy.

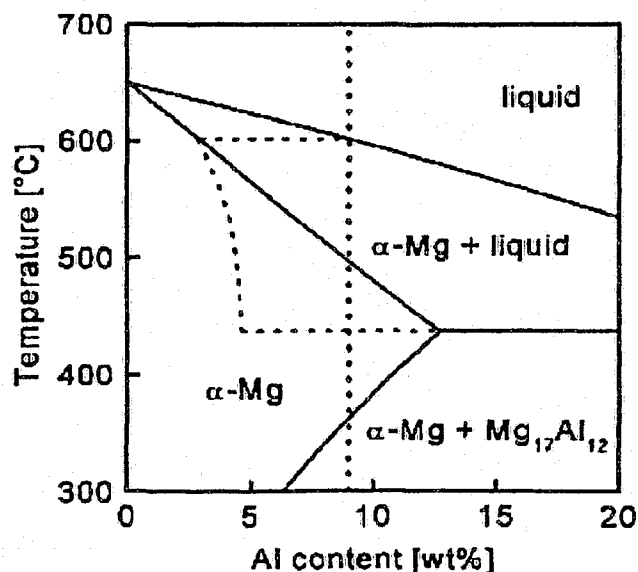


Figure 11: Mg-rich end of the Mg-Al binary phase diagram.<sup>20</sup>

The AZ91 alloy starts to solidify at the liquidus temperature of 595 °C and solidification is complete at the solidus temperature of 470 °C.<sup>6</sup> The Mg-rich section of the binary phase diagram shows a maximum solid solubility of 12.7 wt%Al at the eutectic temperature of 437 °C. Under equilibrium conditions, the Mg-Al alloy should initially solidify as a single phase α-Mg solid solution. Further cooling should lead to the solid-state precipitation of the β-phase within the α-grains.<sup>26</sup>

As evidenced by the microstructure of as-cast Mg-Al alloys, equilibrium solidification almost never takes place. The presence of the metastable eutectic in the as-cast microstructure of virtually all commercial Mg-Al alloys suggests that equilibrium solidification was not followed.<sup>26</sup>

#### 2.4.2 Non-equilibrium solidification

Non-equilibrium solidification begins with the nucleation of primary  $\alpha$ -Mg grains in the temperature range of 600 °C – 650 °C, depending on the aluminum content.

The lamellar eutectic phase ( $\text{Mg}_{17}\text{Al}_{12}$ ) is expected to appear when the aluminum content reaches 33 wt%Al. However, the eutectic phase appears in magnesium alloys containing as little as 2 wt%Al. Therefore, the presence of the  $\text{Mg}_{17}\text{Al}_{12}$  phase in the microstructure is attributed to the non-equilibrium solidification, which causes shifting of the solidus and liquidus lines of the equilibrium phase diagram.<sup>20</sup>

As solidification progresses, the liquid between respective magnesium dendrites (or grains) becomes enriched with solute due to solute rejection (i.e., solute segregation). Solute rejection is the result of the unequal solute diffusion rates in the solid and the liquid phases of the solvent material. Consequently, phases which solidify in the later stages of the solidification process, such as the  $\text{Mg}_{17}\text{Al}_{12}$  eutectic phase, are pushed between the dendrite arms and / or between the magnesium grains. The exact location of the secondary phase depends on the chronological state of the solidification process. As the alloy continues to cool, crystals of hypoeutectic Mg-Al solid solution increase in size, with each layer of atoms added to the crystal surface being richer in aluminum than the preceding one. When the temperature of 470 °C is reached (at which freezing would be complete according to the equilibrium phase diagram) the crystals composition ranges from 1.5 wt%Al at the grain center to approximately 9 wt%Al at the grain surface.

The aluminum concentration in the inter-dendritic regions gradually decreases since some of the aluminum atoms react to form the  $\text{Mg}_{17}\text{Al}_{12}$  phase. The peak in the aluminum concentration occurs at the instant before the  $\text{Mg}_{17}\text{Al}_{12}$  phase precipitates. When the temperature reaches 437 °C, the aluminum concentration at the dendrite edge reaches its maximum of 12.7 wt%Al, which is about 8.5 times that in the dendrite center.<sup>27</sup>

Therefore, the distribution of the solute within the magnesium grains is highly heterogeneous. Further, the departure from equilibrium, caused by the high cooling rates, also affects the  $\text{Mg}_{17}\text{Al}_{12}$  phase morphology.

### 2.4.3 $Mg_{17}Al_{12}$ phase morphology

The  $Mg_{17}Al_{12}$  phase exhibits a wide range of morphologies, depending on the alloy composition and cooling conditions. The morphology may progressively change from fully divorced to partially divorced, granular, fibrous, and finally, to a lamellar structure.<sup>28</sup> The effect of the cooling rate and the solute content on the  $Mg_{17}Al_{12}$  morphology is illustrated in Figure 12.

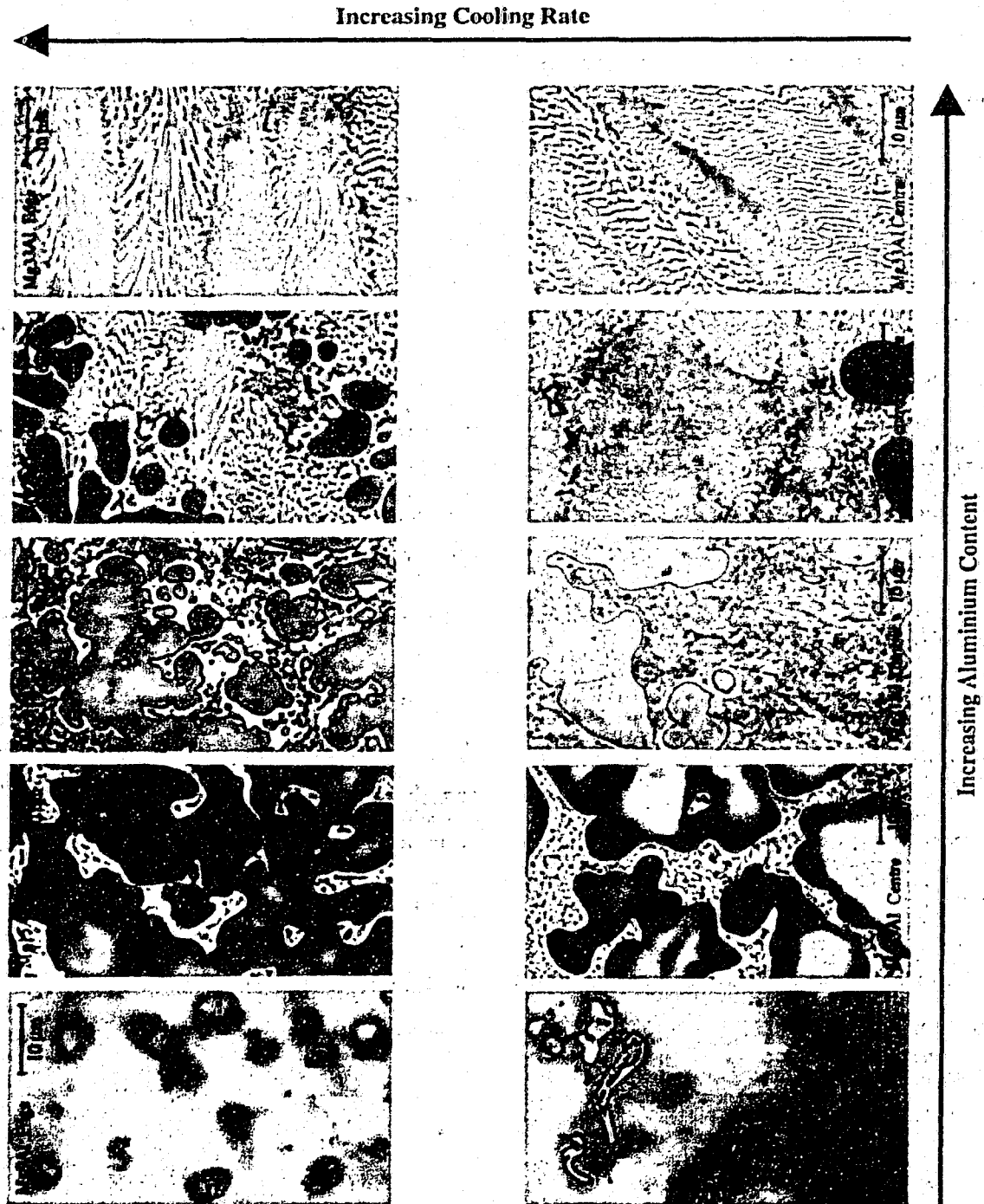


Figure 12: Effect of Al content and cooling rate on the  $Mg_{17}Al_{12}$  morphology.<sup>28</sup>

Alloy cooling rates associated with the conventional casting processes are generally too high to allow equilibrium phase development. Consequently, casting solidification departs from equilibrium predictions, with attendant change in the  $\alpha$ -Mg and the  $Mg_{17}Al_{12}$  phase morphologies. A study on the effect of the alloy cooling rate on the casting microstructure identified several mechanisms of manipulating the casting microstructure via the cooling rate.<sup>28</sup> These are:

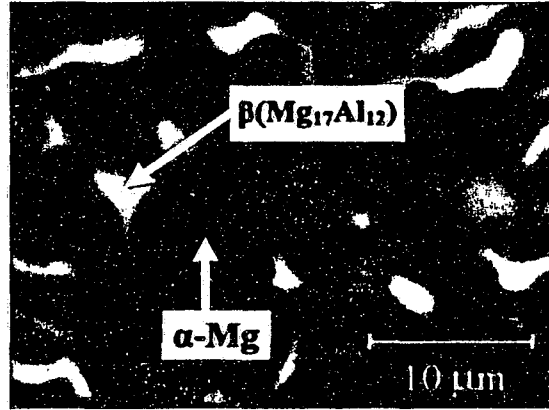
1. It will change the primary magnesium dendrite morphology, which determines the size of the interdendritic regions. Hence, a geometrical constraint on the region where the  $Mg_{17}Al_{12}$  phase can grow is established. Alternatively, variation of the cooling rate affects the number of sites at which the  $Mg_{17}Al_{12}$  phase nucleation may occur.
2. Increasing the cooling rate will lead to lower solute contents in the dendrites.
3. It will modify the gradient of the solute distribution in the liquid ahead of the growing dendrites and therefore the composition profile at the time of the eutectic transformation.
4. It will increase the degree of thermal undercooling before nucleation of the  $Mg_{17}Al_{12}$  phase occurs.

In summary, the cooling rate may dictate the size, shape and distribution of the  $Mg_{17}Al_{12}$  phase in the final microstructure.

When nucleation of the  $Mg_{17}Al_{12}$  phase begins, a halo of this phase deposits on the primary magnesium dendrites. If the cooling rate is slow and the eutectic region is sufficiently large, formation of the  $Mg_{17}Al_{12}$  halo consumes any rejected solute ahead of the solid-liquid interface. Therefore, chemical equilibrium is re-established.<sup>28</sup> In unison with this process, formation of a divorced eutectic or a partially divorced eutectic may occur.

#### 2.4.3.1 Fully divorced eutectic

A fully divorced eutectic morphology is identified by the two eutectic phases ( $\alpha$ -Mg and  $\beta$ -Mg<sub>17</sub>Al<sub>12</sub>) forming separately in the microstructure. Each interdendritic region consists of a single Mg<sub>17</sub>Al<sub>12</sub> particle surrounded by the eutectic  $\alpha$ -Mg, as seen in Figure 13.

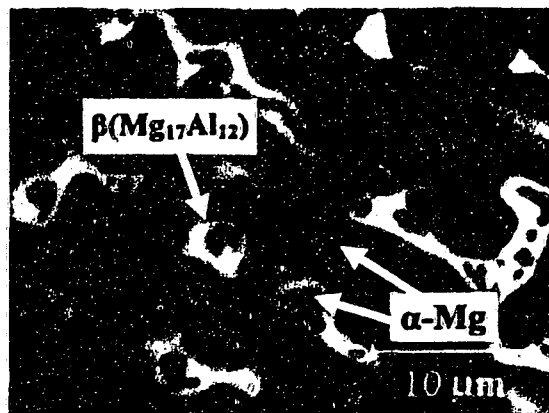


*Figure 13: Fully divorced eutectic microstructure.<sup>20</sup>*

High cooling rates associated with metalcasting result in rapid grain nucleation. Therefore, the interdendritic regions may become isolated from one another. In such cases, the thermal undercooling required for the Mg<sub>17</sub>Al<sub>12</sub> phase nucleation is greater than the undercooling required for the Mg<sub>17</sub>Al<sub>12</sub> particle growth. Consequently, the Mg<sub>17</sub>Al<sub>12</sub> phase solidifies preferentially with a fully divorced morphology.<sup>29</sup>

#### 2.4.3.2 Partially divorced eutectic

A partially divorced eutectic morphology forms under slow cooling conditions and is characterized by islands of eutectic  $\alpha$ -Mg within the Mg<sub>17</sub>Al<sub>12</sub> phase, as seen in Figure 14.



*Figure 14: Partially divorced eutectic microstructure.<sup>20</sup>*

During the last stages of solidification, the amount of developed eutectic phase and its mechanism of formation may affect the mass feeding of the alloy. Independent nucleation and growth of the  $\text{Mg}_{17}\text{Al}_{12}$  phase in the interdendritic liquid is likely to increase the surface area to volume ratio of the feeding channels, thus decreasing the alloy fluidity. On the contrary, concomitant nucleation of the  $\text{Mg}_{17}\text{Al}_{12}$  phase on the  $\alpha$ -Mg grains and the subsequent growth towards the centre of the interdendritic channels may allow the feeding paths to remain open for longer periods of time, thus enhancing alloy fluidity.<sup>28</sup>

Mass feeding during eutectic solidification is also affected by the smoothness of the solid-liquid interface during eutectic growth (i.e., if one of the phases is growing ahead of the other phase during coupled growth). An isothermal, smooth, interface promotes easier mass feeding. An interface in which one of the phases grows with a considerable lead over the other phase would require feeding along increasingly narrower and convoluted paths.<sup>29</sup> Therefore, the morphology of the  $\text{Mg}_{17}\text{Al}_{12}$  eutectic phase is possibly an additional parameter affecting the alloy fluidity.

#### 2.4.3.3 Morphology of the $\text{Mg}_{17}\text{Al}_{12}$ phase

The morphology of the eutectic phase is very sensitive to changes in the alloy composition and cooling conditions. Different morphologies were observed in the same alloy cast under similar conditions or even in nearby regions of the same casting.<sup>22</sup> The predominance of the fully or partially divorced morphologies is mainly a function of the volume fraction of the primary magnesium dendrites, which consequently restrict the eutectic solidification to the interdendritic regions.<sup>25</sup>

The  $\text{Mg}_{17}\text{Al}_{12}$  phase has a body-centered-cubic (BCC) crystal structure and has been reported to form Al plates on the  $(0001)_\alpha$  habit plane.<sup>30</sup> The  $\text{Mg}_{17}\text{Al}_{12}$  phase is often found in the form of a eutectoid structure, precipitated from the solid state. The eutectoid lamellae may follow the crystallographic growth directions of the magnesium HCP crystal structure. Therefore, there may be six growth directions equally prominent along which the  $\text{Mg}_{17}\text{Al}_{12}$  forms. In the case of coarse-grained castings, the lamellae appear to be inclined to each other at a definite angle. On correct positioning of the HCP crystal in the plane of polish, this angle is 60 or 120°. It is also possible that the  $\text{Mg}_{17}\text{Al}_{12}$  precipitate alternatively forms on the HCP pyramidal plane  $(10\bar{1}1)$ , which is the second most densely packed plane of the crystal.<sup>31</sup>



Formation of the lamellar eutectoid by deposition from the supersaturated solid solution is also possible.<sup>32</sup> After a heat treatment at 400 °C, the  $Mg_{17}Al_{12}$  phase may enter slowly into the solution, while the grain boundaries loose their form. Figure 15 and Figure 16 show this phenomenon.

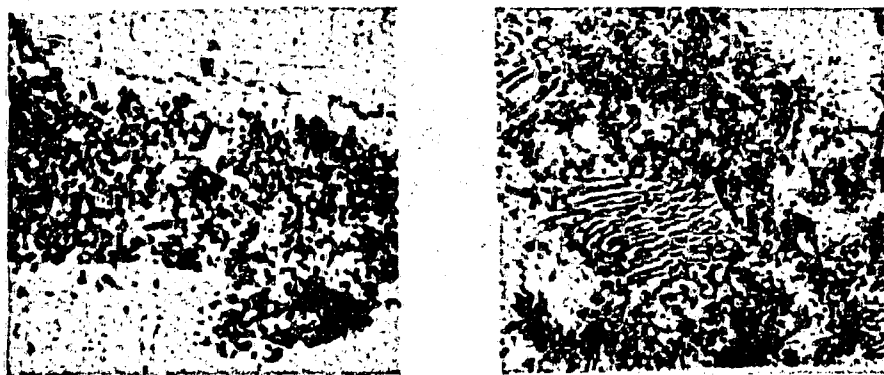


*Figure 15: Eutectoid precipitation in the Mg-6wt%Al alloy (x175).<sup>31</sup>*



*Figure 16: Same as Figure 15; homogenized for 1 hr at 400 °C and slowly cooled (x175).<sup>31</sup>*

In unquenched Mg-Al alloys with over 6 wt%Al, eutectoid in the form of lamellar precipitate forms due to the breakdown of the supersaturated solid solution. Upon heating, the  $Mg_{17}Al_{12}$  phase goes into solution in such a way that the lamellae break up into short pieces and finally into rounded particles.<sup>31</sup> The lamellar breakdown is illustrated in Figure 17.



*Figure 17: Eutectoid structure heated for a short period of time at 400 °C (x400, x500).<sup>29</sup>*

A lamellar structure of the  $Mg_{17}Al_{12}$  phase is desired for good mechanical performance of the alloy.<sup>27</sup> However, since this eutectic is metastable, heat treatment may result in a complete dissolution of the  $Mg_{17}Al_{12}$  phase with consequent loss of strength.<sup>20</sup>

When the formation of the eutectic phase is a secondary process, i.e., it is formed in a small amount within the remaining interdendritic liquid, the typical lamellar symmetry degenerates. When only a small volume fraction of eutectic liquid is present and the cooling rates are high, the eutectic phase forms as discrete large particles around the primary Mg-Al solid solution.<sup>6</sup>

#### 2.4.3.4 Precipitation of the $Mg_{17}Al_{12}$ phase

Completion of eutectic solidification does not necessarily mark the end of phase transformations in the Mg-Al alloys. When the cooling rate is sufficiently slow (typical of sand-casting), precipitation may occur in the supersaturated areas of the  $\alpha$ -Mg grains. Continuous, as well as discontinuous precipitation may be observed in some Mg-Al alloys.<sup>20</sup> Here, strengthening is attributed to the lamellar  $Mg_{17}Al_{12}$  phase formed on the pyramidal or basal planes of the  $\alpha$ -Mg matrix. The shape, orientation and distribution of the precipitate particles are important factors in determining the strength of the alloy.<sup>32</sup>

Magnesium alloys show generally three types of precipitation behavior.<sup>33</sup> These are:

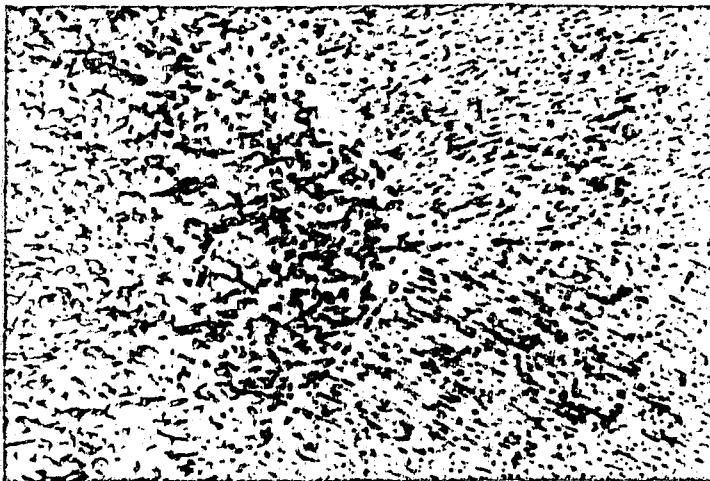
1. The rejection of the equilibrium solute-rich phase with little or no crystallographic coherency with the matrix solid solution. Age hardening is negligible, although some dispersion hardening may result from the precipitate orientation. Mg-Al alloys show this behavior only for narrow compositional ranges and under specific solidification conditions.
2. The formation of the non-equilibrium or transition precipitate which enjoys pronounced coherency with the solid-solution matrix. This precipitate allows the development of true age hardening.
3. The simultaneous recrystallization and precipitation of the equilibrium solute-rich phase at an advancing front throughout individual grains. This process is called "discontinuous precipitation" or "recrystallization reaction".

In general, continuous and discontinuous type of precipitation occurs simultaneously in commercial Mg-Al alloys. Research indicates that the characteristics of the respective precipitates depends on several factors:<sup>34,35,36,37</sup>

1. The discontinuous precipitation is predominant at lower aging temperatures. Above 300 °C, the continuous precipitate, however, is the major type.
2. With higher temperature, longer time and lower aluminum content, the precipitate is coarser and the lamellar spacing of the discontinuous precipitate increases.
3. The continuous precipitate is oriented parallel to the (0001) plane and the  $[1\bar{1}20]$  growth direction of the magnesium matrix.
4. The ratio of the continuous precipitate to the discontinuous precipitate is increased by the formation of  $[10\bar{1}2]$  twins in the alloy before aging.

#### 2.4.3.4.1 Morphology of the continuous precipitate

In continuous precipitation, the new phase precipitates uniformly throughout the matrix and often exhibits a characteristic orientation relative to the parent phase. Furthermore, since lattice coherency usually prevails at the conjugate planes, the precipitates tend to assume a particular shape and lie in a specific orientation with respect to the matrix lattice. It is common to find the precipitates in the form of plates lying parallel to low-index planes of the matrix.<sup>38</sup> The continuous precipitation with a Widmānstätten (or crystallographically oriented) structure is depicted in Figure 18 (a).



(a)



(b)

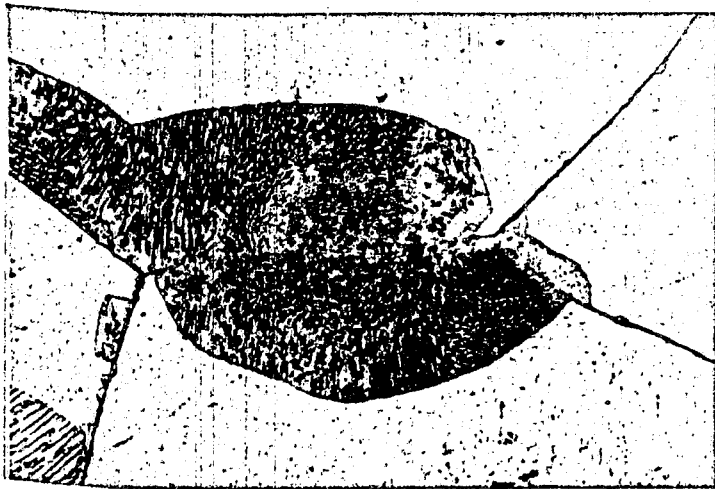
Figure 18: Continuous precipitation of  $Mg_{17}Al_{12}$  in the Mg-8wt%Al alloy; (a) Optical micrograph ( $\times 1000$ )<sup>3</sup> and (b) Scanning Electron Micrograph.<sup>20</sup>

#### 2.4.3.4.2 Morphology of the discontinuous precipitate

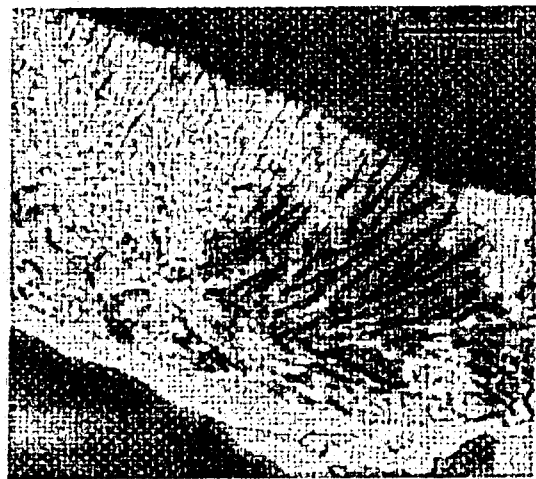
In discontinuous precipitation, the supersaturated matrix decomposes through a reaction involving the formation of colonies of a two-phase mixture, which grows behind a moving boundary, consuming the parent phase. The morphology most often consists of alternating lamellae of the precipitated phase and solute depleted matrix. In contrast to the continuous precipitation, during discontinuous precipitation, the matrix recrystallizes during the eutectic reaction and exhibits a discontinuity in composition and crystallographic orientation across the reaction front.<sup>38</sup>

The bulk of the precipitation in the Mg-Al alloys occurs by discontinuous precipitation. This involves the growth of the lamellar  $Mg_{17}Al_{12}$  precipitate into the  $\alpha$ -Mg grains. The aluminum in the supersaturated dendrite tips detaches from the  $\alpha$ -Mg solid and forms  $Mg_{17}Al_{12}$  lamellae, leaving the  $\alpha$ -Mg between the lamellae depleted in aluminum.<sup>20</sup>

The discontinuous precipitation appears to form in the  $\alpha$ -Mg regions near the eutectic phase, as these regions have higher aluminum content.<sup>3</sup> The discontinuous precipitate is illustrated in Figure 19.



(a)



(b)

Figure 19: Discontinuous precipitation of  $Mg_{17}Al_{12}$  in the Mg-8wt%Al alloy; (a) Optical micrograph (x500)<sup>3</sup> and (b) Scanning Electron Micrograph.<sup>20</sup>

Ternary-based commercial alloys with zinc and up to 10 wt%Al also show discontinuous precipitation. However, when the Al-Zn ratio approaches unity, ternary Mg-Al-Zn alloys cease to form the discontinuous precipitate.<sup>3</sup>

The effect of the cooling rate on the formation of the discontinuous precipitate was also studied.<sup>4</sup> As Figure 20 illustrates, rapidly solidified alloys exhibit relatively homogeneous dispersion of the second phase. However, as Figure 21 suggests, slow cooling rates promote preferential precipitation of the  $Mg_{17}Al_{12}$  phase near the grain boundaries.<sup>22</sup>

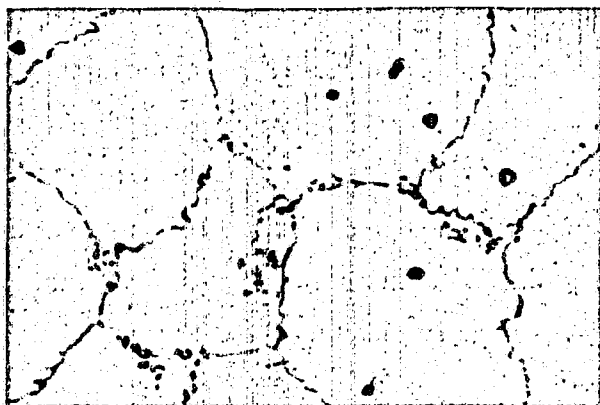


Figure 20: Mg-9wt%Al alloy sand cast and quenched (x200).<sup>22</sup>

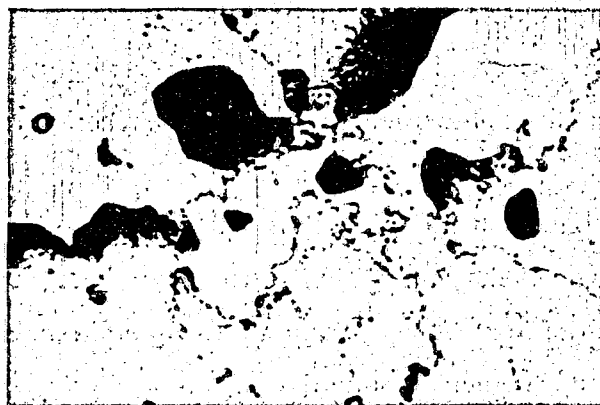


Figure 21: Mg-9wt%Al alloy sand cast and slowly cooled (x200).<sup>22</sup>

## 2.5 Defect formation

Magnesium-aluminum alloys have a relatively wide freezing range. As a result, they are susceptible to a variety of casting defects including segregation, porosity and hot tearing. Until now, alloy optimization to minimize porosity has not been undertaken to the same degree as it has been done for the traditional Al-Si alloys.

The microstructure in magnesium castings is highly non-uniform. Most of the intermetallic phase segregates to the last regions to solidify. Since castings are not heat-treatable, the phase and solute non-uniformity cannot be reduced by heat treatment.<sup>27</sup> Therefore, it is vital to minimize casting defects in the as-cast condition of the alloy.

### 2.5.1 Porosity

The level of porosity and its distribution within the casting are critical factors affecting casting quality.<sup>39</sup> Porosity manifests itself in various forms: massive shrinkage cavities, dispersed gas pores or macro- and micro-porosity.

The density of the liquid AZ91E alloy is approximately 4% lower than that of the solid alloy. Consequently, a casting will experience volumetric contraction during the solidification process. This volumetric contraction must be compensated for by a change in the outer contours of the casting or by formation of internal cavities, i.e., porosity. While the solidification shrinkage in pure metals and alloys with narrow solidification intervals commonly causes formation of macroscopic cavities (located in the last regions to solidify), alloys with long freezing ranges tend to form distributed microporosity.<sup>40</sup>

Solidification shrinkage and the evolution of dissolved gas occur in unison and act collaboratively to form microporosity. As a result, mass feeding during the last stages of solidification is an important factor affecting the volume fraction of the casting porosity.<sup>20</sup>

Porosity in the Mg-Al alloys was seen to correlate with the solute concentration in the alloy, as observed in Figure 22. The peak in the casting porosity at about 9 wt%Al was related to the worst combination of long mushy zone, poor interdendritic feeding and high eutectic volume fraction.<sup>20</sup>

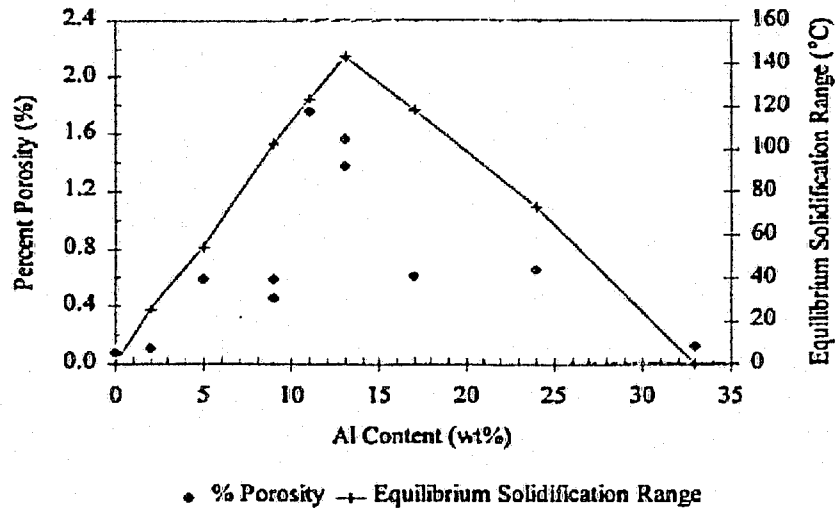


Figure 22: Effect of Al content on the casting porosity.<sup>20</sup>

#### 2.5.1.1 Shrinkage porosity

The main disadvantage of the AZ91 magnesium alloys is their tendency to form shrinkage porosity. This type of porosity, seen in Figure 23, results from solidification shrinkage that is not compensated for by feeding of liquid metal to the interdendritic regions.<sup>41</sup> This defect significantly lowers the tensile strength, elongation and pressure tightness of the casting. Implementation of chills and risers in a casting design may decrease the probability of nucleating shrinkage cavities by effectively feeding liquid metal to the interdendritic regions during casting solidification.<sup>41</sup>

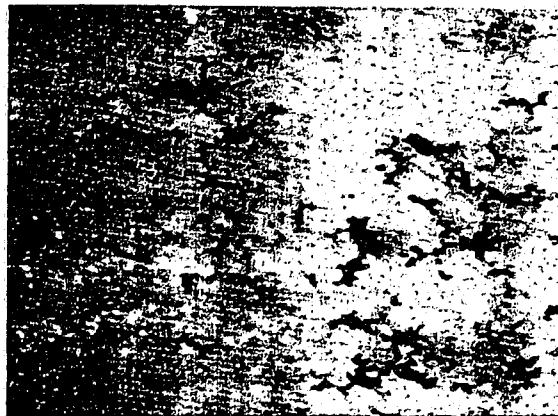


Figure 23: Typical shrinkage microporosity in Mg-Al castings.<sup>41</sup>

The volume fraction of shrinkage porosity may be further reduced by establishing directional solidification. During directional solidification, the alloy may solidify at the mold walls, while the center of the flow channel remains open. The bulk flow ceases when the metal front sluggishness is significant enough to cause flow stoppage.<sup>42</sup> Even though beneficial, directional solidification must be carefully controlled. Significant melt superheating is often employed to ensure delivery of the molten metal to all sections of the casting. This can result in overheating of the mold walls, which causes them to remain hot over a longer periods of time. Such non-uniform mold temperature may be conducive to the formation of shrinkage porosity in other areas of the casting.<sup>22</sup>

### 2.5.1.2 Gas porosity

Gas porosity in magnesium alloy castings is mainly attributed to the high solubility of the hydrogen gas in liquid magnesium. As can be observed in Figure 24, magnesium alloys have a very high affinity to absorb hydrogen from the surroundings during melting operations. Further, owing to their low specific gravity and their tendency to oxidize in the liquid state, magnesium alloys are also prone to form gas bubbles filled with oxide skin.<sup>43</sup>

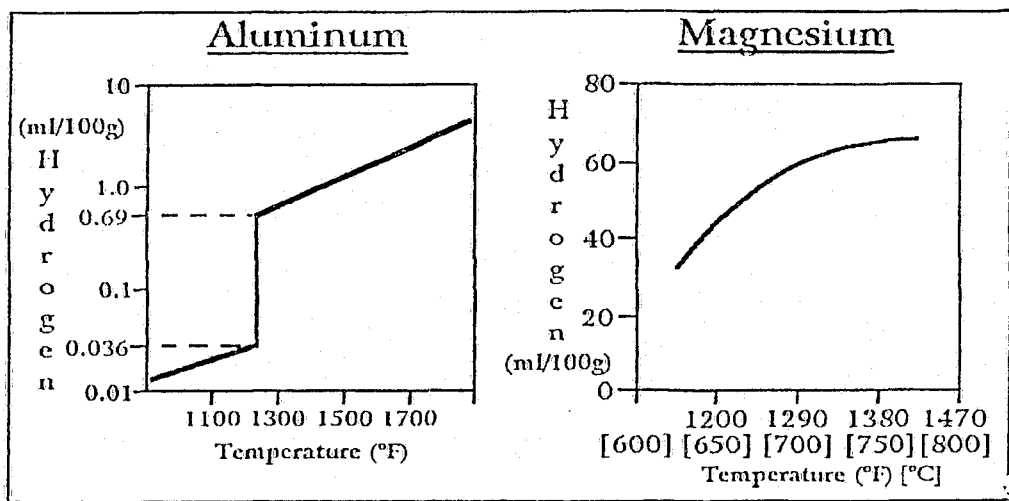


Figure 24: Hydrogen gas solubility in molten Al and Mg.<sup>43</sup>

Criterion functions, discussed in Section 2.7, were developed to predict the levels of microporosity in castings. Niyama, LCC and FI criterion functions, for example, were employed to predict microporosity levels in aluminum alloys cast by the LFC process.<sup>12</sup> These functions showed reasonably good correlation with experimental results; however, their suitability for magnesium alloys is unknown.



### 2.5.1.3 Solute segregation and porosity

In alloys where the volume fraction of the eutectic is sufficiently high to form a continuous network along grain- and dendrite-boundaries, macroscopic flow of the eutectic phase is possible. Therefore, the last regions to solidify may act as a feeder for the surrounding parts of the casting. This results in a higher volume fraction of micropores in these regions. Since the moving liquid is enriched in the alloying elements, this mechanism also promotes macrosegregation.<sup>40</sup>

Porosity in magnesium alloys was found to correlate with the distribution of Al and Zn in the casting.<sup>41</sup> This trend was attributed to the inverse segregation phenomenon. During inverse segregation, melt enriched in alloying elements is drawn outwards to the colder regions by the growing shrinkage cavities, causing an interdendritic flow. Such mechanism results in an interdendritic porous network with regions depleted in Al and Zn.<sup>41</sup>

### 2.5.1.4 Adam's Riser Equation

Adam's Riser Equation (A.R.E.) is based on the optimal relationship between the local solidification times of the riser and the casting. This model correlates the volumes of the riser and the casting to the surface areas of the riser and the casting.<sup>44</sup>

$$(1 - \beta) \left( \frac{V_r}{V_c} \right) = \frac{A_r}{A_c} + \beta \quad (3)$$

Where:

$V_r$  = Volume of the riser

$V_c$  = Volume of the casting

$A_r$  = Surface area of the riser

$A_c$  = Surface area of the casting

$\beta$  = Amount of solidification contraction =  $(\rho_{\text{solid}} - \rho_{\text{liquid}}) / \rho_{\text{solid}}$

The amount of solidification shrinkage is related to the geometry of the casting via the  $V_r/V_c$  and  $A_r/A_c$  ratios. Based on Adam's theory, a prediction line can be drawn on the  $V_r/V_c$  vs.  $A_r/A_c$  graph. The region below the A.R.E. line corresponds to castings with no porosity, while the region above the A.R.E. line corresponds to casting conditions where solidification shrinkage will occur (see Figure 39).

The solidification contraction,  $\beta$ , is material specific. If there is no solidification contraction, i.e.,  $\beta = 0$ , then the density of the liquid metal is the same as the density of the solid metal. For all commercial metals, however, this is never the case.

## 2.6 AZ91E density

The density of the AZ91 series alloys at room temperature is  $1.810 \text{ g/cm}^3$ .<sup>9</sup> Deviations from this value can be attributed to the solidification mode associated with the various casting processes and casting geometry. For example, Figure 25 depicts the effect of pouring temperature on the alloy density.

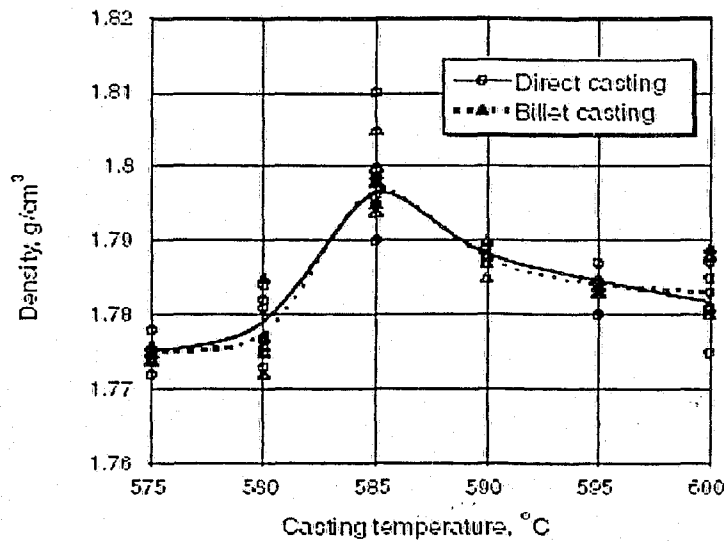


Figure 25: Effect of casting temperature on the alloy density.<sup>45</sup>

Casting density can be related to the average casting porosity. This relationship can be expressed on the percentage basis as:

$$\% \text{Porosity} = \left( \frac{\text{Theoretical\_density} - \text{Experimental\_density}}{\text{Theoretical\_density}} \right) \times 100\% \quad (4)$$

## 2.7 Thermal analysis

There are many techniques, such as the Differential Thermal Analysis (DTA), Diffraction Scanning Calorimetry (DSC) and Thermo-Gravimetric Analysis (TGA) available for investigating solidification of alloys. Unfortunately, these methods often prove to be inadequate for investigating the non-equilibrium solidification of castings, since they are designed to measure only equilibrium properties.<sup>46</sup>

Thermal analysis is a reliable technique to study solidification of castings. The first step involves the recording of the temperature data as the alloy cools through its freezing range. The second step is to plot the temperature versus time, which gives the cooling curve of the alloy. Thermal analysis is the study and interpretation of such cooling curves.<sup>41</sup> Figure 26 is a sample cooling curve (obtained in this research) with its first derivative plot.

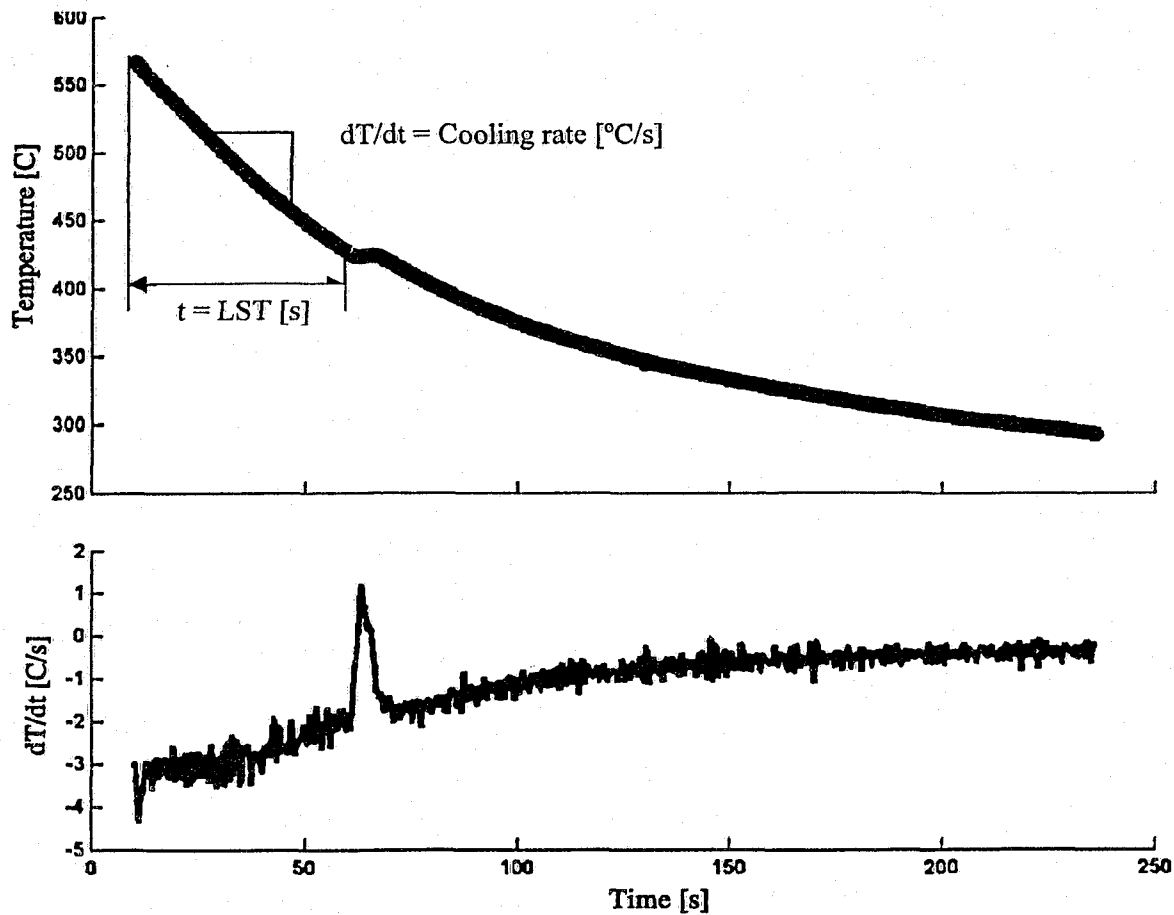


Figure 26: Typical cooling curve for the AZ91E alloy.

Parameters relating to the thermal analysis may be defined and used in further analysis of the casting solidification process. The fundamental parameters are:

*Local Solidification Time, LST ( $t_f$ )* – time required for the metal to cool from the liquidus to the non-equilibrium solidus temperature.<sup>12</sup>

*Cooling Rate, CR ( $dT/dt$ )* – rate of temperature drop between the liquidus and the solidus temperatures.

*Solidus Velocity ( $V_s$ )* – velocity of the solidus wave, calculated as  $V_s = d/\Delta t$ , where  $d$  is the distance between two thermocouples and  $\Delta t$  is the difference in local solidification times.  $V_s$  indicates the time available for feeding during the last stages of solidification.

*Temperature Gradient ( $G, dT/dx$ )* – temperature drop between two adjacent locations within the casting.

The above parameters were observed to have a strong relationship with porosity formation in various castings. Therefore, thermal analysis parameter based criterion functions were experimentally developed in an attempt to correlate the thermal analysis results to the casting porosity.<sup>12</sup> The most popular are:

Thermal Parameter Index, TPI:

$$TPI = GV_s \quad (5)$$

Freezing Index, FI:

$$FI = G/t_f \quad (6)$$

Gradient Acceleration Parameter, GAP:

$$GAP = GV_s / t_f \quad (7)$$

Niyama function:

$$Niyama = G / (CR)^{0.5} \quad (8)$$

LCC function:

$$LCC = Gt_f / V_s \quad (9)$$

The significance of these parameters on the actual physical phenomena was studied extensively <sup>5, 12</sup> and the following conclusions were asserted:

1. A large temperature gradient corresponds to an effective interdendritic feeding.
2. LST increases as casting section thickness increases. A steep LST profile indicates that directional solidification was established in the casting during solidification.
3. For long castings, the lowest point of the temperature gradient profile is usually in the middle of the casting. This indicates a hot spot that served as a feeder to the adjacent locations of the casting.
4. A logarithmic relationship was found between casting density and the temperature gradient. Steep temperature gradients narrow the mushy zone, thus increasing the probability of directional solidification.
5. An increase in the casting density was associated with a decrease in solidus velocity.

### ***2.7.1 Computer Aided Cooling Curve Analysis***

Computer-Aided Cooling Curve Analysis (CA-CCA) of alloys is used extensively for the evaluation of processing and material parameters. It is implemented to predict alloy composition, latent heat of solidification, evolution of the solid fraction, the amounts and types of phases that solidify and even melt flow stoppage point.<sup>47</sup>

The shape of the cooling curve is the result of the heat lost to the surroundings by the solidifying metal. The various events that can be observed on the cooling curve may be associated with the various transformations occurring in the alloy during solidification.

The use of the cooling curve first derivative plot, which is the cooling rate, further improves the accuracy of determination of the characteristic features of the cooling curve. A zero value on the first derivative curve indicates a minimum or maximum on the cooling curve. Thus, the time-temperature coordinates can be precisely identified.

### 2.7.2 Data smoothing

Superimposed upon and indistinguishable from the primary output of any experiment in which quantitative information is extracted, are random errors which, regardless of their source, are characteristically described as noise.<sup>48</sup> It is of fundamental importance to remove as much noise as possible without degrading the underlying information. Therefore, the methods of data filtering are important both as an end in themselves and as a prelude to the further treatment of the experimental data. In this research, data smoothing techniques were used to reduce noise from the temperature vs. time data collected during casting solidification.

#### 2.7.2.1 The method of "Least-Squares"

When experimental data is available in high densities, the least squares fit is often used to rid the experimental data of noise. The method of least squares filtering attempts to fit a curve through a set of data points. For example, a cubic curve  $y = a_3x^3 + a_2x^2 + a_1x + a_0$  can be used to fit the experimental values.

The  $a$ 's are to be selected such that when each abscissa point is substituted into this equation, the square of the differences between the computed numbers,  $y$ , and the observed numbers is a minimum for the total of the observations used in determining the coefficients. All of the error is assumed to be in the ordinate and none in the abscissa.<sup>48</sup> Other data fitting curves, such as exponentials, may also be used for data smoothing.

## Chapter 3 – Experimental Procedure

This chapter outlines the experimental plan and the related details. Pattern assembly, mold assembly, casting procedures, data acquisition for thermal analysis and metallographic procedures are described.

### 3.1 Project structure

This project required co-operation between Ryerson University's Centre for Near-Net-Shape Casting Facility and CANMET's Material Testing Laboratory, in Ottawa. CANMET-MTL facilities were used for melting and casting the AZ91E alloy in a controlled environment, which included degassing and melting of the alloy under suitable protective atmosphere.

The experiments were designed with a view to investigating the effect of the following LFC process parameters on the casting quality and mold filling characteristics:

- Vacuum level
- Pouring temperature
- Foam density and bead fusion
- Casting section thickness

Figure 27 shows a flow chart of the experiments carried out. Each branch of the flow chart represents one casting trial. In order to verify data repeatability, all casting experiments were repeated at least once. Thus, a total of 20 castings were produced, including several trial-and-error castings to optimize the LFC process.

The experimental alloy (AZ91E) was poured under vacuum and no-vacuum (gravity) conditions at two temperatures of 660 °C and 700 °C. Two densities of foam (0.0208 g/cm<sup>3</sup> and 0.0256 g/cm<sup>3</sup>) and four different section thicknesses (1.0 cm, 1.5 cm, 2.0 cm and 2.5 cm) were used to study the solidification process.

Vacuum:

Pouring  
temperature:

Foam density /  
bead fusion

Section  
thickness:

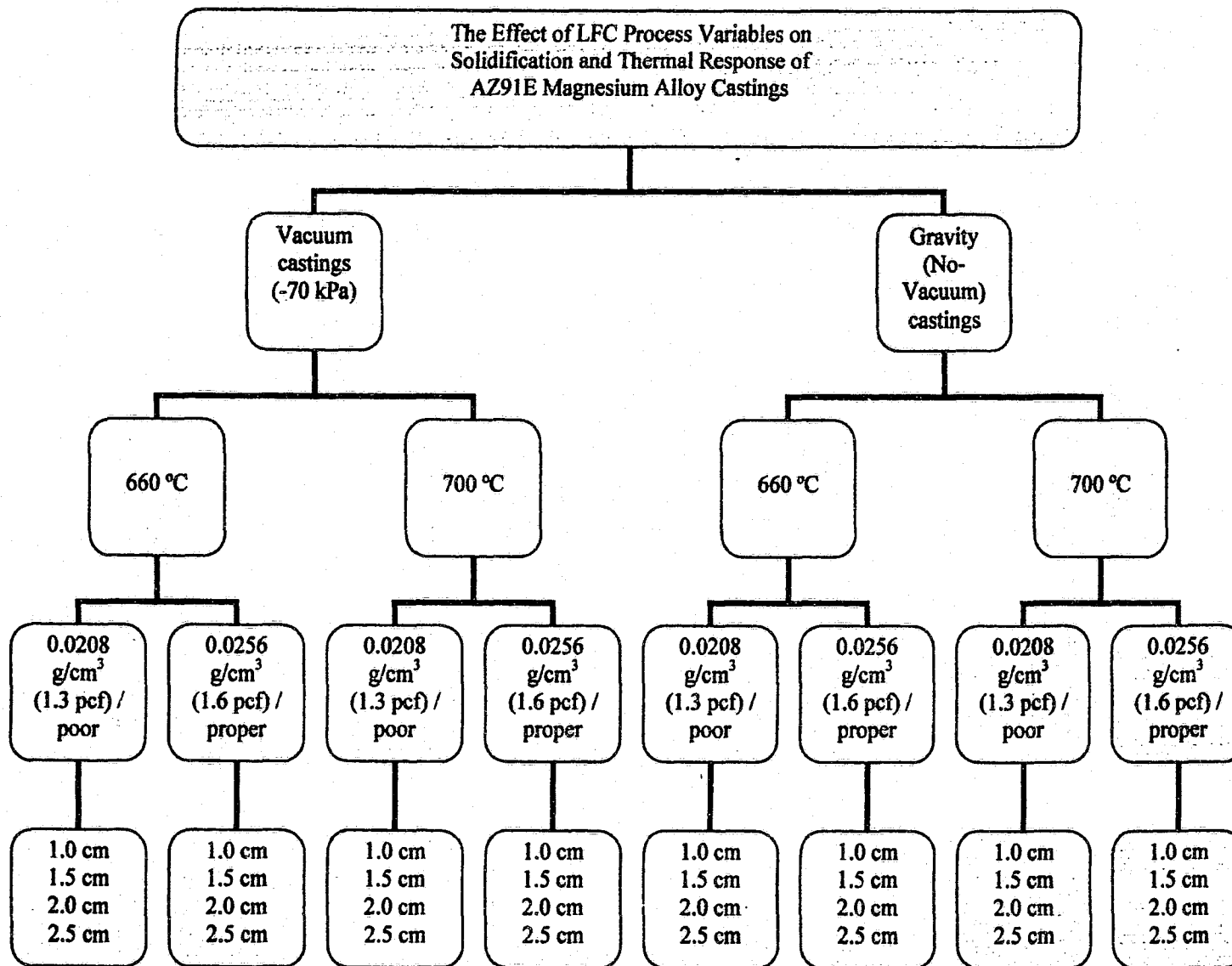
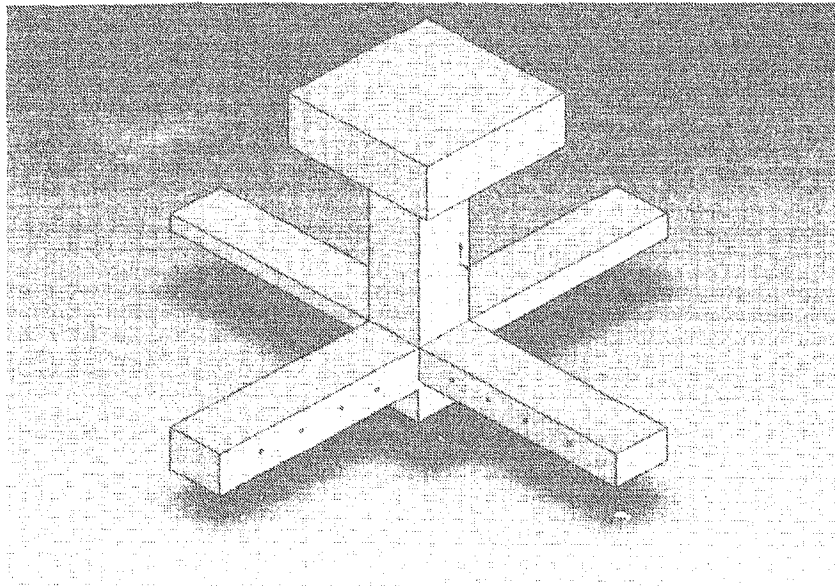


Figure 27: Experimental plan.

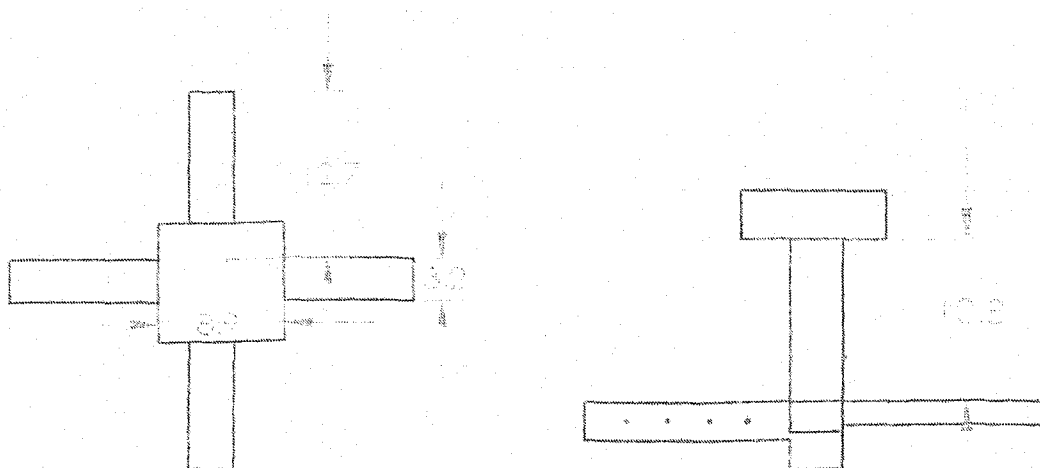


### 3.2 Pattern assembly

It was necessary to investigate the effect of the casting section thickness on the metal flow behavior and solidification characteristics. A foam pattern seen in Figure 28 and Figure 29 with four horizontal bars was constructed. The individual bars were 1.0 cm, 1.5 cm, 2.0 cm and 2.5 cm thick.



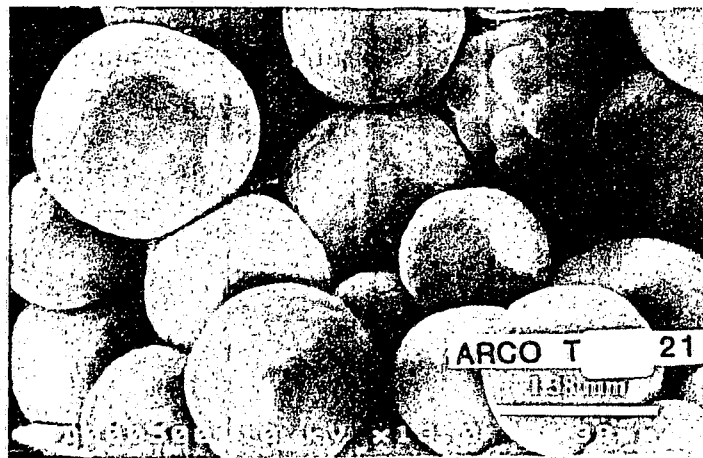
*Figure 28: 3D View of the casting foam pattern.*



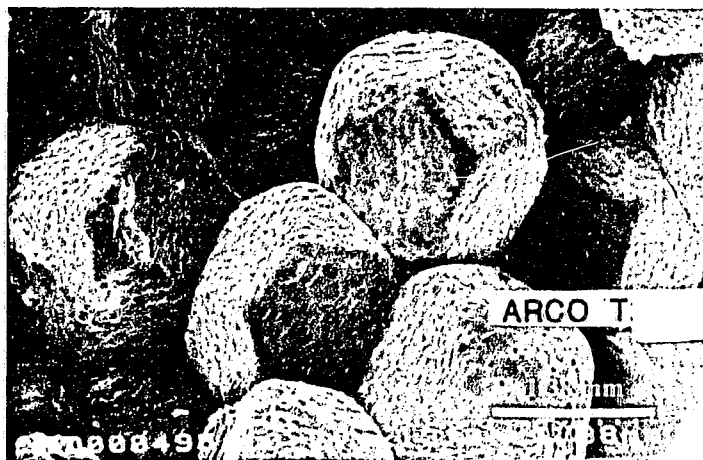
*Figure 29: Dimensions of the pouring biscuit and overall bar dimensions, in cm.*

Patterns were constructed by cutting polystyrene foam slabs of two known densities:  $0.0208 \text{ g/cm}^3$  (1.3 pcf) and  $0.0256 \text{ g/cm}^3$  (1.6 pcf). As they were obtained from two independent suppliers, these foam slabs also had different levels of bead fusion. The low-density foam slab had poorly fused beads, while the high-density foam slab had properly fused beads. The degree of bead fusion was qualitatively assessed by visual inspection according to the industry standards.

The following SEM images, Figure 30 and Figure 31, illustrate the distinction between the two different levels of bead fusion for the ARCO T21 foam.



*Figure 30: Poorly fused ARCO T21 foam.<sup>49</sup>*



*Figure 31: Well fused ARCO T21 foam.<sup>49</sup>*

All individual foam pieces were cut with a Nichrome hot wire. The pattern was assembled using a hot melt glue (Styrobond 527) by applying a thin layer of molten glue to the mating surfaces to be joined. Any excess glue was immediately removed.

### **3.3 Ceramic coating slurry**

The ceramic coating slurry used in this research was the low-refractory StyroShield 6450, obtained from HA International, Inc. Prior to use, the coating slurry was mixed for 20 minutes to ensure a homogeneous distribution of the refractory particulates. Also, the specific gravity of the coating slurry was adjusted to a 40 Baume level. The coating slurry viscosity was measured with the Brookfield RVDV+ProII viscometer. The measured viscosity was 357 cp at 20 °C.

The foam pattern was dipped into the pail with the slurry and then placed into a rotating machine. This machine continuously rotated the foam pattern to ensure uniform coating thickness. After 5 minutes of rotating, the coating was dry to the touch and the pattern was placed into a circulating hot-air oven. The free-stream temperature in the oven was set to 54 °C (130 °F) and the pattern was allowed to dry for a minimum of 12 hours.

### **3.4 Installation of thermocouples**

In order to collect real-time temperature data of the solidifying casting, 16 K-Type thermocouples were installed in the foam pattern, 4 per horizontal bar.

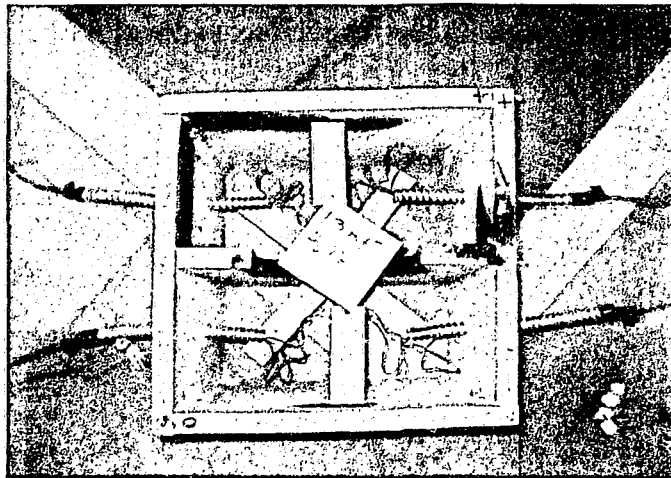
The thermocouples were connected to a Daytronic System10 DataPac data acquisition unit. The data acquisition system was calibrated (Fluke 714 temperature calibrator) prior to use. Also, every thermocouple was tested for functionality prior to being installed into the foam pattern. For each experiment, temperature data was collected for a total of 360 seconds at a rate of 7 readings / second.

### **3.5 Casting box**

A new casting box was designed to enable easy installation of the thermocouple probes into the foam pattern (Figure 32). The foam pattern was positioned diagonally in the box. Thermocouple wire conduits were installed in the walls of the wooden box to allow accurate placement of the thermocouples. These conduits were covered with plastic sheathing, to prevent vacuum leak during experiments. Also, entrances

of the conduits into the wooden box were sealed with plumber's putty to prevent vacuum leaks. All internal edges of the box were sealed with a commercial grade silicone to prevent vacuum leaks through the sides of the mold box.

A 19 mm hole was drilled in the bottom of the casting box to facilitate connection of a vacuum exhaust fitting. This hole was covered with a steel mesh (WS Tyler M100) from the inside of the box. The purpose of the mesh was to prevent contamination of the vacuum system with fine dust and molding sand particles.



*Figure 32: Top view of the casting box with instrumented foam pattern.*

### **3.5.1 Mold medium**

In order to prevent dangerous reactions between the liquid magnesium and the surrounding mold medium, sodium-silico-fluoride (Na-SiF) inhibitor was used in conjunction with the synthetic mullite sand (AFS35 GFN). The inhibitor was mixed into the sand in the ratio of 1.16 kg of Na-SiF inhibitor for every 100 kg of sand.

### *3.5.2 Mold vibration*

After installing the coated foam pattern into the casting box, loose mullite sand was rained around it. Extreme caution was taken to prevent loosening of the thermocouples from the foam pattern. When the sand level reached the pattern's pouring biscuit, a steel pouring cup was placed over the foam biscuit. Then, sand filling continued until the sand level reached the top of the steel pouring cup. The entire mold was vibrated for 1 minute at 1 g acceleration. The acceleration was monitored with the IRD Mechanalysis 838 accelerometer.

For casting trials under vacuum pressure, the top of the casting box was sealed with a clear PVC sheet. Figure 33. This sheet overlapped the edges of the casting box and was further secured with several layers of duct tape.

When the vacuum was applied during mold filling, a pressure transducer continuously monitored the vacuum pressure in the system manifold.



*Figure 33: Sealing of the casting box with a PVC sheet.*

### 3.6 Melting

Melting and casting of the magnesium alloy AZ91E was carried out by the technical staff at CANMET-MTL facility. The AZ91E alloy was melted in an electric resistance furnace under 0.5% SF<sub>6</sub> + CO<sub>2</sub> protective atmosphere. The melt was prepared from a virgin ingot supplied by the Near-Net-Shape Research Group. The chemical composition of the alloy is given in Table 2.

Table 2: Chemical composition of AZ91E, in wt%.<sup>9</sup>

	Al	Mn	Zn	Si	Fe	Cu	Ni	other	Mg
AZ91-E	8.1 – 9.3	0.2 – 0.4	0.4 – 1.0	0.20 (max)	0.005 (max)	0.015 (max)	0.0010 (max)	0.31	balance

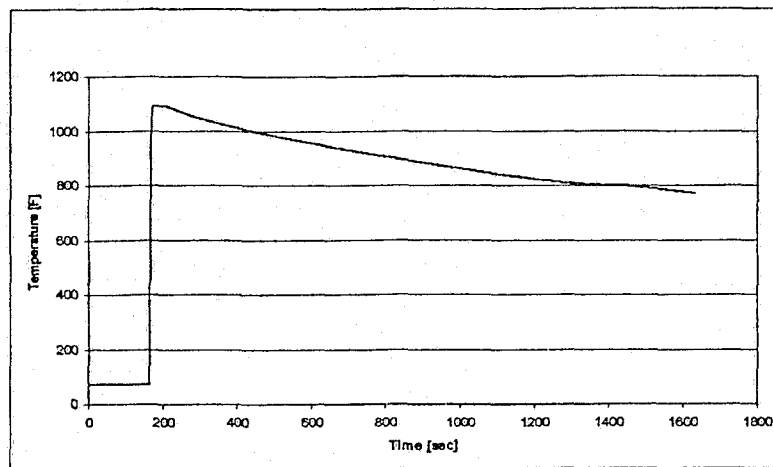
The castings were produced on June 7, 2004 (700 °C) and June 24, 2004 (660 °C). A total of 27.5 kg of AZ91E was melted in a steel crucible. After melting the alloy in the crucible, degassing was carried out with argon gas for 10 minutes. Table 3 illustrates the sequence of events that occurred:

Table 3: Typical casting sequence.

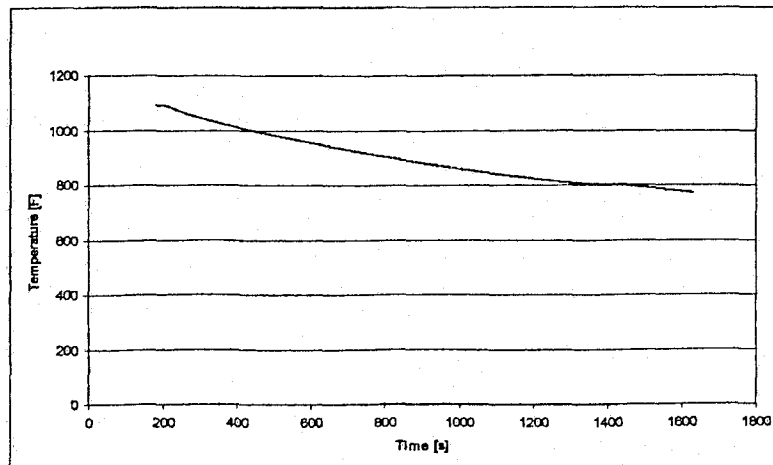
Step	660 °C Pouring Temperature	700 °C Pouring Temperature
1	Furnace was charged	Furnace was charged
2	Melting of alloy completed. Hold at 660 °C	Melting of alloy completed. Hold at 700 °C
3	Degassed with Ar for 10 min at 661 °C	Degassed with Ar for 10 minutes at 720 °C
4	Casting 1 – 1.3 pcf, -70 kPa, 660 °C	Casting 1 – 1.6 pcf, -78 kPa, 701 °C
5	Casting 2 – 1.6 pcf, -70 kPa, 660 °C	Casting 2 – 1.3 pcf, -68 kPa, 701 °C
6	Casting 3 – 1.3 pcf, -70 kPa, 660 °C	Casting 3 – 1.6 pcf, -68 kPa, 701 °C
7	Casting 4 – 1.6 pcf, -70 kPa, 660 °C	Casting 4 – 1.3 pcf, -68 kPa, 701 °C
8	Casting 5 – 1.3 pcf, 0 kPa, 662 °C	Casting 5 – 1.6 pcf, 0 kPa, 700 °C
9	Casting 6 – 1.6 pcf, 0 kPa, 660 °C	Casting 6 – 1.3 pcf, 0 kPa, 701 °C
10	Casting 7 – 1.3 pcf, 0 kPa, 660 °C	Casting 7 – 1.6 pcf, 0 kPa, 698 °C
11	Casting 8 – 1.6 pcf, 0 kPa, 660 °C	Casting 8 – 1.3 pcf, 0 kPa, 700 °C

### 3.7 Treatment of experimental data

The data acquisition system was activated and thermocouple data collection began a few seconds before the molten metal was poured into the mold. A minimum of 2520 data points along the cooling curve were collected for every experiment. In order to accurately carry out the first derivative analysis, it was necessary to remove the initial data points from the collected temperature data set. These data points corresponded to the room temperature readings of the mold. Due to the initial low-temperature data, seen in Figure 34, it was difficult to accurately fit a cubic spline into the temperature profile. Therefore, a modified data set, shown in Figure 35, was used for thermal analysis.



*Figure 34: Raw temperature data.*



*Figure 35: Modified temperature data.*

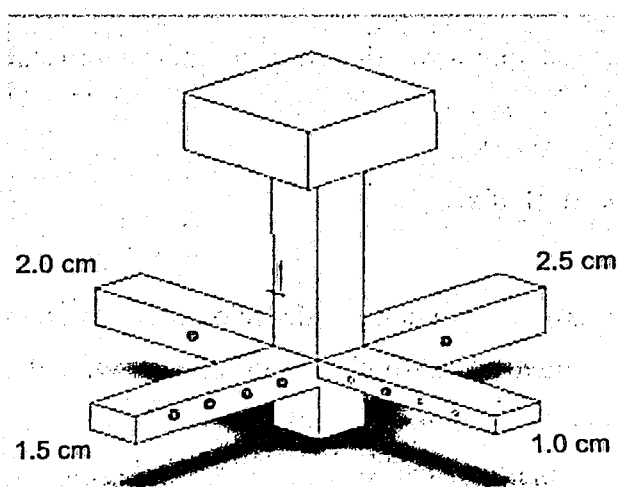
The modified temperature data was imported to Matlab 6.0 software. In this program, a data fitting tool called “Spline Tool” was used to accurately determine the 1<sup>st</sup> derivative curve of the cooling curve. The error associated with data fitting was monitored for every experiment and was maintained between 7 – 10%. The resulting spline curve was filtered in the “Spline Tool” package to eliminate temperature oscillations and determine the temperature / time features of the original cooling curve.

### 3.8 Casting sectioning

Castings were sectioned on a vertical band saw with a course steel blade. Extreme care was taken to prevent overheating and ignition of the magnesium dust during machining operations. The following procedure of selecting metallographic samples was used:

1. Samples from the first set of casting trials (not repeats) were selected.
2. Samples at a distance of 5 cm from the sprue were prepared for all section thicknesses.
3. For all 1.5 cm thick horizontal bars, metallographic samples (corresponding to the thermocouple locations) were prepared from the entire length of the bar; i.e., at 2.5 cm, 5.0 cm, 7.6 cm and 10.2 cm distance from the sprue.

A schematic diagram shown in Figure 36 illustrates the above procedure. Dots indicate the locations of the metallographic samples.



*Figure 36: Locations of metallographic samples.*



### 3.9 Casting density measurements

In order to determine the overall average density of each casting sample, Archimede's principle was utilized. Sample specific gravity was calculated using Equation 10:

$$\text{Specific gravity} = \frac{W_{air}}{W_{s/w} - W_{c/w}} \quad (10)$$

Where:

$W_{air}$  = Weight of sample in air

$W_{s/w}$  = Weight of sample (suspended on a thread in a cup of water), cup and water

$W_{c/w}$  = Weight of cup and water

The sample density was obtained by multiplying the calculated sample specific gravity by the density of water.

A Scientech SP350 balance was used to measure the weight of the casting samples to an accuracy of 0.001 grams. This balance was calibrated prior to use with calibration weights of 200g, 100g, 50g, 10g, 5g, 2g and 1g.

A 0.139 mm thick thread was used to suspend specimens in a cup filled with water. Care was taken to prevent the specimens from touching the walls of the cup.

Uncertainty analysis of the measured values was determined according to standard techniques.<sup>50</sup>

### 3.10 Casting microstructure analysis

Selected casting specimens were ground on a belt grinder to remove any sharp edges and to obtain a plane surface. Then, samples were mounted in transoptic Lucite powder. Buehler SimpliMet 2000 automatic mounting press was used to mount the specimens. Heating time of 20 minutes followed by a cooling time of 7 minutes was adopted for all samples, as it provided the best curing conditions for the Lucite resin. The details of the metallographic polishing procedure are in Table 4:

*Table 4: Metallographic specimen polishing procedure.*

Step	Abrasive Grit / Cloth	RPM	Load [kg]	Duration [min] until plane
1	120 SiC	300	11.3	1
2	320 SiC	300	11.3	1
3	1200 SiC	300	2.2	1
4	6µm diamond paste, Texmet	150	2.2	6
5	1µm diamond paste, Texmet	150	2.2	4
6	Colloidal Silica, Chemomet (manual)	-	-	1

Steps 1 – 5 were completed on the Leco AP-60 automatic polisher. Final polishing (Step 6) involved the use of a Buehler Mastermet colloidal silica polishing suspension and a Buehler Chemomet I polishing cloth.

In order to reveal the grain boundaries and the eutectic  $Mg_{17}Al_{12}$  phase, the metallographic specimens were etched by a glycol solution. This solution was prepared from 1 mL  $HNO_3$ , 24 mL  $H_2O$  and 75 mL ethylene glycol. The etchant was gently swabbed on the specimen surface for 10 seconds. The surface was immediately washed with ethanol and the specimen was dried in hot air.

### *3.10.1 Optical image analysis*

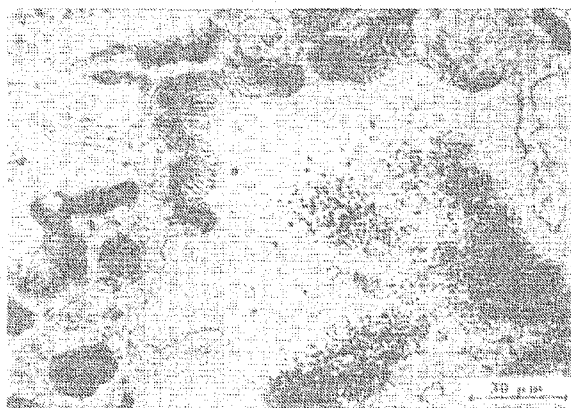
A Leitz Metallux3 microscope instrumented with a Sony CCD camera was connected to a personal computer with Buehler Omni-Met software. Image analysis routines were created in the Omni-Met software to determine:

- Percent area of the combined porosity
- Percent area of the  $Mg_{17}Al_{12}$  phase
- Lamellar spacing of the  $Mg_{17}Al_{12}$  phase

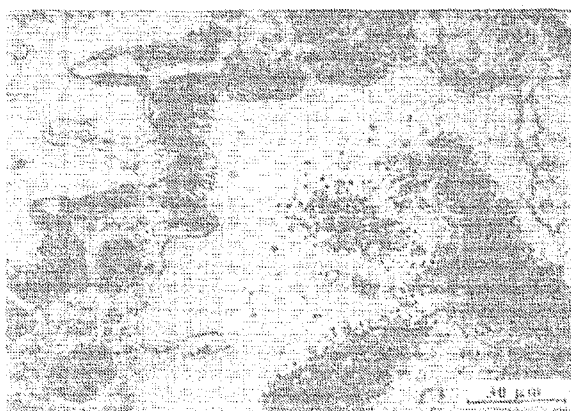
In order to determine the percent area of the combined porosity present in the casting sample, a minimum of 15 image fields at a magnification of 100x were analyzed.

For calculating the percent area of the  $Mg_{17}Al_{12}$  phase present in the casting sample, a minimum of 20 image fields at a magnification of 500x were analyzed.

Figure 37 and Figure 38 demonstrate the degree of bitplane capture used by the Omni-Met software.



*Figure 37: Observed  $Mg_{17}Al_{12}$  phase.*



*Figure 38: Areas included in the  $Mg_{17}Al_{12}$  percent area calculation.*

When calculating the  $Mg_{17}Al_{12}$  lamellar spacing, a magnification of 1250x was used and a minimum of 20 measurements from a minimum of three distinct locations on the sample were analyzed. In all cases, spacing between parallel lamellae was measured.

## Chapter 4 – Results and Discussion

Analysis of casting soundness based on the casting surface finish and density measurements is described. The metal flow behavior is evaluated using the visual inspection of the frozen metal front as well as the velocity of the liquid metal front. The results of thermal analysis follow, with a focus on the cooling rate and the local solidification time. The results of optical microscopy, in particular, the distribution of the casting porosity and the morphology of the  $Mg_{17}Al_{12}$  phase, are discussed.

### 4.1 Adam's Riser Equation

Adam's Riser Equation (A.R.E.) was used to identify casting bars with high predisposition for shrinkage porosity. Using Equation 3, a theoretical line separating the sound and un-sound (shrinkage-prone) regions was plotted. Data for the A.R.E. are presented in Table 5 and Table 6 below.

*Table 5: Alloy data used in A.R.E model.*

Density of solid AZ91E, $\rho_s$ [g/cm <sup>3</sup> ]	1.810
Density of liquid AZ91E, $\rho_l$ [g/cm <sup>3</sup> ]	$1.810 - 0.0001(T[^\circ\text{C}])$
Solidification contraction, $\beta$	0.033

*Table 6: Casting geometry data.*

Assembly Component	Height [cm]	Width [cm]	Thickness [cm]	Volume [cm <sup>3</sup> ]	Area [cm <sup>2</sup> ]
Riser	15.0	3.2	3.2	153	213
1.0 cm bar	1.0	12.7	3.2	41	113
1.5 cm bar	1.5	12.7	3.2	61	129
2.0 cm bar	2.0	12.7	3.2	81	145
2.5 cm bar	2.5	12.7	3.2	102	161

As can be seen in Figure 39, the calculated data points for the 2.0 cm and 2.5 cm thick bars were relatively close to the A.R.E. prediction line. Hence, these bars had a higher tendency to form shrinkage porosity than the 1.0 cm and 1.5 cm thick bars, which were further away from the sound / un-sound boundary line.

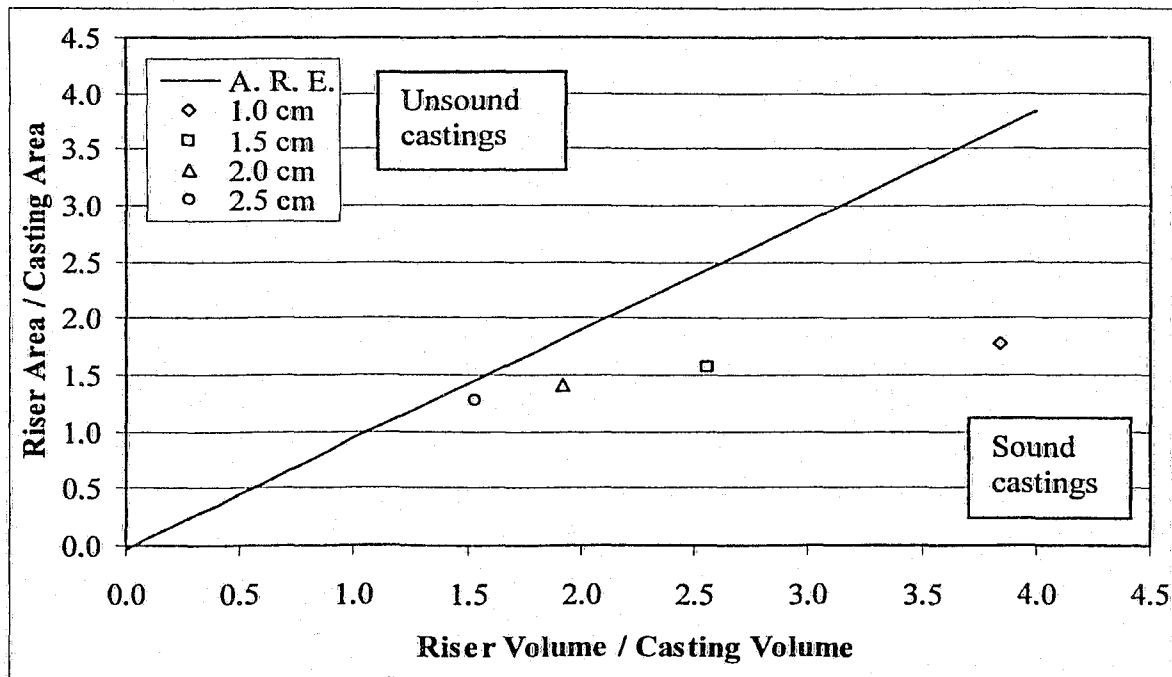


Figure 39: A. R. E. plot.

A detailed analysis of the optical porosity measurements is presented later in Section 4.9. However, conclusions pertinent to the A.R.E. theory are the following:

1. For gravity castings, i.e., castings produced without vacuum, the casting porosity increased with increasing section thickness. This trend was in agreement with: (a) Adam's riser theory; and (b) the fact that with increasing section thickness, the potential for entrapment of the EPS pyrolysis products in the casting cavity increased.
2. For castings produced under vacuum, the casting porosity was seen to decrease with increasing section thickness. Therefore, Adam's riser theory was not valid for these casting conditions. This trend in porosity was attributed to the effective removal of the liquid-EPS residue from the casting cavity as a result of the applied vacuum. Although thicker casting sections possibly generated more pyrolysis products, the thicker bars also had a greater surface area through which the liquid-EPS and gaseous-EPS pyrolysis products could escape into the surrounding sand. Thus, the thicker horizontal bars enabled higher liquid-EPS residue extraction rates, effectively decreasing the probability of liquid-EPS entrapment. As a result, the porosity did not increase with increasing section thickness.

Therefore, it was observed that A.R.E. was applicable to the AZ91E magnesium alloy cast by the LFC process under gravity conditions; however, it was not valid for the vacuum assisted castings.

## 4.2 Overall casting quality

Casting surfaces were qualitatively inspected for defects. Assessment of the casting surface often provided indications of the mold filling behavior and the casting soundness. Casting defects such as misruns, folds and river-like impressions in the casting surfaces were often observed.

Vacuum-related casting defects were identified. For instance, the application of vacuum during mold filling caused the molten metal to penetrate the inter particle cavities of the surrounding sand mold. As a result, the casting surface was rough and covered with grains of sand.

Defects associated with a relatively low pouring temperature and inadequate removal of the liquid-EPS pyrolysis products were observed. In casting trials with the 660 °C pouring temperature, the primary degradation products were liquid-EPS. During the mold filling process the majority of these products were pushed to the metal-mold interface where they encountered relatively cold sand. Consequently, the liquid-EPS products began to coalesce and harden. As a result, lumps of sand contaminated with solidified liquid-EPS were seen to adhere to the casting surfaces. These sand lumps were easily removed with a wire brush.

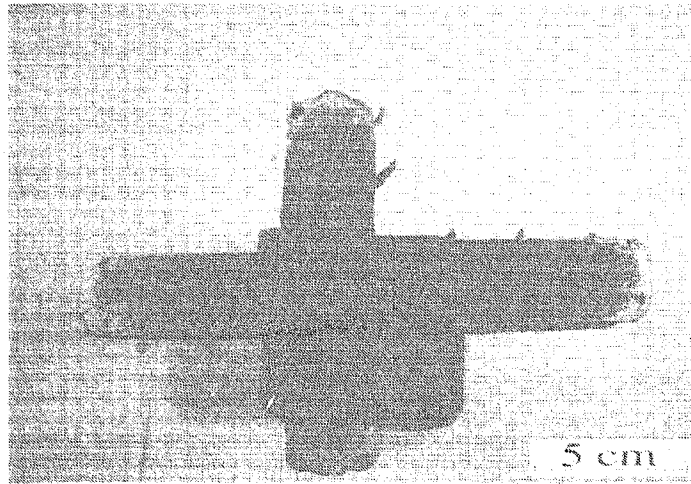
The quantitative results of the casting density analysis and casting mold filling (Sections 4.3 and 4.4) complement the qualitative casting analysis of this section.

It will be apparent from the following discussion that optimal casting conditions were not attained for different combinations of LFC casting parameters. This resulted in castings with significant defects. Since these casting defects were unique to individual casting conditions, each combination of LFC casting parameters is discussed separately.

### 4.2.1 Casting Condition: 660 °C, 1.3 pcf foam, with vacuum

The castings produced at the 660 °C pouring temperature, with 1.3 pcf foam and applied vacuum were not sound. The horizontal bars did not fill completely, thus producing severe misruns, as seen in Figure 40. Also, sharp edges of the horizontal bars were not retained along their length. These observations suggest, that the molten metal did not possess sufficient thermal energy to completely decompose and remove the foam pyrolysis products from the casting cavity.

As with other castings produced under vacuum, sand mold penetration by the liquid metal during mold filling occurred on the bottom face of the casting (which was adjacent to the vacuum exhaust). However, the degree of the mold penetration in this trial was not as severe as in the other vacuum casting trials.



*Figure 40: Casting: 660 °C / 1.3 pcf / with vacuum, bottom side.*

Past research <sup>44</sup> shows, that during filling of open cavity molds, the metal flow length is governed by the solidification kinetics of the metal. When the fraction of solids in the alloy reaches a critical value ("coherency fraction of solids"), the metal flow ceases. At the coherency point, chunks of solid metal begin to form and impede further metal flow. On a microscopic level, this event corresponds to the interlocking of dendrite arms.

In this casting trial, rough and irregular profiles of the frozen metal fronts were observed. Figure 40 and Figure 41 show that these regions of irregularity contained chunks of solidified metal. Due to the application of the vacuum, the molten metal was pulled into the casting cavity and carried partially solidified metal. Thus, the metal flow continued beyond the coherency point. This mode of filling resulted in surface as well as internal macroscopic defects, which were observed upon sectioning of the castings.

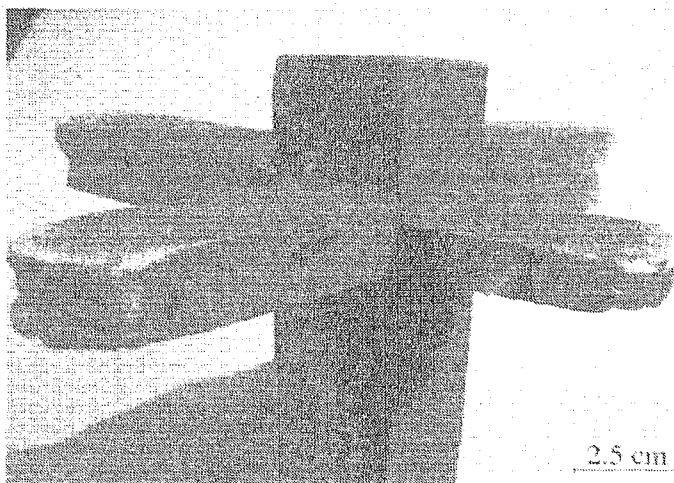
The effect of the vacuum on the curvature of the metal front profile is seen Figure 42. From this figure it is evident, that in the case of the 1.5 cm, 2.0 cm and 2.5 cm thick bars, the metal fronts had a concave profile. However, in the case of the 1.0 cm thick bar, the metal front remained convex. This behavior can be explained by observing the effect of the section thickness on the liquid metal surface tension. It can be shown, that the surface tension is proportional to the metallostatic pressure ( $\Delta p$ ), flow channel width ( $l$ ) and the coefficient of surface tension ( $\gamma_s$ ) via:  $\Delta p \sim \gamma_s / l$ . Since  $\Delta p$  was the same for all horizontal bars,

then it is evident that due to the relatively high metal surface tension in the 1.0 cm thick horizontal bar, the metal front profile remained convex.

The change of the metal front curvature for the thicker horizontal bars agrees with the predictions of Liu et. al.<sup>17</sup> who suggest that application of vacuum preferentially draws the liquid metal against the mold walls. As a result, the metal front profile changed from convex to concave.



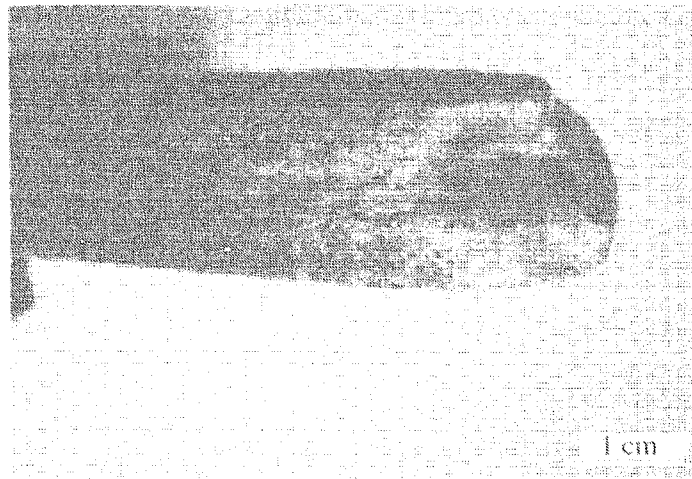
*Figure 41: Partially solidified chunks in the frozen metal front.*



*Figure 42: Concave metal front profiles of the 1.5 cm, 2.0 cm and 2.5 cm thick bars.*

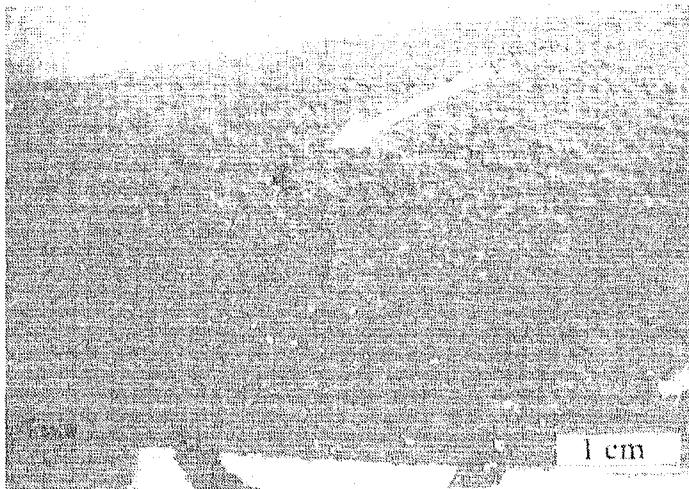
As a consequence of the altered metal front curvature (i.e., concave profile), the liquid-EPS pyrolysis products possibly agglomerated in the center regions of the flow channel and did not escape to the metal-mold interface. At later stages of the filling process, the liquid-EPS products were possibly pushed by the advancing metal front towards the sides of the flow channel. The residency time of the liquid-EPS in these areas was sufficiently long to allow formation of river-like impressions in the casting surface, as observed in Figure 43.



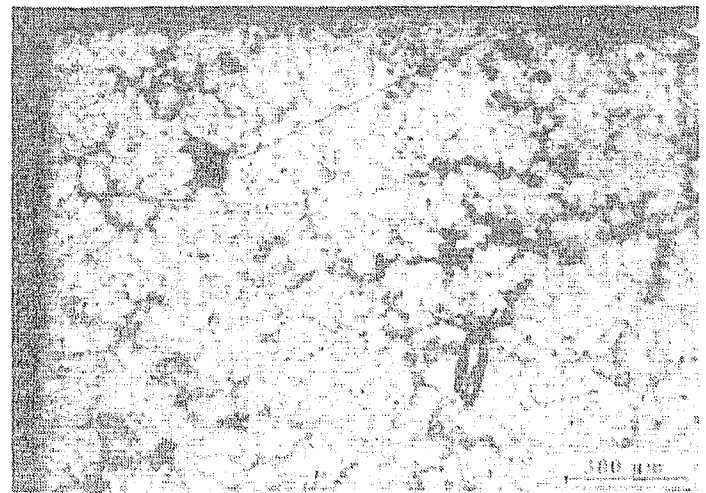


*Figure 43: River-like impressions caused by the liquid-EPS residue: 2.0 cm thick bar.*

Additional casting defects were identified on the upper surfaces of the horizontal bars. Figure 44 shows cavities (pores) on the top face of the horizontal bar. These surface cavities were identified by optical microscopy as extensions of complex sub-surface shrinkage porosity networks, as observed in Figure 45. This defect is highly undesirable, as it compromises the pressure tightness and the strength of any cast component.



*Figure 44: Surface extension of shrinkage porosity.*



*Figure 45: Subsurface shrinkage porosity network.*

The formation of shrinkage networks suggests presence of inadequate feeding of liquid metal to the casting bar during the last stages of solidification. In practice, this defect could be avoided with the use of properly sized risers.

#### 4.2.2 Casting Condition: 660 °C, 1.6 pcf foam, with vacuum

Castings poured at the 660 °C pouring temperature, with 1.6 pcf foam and applied vacuum show improved casting fill, relative to the preceding casting trial. Therefore substitution of the high density 1.6 pcf foam instead of the low density 1.3 pcf foam increased the metal flow lengths of all horizontal bars. This result, however, contradicts established experimental data.<sup>51, 52</sup> Typically, high density foams extract more energy (thermal and kinetic) from the molten metal than the low density foams, due to the increased mass of the polymer which needs to be pyrolyzed. There are rare instances,<sup>53, 54</sup> however, when the low density foams were seen to enhance alloy flow lengths when compared to high foam density casting trials. These anomalies were generally attributed to the non-homogeneity of the foam and no quantitative explanation of this behavior has been found in the literature. An explanation of this unusual effect of the foam density on the flow length using quantitative results of the thermal analysis is presented later in Section 4.6.

As Figure 46 and Figure 47 illustrate, metal penetration occurred on the bottom sides of the horizontal bars, which were adjacent to the vacuum exhaust. This casting defect was difficult to remove, thus greatly degenerating the surface finish of the casting.

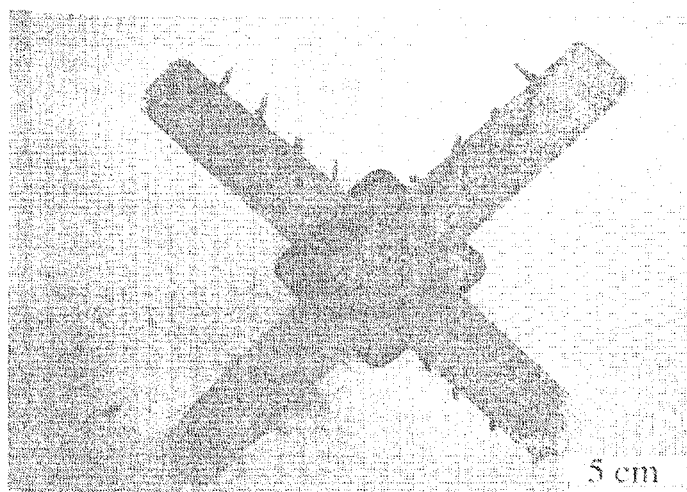


Figure 46: Casting: 660 °C / 1.6 pcf / with vacuum, bottom side.

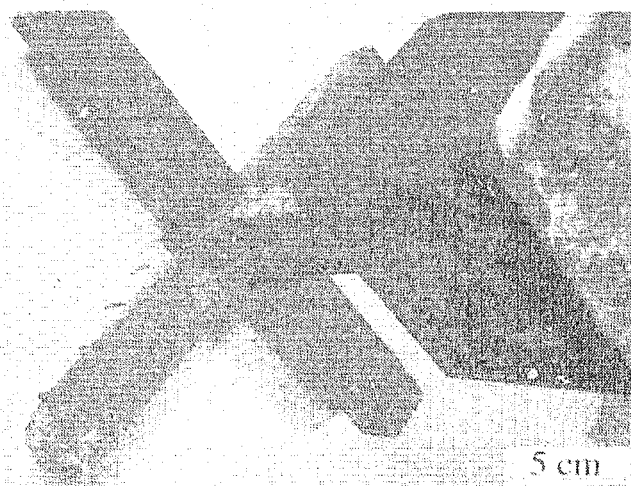
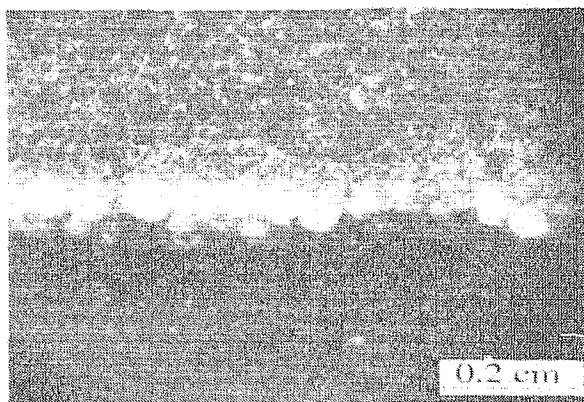
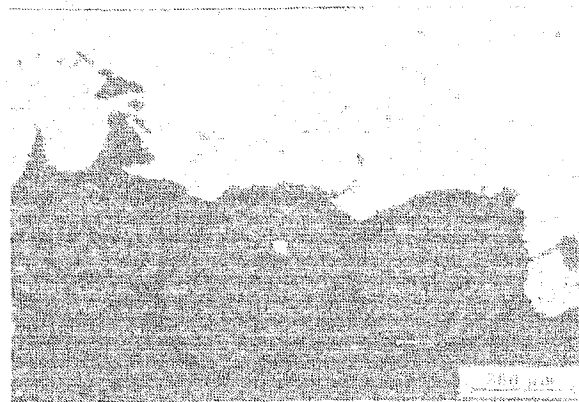


Figure 47: Casting: 660 °C / 1.6 pcf / with vacuum, top side.

Figure 48 and Figure 49 are stereo micrographs showing the bottom edge of a casting specimen with sand grains embedded in the casting. As will be apparent from Section 4.2.5, the degree of metal penetration was a function of the alloy pouring temperature.



*Figure 48: Sand grains adhering to the bottom side of the casting.*



*Figure 49: Micrograph of sand grains adhering to the bottom side of the casting.*

Similarly as in the previous casting condition (Section 4.2.1), inspection of the flow tip revealed the presence of partially solidified chunks at the metal front. However, as Figure 50 shows, the average diameter of these chunks decreased from 0.8 cm in the previous casting trial to 0.4 cm in the current casting trial.



*Figure 50: Metal front of the 1.0 cm thick bar.*

Considering the relatively low pouring temperature of this trial, the rate of transformation of the solid polystyrene pattern to gaseous pyrolysis products was expected to be slow. This possibly caused the liquid-EPS residue to agglomerate at the metal-mold interface. In some regions of the interface, the liquid-EPS products wicked through the ceramic coating and hardened upon contacting the cool compacted sand.

This was confirmed by the adhering sand grains on the casting surfaces, as shown in Figure 51. This transport mechanism was further represented by a discoloration of the ceramic coating. The lighter colors of the coating in Figure 51 corresponded to the regions where liquid-EPS resided for a long period of time and the molten metal did not burn the ceramic coating. On the other hand, regions where molten metal came into contact with the ceramic coating were burned and showed dark brown color. The presence of the liquid-EPS products was verified by inspection of Figure 52 which is an enlarged view of the area. In the latter figure, an impression in the casting surface created by the liquid-EPS products was identified. Further, Figure 52 also shows the remains of the solid-EPS foam in the regions where liquid-EPS agglomerated between the molten metal and the surrounding sand. This confirms, that the liquid-EPS products posed as a significant thermal barrier between the molten metal and the solid-EPS ahead of the advancing metal front. Figure 53 schematically illustrates this situation.

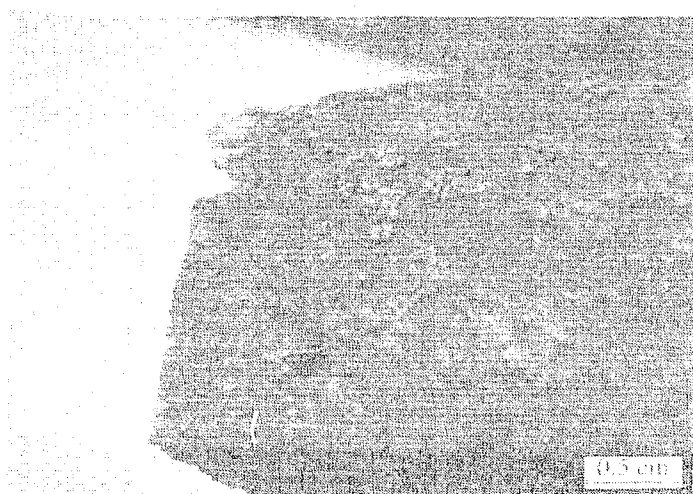


Figure 51: Burned-on ceramic coating and liquid-EPS channel.

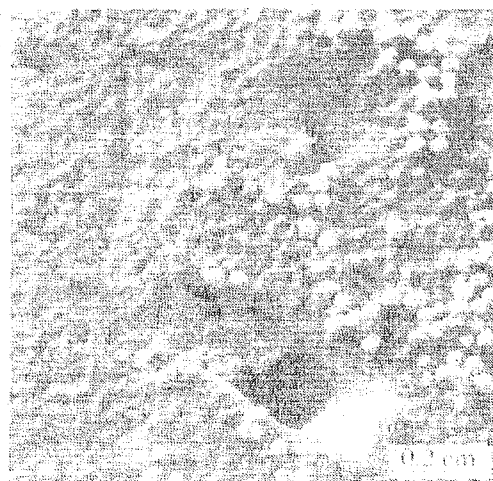


Figure 52: Enlarged liquid-EPS channel from Figure 51.

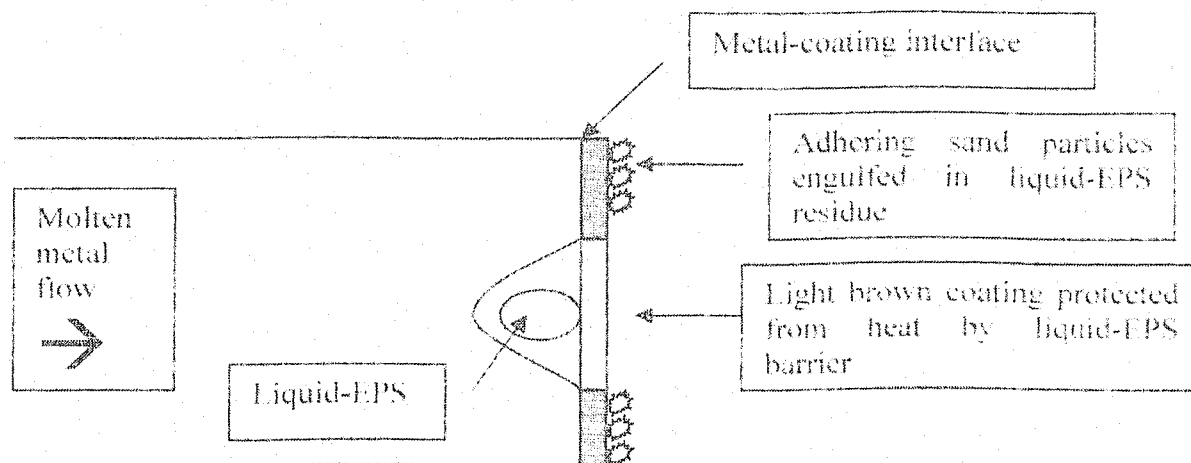
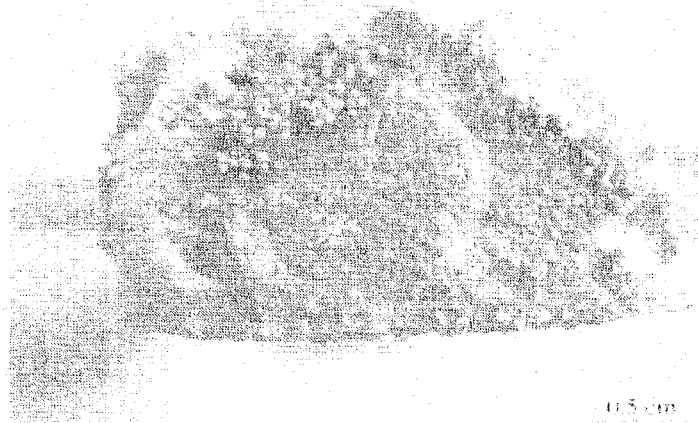


Figure 53: Liquid-EPS barrier at the metal-coating interface

Additional evidence of incomplete liquid-EPS transport from the metal-mold interface to the surrounding sand was observed in Figure 54. Here, distinct regions were observed on the end face of the casting bar. Portions of the ceramic coating burned by the liquid metal flaked off, while the regions through which only partial transport of the liquid-EPS residue occurred appear "wet" and contain adhering sand particles.



*Figure 54: Liquid-EPS "wet" marks.*

#### 4.2.3 Casting Condition: 660 °C, 1.3 pcf foam, without vacuum

The combination of the low pouring temperature, low foam density and the absence of vacuum resulted in a casting with the shortest flow lengths, as observed in Figure 55. Despite the misruns, the trend of increasing flow length with increasing section thickness was noted.



Figure 55: Casting: 660 °C / 1.3 pcf / without vacuum, bottom side.

In these gravity castings, metal penetration did not occur. Further, as Figure 56 and Figure 57 show, the frozen metal front profiles were convex without any indication of partially solidified chunks at the frozen metal front. This suggests that flow stoppage occurred due to the loss of melt superheat and the coherency solid fraction.

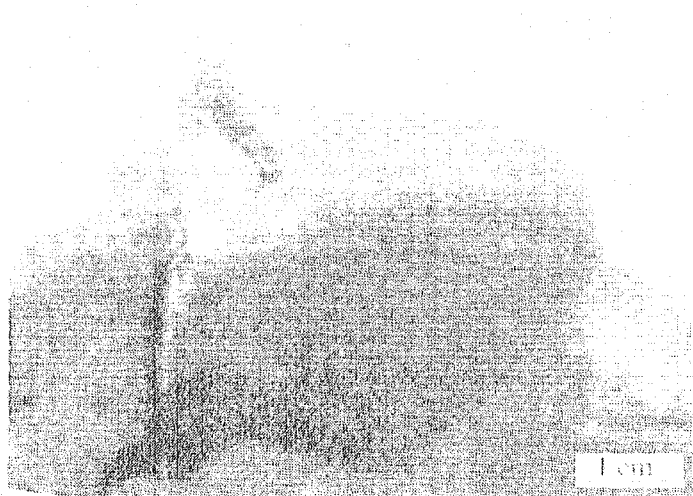


Figure 56: Frozen metal front of the 1.0 cm thick bar.

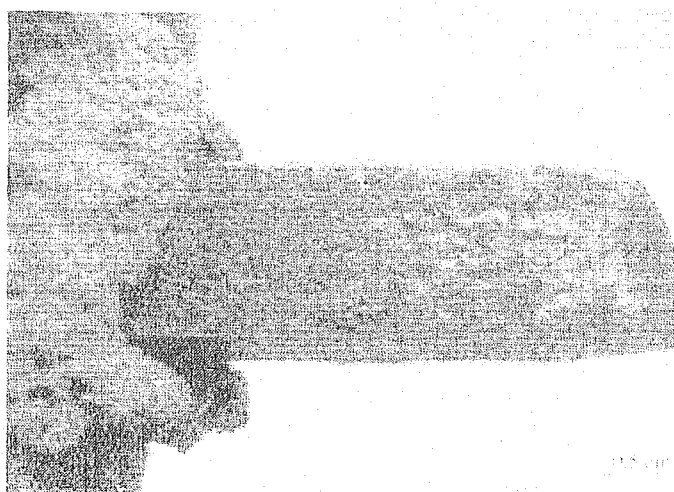
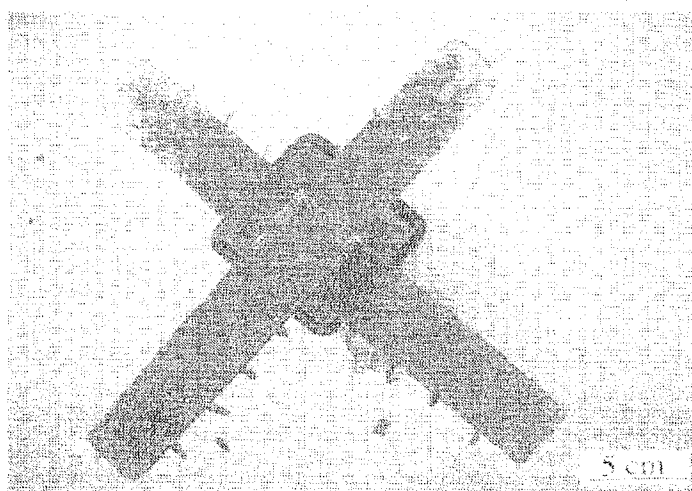


Figure 57: Convex metal front of the 1.5 cm thick bar.

#### *4.2.4 Casting Condition: 660 °C, 1.6 pcf foam, without vacuum*

The combination of the 660 °C pouring temperature, 1.6 pcf foam and the absence of vacuum resulted in a casting with misruns. As already observed in Section 4.2.2 with vacuum trials, increasing the foam density improved the molten metal flow length. Comparing Figure 55 and Figure 58, the increased casting fill is evident.

Similarly, as with the 1.3 pcf gravity casting trials, liquid metal penetration of the mold sand did not occur. In addition, as observed in Figure 59, the metal front profiles were convex, as expected for gravity casting conditions.



*Figure 58. Casting: 660 °C, 1.6 pcf, without vacuum, bottom side.*



*Figure 59. Convex metal front of the 1.0 cm thick bar.*

As Figure 60 shows, the 1.0 cm thick bar contained a fold defect. A stereo micrograph of the folded region is presented in Figure 61. Typically, folds result from the incomplete fusion of two molten metal fronts as a result of thermal or velocity gradients. Thermal gradients arise from non-uniform casting temperatures, whereas velocity gradients are established by the geometrical constraints of the casting design. These constraints possibly separate a single metal flow into multiple streams. In order to minimize the occurrence of the fold defects, the gating system should be re-designed to allow faster metal velocities and provide higher metallostatic pressures. In addition, implementing higher pouring temperatures would enable the liquid metal to remain fluid for longer periods of time, thus facilitating complete fusion of the separated metal fronts.



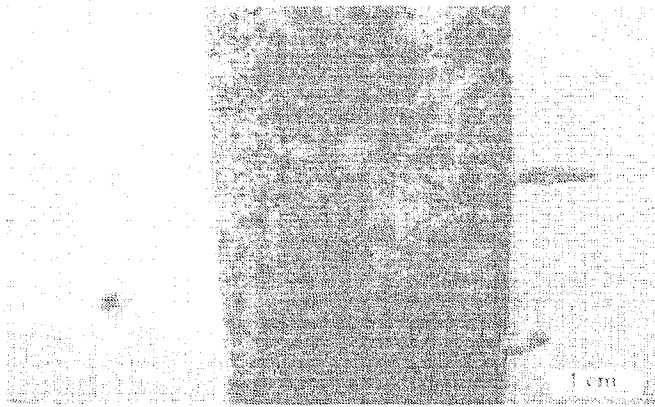


Figure 60: Fold defect in the 1.0 cm thick bar.

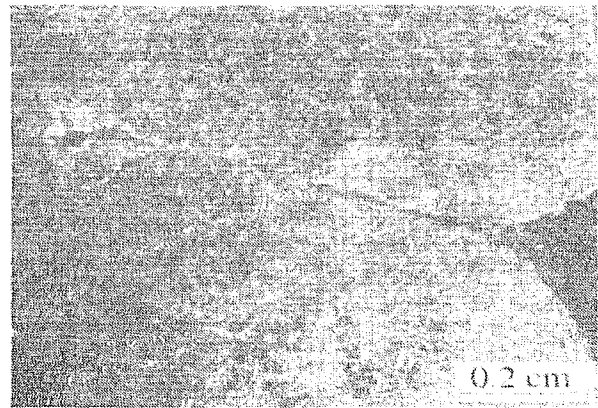


Figure 61: Stereo micrograph of the fold defect in Figure 60.

#### 4.2.5 Casting Condition: 700 °C, 1.6 pcf foam, with vacuum

Increasing the pouring temperature from 660 °C to 700 °C increased the metal flow length in all horizontal bars, thus improving casting fillability. For the current combination of the casting parameters, all horizontal bars filled completely and the bar edges retained their sharpness. Therefore, it appears that the foam decomposition process became easier due to the increased heat content of the molten metal.

It can be shown (Appendix A), that the energy required to decompose 1 cm<sup>3</sup> of the solid-EPS foam is approximately 43 J. In the case of the AZ91E alloy, a 1 cm<sup>3</sup> of a 40 °C superheated liquid metal (660 °C pouring temperature) contains 828 J of energy. Similarly, a 1 cm<sup>3</sup> of a 100 °C superheated metal (700 °C pouring temperature) contains 930 J of energy. The energy difference between the two pouring temperatures is approximately 100 J. As a result, based solely on the energy calculation, the 40 °C superheat increase may have potentially doubled the flow length. However, such an increase was not observed due to thermo-physical changes in the EPS pyrolysis process associated with the high pouring temperatures.

With respect to enhancing the metal flow length, increasing the pouring temperature was beneficial. However, as with earlier vacuum trials, metal penetration was again observed. As seen in Figure 62, the entire bottom side of the casting was covered with embedded sand while the top side of the casting remained relatively clean, as seen in Figure 63. With the higher pouring temperature, the liquid metal viscosity possibly decreased and the metal penetration of the inter-particle cavities of the surrounding sand mold was easier. Comparing Figure 48 to Figure 64, it was noted, that in some cases of the 700 °C



pouring temperature trials, the molten metal fully engulfed the sand grains (Figure 65), which became a part of the casting.

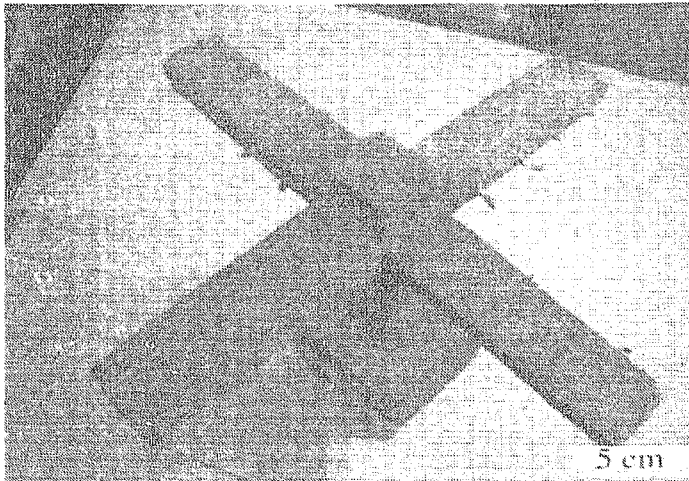


Figure 62: Casting: 700 °C / 1.6 pcf / with vacuum, bottom side.

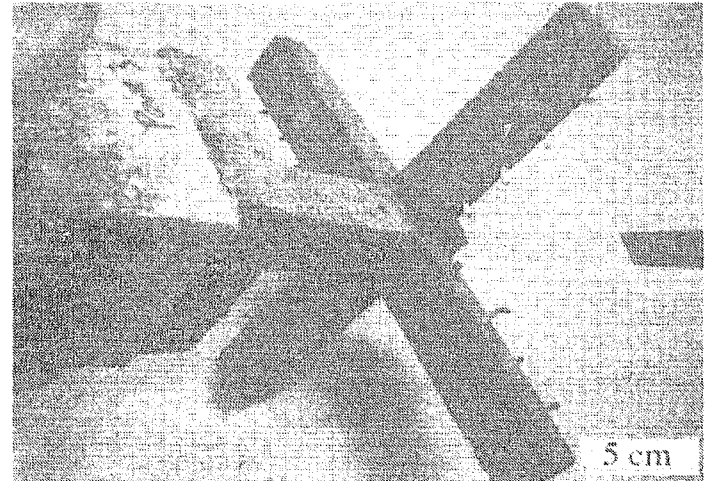


Figure 63: Casting: 700 °C / 1.6 pcf / with vacuum, top side.

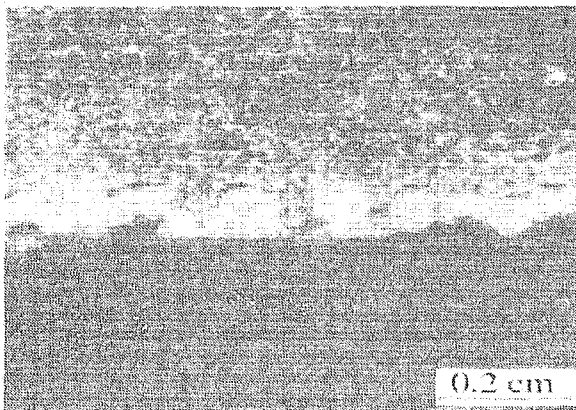


Figure 64: Adhering sand grains at the bottom side of the casting.

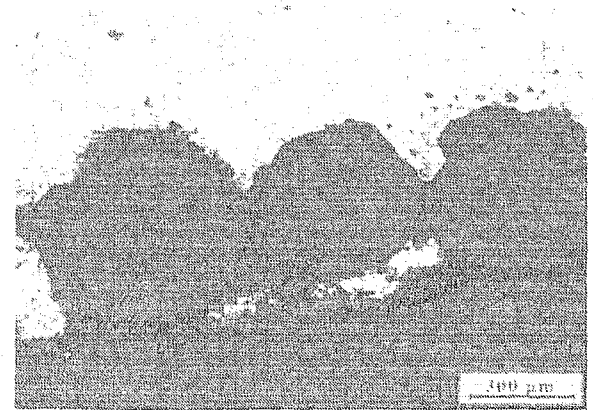
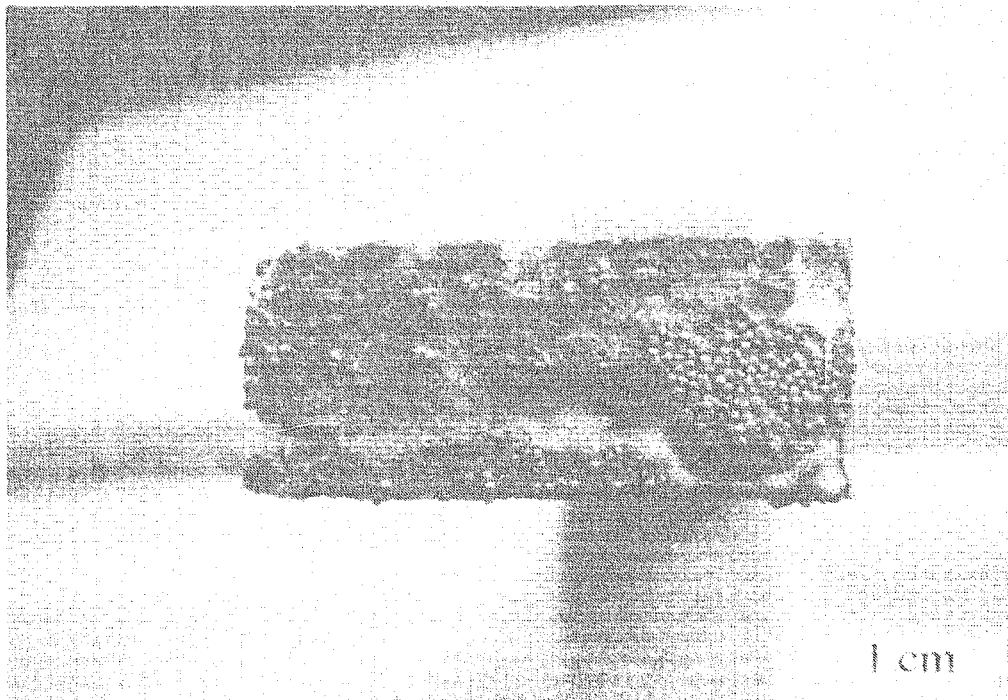


Figure 65: Sand grains engulfed by the frozen alloy.

In addition to the mold penetration defects, entrapped liquid-EPS products further reduced the casting surface finish quality. Figure 66 shows, that the liquid-EPS products were pushed by the advancing molten metal front towards the end of the flow channel. Upon solidification, the pools of the liquid-EPS residue generated river-like impressions on the end face of the horizontal bar. In this particular case, the quantity of agglomerated liquid-EPS was sufficient to hinder the heat transfer from the molten metal to the solid-EPS ahead of the metal front to such extent that the solid-EPS foam bead structure was fully retained, as seen in Figure 66.

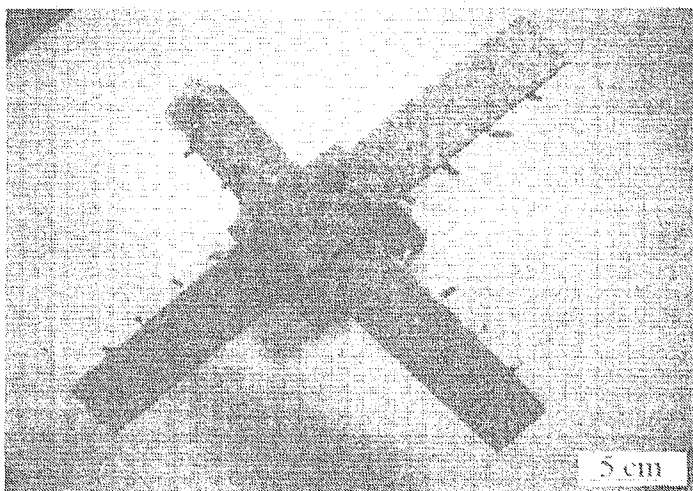


*Figure 66: End face of the 1.5 cm thick bar.*

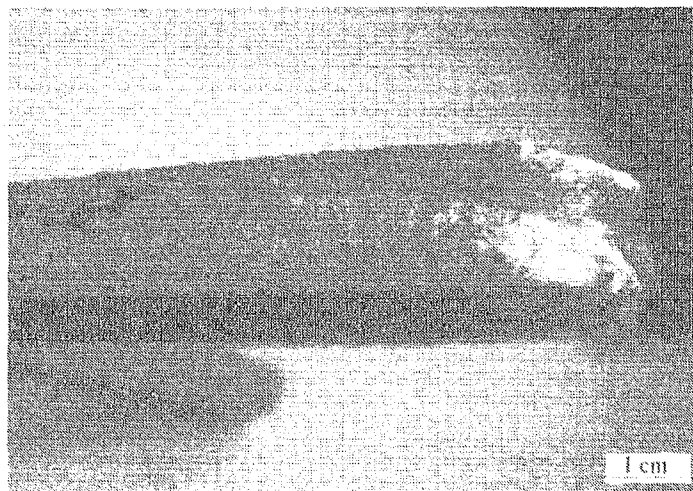
#### *4.2.6 Casting Condition: 700 °C, 1.3 pcf foam, with vacuum*

The combination of the 700 °C pouring temperature, 1.3 pcf foam and application of vacuum resulted in a casting with misruns in the 1.0 cm thick bar. Comparing Figure 55 and Figure 67, an improvement in casting fill was generally observed and was attributed to the higher melt temperature.

Due to the application of vacuum, the upper and lower portions of the metal flow in the horizontal channel advanced faster at the mold walls than the center regions of the horizontal bar, as seen in Figure 68. As a result, a concave metal front profile was established. Consequently, the mid sections of the horizontal bars contained river-like impressions along the entire length of the bar. These impressions were caused by the liquid-EPS products.



*Figure 67: Casting: 700 °C / 1.3 pcf / with vacuum, bottom side.*



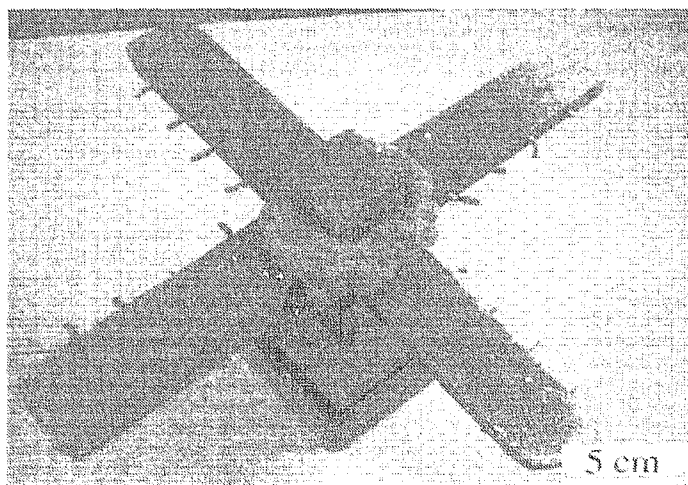
*Figure 68: Concave metal front of the 1.5 cm thick bar.*

The depth of the liquid-EPS impressions increased with increasing distance along the bar. This suggests that the volume of the liquid-EPS products increased with increasing flow distance as well. Therefore, it is possible, that the liquid-EPS residue removal process became more difficult due to the supersaturation of the ceramic coating with the EPS degradation products, resulting in clogging of the pores of the ceramic coating.

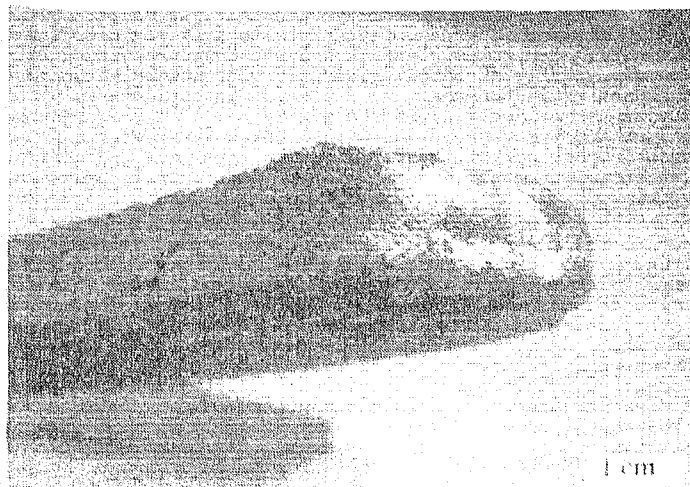
#### *4.2.7 Casting Condition: 700 °C, 1.6 pcf foam, without vacuum*

The combination of 700 °C pouring temperature, 1.6 pcf foam and the absence of vacuum resulted in a casting with a smooth surface finish. As Figure 69 shows, metal penetration defect did not occur in this casting trial. In the case of the vacuum castings, the concave liquid metal front forced the liquid-EPS residue to agglomerate in the center regions of the flow channel. However, in the present gravity casting trials, the metal front profile was convex, as seen in Figure 70 and, as a result, the river-like impressions were seen across the entire side of the horizontal bar (Figure 71).

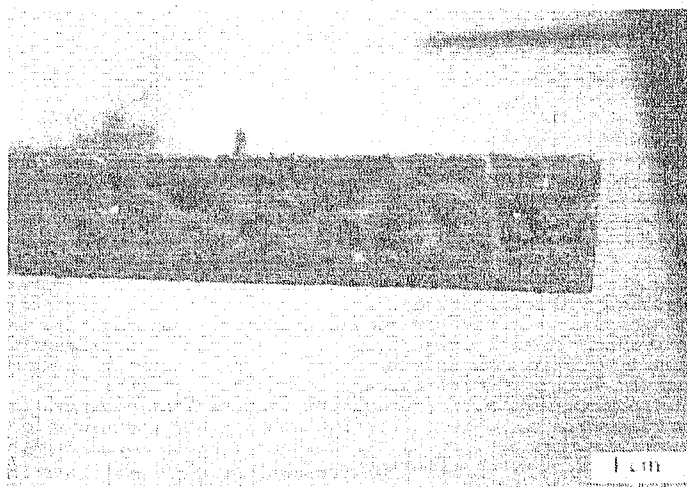
Furthermore, as Figure 70 illustrates, the metal front profile was relatively smooth, which suggests the absence of partially solidified metal during mold filling.



*Figure 69: Casting: 700 °C / 1.6 pcf / without vacuum, bottom side.*



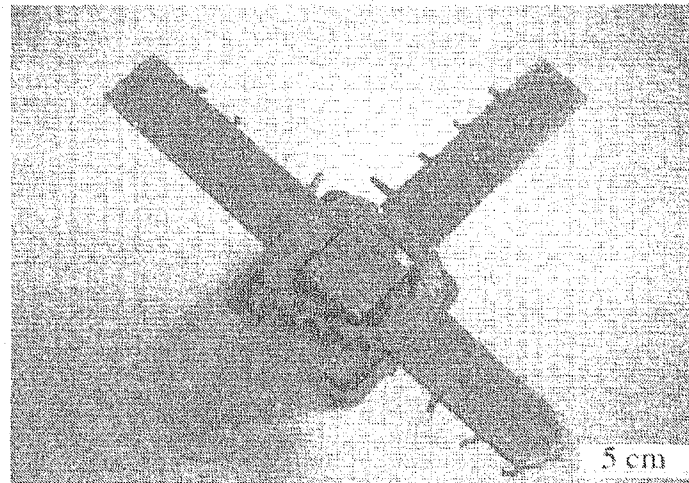
*Figure 70: Convex metal front of the 1.0 cm thick bar.*



*Figure 71: River-like impressions on the sides of the 1.5 cm thick bar.*

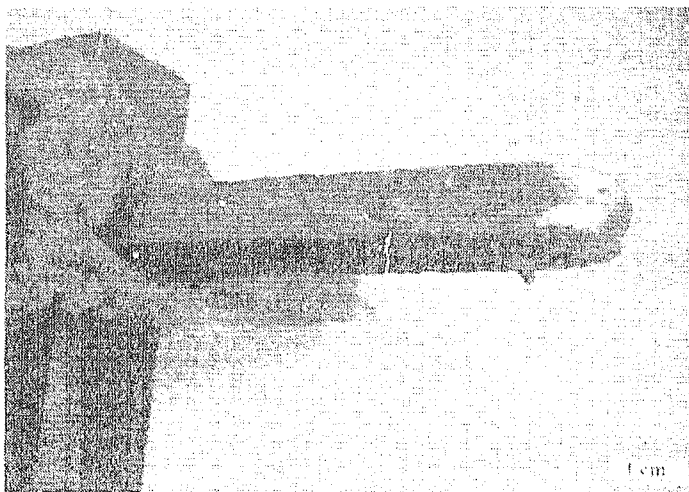
#### *4.2.8 Casting Condition: 700 °C, 1.3 pcf foam, without vacuum*

The combination of 700 °C pouring temperature, 1.3 pcf foam and the absence of vacuum resulted in a smooth overall surface finish. Comparing Figure 55 to Figure 72, an increase in the metal flow length was observed and attributed to the higher pouring temperature.

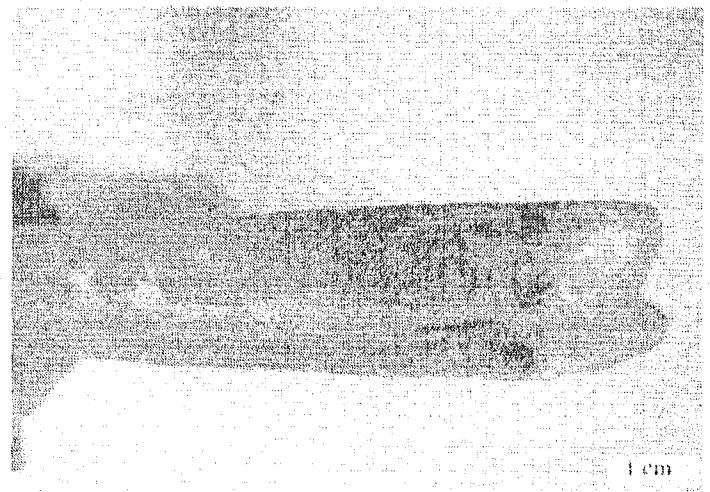


*Figure 72: Casting: 700 °C / 1.3 pcf, without vacuum, bottom side.*

In the current casting trial, the depth of the river-like impressions on the surfaces of the casting bars were the greatest for any combination of casting parameters studied. This is clearly observed in Figure 73 and Figure 74.



*Figure 73: Convex metal front of the 1.0 cm thick bar.*



*Figure 74: Concave metal front profile and liquid-EPS residue marks of the 2.0 cm thick bar.*

In addition, Figure 75 and Figure 76 show that the volume fraction of the liquid-EPS products was large enough to possibly cause separation of the metal flow into two streams. As a result, a longitudinal fold defect was created.

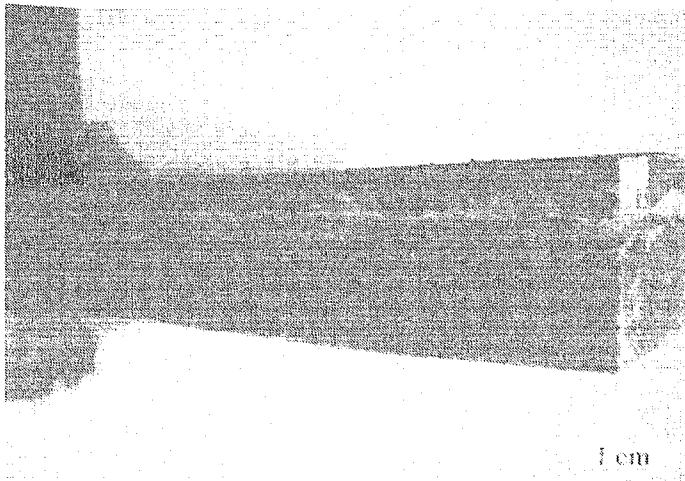


Figure 75: Liquid-EPS defect in the 2.5 cm thick bar.

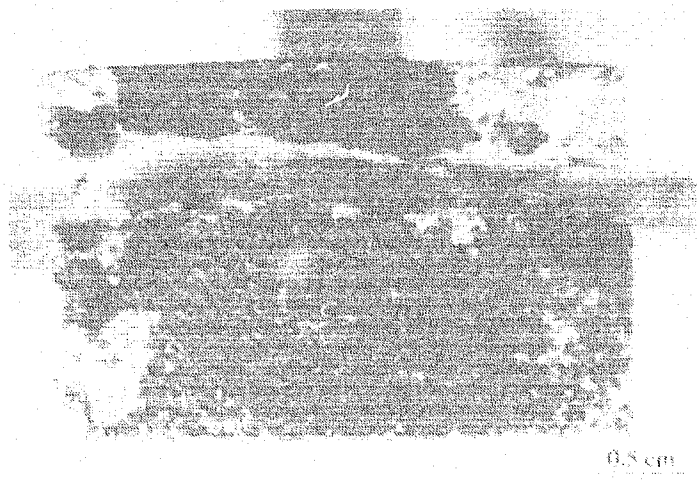


Figure 76: End face of the 2.5 cm thick bar.

#### 4.2.9 Section summary

The Adam's riser theory was validated for estimating porosity levels in gravity castings. However, this porosity prediction model was seen to be inadequate for castings produced under vacuum.

The effect of vacuum on the metal front profile was clearly observed. For vacuum castings, the molten metal front profile was concave. However, for gravity castings, the metal front remained convex.

The foam density and bead fusion had a significant effect on the casting fillability. Frequent liquid-EPS defects were observed in the 1.3 pcf foam castings, which suggests ample generation of liquid-EPS products during the foam depolymerization process.

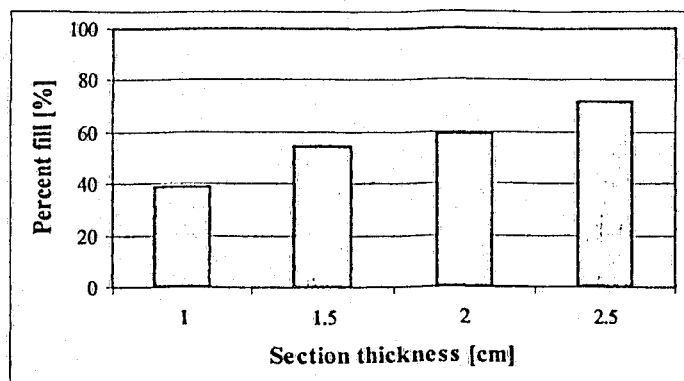
Increasing the pouring temperature improved the casting fillability due to the relatively easier pyrolysis process. However, it also increased the degree of metal penetration into the surrounding sand, thus degenerating the casting surface finish.

### 4.3 Casting fill and flow length

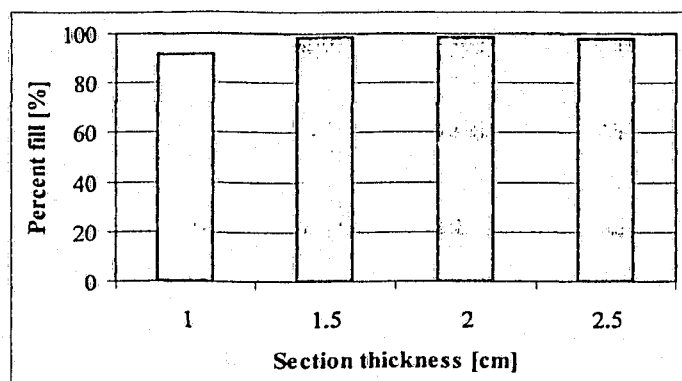
The percent casting fill was calculated by dividing the actual (measured) metal flow length in a horizontal bar by the total length of the bar. The uncertainty in percent fill measurement was 0.7%. The casting fillability and the metal flow length were observed to mainly depend on the alloy pouring temperature.

#### 4.3.1 Pouring temperature: 660 °C

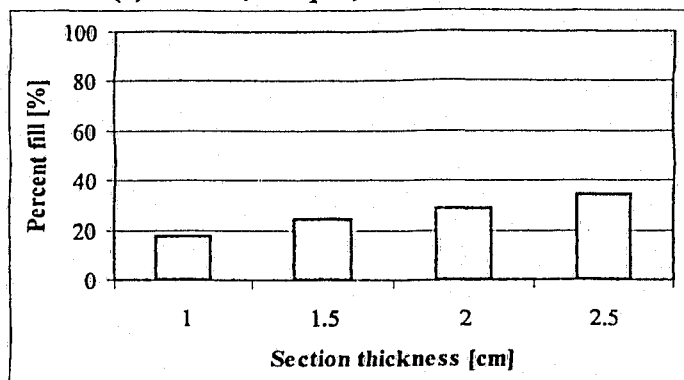
The percent fill results are presented in Figure 77. It was observed that the casting section thickness affected the casting percent fill. All casting trials showed an increase in the alloy flow length with an increase in the casting section thickness. However, the increase in the casting fill was not proportional to the increase in the casting section thickness. For vacuum castings produced from the 1.3 pcf foam, the percent fill increased at a rate of 22% / cm increase in section thickness. In gravity castings produced with the 1.3 pcf foam, the percent fill increased at a rate of 12% / cm increase in section thickness.



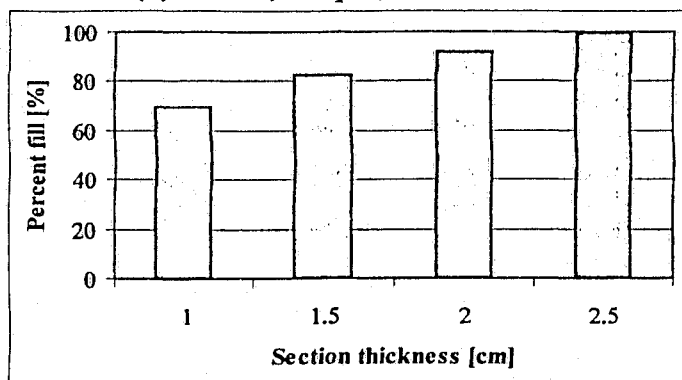
(a) 660 °C, 1.3 pcf, with vacuum



(b) 660 °C, 1.6 pcf, with vacuum



(c) 660 °C, 1.3 pcf, without vacuum



(d) 660 °C, 1.6 pcf, without vacuum

Figure 77: Casting percent fill: 660 °C pouring temperature trials.



In the case of gravity castings produced with the 1.6 pcf foam, the percent fill increased at a rate of  $\sim 21\%$  / cm increase in section thickness. For the case of 1.6 pcf castings produced under vacuum, exact numerical results were not available due to incomplete filling of the horizontal bars.

These trends can be possibly explained by noting that the surface area of the 2.5 cm thick horizontal bar was 40% larger than that of the 1.0 cm thick horizontal bar. Therefore, the volume of liquid-EPS products passing through a unit area of the coating was potentially reduced with a thicker section. As a result, clogging of the coating pores by the liquid-EPS residue was avoided in the thicker bars and the liquid-EPS transport through the ceramic coating was relatively easy, thus allowing increased casting percent fill. The most significant factor, however, believed to affect the percent casting fill was the degree of the bead fusion of the expanded polystyrene foam.

Foam density and bead fusion were seen to have a significant effect on the casting fill. As Figure 77 (a) vs. (b) and (c) vs. (d) illustrate, the substitution of the well fused high density foam (1.6 pcf) instead of the poorly fused low density foam (1.3 pcf) considerably improved the casting fill. As discussed in earlier sections, such a trend contradicts typical LFC observations, where higher density foams were seen to pose greater resistance to the advancing metal front. Further, high density foams were seen to extract more thermal energy from the molten metal during depolymerization, thus promoting rapid alloy solidification. Based on these arguments, the percent fill in the high density foam castings was expected to be reduced.

Niemann<sup>55</sup> investigated the effect of foam density on the mechanical properties of the EPS foam patterns. His work suggests, that with increased density, the tensile, flexural and compressive strength of the EPS foam increases. For example, in the case of the tensile strength, the  $0.026 \text{ g/cm}^3$  (1.6 pcf) foam was  $\sim 30\%$  stronger than the  $0.0208 \text{ g/cm}^3$  (1.3 pcf) foam. Niemann also concluded that the flexural and tensile strengths were adversely affected by poor bead fusion.

Rossacci<sup>56</sup> investigated the influence of bead fusion on the foam pattern degradation and casting formation in the LFC process. His research involved foams of the same density with varying levels of bead fusion. Rossacci hypothesized, that low EPS bead fusion may enable penetration of hot mold gases deep into the non-degraded EPS pattern, as shown in Figure 78. The transport of the hot mold gases into the solid-EPS pattern may initiate preheating, collapse and viscous residue formation in the pattern well ahead of the metal front. In the patterns with high degree of bead fusion; however, the hot mold gases cannot penetrate through the bead structure easily and are eliminated through the coating. This mechanism is schematically illustrated in Figure 78.



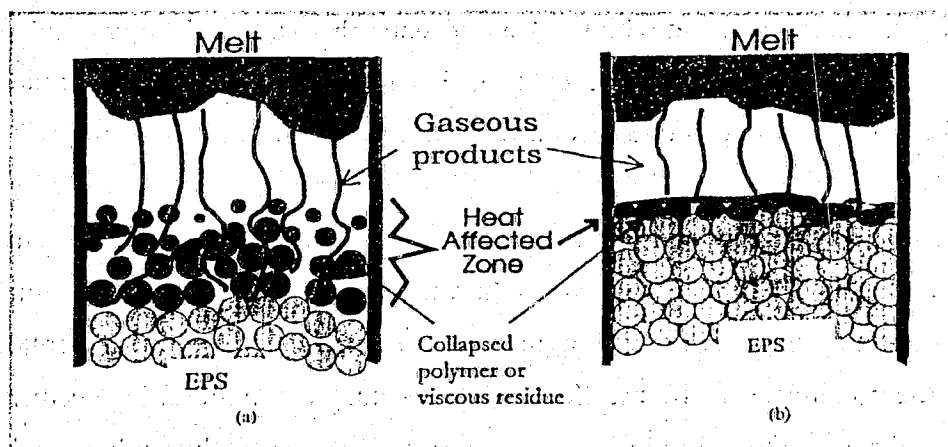


Figure 78: Heat affected zones in EPS foams of different bead fusion.<sup>56</sup>

Figure 79 and Figure 80 are stereo micrographs of the poorly fused 1.3 pcf foam and the well fused 1.6 pcf foam used in this research. The arrows in Figure 79 indicate random voids observed between respective EPS beads of the 1.3 pcf foam. The presence of these voids may have potentially enabled transfer of hot mold gases from the metal well into the foam pattern.

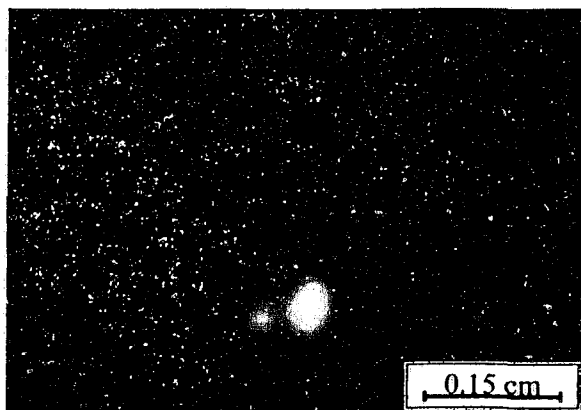


Figure 79: Poorly fused 1.3 pcf foam.

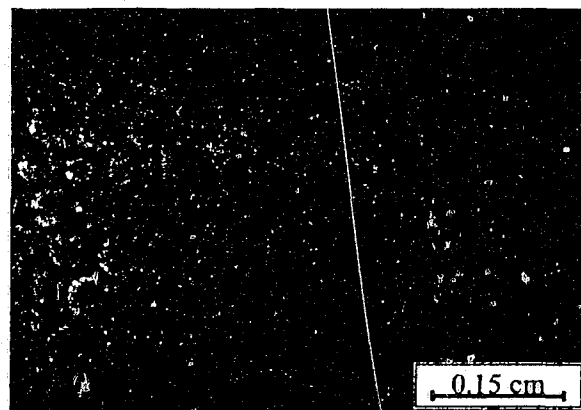


Figure 80: Well fused 1.6 pcf foam.

Due to the reduced cell strength of the poorly fused low density foam pattern (1.3 pcf) used in this research, it is possible that the foam collapse and depolymerization process began well ahead of the molten metal front. During depolymerization of the EPS pattern, C-C bonds may have been broken by random scission and, as a result, dimer, trimer and tetramer molecules formed a thick viscous residue (liquid-EPS) well ahead of the advancing metal front. The presence of these liquid-EPS degradation products may have increased the frictional forces on the molten metal flow. Consequently, the metal flow length decreased when the poorly fused 1.3 pcf foam was used, in comparison to the 1.6 pcf foam casting trials.

Therefore, it is possible, that it was not only the foam density which affected the molten metal flow length, but also the volume fraction of the liquid-EPS residue generated during the casting process. The results indicate, that the effect of bead fusion superseded the effect of the foam density in affecting the metal flow.

#### 4.3.2 Pouring temperature: 700 °C

Increasing the pouring temperature from 660 °C to 700 °C notably increased the casting percent fill, as observed in Figure 81. With additional melt superheat, the percent fill possibly increased due to: a) increased enthalpy of the metal which resulted in easier EPS degradation (viz., Section 4.2.5); and b) decreased metal viscosity promoting easier molten metal flow during the mold filling process.

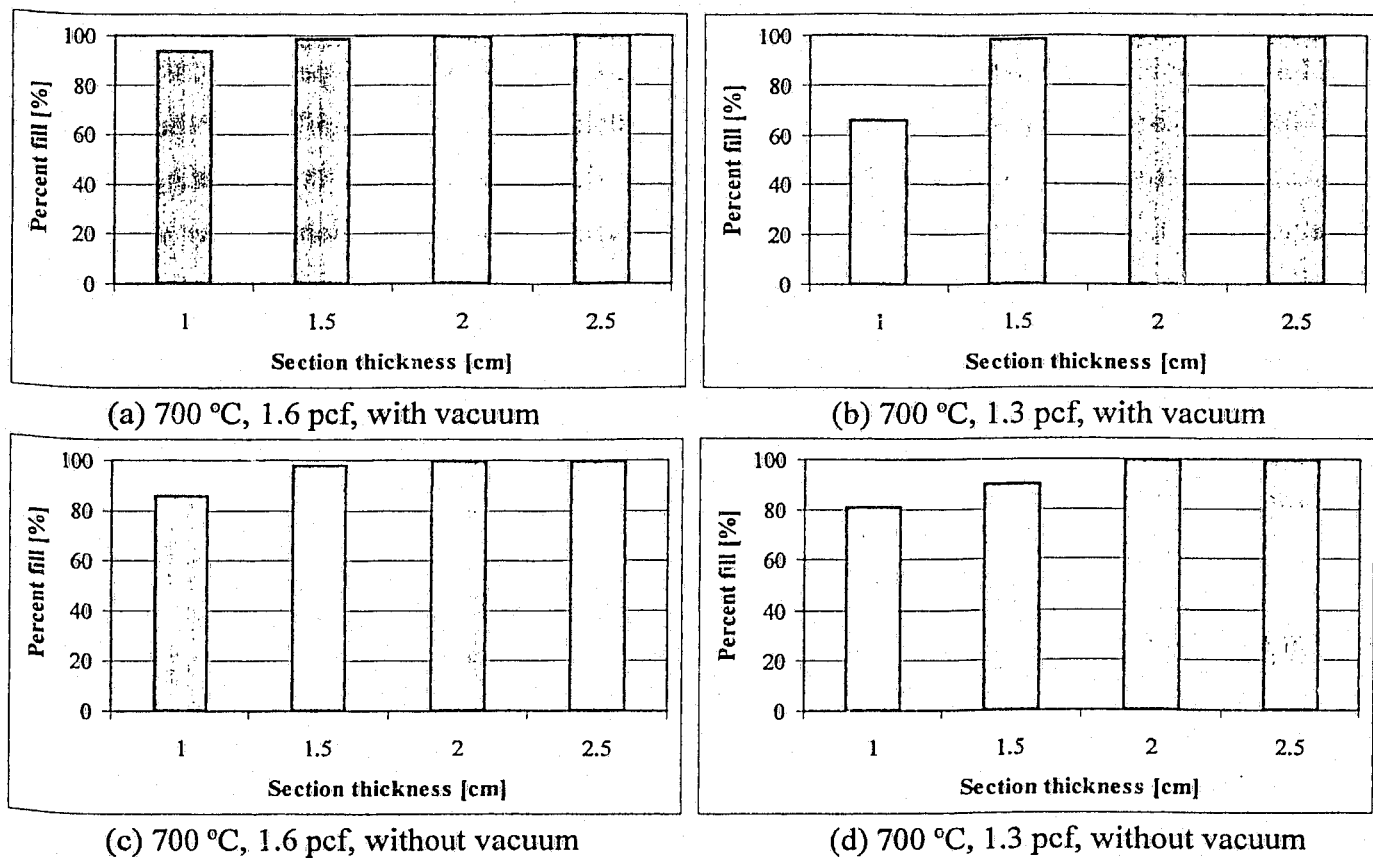


Figure 81: Casting percent fill: 700 °C pouring temperature trials.

Virtually all of the 1.5 cm, 2.0 cm and 2.5 cm thick bars filled completely. It was not possible to comment on any developing trends in the bars since the true metal flow lengths were unknown. However, the effect of the EPS foam density on the percent fill was readily observed in the 1.0 cm thick horizontal bars.

Similarly, as in the case of the 660 °C pouring temperature casting trials, the alloy flow length increased with the use of the high density foam, which was again attributed to the relative amounts of the liquid-EPS products generated during depolymerization of the foam patterns.

It was of interest to compare the effect of pouring temperature and the foam density on the percent fill of the vacuum cast 1.0 cm thick bars. In the case of the 1.6 pcf foam castings, the percent fill of the 1.0 cm thick bar improved from 92 to 94% with an increase in the pouring temperature. However, in the case of the 1.3 pcf foam castings, the percent fill improved considerably from 39 to 65% with an increase in the pouring temperature. It was suggested earlier<sup>57,58</sup> that an increase in metal superheat reduces the viscosity of the liquid-EPS residue, thus enabling easier liquid-EPS products removal from the casting cavity. Therefore, following the argument of Rossacci, if the volume fraction of the liquid-EPS products in the 1.6 pcf castings was indeed less than that in the case of the 1.3 pcf foam castings, the effect of the pouring temperature in the 1.6 pcf foam castings would be minimal, since only small volume fraction of the liquid-EPS residue in the casting cavity was affected. On the contrary, for the 1.3 pcf foam castings, large volume fractions of the liquid-EPS residue were generated due to the foam's poor bead fusion. Consequently, greater volume fractions of the liquid-EPS products were affected, thus resulting in a more appreciable metal flow length increase. Therefore, these experimental observations further validate the applicability of Rossacci's hypothesis for the current work.

The maximum casting fill was achieved in vacuum castings poured at 700 °C pouring temperature with the 1.6 pcf foam patterns. The minimum casting fill was produced in gravity castings poured at 660 °C pouring temperature with the 1.3 pcf foam patterns.

#### **4.3.3 Section summary**

Increasing the pouring temperature possibly increased the casting fillability due to the decreased AZ91E alloy viscosity. Moreover, increasing the pouring temperature made the foam depolymerization process relatively easier, thus increasing the metal flow lengths.

Poor bead fusion of the 1.3 pcf foam patterns appeared to adversely affect the casting fillability, possibly due to the premature collapse of the solid-EPS foam ahead of the molten metal front. As a result, higher volume fractions of the liquid-EPS residue were likely generated in the 1.3 pcf foam castings than in the 1.6 pcf foam castings, which resulted in a shorter metal flow lengths.

#### 4.4 Casting density and soundness

A sound casting is free of external defects, such as misruns, as well as internal defects, such as internal cavities. The former class of defects was discussed in Section 4.2 earlier, while the latter is the topic of this section.

Liquid-EPS products were observed to influence the formation of macroporosity and internal cavities in the horizontal bars. These pyrolysis products were seen to remain entrapped in the interior of the horizontal bars, with consequent formation of cavities ranging in width from 0.5 mm to 5 mm.

The measured densities of several casting sections exceeded the theoretical alloy density. Inclusions originating mainly from entrapped sand were identified as possible causes of these anomalies.

The dense segments of the castings were associated with small temperature gradients and low solidus velocities during solidification. Thus, it appears that the localized solidification conditions affected the volume fraction of shrinkage porosity, which in turn affected the casting density.

The uncertainty associated with the specimen density measurements did not exceed 1% and the uncertainty associated with the solidus velocity calculation did not exceed 7%.

The data points presented in the plots of this section correspond to the average density values for the initial and the repeat casting trials. In these graphs, error bars were intentionally omitted for clarity. The density values typically varied from the presented average value by a maximum of 0.01 g/cm<sup>3</sup>.

Further, since each average data point is based only on two measurements (initial trial and a repeat trial), the error bar maximum and minimum values would correspond to the two measured data points.

Also, the lines connecting the data points in the figures were inserted for ease of following the developing trends in the respective horizontal bars.

Each combination of the LFC casting parameters affected the casting density distribution to a different degree. As a result, individual casting conditions are discussed separately.

#### 4.4.1 Casting Condition: 660 °C, 1.3 pcf foam, with vacuum

The combination of the 660 °C pouring temperature, 1.3 pcf foam and application of vacuum resulted in the average casting density of 1.79 g/cm<sup>3</sup> with a standard deviation of  $2.68 \times 10^{-2}$  g/cm<sup>3</sup>. Using Equation 4, the theoretical average casting porosity level was calculated to be 0.66%. Figure 82 shows the variation in the casting density along the horizontal bar for different section thicknesses. It was not possible to obtain sufficient data to generate the “solidus velocity vs. distance from sprue” plot for this condition due to experimental difficulties.

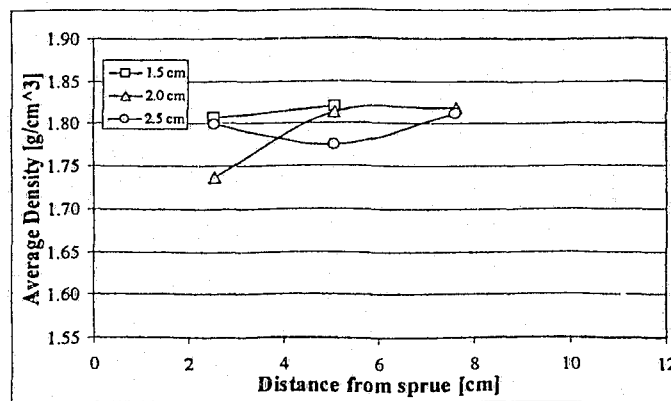


Figure 82: Average density distribution for trial: 660 °C / 1.3 pcf / with vacuum.

The casting density of the 2.0 cm thick bar reached a minimum of 1.73 g/cm<sup>3</sup> near the sprue. This decrease in the casting density was attributed to a high fraction of sub-surface shrinkage porosity, as observed in Figure 83. The 1.0 cm, 1.5 cm and 2.5 cm thick horizontal bars contained shrinkage porosity as well. However, as Figure 84 illustrates, instead of massive sub-surface shrinkage pores, inter-dendritic shrinkage cavities formed throughout the casting.

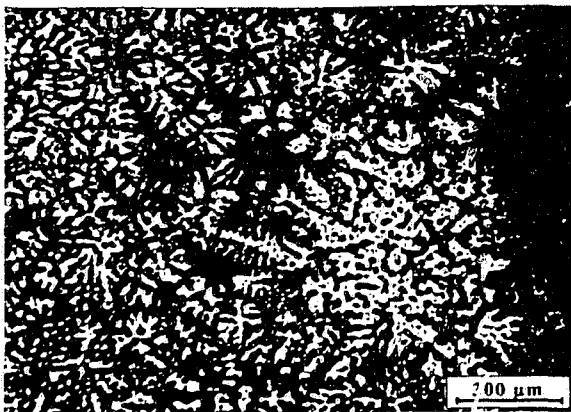


Figure 83: Sub-surface shrinkage porosity in the 2.0 cm thick bar.

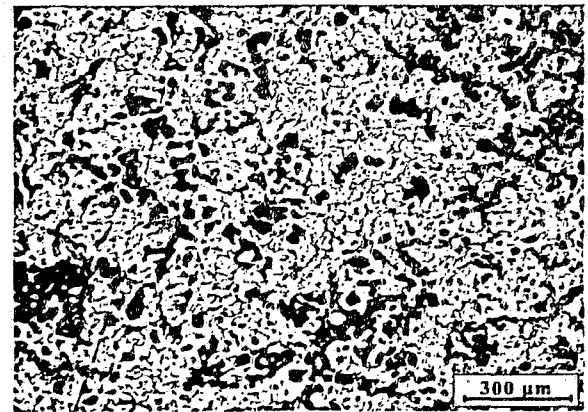
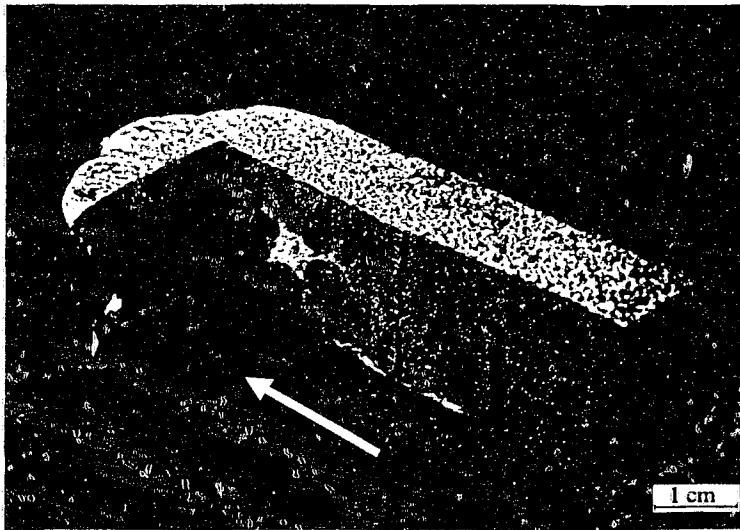


Figure 84: Interdendritic shrinkage porosity in the 2.5 cm thick bar.

The decrease in the density of the 2.5 cm thick bar at the 5 cm distance from the sprue suggests the presence of cavities in the casting bar. Two factors may have contributed to this casting defect. First, this location possibly served as a feeder of liquid metal to the surrounding casting locations during the final stages of solidification.

Secondly, as Figure 85 suggests, the decrease in the casting density at a distance of 5 cm from the sprue was the result of macroscopic cavities. These cavities possibly formed due to two factors. First, the metal flow in the vacuum castings consisted of liquid metal and partially solidified chunks, as seen in Figure 85 in the region of the cavity. Secondly, since the internal cavity was located mainly in the center-region of the horizontal bar, it is possible that the agglomerated liquid-EPS products were entrapped in the casting channel during mold filling and also contributed to the formation of the cavity.



*Figure 85: Sectioned 2.5 cm thick horizontal bar.*  
← : Direction of flow

As Figure 40 illustrates, the current combination of LFC parameters produced misruns in the horizontal bars. It was indeed difficult to obtain a complete casting. The solidus velocity at the entrance of the horizontal bar ranged between 4 – 12 cm/s for the 1.5 cm, 2.0 cm and 2.5 cm thick bars, with different temperature gradients present in the respective horizontal bars (Section 4.8). Therefore, simultaneous feeding of thin and thick sections from a single sprue was not successful in this casting trial. To improve the casting fill, risers and feeders should have been used to provide additional liquid metal to the horizontal bars and possibly manipulate the temperature distribution within the casting.

#### 4.4.2 Casting Condition: 660 °C, 1.6 pcf foam, with vacuum

For castings produced with the 660 °C pouring temperature, 1.6 pcf foam and cast under vacuum, the average casting density was 1.78 g/cm<sup>3</sup> with a standard deviation of  $7.48 \times 10^{-2}$  g/cm<sup>3</sup>. Also, the theoretical average casting porosity was 1.93%. The density and solidus velocity profiles for individual horizontal bars are presented in Figure 86 and Figure 87.

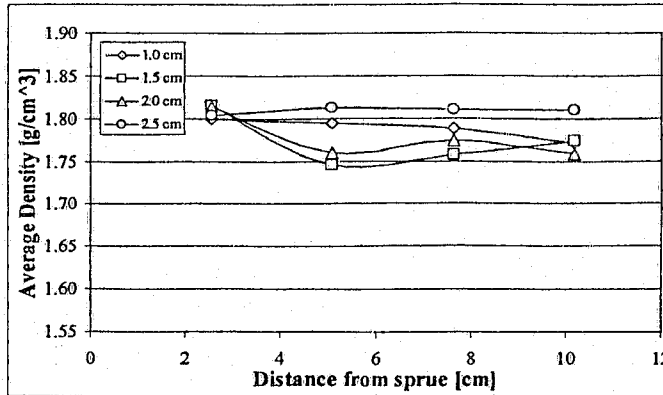


Figure 86: Average density distribution for trial: 660 °C / 1.6 pcf / with vacuum.

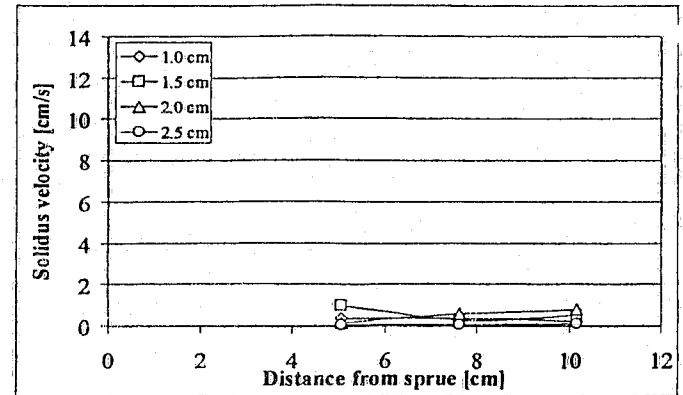


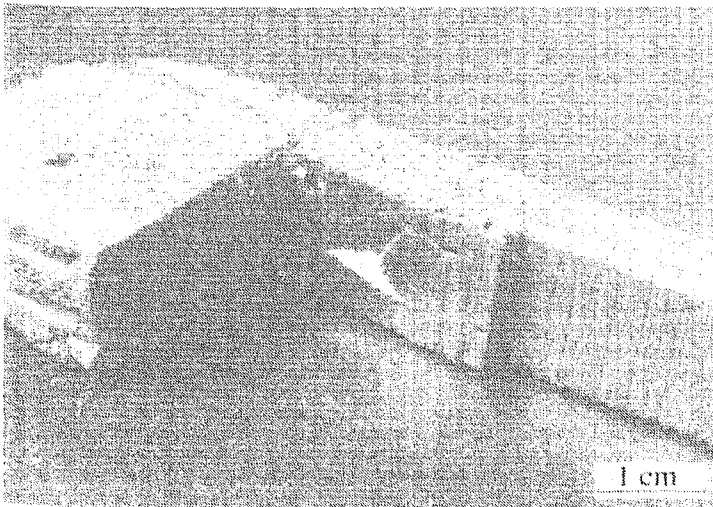
Figure 87: Solidus velocity for trial: 660 °C / 1.6 pcf / with vacuum.

The density values in the 2.5 cm thick bar approached the theoretical density of the AZ91E alloy. For the 2.5 cm thick bar, the mean density was 1.81 g/cm<sup>3</sup> with a standard deviation of  $4.12 \times 10^{-3}$  g/cm<sup>3</sup>. The measured optical porosity in the 2.5 cm thick bar was 0.73% (viz., Section 4.9), the lowest for all horizontal bars in this trial.

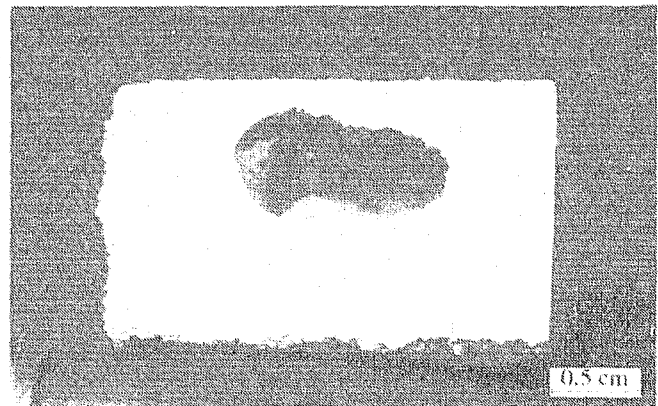
Further, the solidus velocity in the 2.5 cm thick bar was the slowest of all horizontal bars. This suggests that the solidification front traveled slowly along the horizontal bar, thus possibly allowing the liquid metal to feed the interdendritic regions and prevent formation of shrinkage cavities. As a result, relatively dense horizontal bar was produced.

The 1.0 cm thick horizontal bar also showed a relatively uniform density distribution along the length of the bar. The density ranged between 1.77 – 1.80 g/cm<sup>3</sup> with an average and a standard deviation of 1.78 g/cm<sup>3</sup> and  $1.22 \times 10^{-2}$  g/cm<sup>3</sup>, respectively. In this case, the possibility of establishing directional solidification was rejected since the solidus plot (Figure 87) decreased near the flow tip. Such trend indicates the presence of heat waves passing through the horizontal bar.

The 1.5 cm and 2.0 cm thick bars exhibit fluctuations in the casting density along the length of the horizontal bars. These fluctuations did not appear to result either from solidification shrinkage or ineffective directional solidification. As in the previous casting condition, flow of partially solidified metal and entrapped liquid-EPS likely contributed to the formation of internal casting voids. Figure 88 and Figure 90 show the interior of the 1.5 cm and 2.0 cm thick bars, respectively. As Figure 89 suggests, the minimum at the 4 cm distance from the sprue of the 1.5 cm thick bar was seen to result from macroscopic cavities caused by the liquid-EPS residue.



*Figure 88: Sectioned view of the 1.5 cm thick horizontal bar.*



*Figure 89: Internal cavity in the 1.5 cm thick bar at the 2.5 cm distance from the sprue.*

As observed in Figure 90, macroscopic voids were present along the entire length of the 2.0 cm thick horizontal bar. These voids ranged from 0.2 cm to 1.5 cm in width. Both, the 1.5 cm and the 2.0 cm thick horizontal bars contained large cavities near the frozen metal fronts. This suggests that the liquid-EPS residue was possibly pushed by the molten metal front during the mold filling process, and, as the metal front advanced through the solid-EPS pattern, the residue was unable to float to the metal-mold interface (due to the concave metal front profile). As a result, macroscopic voids formed in the interior of the casting bar.



In addition to the presence of large volume fractions of liquid-EPS products, the metal flow was hindered due to the presence of partially solidified chunks of AZ91E. Inspection of the interior of the casting bar near the flow tip revealed metal chunks approximately 0.9 cm in width, as shown in Figure 91.

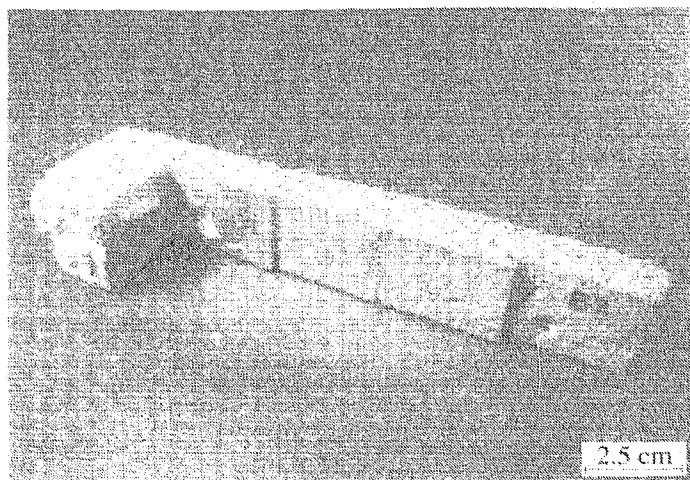


Figure 90: Sectioned view of the 2.0 cm thick bar.

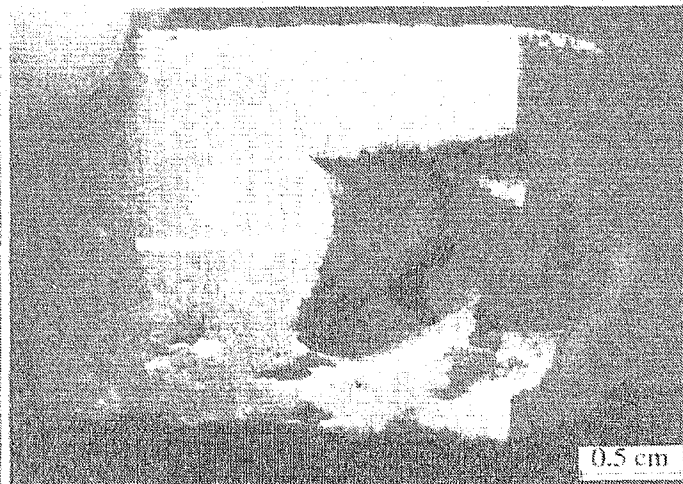
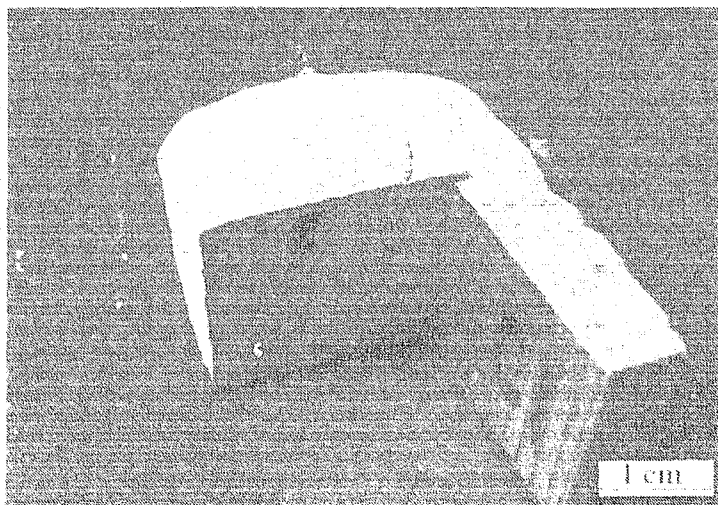


Figure 91: Frozen metal chunks near the flow tip of the 2.0 cm thick bar.

→: Direction of flow

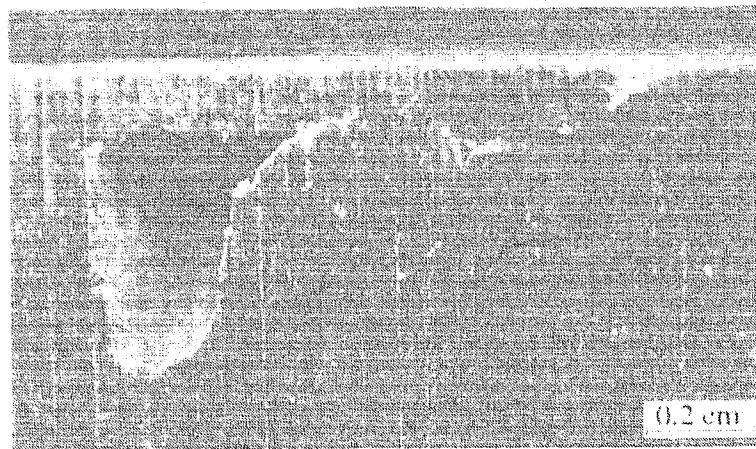
#### *4.4.3 Casting Condition: 660 °C, 1.3 pcf foam, without vacuum*

Castings produced with the 660 °C pouring temperature, the 1.3 pcf foam under gravity conditions did not fill sufficiently to provide data for density and solidus velocity analysis. However, sectioning of the 2.5 cm thick horizontal bar revealed entrapped liquid-EPS products near the upper surface of the horizontal bar, as shown in Figure 92. In this figure, a 4.5 mm wide cavity was found near the upper surface of the horizontal bar.

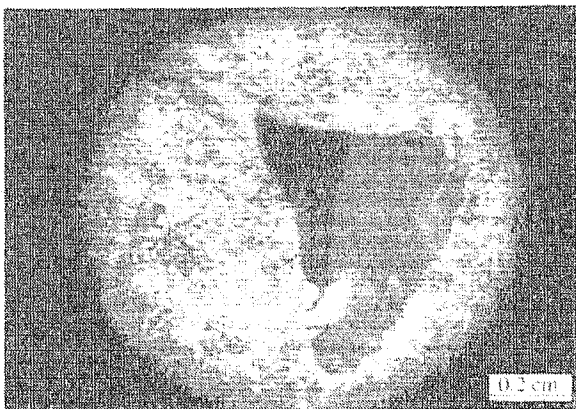


*Figure 92: Sectioned view of the 2.5 cm thick bar.*

Under gravity casting conditions, the liquid-EPS products floated to the top of the casting channel during mold filling. Upon reaching the metal-mold interface, they wicked through the ceramic coating to the surrounding sand. In this casting trial, however, the freezing of the metal front possibly did not allow the liquid-EPS residue to reach the metal-mold interface. As a result, an internal cavity formed. Figure 93 is an enlarged view of this cavity. Figure 94 and Figure 95 are stereo micrographs showing hardened EPS residue adhering to the cavity walls. These figures prove that liquid-EPS residue was present in this casting cavity and was likely the primary cause of the cavity formation.



*Figure 93: Subsurface cavity in the 2.5 cm thick bar.*



*Figure 94: Liquid-EPS residue adhering to the internal cavity walls.*



*Figure 95: Liquid-EPS residue, enlarged.*

Further, Figure 93 also shows a fold-like extension originating from the cavity towards the casting surface. Thus, it is possible that, after the liquid-EPS entrapment in the casting occurred, gaseous products of liquid-EPS pyrolysis could have escaped through a narrow path to the casting surface.

#### 4.4.4 Casting Condition: 660 °C, 1.6 pcf foam, without vacuum

The combination of the 660 °C pouring temperature, 1.6 pcf foam and the absence of vacuum resulted in the average casting density of 1.81 g/cm<sup>3</sup> with a standard deviation of  $3.19 \times 10^{-3}$  g/cm<sup>3</sup>. The density values of the individual casting sections occasionally exceeded the theoretical AZ91E alloy density. As a result, it was not possible to utilize Equation 4 to estimate the theoretical average % porosity for the castings. The density and solidus velocity profiles for individual horizontal bars are presented in Figure 96 and Figure 97.

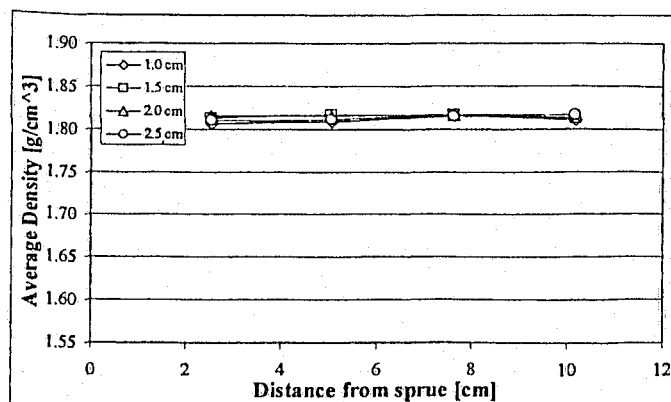


Figure 96: Average density distribution for trial: 660 °C / 1.6 pcf / without vacuum.

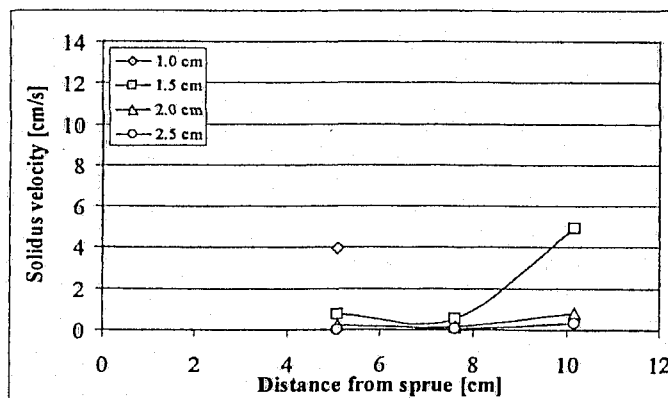


Figure 97: Solidus velocity for trial: 660 °C / 1.6 pcf / without vacuum.

Comparing the current no-vacuum trial to that of the castings produced under vacuum (Section 4.4.2), it was observed that vacuum increased the casting density variation. For the vacuum trials with the 1.6 pcf foam, the casting density ranged between 1.75 – 1.81 g/cm<sup>3</sup> with a standard deviation of  $7.48 \times 10^{-2}$  g/cm<sup>3</sup>, whereas for the castings produced under gravity conditions in the current trial, the casting density ranged between 1.81 – 1.82 g/cm<sup>3</sup>, with a standard deviation of  $3.19 \times 10^{-3}$  g/cm<sup>3</sup>. This supports earlier suggestion that the metal flow in vacuum castings possibly consisted of a liquid metal carrying partially solidified chunks, which cooled separately from the bulk liquid metal. As a result, vacuum castings had an inhomogeneous internal structure which caused a higher casting density variance. Clearly, the casting soundness was compromised by the vacuum.

In castings produced without vacuum, directional solidification was established. As observed in Figure 97, the solidus velocity profiles generally increased with increasing distance from the sprue. This suggests, that casting locations near the flow tip solidified faster than locations near the sprue, which is a requirement for the establishment of directional solidification.

As a result of directional solidification, there seems to be a general trend of an increasing casting density with increasing distance from the sprue. Such a trend was confirmed by the analysis of the cooling rates in the respective horizontal bars. As shown in Figure 98, the cooling rates increased with the distance from the sprue.

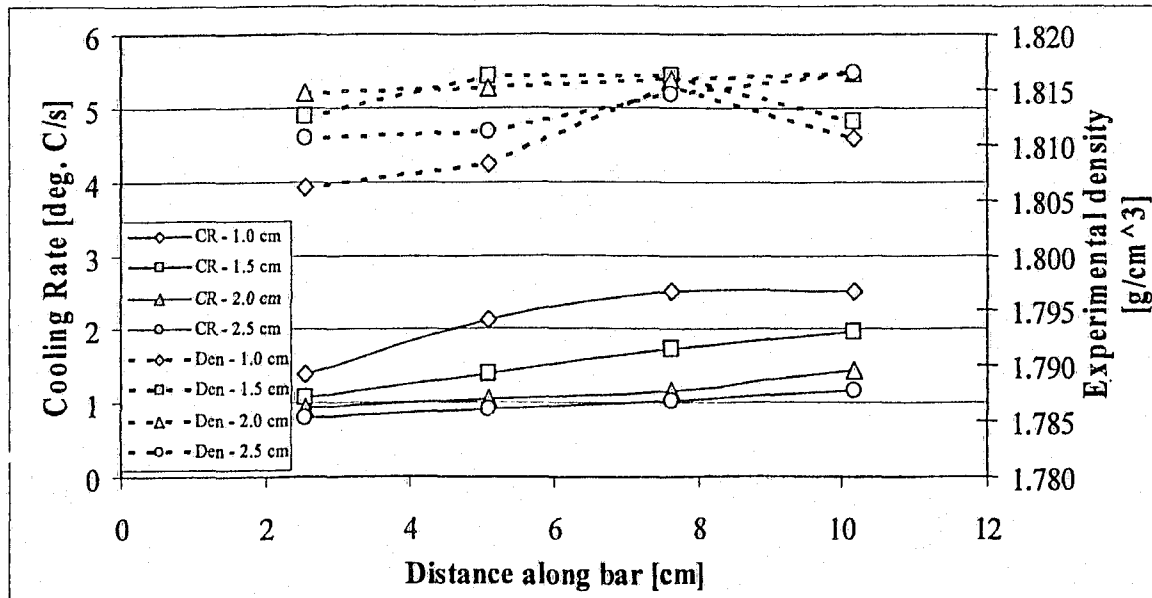


Figure 98: Effect of section thickness on the cooling rate and the casting density.

#### 4.4.5 Casting Condition: 700 °C, 1.6 pcf foam, with vacuum

The combination of the 700 °C pouring temperature, 1.6 pcf foam and application of vacuum resulted in the average casting density of 1.82 g/cm<sup>3</sup> with a standard deviation of  $9.20 \times 10^{-3}$  g/cm<sup>3</sup>. Many locations of the horizontal bars had density values in excess of the published density of the AZ91E magnesium alloy. The density and solidus velocity profiles for individual horizontal bars are presented in Figure 99 and Figure 100.

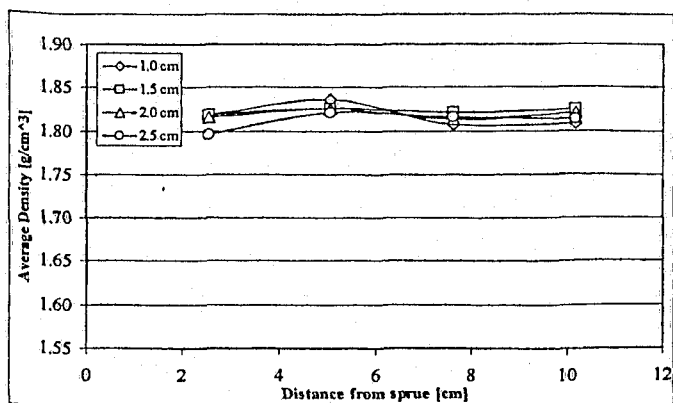


Figure 99: Average density distribution for trial: 700 °C / 1.6 pcf / with vacuum.

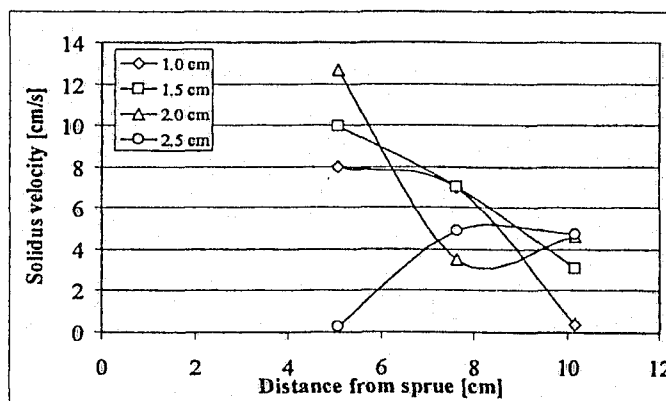


Figure 100: Solidus velocity for trial: 700 °C / 1.6 pcf / with vacuum.

The high density in the casting bars was attributed to the presence of inclusions. Figure 62 clearly illustrated that the application of vacuum caused liquid metal to penetrate the sand mold. During such a process, the molten alloy possibly caused a localized erosion of the sand, resulting in a carryover of the eroded sand into the casting cavity. As Figure 101 and Figure 102 show, sand fragments were present in the casting interior near the casting surface.

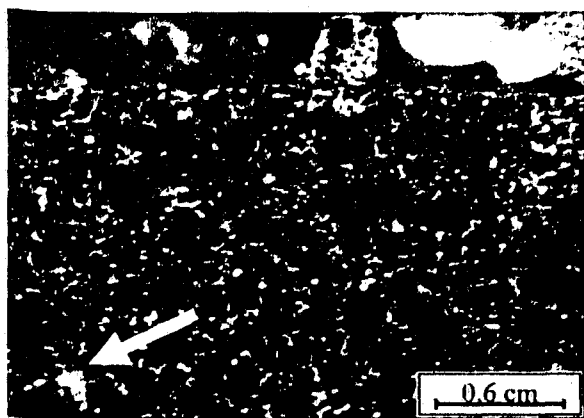


Figure 101: Sand inclusion near the metal-mold interface.

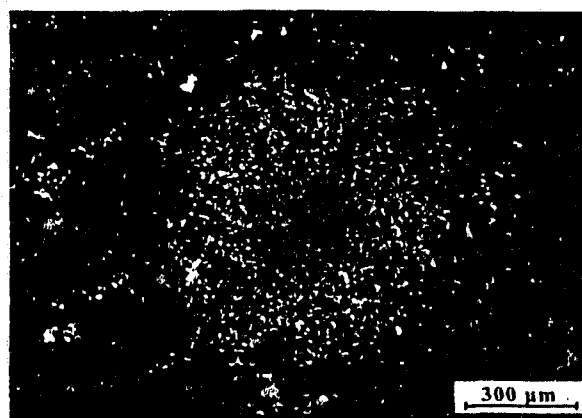


Figure 102: Detailed view of the sand inclusion in Figure 101.

In addition to the high casting density values, density fluctuations along the length of the casting bar were observed. As Figure 99 shows, all horizontal bars exhibited this behavior. The fluctuations in the casting density were attributed to the following factors. First, the presence of partially solidified chunks resulted in non-homogeneous casting density, as already discussed in Section 4.2.6. Secondly, the presence of the solid chunks possibly obstructed the incoming liquid metal feed during the last stages of solidification. As a result, regions with inadequate liquid metal feed contained shrinkage pores, thus decreasing the casting density.

#### 4.4.6 Casting Condition: 700 °C, 1.3 pcf foam, with vacuum

The average density for the castings produced at the 700 °C pouring temperature, with 1.3 pcf foam pattern cast under vacuum was 1.81 g/cm<sup>3</sup> with a standard deviation of  $3.78 \times 10^{-2}$  g/cm<sup>3</sup>. The theoretical average casting porosity was less than 0.05%. With the exception of the 1.0 cm bar, the density values in the 1.5 cm, 2.0 cm and 2.5 cm thick bars ranged between 1.76 – 1.83 g/cm<sup>3</sup> with an average of 1.82 g/cm<sup>3</sup> and a standard deviation of  $1.52 \times 10^{-2}$  g/cm<sup>3</sup>. The density and solidus velocity profiles for individual horizontal bars are presented in Figure 103 and Figure 104.

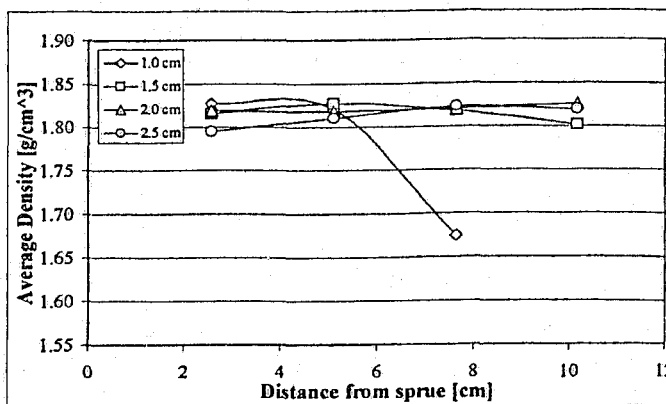


Figure 103: Average density distribution for trial:  
700 °C / 1.3 pcf / with vacuum.

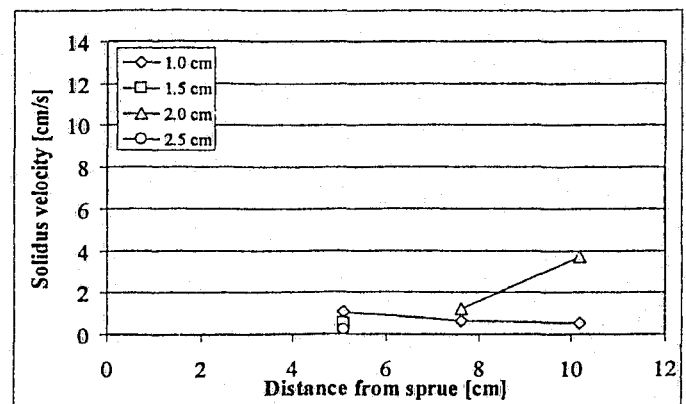
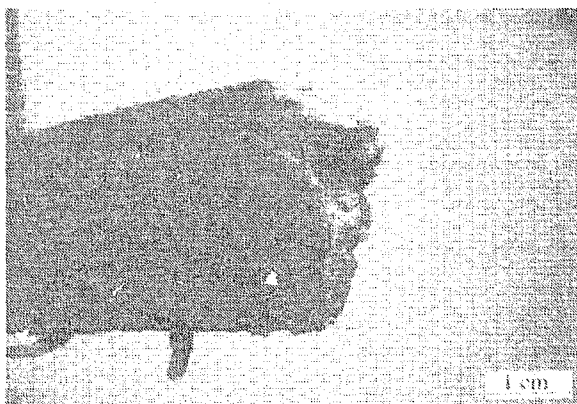


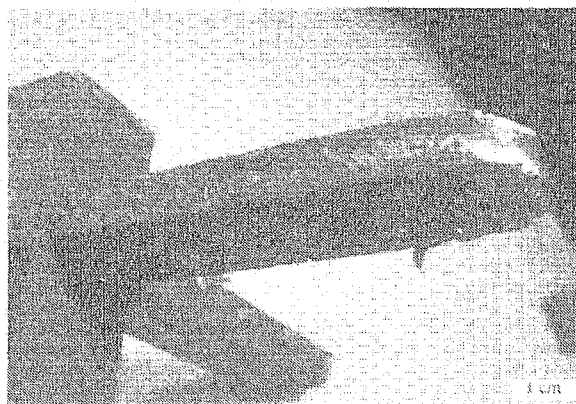
Figure 104: Solidus velocity for trial:  
700 °C / 1.3 pcf / with vacuum.

As Figure 103 shows, the 1.0 cm thick bar exhibits a sharp decrease in the casting density with increasing distance from the sprue. Figure 105 and Figure 106 show the 1.0 cm thick bar from the two (initial and repeat) casting trials. It appears that the decrease in the casting density near the frozen metal front was to an extent caused by the metal chunks restricting the liquid metal feed.

Further, as Figure 106 suggests, liquid-EPS products agglomerated at the advancing metal front and were pushed towards the end of the flow channel. As a result, the maximum volume of the liquid-EPS residue was present at the frozen metal front, further contributing to a decrease in the casting density.

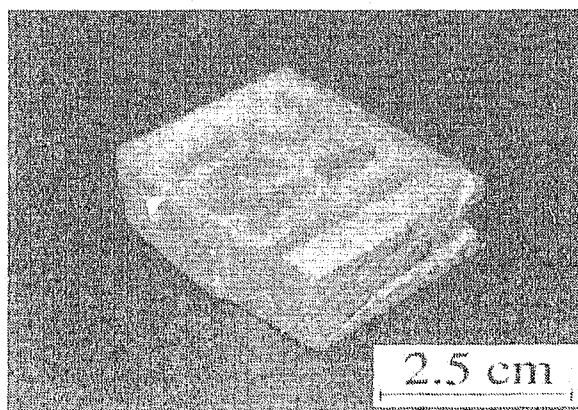


*Figure 105: Solidified metal chunks at the metal front of the 1.0 cm thick bar.*



*Figure 106: Liquid-EPS impressions along the sides of the 1.0 cm thick bar.*

Figure 107 is a sectioned specimen of the 1.0 cm thick bar near the 8 cm distance from the sprue. The sides of the specimen show river-like marks caused by the liquid-EPS residue. During stamping of the samples, for identification purposes, the surface of the specimen fractured and revealed a massive internal void. This suggests that a high volume fraction of liquid-EPS products accumulated at the metal-mold interface and was entrapped in the casting. All of these factors contributed to the variation of the localized casting density.



*Figure 107: Internal casting cavities in the 1.0 cm thick bar at 8 cm distance from the sprue.*



#### 4.4.7 Casting Condition: 700 °C, 1.6 pcf foam, without vacuum

The combination of the 700 °C pouring temperature, 1.6 pcf foam and the absence of vacuum resulted in the average casting density of  $1.81 \text{ g/cm}^3$  with a standard deviation of  $5.92 \times 10^{-3} \text{ g/cm}^3$ . Thus, the absence of vacuum during mold filling improved density uniformity. Further, relatively slow solidus velocities in this casting trial suggest the possibility of molten metal mass feeding for long periods of time, which prevented formation of interdendritic shrinkage cavities. The density and solidus velocity profiles for individual horizontal bars are presented in Figure 108 and Figure 109.

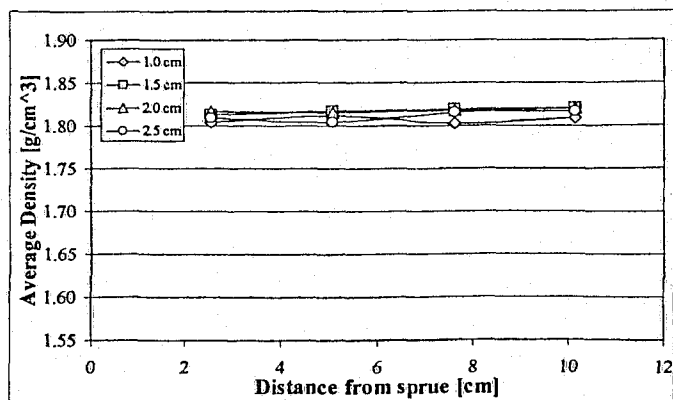


Figure 108: Average density distribution for trial: 700 °C / 1.6 pcf / without vacuum.

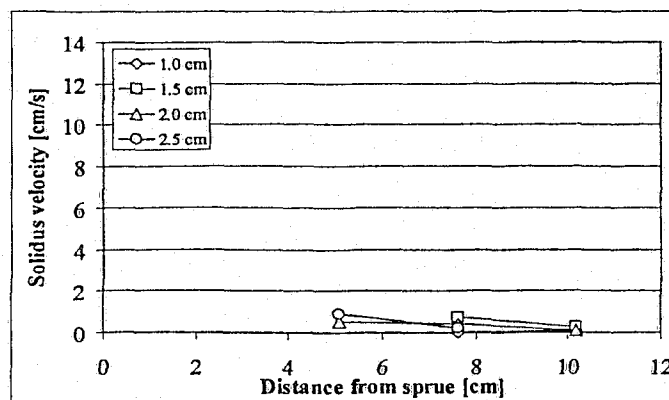


Figure 109: Solidus velocity for trial: 700 °C / 1.6 pcf / without vacuum.

#### 4.4.8 Casting Condition: 700 °C, 1.3 pcf foam, without vacuum

The combination of the 700 °C pouring temperature, 1.3 pcf foam and the absence of vacuum resulted in an average casting density of  $1.82 \text{ g/cm}^3$  with a standard deviation of  $4.90 \times 10^{-3} \text{ g/cm}^3$ . As Figure 110 shows, the 1.5 cm thick bar exhibited unusual density distribution along the horizontal bar. The casting density reached a maximum value of  $1.83 \text{ g/cm}^3$ , significantly exceeding the theoretical density of the AZ91E alloy. The cause of this anomaly is unknown. However, occurrence of this anomaly was associated with a decrease in the cooling rate and the solidus velocity, as evidenced by Figure 111.

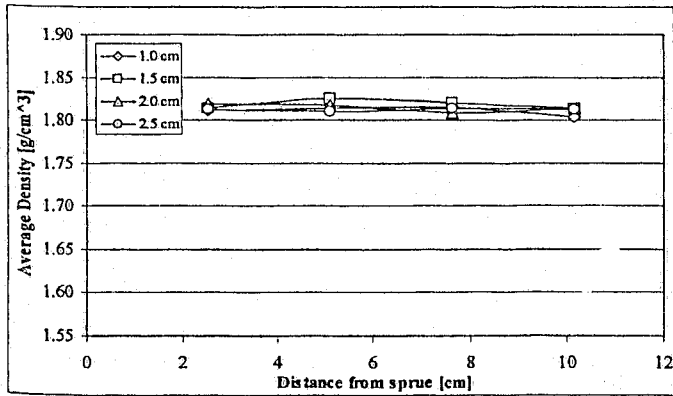


Figure 110: Average density distribution for trial: 700 °C / 1.3 pcf / without vacuum.

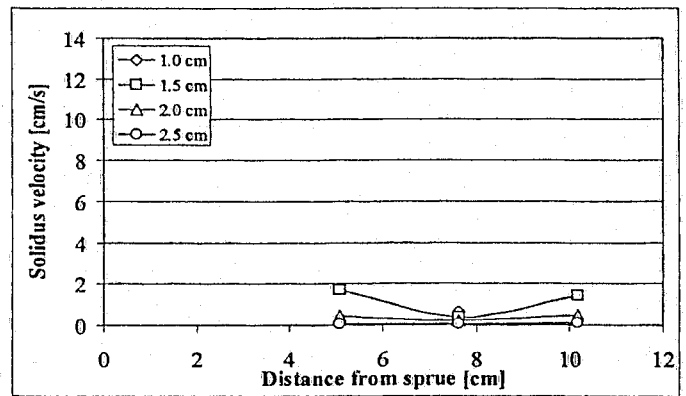


Figure 111: Solidus velocity for trial: 700 °C / 1.3 pcf / without vacuum.

The density measurements for all casting trials for different section thicknesses were plotted in Figure 112. The scatter in the density data was attributed to the variation of the LFC process parameters.

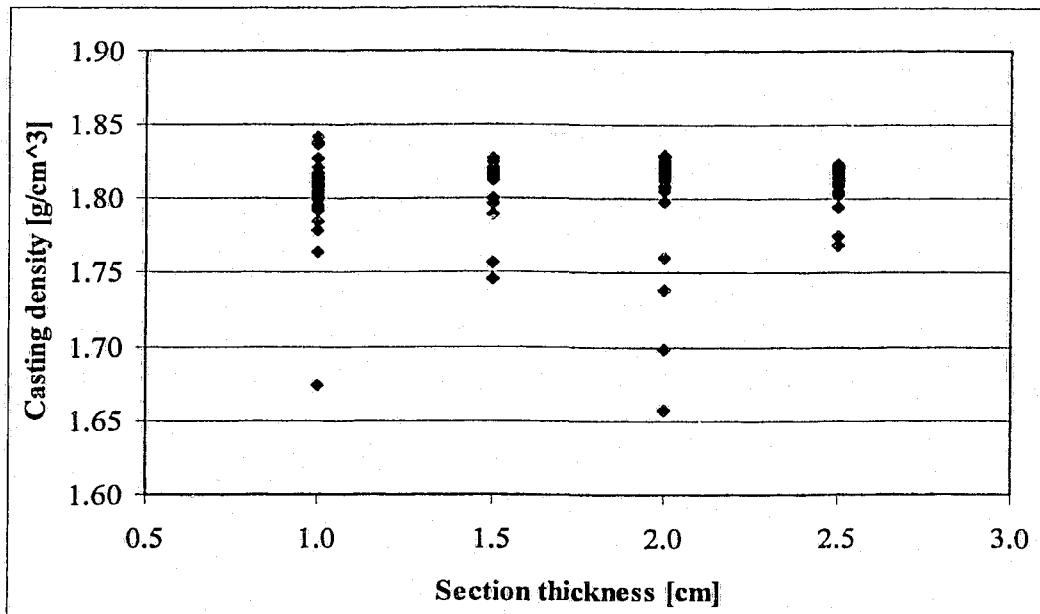


Figure 112: Casting density data for all casting trials.

#### 4.4.9 Statistical analysis

The objective of the statistical analysis was to verify, whether or not selected LFC process parameters affected the casting density.

The null hypothesis was established with the view to determining whether or not a given LFC parameter affected the casting density (based on the density variances associated with the parameter). It was not the objective of the statistical analysis to hypothesize the population (alloy) density.

In order to determine which casting trial affected the average casting density, a test statistic based on the Student's t-distribution was used:

$$\bar{t} = \frac{\bar{x} - \mu'}{s / \sqrt{n'}} \quad (11)$$

Where:

$\bar{x}$  = Casting sample average density

$\mu'$  = Population density = theoretical density of the alloy = 1.810 g/cm<sup>3</sup>

$s$  = Sample standard deviation

$n'$  = Sample size

The acceptance or rejection of the null hypothesis was based on calculating the  $P_{\alpha\text{-max}}$  value from the experimental test statistic. The following decision criteria were selected:

- If  $P_{\alpha\text{-max}} < 80\%$ , the null hypothesis was accepted (i.e., the LFC parameters did not affect the average casting density).
- If  $P_{\alpha\text{-max}} > 90\%$ , the null hypothesis was rejected (i.e., the LFC parameters did affect the average casting density).
- If  $80\% < P_{\alpha\text{-max}} < 90\%$ , no decision was rendered. In such cases, more experimental data would be required to make an accurate decision.

The results of the statistical analysis are presented in Table 7.

Table 7: Effect of individual casting trials on the casting density.

Trial	Sample size, n'	$t_{0.025,n'}$	$P_{\alpha-\max}$ [%]	Hypothesis
660 °C / 1.3 pcf / with vacuum	9	1.219	86.00	No-decision
660 °C / 1.6 pcf / with vacuum	16	2.958	99.48	Reject
660 °C / 1.3 pcf / without vacuum	-	-	-	-
660 °C / 1.6 pcf / without vacuum	16	3.071	99.60	Reject
700 °C / 1.6 pcf / with vacuum	16	2.542	98.90	Reject
700 °C / 1.3 pcf / with vacuum	16	0.201	58.00	Accept
700 °C / 1.6 pcf / without vacuum	16	1.665	94.00	Reject
700 °C / 1.3 pcf / without vacuum	16	2.601	99.10	Reject

Therefore, based on the results of the above statistical analysis, it is evident, that with the exception of the 700 °C / 1.3 pcf / with vacuum casting trial, the respective casting parameters (i.e., pouring temperature, foam density and applied vacuum) indeed affected the average casting density. In the case of the 660 °C / 1.3 pcf / with vacuum casting trial, the  $P_{\alpha-\max}$  value corresponds to the “no-decision” region of the hypothesis testing technique. As a result, more experimental data would be required to make a definite conclusion.

The results of Section 4.4 were also analyzed using the analysis of variance (ANOVA) technique. This analysis allowed the determination of whether or not a selected casting parameter influenced the average casting density (based on its impact on the casting density variance). This analysis was carried out in the MS Excel Data Analysis tool. A Fisher F-statistic was calculated and used to obtain the  $P_{\alpha-\max}$  value for rejection of the null hypothesis. The Fisher random variable was defined as: <sup>59</sup>

$$F = \frac{\chi_1^2 / \nu_1}{\chi_2^2 / \nu_2} \quad (12)$$

This test statistic applied to any combination of casting parameters involving two statistically independent  $\chi^2$  random variables with  $\nu_1$  and  $\nu_2$  degrees of freedom. In most cases,  $\nu_1$  and  $\nu_2$  were equal to 1.

The ANOVA analysis was used to determine whether or not the pouring temperature and the application of vacuum affected the average casting density of the 1.6 pcf foam castings. This analysis was treated as a 2-factor experiment with replication.

The results of the ANOVA analysis as processed by MS Excel are presented in Table 8. Detailed results are presented in Appendix B.1.

*Table 8: Effect of pouring temperature and vacuum on the casting density, ANOVA results.*

Source of Variation	F-statistic	$P_{\alpha-\max}$ [%]	Hypothesis
Pouring temperature	2.94	69.50	Accept
Application of vacuum	3.42	70.50	Accept
Interaction	3.65	71.70	Accept

The ANOVA analysis suggests, that there were no interactive effects between the alloy pouring temperature and the applied vacuum. Further, there was no effect of the pouring temperature on the casting density; as well as, there was no effect of the vacuum on the casting density.

These statistical results agree with conclusions made in earlier sections. Since the 1.6 pcf foam castings contained only relatively small volume fractions of liquid-EPS products, the effect of vacuum and pouring temperature was not very noticeable. If greater volume fractions of liquid-EPS products were present, the effect of the vacuum and the pouring temperature would be possibly more pronounced. Such behavior was observed qualitatively earlier in the 1.3 pcf foam trials; however, lack of experimental density data prevented carrying out the ANOVA analysis for these casting trials.

The ANOVA analysis was also used to verify whether the foam density and the application of vacuum influenced the average casting density in the 660 °C and 700 °C pouring temperature casting trials.

The ANOVA analysis for the 660 °C pouring temperature trials produced the following results (Table 9):

*Table 9: Effect of foam density and vacuum on the casting density in the 660 °C pouring temperature trials, ANOVA results.*

Source of Variation	F-statistic	$P_{\alpha-\max}$ [%]	Hypothesis
Foam density	0.12	50.30	Accept
Presence of vacuum	3.66	71.50	Accept
Interaction	0.03	50.01	Accept

The ANOVA analysis for the 700 °C pouring temperature trials produced the following results (Table 10):

*Table 10: Effect of foam density and vacuum on the casting density in the 700 °C pouring temperature trials, ANOVA results.*

Source of Variation	F-statistic	P <sub><math>\alpha</math>-max</sub> [%]	Hypothesis
Foam density	0.65	54.00	Accept
Presence of vacuum	0.39	52.10	Accept
Interaction	0.31	51.20	Accept

The common conclusions for both pouring temperatures were:

There were no interactive effects between the foam pattern density and the applied vacuum. Further, it was determined, that neither foam density nor the application of vacuum affected the average casting density.

Detailed results of the ANOVA analysis are presented in Appendix B.2 (660 °C pouring temperature) and Appendix B.3 (700 °C pouring temperature).

#### ***4.4.10 Section summary***

The application of vacuum during mold filling resulted in the molten metal flow past the dendrite coherency point. As a result, flow of partially solidified metal occurred. Consequently, macroscopic voids formed in the interior of several casting bars. These voids were prominent especially in the 660 °C pouring temperature casting trials, where entrapped liquid-EPS possibly further increased the size of the cavities.

Statistical analysis revealed that castings produced under vacuum had a greater variance of the casting density. This is indicative of a heterogeneous casting structure. Increasing the pouring temperature improved the casting density uniformity, due to a possible reduction of entrapped liquid-EPS products in the horizontal bars.

Entrapped liquid-EPS products were seen to create voids in the interior of the horizontal bars. Further, it appears that the molten metal did not possess sufficient energy to pyrolyze the liquid-EPS products, since hardened EPS residue was observed on the cavity walls.

In several instances, the casting density was seen to exceed the theoretical alloy density. In these cases, sand inclusions were identified as a potential source of the anomaly.

## 4.5 Metal velocity

The metal front velocity was calculated from the dynamic temperature data collected by the data acquisition system during mold filling. For each thermocouple, a maximum temperature was recorded. Determining the time delay between the temperature maxima of adjacent thermocouples enabled the calculation of the molten metal velocity. The uncertainty associated with the metal velocity measurements did not exceed 4%.

The data points in the “Average metal velocity” plots correspond to an average metal velocity in two casting trials (initial and repeat). As in Section 4.4, error bars were omitted from these plots for clarity.

The metal behavior seemed to be affected by every combination of the investigated LFC parameters. Therefore, respective casting conditions were examined and their effect on the metal velocity discussed.

### 4.5.1 Casting Condition: 660 °C, 1.3 pcf foam, with vacuum

In the casting trial with the 660 °C pouring temperature, 1.3 pcf foam and applied vacuum, the average metal velocity was 1.6 cm/s with a standard deviation of 0.7 cm/s. As Figure 113 indicates, the 1.0 cm and 1.5 cm thick bars did not fill sufficiently to allow calculation of the velocity profiles for these bars. In the case of the 2.0 cm and 2.5 cm thick bars, only partial velocity profiles were available (see Section 4.4.1).

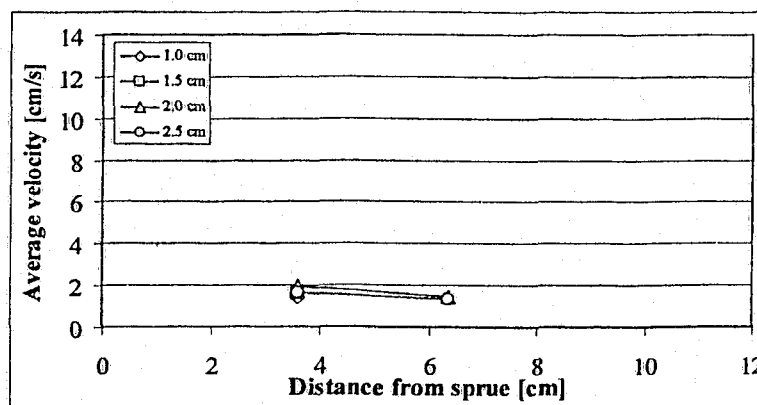


Figure 113: Average metal velocity for trial: 660 °C / 1.3 pcf / with vacuum.



The metal velocities near the entrance of the horizontal channels were similar for all section thicknesses, ranging between 1.4 – 1.9 cm/s with a standard deviation of 0.3 cm/s. As the metal front advanced, the metal velocity was observed to decrease with increasing flow length. Since the molten metal was solidifying as it progressed through the foam pattern, its viscosity as well as the solid fraction increased, thus slowing down the metal flow.

#### 4.5.2 Casting Condition: 660 °C, 1.6 pcf foam, with vacuum

The casting condition with the 660 °C pouring temperature, 1.6 pcf foam and applied vacuum resulted in an average metal velocity of 6.4 cm/s with a standard deviation of 2.0 cm/s.

In this casting trial, the metal velocities ranged between 4.0 – 11.5 cm/s. Comparing these values to those of castings produced with the 1.3 pcf foam (Section 4.5.1), a general increase in metal velocities was observed. As discussed earlier, it is likely that the 1.3 pcf poorly fused foam may have produced larger volume fractions of the liquid-EPS residue. As a result, the friction in the casting channel increased due to the accumulation and adherence of the liquid-EPS products to the mold walls. Consequently, the metal velocity was slower in the 1.3 pcf foam castings than in the case of the 1.6 pcf foam castings.

Metal velocity oscillations developed in the longitudinal direction of the flow, as observed in Figure 114. These oscillations were characteristic of the progressive mold filling during LFC.

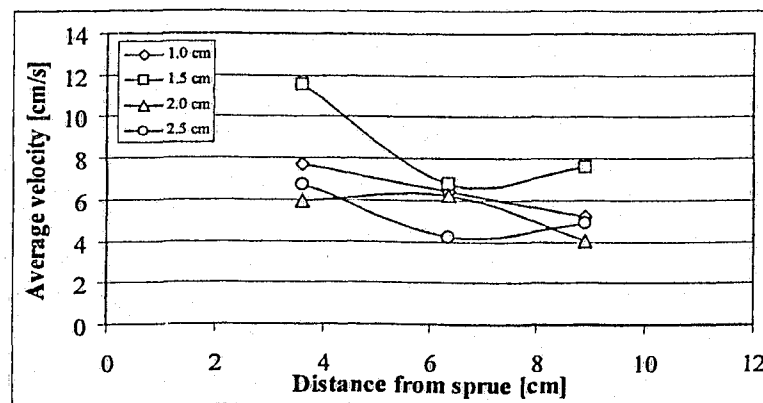


Figure 114: Average metal velocity for trial: 660 °C / 1.6 pcf / with vacuum.

As previously discussed<sup>60</sup> the amplitude of these velocity oscillations decreased with increasing distance from the sprue. Further, these oscillations disappear at higher pouring temperatures, where the foam degradation and removal process becomes energetically easier.

#### 4.5.3 Casting Condition: 660 °C, 1.6 pcf foam, without vacuum

The combination of the 660 °C pouring temperature, 1.6 pcf foam and the absence of vacuum resulted in an average metal velocity of 2.8 cm/s, with a standard deviation of 1.1 cm/s.

Comparing the current results (Figure 115) with those of Section 4.5.2, it was observed that the average metal velocity decreased from 6.4 cm/s in the vacuum trial to 2.8 cm/s in the current gravity trial. This decrease in metal velocity was attributed to the slower extraction rate of the EPS pyrolysis products from the casting cavity during the gravity filling process. This result supports the conclusions of Liu et. al. (see Section 2.2.1.2).

Furthermore, comparing the standard deviations of the similar vacuum trial (2.0 cm/s) to the current casting condition, it appears that the application of vacuum caused a significant variation in the metal velocity. This observation complements the results of Section 4.2 and Section 4.4.

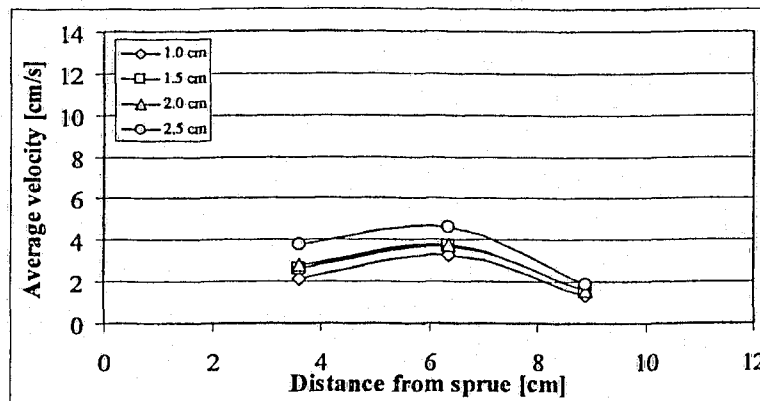


Figure 115: Average metal velocity for trial: 660 °C / 1.6 pcf / without vacuum.

#### 4.5.4 Casting Condition: 700 °C, 1.6 pcf foam, with vacuum

The combination of the 700 °C pouring temperature, 1.6 pcf foam and applied vacuum, resulted in an average metal velocity of 6.3 cm/s, with a standard deviation of 1.4 cm/s.

In this casting trial, the metal velocities ranged between 4.6 – 8.3 cm/s. Comparing Figure 114 and Figure 116, it is evident that the increase in pouring temperature generally increased the metal velocities in the horizontal bars. This change was attributed to the greater heat content of the molten metal (see Appendix A), which caused the EPS degradation process to be relatively easier, with attendant increase in the metal flow length and velocity.

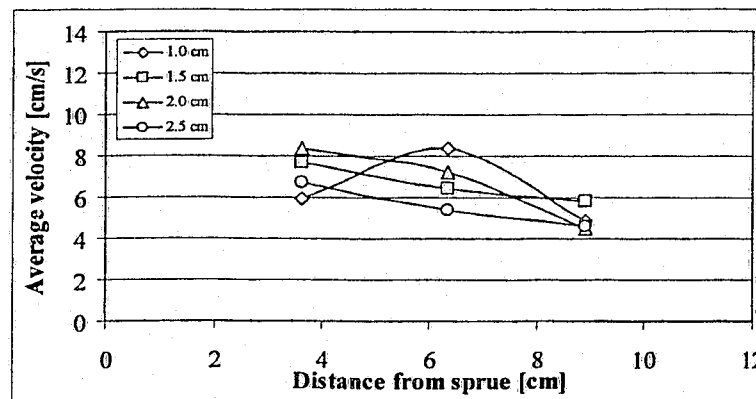


Figure 116: Average metal velocity for trial: 700 °C / 1.6 pcf / with vacuum.

As observed in Figure 116, the metal velocity generally decreased with increasing section thickness. This trend was contrary to, for example, casting trials with the 660 °C pouring temperature, 1.6 pcf foam, cast under gravity conditions. The current velocity trend was attributed to the presence of the vacuum. Due to the enhanced extraction of the pyrolysis products from the casting cavity, the metal flow behavior resembled that of the open-cavity casting processes (such as sand-casting). Therefore, the application of vacuum again caused an appreciable departure from the typical LFC flow behavior.

#### 4.5.5 Casting Condition: 700 °C, 1.3 pcf foam, with vacuum

The combination of the 700 °C pouring temperature, 1.3 pcf foam and applied vacuum, produced castings with an average metal velocity of 3.3 cm/s and a standard deviation of 0.7 cm/s.

The metal velocities in this casting trial ranged between 2.4 – 4.8 cm/s, as observed in Figure 117. In comparison with the previous casting condition where a 1.6 pcf foam was used, a decrease in metal velocity was again observed in this 1.3 pcf foam trial.

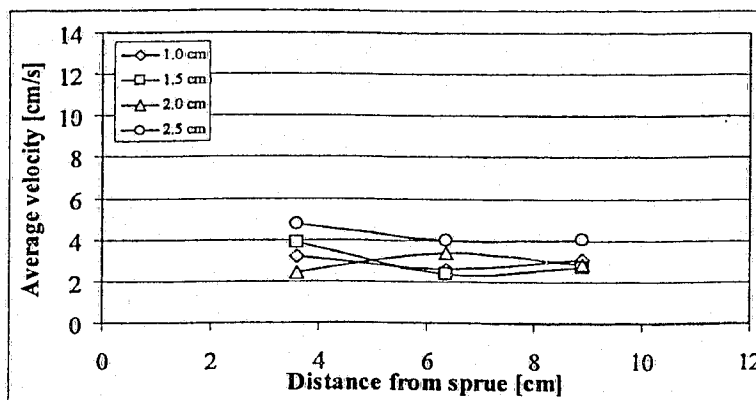


Figure 117: Average metal velocity for trial: 700 °C / 1.3 pcf / with vacuum.

In this casting trial, the metal velocity generally increased with increasing section thickness, which was contrary to the trend observed in the previous casting condition. Since a vacuum was applied in both cases, it was expected that similar trends would develop for the 1.6 pcf and the 1.3 pcf casting trials. However, possibly due to the higher volume fraction of the liquid-EPS products in the current 1.3 pcf foam castings, the metal velocity was affected by additional factors, such as the potential clogging of the ceramic coating's pores. Such an event would result in the accumulation of the liquid-EPS products at the metal-mold interface. Since a thinner horizontal bar would generate less liquid-EPS residue, then higher metal velocities would be expected relative to the thicker horizontal bar.

#### 4.5.6 Casting Condition: 700 °C, 1.6 pcf foam, without vacuum

In this casting trial, the combination of the 700 °C pouring temperature, 1.6 pcf foam and the absence of the vacuum yielded an average metal velocity of 3.3 cm/s with a standard deviation of 0.8 cm/s. In this casting trial, the metal velocity ranged between 2.4 – 5.2 cm/s.

The 1.5 cm and 2.5 cm thick bars showed a tendency for metal velocity oscillations. Comparing the velocity profiles of the similar 660 °C casting trial, Figure 115, to the current velocity results, Figure 118, it seems that the amplitude of metal oscillations decreased with an increase in the pouring temperature. Indeed, the metal velocity standard deviation decreased from 2.1 cm/s to 0.8 cm/s. This supports earlier work,<sup>60</sup> where metal oscillations were also seen to relate to the alloy pouring temperature.

Further, at increased pouring temperatures, a potentially higher volume fraction of gaseous-EPS products evolved in the casting cavity. These gaseous-EPS products are known to be easily removed to the surrounding sand. Therefore, possibly as a result of the lower fraction of the liquid-EPS residue generated during the mold filling of the 1.6 pcf castings, higher metal velocities were observed.

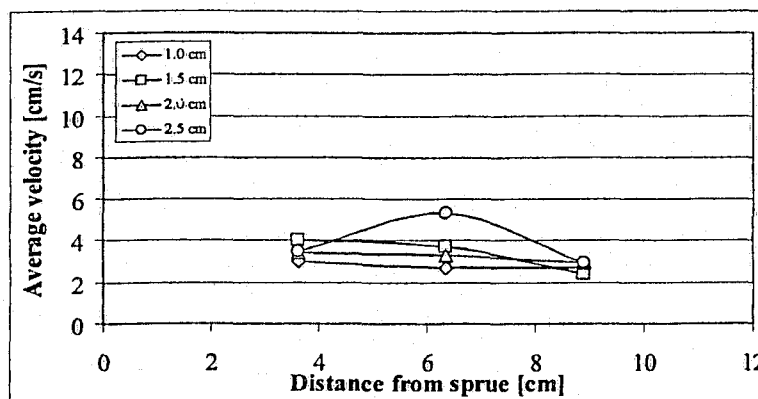


Figure 118: Average metal velocity for trial: 700 °C / 1.6 pcf / without vacuum.

#### 4.5.7 Casting Condition: 700 °C, 1.3 pcf foam, without vacuum

The combination of the 700 °C pouring temperature, 1.3 pcf foam and the absence of vacuum resulted in an average casting metal velocity of 1.5 cm/s with a standard deviation of 0.1 cm/s.

This combination of LFC parameters resulted in the slowest and most uniform metal velocities for all 700 °C pouring temperature casting trials.

Comparing Figure 117 and Figure 119, the effect of vacuum on the metal velocity was again observed. Application of vacuum significantly increased the molten metal velocity.

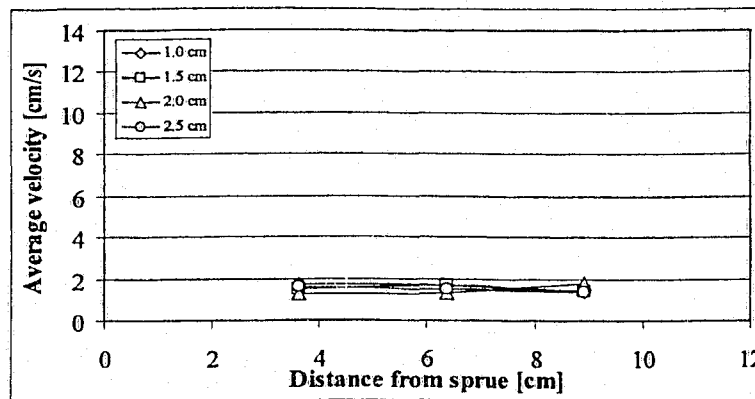


Figure 119: Average metal velocity for trial: 700 °C / 1.3 pcf / without vacuum.

A summary of the average metal velocities and standard deviations for investigated casting trials is presented in Table 11.

Table 11: Metal velocities and the velocity standard deviations for different casting conditions.

660 °C Pouring temperature	Average metal velocity [cm/s]	Metal velocity standard deviation [cm/s]	700 °C pouring temperature	Average metal velocity [cm/s]	Metal velocity standard deviation [cm/s]
1.6 pcf / with vacuum	6.4	2.0	1.6 pcf / with vacuum	6.3	1.4
1.3 pcf / with vacuum	1.6	0.7	1.3 pcf / with vacuum	3.3	0.7
1.6 pcf / without vacuum	2.8	1.1	1.6 pcf / without vacuum	3.3	0.8
1.3 pcf / without vacuum	-	-	1.3 pcf / without vacuum	1.5	0.1

Comparing the respective casting trials, there seems to be a trend of certain casting conditions promoting faster metal velocities. Table 12 ranks the respective casting conditions based on the metal velocities in the horizontal bars.

*Table 12: Ranking of casting conditions based on the average metal velocities.*

<b>660 °C pouring temperature</b>	<b>700 °C Pouring temperature</b>
1.6 pcf foam, with vacuum – FASTEST	1.6 pcf foam, with vacuum – FASTEST
1.6 pcf foam, without vacuum	1.6 pcf foam, without vacuum
1.3 pcf foam, with vacuum	1.3 pcf foam, with vacuum
1.3 pcf foam, without vacuum – SLOWEST	1.3 pcf foam, without vacuum - SLOWEST

#### **4.5.8 Section summary**

The molten metal velocity was seen to oscillate in the longitudinal direction of the flow. This behavior was attributed to the sequential mold filling mechanism of the LFC process.

Metal velocity in the 1.6 pcf foam casting trials was seen to be higher than in the 1.3 pcf foam trials. This behavior was explained by the increased volume fraction of the liquid-EPS products present in the 1.3 pcf foam castings. The liquid-EPS products possibly accumulated at the metal-mold interface causing increased frictional resistance to the metal flow.

Castings produced under vacuum exhibited higher metal velocities than gravity castings. This effect of the vacuum was attributed to the effective extraction of the liquid-EPS products from the casting cavity.

Metal flow in the vacuum castings resembled that of open-cavity mold casting processes. For the vacuum casting trials, the metal velocity decreased with increasing distance from the sprue. However, gravity castings exhibited metal velocity oscillations, indicating that the metal flow was governed by the degradation rates of the solid-EPS foam.

The analysis of the metal velocity variances indicates that the application of vacuum decreased the metal velocity uniformity. This result suggests that the metal flow in the vacuum castings was more random. Also, increasing the pouring temperature seemed to increase the metal velocity and the metal velocity uniformity. This effect was more pronounced in the 1.3 pcf foam castings, where greater volume fractions of the liquid-EPS products were present.

#### 4.6 Local solidification time and the cooling rate

Local Solidification Time (LST) was calculated as the time required for the casting to cool from the non-equilibrium (experimental) liquidus temperature to the non-equilibrium (experimental) solidus temperature. The non-equilibrium solidus temperature was assumed to equal the eutectic reaction temperature. The non-equilibrium temperatures were used for the analysis due to the evident departure from equilibrium solidification conditions.

The Cooling Rate (CR) was determined by calculating the temperature drop from the non-equilibrium liquidus to the non-equilibrium solidus temperatures and dividing this value by the time required for the temperature drop to occur.

The uncertainty associated with the LST and CR measurements did not exceed 1%.

It was found that the local solidification time increased with increasing section thickness. Alternatively, the cooling rate decreased with increasing section thickness. This trend was expected, since a thicker section contained greater mass of the hot alloy, thus remaining hotter for longer periods of time.

In the gravity casting trials, the cooling rate seemed to correlate with the metal flow length. This trend was in agreement with the conventional casting processes, where an increase of the cooling rate promotes faster solid fraction development with attendant increase in the metal viscosity and a decrease in the alloy flow length. Such a behavior, however, was not observed in vacuum castings. As an example, Table 13 presents the cooling rates in the 1.0 cm thick bar at a distance of 2.5 cm from the sprue, for different casting conditions. The cooling rates and corresponding flow lengths indicate, that despite the higher cooling in vacuum trials, the metal flow-lengths exceeded those of the corresponding gravity castings.

*Table 13: Cooling rates and flow lengths in the 1.0 cm thick horizontal bars.*

Condition	660 °C, 1.3 pcf, VAC	660 °C, 1.6 pcf, VAC	660 °C, 1.3 pcf, No-VAC	660 °C, 1.6 pcf, No-VAC	700 °C, 1.6 pcf, VAC	700 °C, 1.3 pcf, VAC	700 °C, 1.6 pcf, No-VAC	700 °C, 1.3 pcf, No-VAC
Cooling Rate (°C / s)	1.38	1.39	0.83	1.25	1.48	1.48	1.4*	1.4*
Flow Length (cm)	4.9	11.7	2.3	8.8	11.9	8.3	10.9	10.3

\* Extrapolated values



Therefore, these results show a relationship with earlier observations (Section 4.2.1) where the application of vacuum was seen to cause molten metal flow beyond the dendrite coherency point. As a result, the concept of dendrite coherency cannot be adopted for vacuum assisted castings.

The results of the thermal analysis are discussed with respect to the two pouring temperatures.

#### ***4.6.1 Pouring temperature: 660 °C***

The LST in the 2.0 cm and 2.5 cm thick bars decreased linearly with increasing distance from the sprue, as seen in Figure 120. The  $R^2$  values for linear trend lines ranged between 0.996 and 0.999.

Examining the LST curves for the 1.0 cm and 1.5 cm thick bars in Figure 120, it was noted that the LST profiles depart from linearity near the sprue. This departure was possibly the result of the proximity effect of the sprue. The locations of the horizontal bars adjacent to the sprue remained hotter for longer periods of time due to the relatively high thermal energy content of the sprue. The proximity effect was more pronounced in the thinner casting sections, where a relatively large thermal gradients between the sprue and the casting section were established.

Upon extending the 1.0 cm bar and 1.5 cm bar LST profiles to the left, i.e., towards the sprue, it seems that the LST trends approach a similar LST value as the 2.0 cm and 2.5 cm thick bars. For the 660 °C pouring temperature trials, this common LST value was between 177 – 208 seconds. This suggests, that the LST of the sprue was within this range. As a result, the maximum time allowed for a complete filling of the casting was less than 210 seconds.

The results of this research repeatedly demonstrated that the flow lengths of the 1.3 pcf castings were less than those of the 1.6 pcf foam castings. Such results were contrary to numerous experimental observations.<sup>51, 52</sup> Explanation of this counter-intuitive metal flow behavior was attempted utilizing the results of the thermal analysis. Table 14 shows the average cooling rates for different casting conditions.

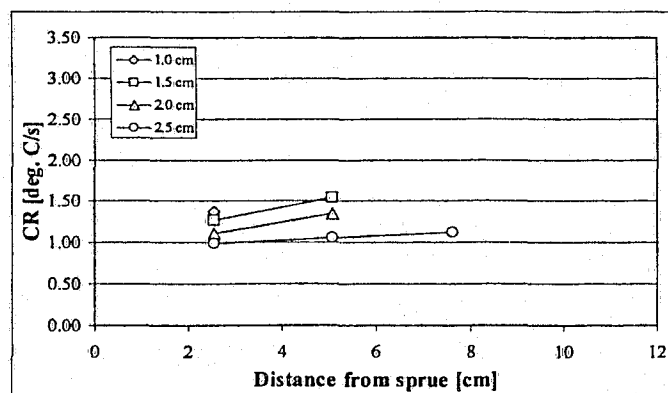
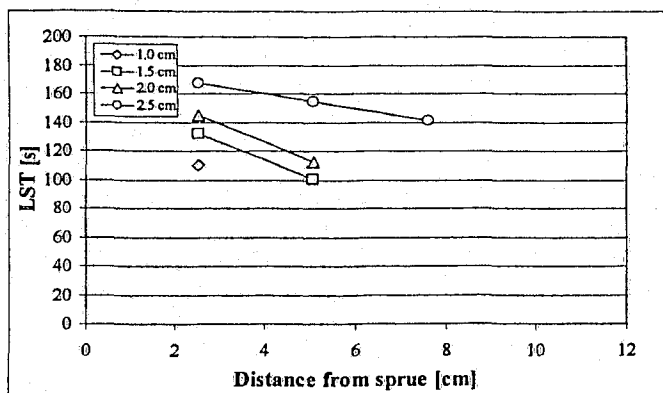
Table 14: Average cooling rates in the horizontal bars for different casting conditions.

Section thickness [cm]	Casting Condition			
	660 °C / 1.3 pcf / VAC	660 °C / 1.6 pcf / VAC	660 °C / 1.3 pcf / No-VAC	660 °C / 1.6 pcf / No-VAC
1.0	1.38	2.13	0.83	1.34
1.5	1.40	1.54	0.95	1.33
2.0	1.23	1.15	0.92	1.09
2.5	1.06	0.98	0.85	0.94

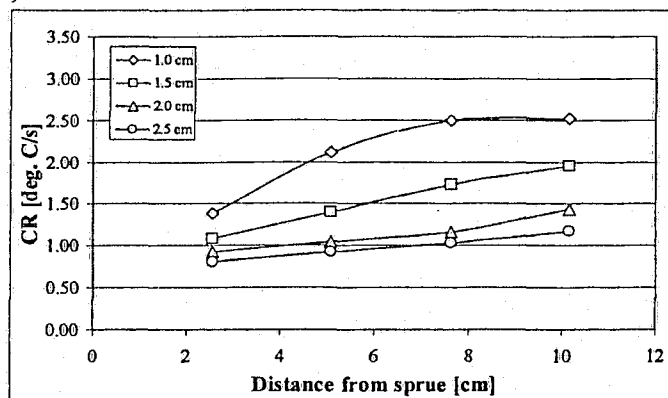
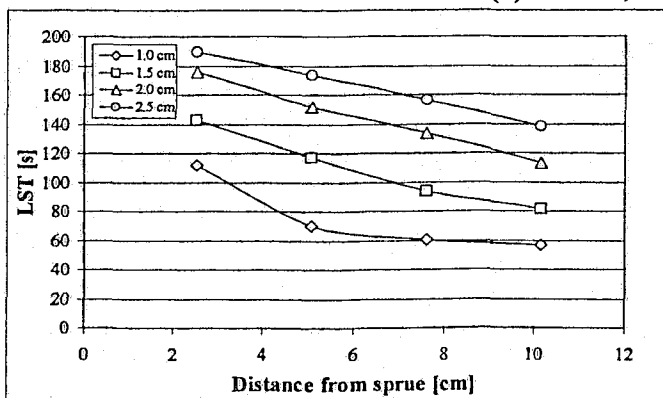
This data shows that, in general, the 1.6 pcf foam castings exhibit higher cooling rates than the 1.3 pcf foam castings. Therefore, as expected, the 1.6 pcf foam indeed extracted more heat energy from the molten metal than the 1.3 pcf foam. This result is fully in agreement with the observations of other researchers,<sup>13,51,52,54</sup> since the depolymerization process of the 1.6 pcf foam requires more energy than the depolymerization of the 1.3 pcf foam.

In spite of the higher cooling rates in the 1.6 pcf castings, however, the metal flow lengths exceeded those of the 1.3 pcf castings. This suggests, that it was not necessarily the exothermic process of solid-EPS foam removal that caused the anomalous metal flow behavior (i.e., metal flow length was not governed by the freezing rate of the alloy). Instead, it was the quantity and the mechanism of the liquid-EPS residue removal from the casting cavity, which seemed to play a fundamental role in controlling the mold filling process.

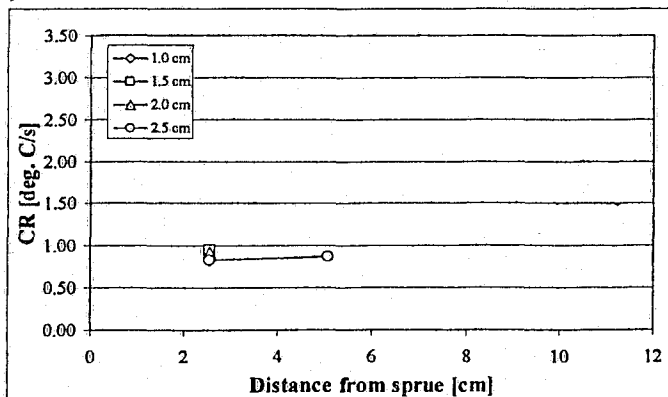
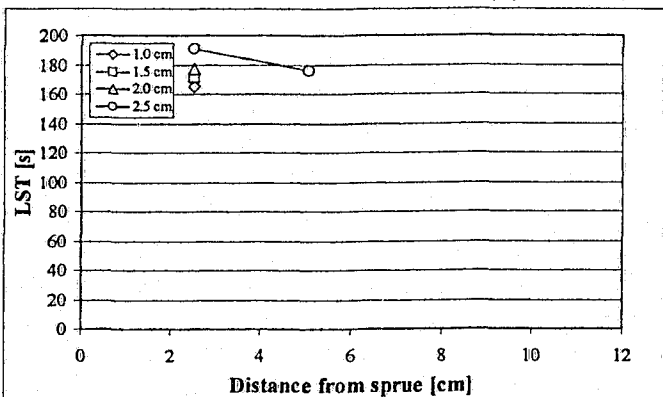
It is evident from Section 4.2, that significant quantities of entrapped liquid-EPS were present in the 1.3 pcf castings (surface and interior). The excessive volume of the liquid-EPS products in the casting cavity was likely the result of the poor bead fusion which caused premature degradation of the solid-EPS pattern ahead of the molten metal front. Consequently, the EPS bead fusion level was identified as a critical foam property that influenced the metal flow length and metal velocity, to a greater extent than the foam density.



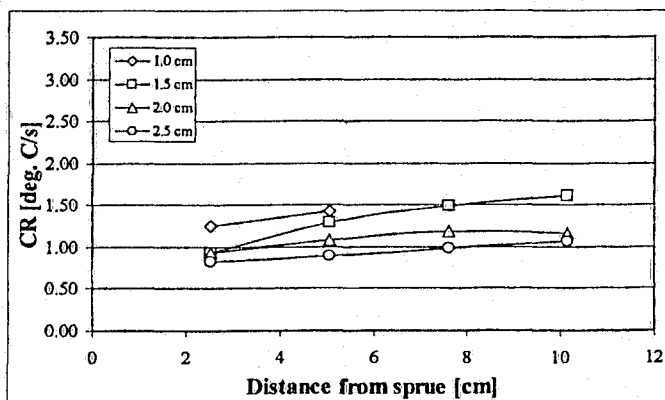
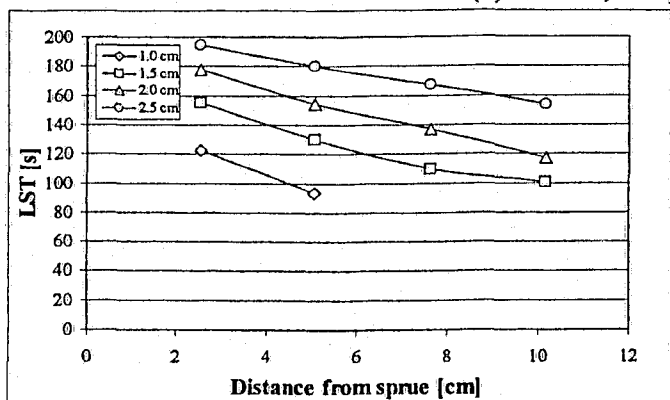
(a) 660 °C, 1.3 pcf, with vacuum



(b) 660 °C, 1.6 pcf, with vacuum



(c) 660 °C, 1.3 pcf, without vacuum



(d) 660 °C, 1.6 pcf, without vacuum

Figure 120: LST and CR results for the 660 °C pouring temperature casting trials.

#### 4.6.2 Pouring temperature: 700 °C

An increase in the pouring temperature from 660 °C to 700 °C resulted in a more pronounced proximity effect of the sprue on the LST profiles of respective horizontal bars. As observed in Figure 120, the sprue proximity effect in the 660 °C pouring temperature castings was evident as far as 5 cm along the bars. For the castings poured at 700 °C, the sprue proximity effect increased as far as 8 cm from the sprue.

Furthermore, it is possible that as a consequence of greater temperature gradients between the sprue and the horizontal bars, directional solidification was established in the 700 °C castings.

As Figure 121 shows, an increase in the pouring temperature did not appreciably affect the LST profiles in respective horizontal bars.

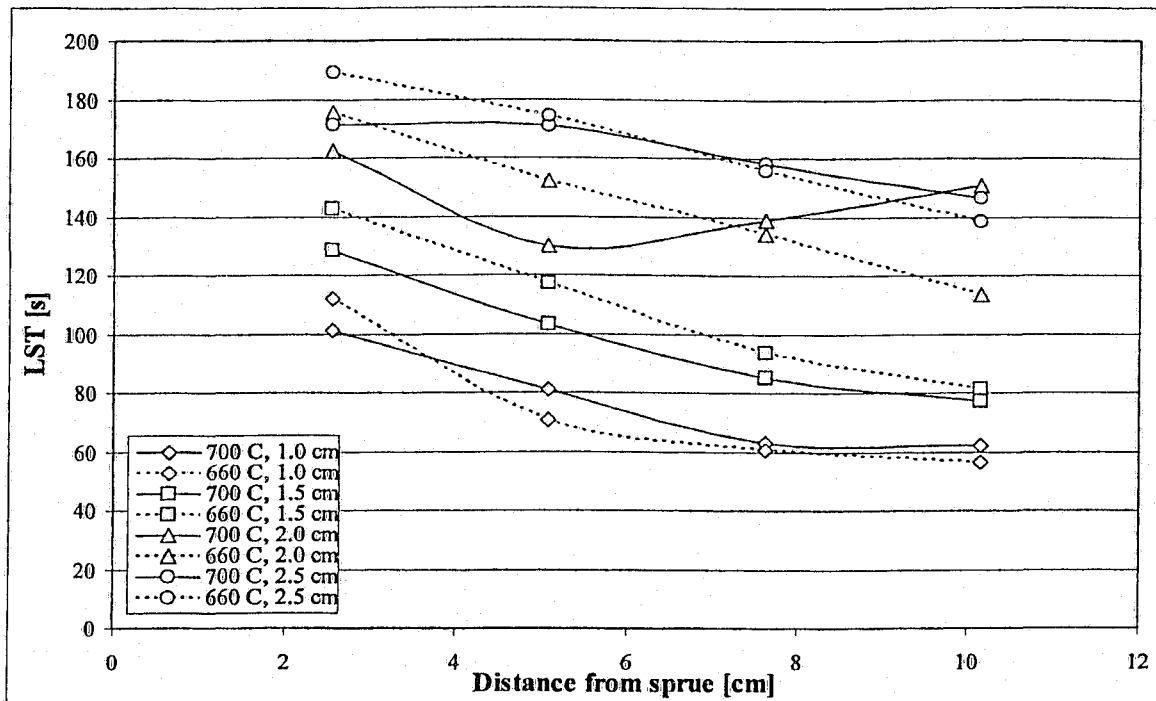


Figure 121: Effect of pouring temperature on the LST of the vacuum cast 1.6 pcf foam castings.

Also, the increase of the pouring temperature did not appreciably change the casting cooling rate, as observed in Figure 122.

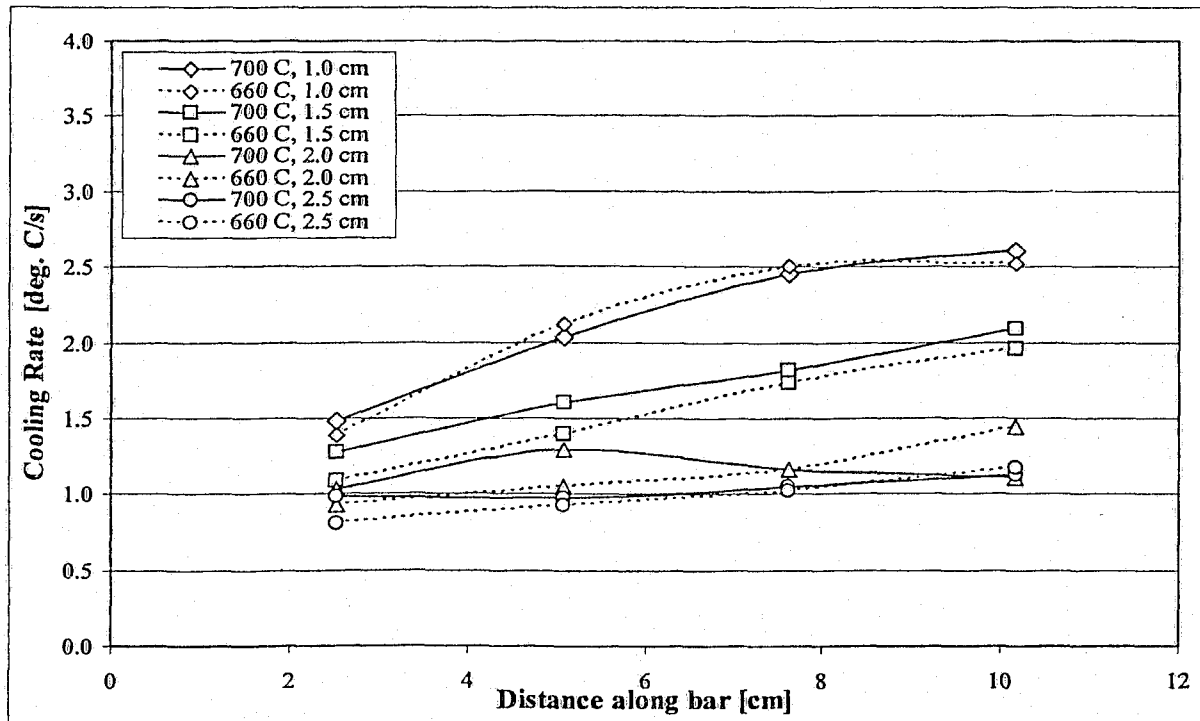


Figure 122: Effect of pouring temperature on the CR of the vacuum cast 1.6 pcf foam castings.

Therefore, it appears that an increase of the melt superheat by 40 °C did not have a significant impact on the cooling rate or the local solidification time of the castings. Validity of this claim would suggest, that the enhancement of the alloy flow lengths as a result of increased pouring temperature was not solely caused by the slower alloy solidification. Instead, the added melt superheat affected the EPS degradation process. In particular, it caused a decrease in the viscosity of the liquid-EPS products, which allowed increased mold filling.

To verify this claim, ANOVA analysis was carried out with the pouring temperature and section thickness as the two factors investigated. The objective was to determine whether or not the section thickness or the alloy pouring temperature had an effect on the casting cooling rate. The results of the analysis are presented in Table 15. The details of the ANOVA analysis are presented in Appendix B.4.

Table 15: Effect of section thickness and pouring temperature on the local solidification time, ANOVA results.

Source of Variation	F-statistic	$P_{\alpha-\max}$ [%]	Hypothesis
Section thickness	67.9	92.50	Reject
Pouring temperature	0.003	50.01	Accept
Interaction	2.7	68.50	Accept

Based on the results of the ANOVA analysis, it can be concluded that the section thickness significantly affected the casting cooling rate, while the pouring temperature did not. Therefore, these conclusions indicate that the volume fraction of the liquid-EPS products in the casting cavity (function of section thickness) was of fundamental importance in affecting the alloy cooling rate and the casting mold filling.

As observed in Figure 123, the effect of vacuum on the cooling rate was noticeable. Casting bars produced under vacuum conditions experienced higher cooling rates. It is of interest to note, that the shape of the cooling rate profiles along the bars were similar for the vacuum and the gravity casting trials.

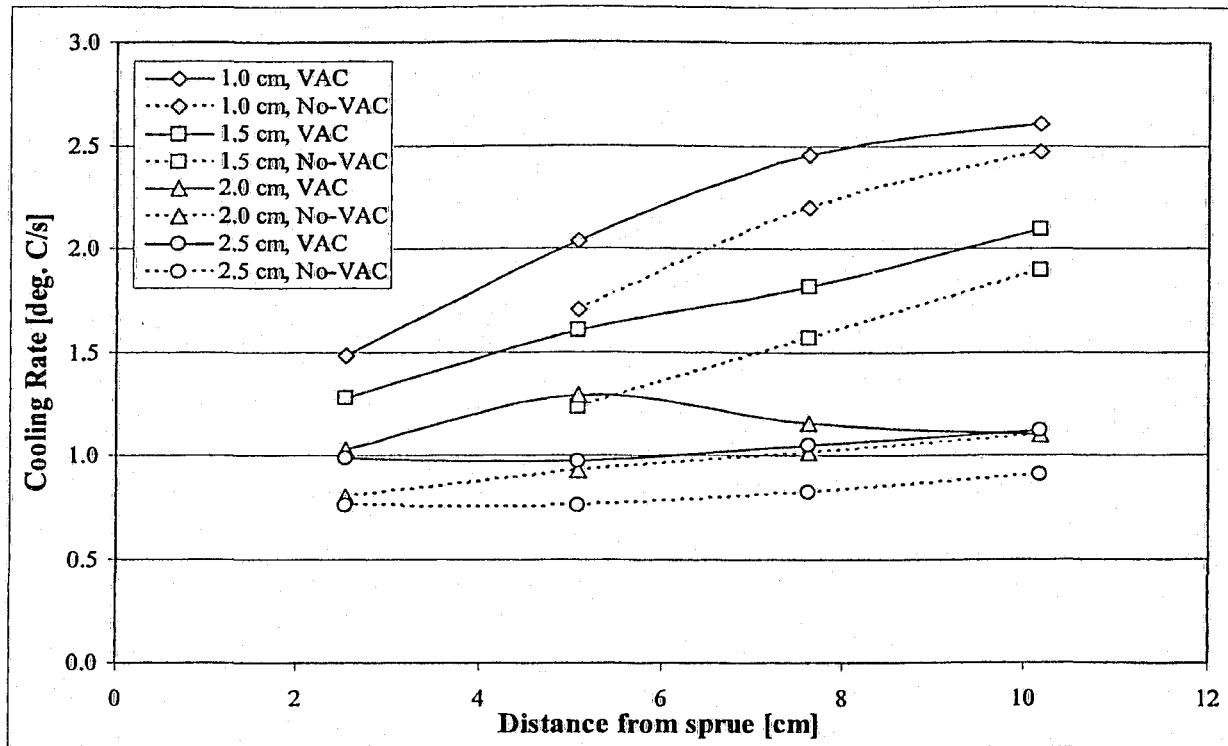


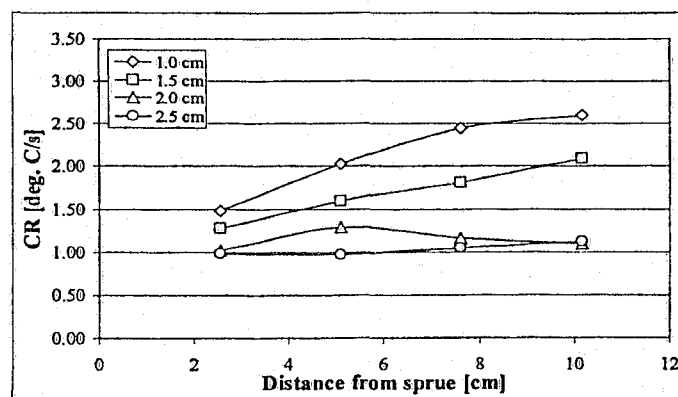
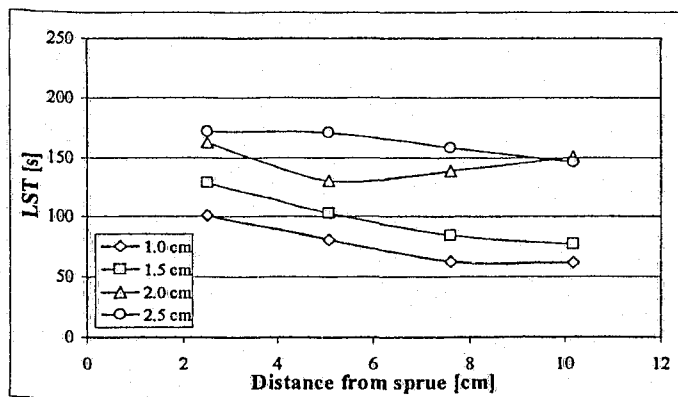
Figure 123: Effect of vacuum on the CR of the 1.6 pcf foam castings poured at 700 °C.

As Table 16 shows, the cooling rate decreased with increasing section thickness. It was noted that the effect of the vacuum on the cooling rate of individual horizontal bars was not consistent. The vacuum increased the cooling rate in the 1.0 cm thick horizontal bar by 1.08%, whereas in the 2.5 cm bar, the vacuum increased the cooling rate by 27.25%. This was possibly due to the increased surface area of the thicker casting section.

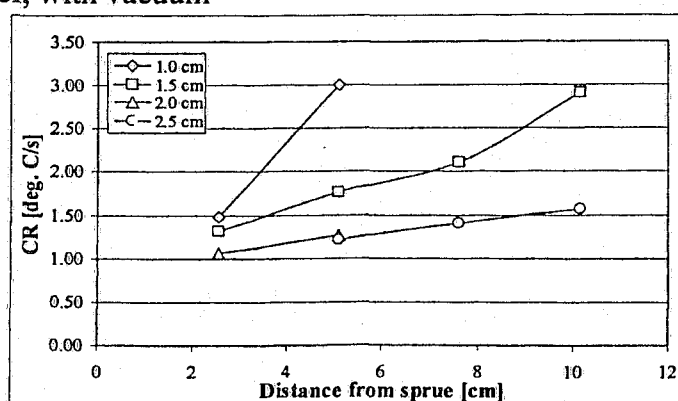
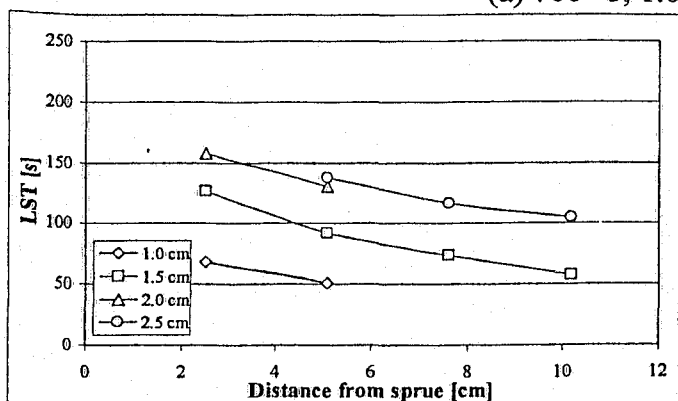
*Table 16: Effect of vacuum on the average cooling rates in the horizontal bars.*

Section Thickness [cm]	Cooling rate [°C /s]		% Difference
	700 °C / 1.6 pcf / VAC	700 °C / 1.6 pcf / No-VAC	
1.0	2.14	2.12	1.1
1.5	1.69	1.56	8.4
2.0	1.14	0.96	19.3
2.5	1.03	0.81	27.3

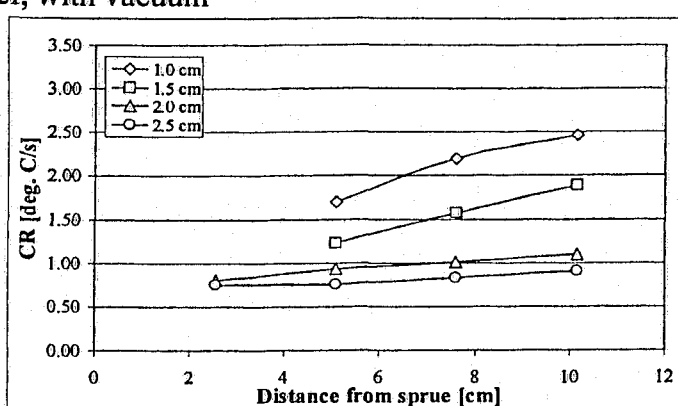
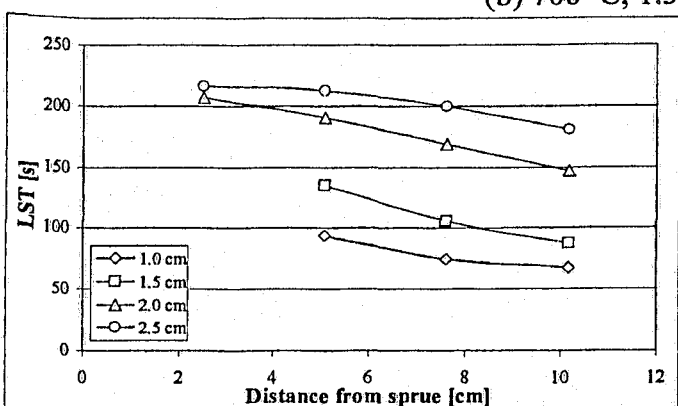
Plots of “LST vs. Distance from sprue” and “CR vs. Distance from sprue” for individual casting conditions are presented in Figure 124.



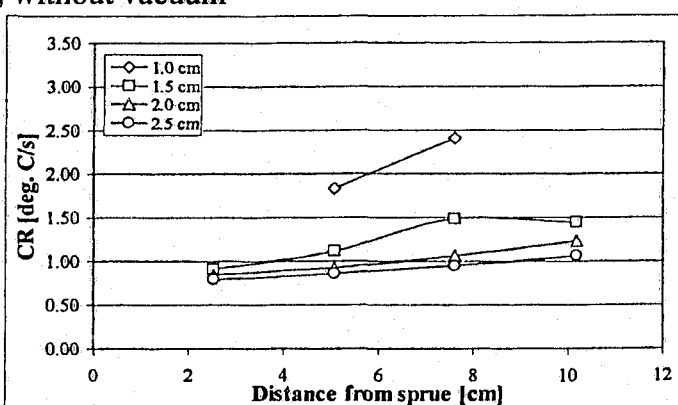
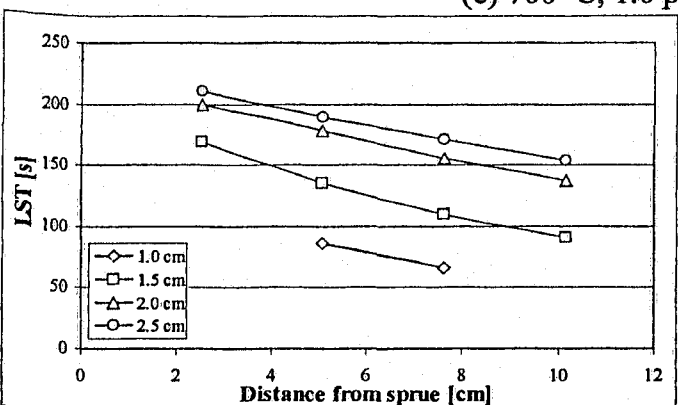
(a) 700 °C, 1.6 pcf, with vacuum



(b) 700 °C, 1.3 pcf, with vacuum



(c) 700 °C, 1.6 pcf, without vacuum



(d) 700 °C, 1.3 pcf, without vacuum

Figure 124: LST and CR plots for the 700 °C pouring temperature casting trials.



#### 4.6.3 Chvorinov's rule

Chvorinov<sup>61</sup> related the casting solidification time to the casting volume to surface area ratio, also known as the casting modulus. Shivkumar<sup>15</sup> reported that the lost foam casting process deviates from Chvorinov's rule for different sand mold materials. However, there is no literature available on the applicability of the Chvorinov's rule to the LFC of magnesium alloys.

Data collected for all casting trials was plotted in Figure 125. This plot suggests that, in general, the value of Chvorinov's constant for LFC of magnesium alloys ( $k$ ) is 324.6 and the value of the exponent ( $n$ ) is 1.4.

Previous research<sup>5</sup> on aluminum alloys cast by the LFC process suggested an exponent value of 2.0. This indicates, that magnesium alloys do not respond to the increased local solidification time (for example via increased section thickness) to the same degree as aluminum alloys. To obtain an equivalent LST with a magnesium alloy, a thicker section would be necessary than in the case of an aluminum alloy casting.

As can be observed from Figure 125, there was a significant scatter in the LST data for individual casting modulus values. This scatter was likely the result of varying pouring temperature, vacuum and different foam types. Chvorinov's plots for individual casting conditions are presented in Figure 126.

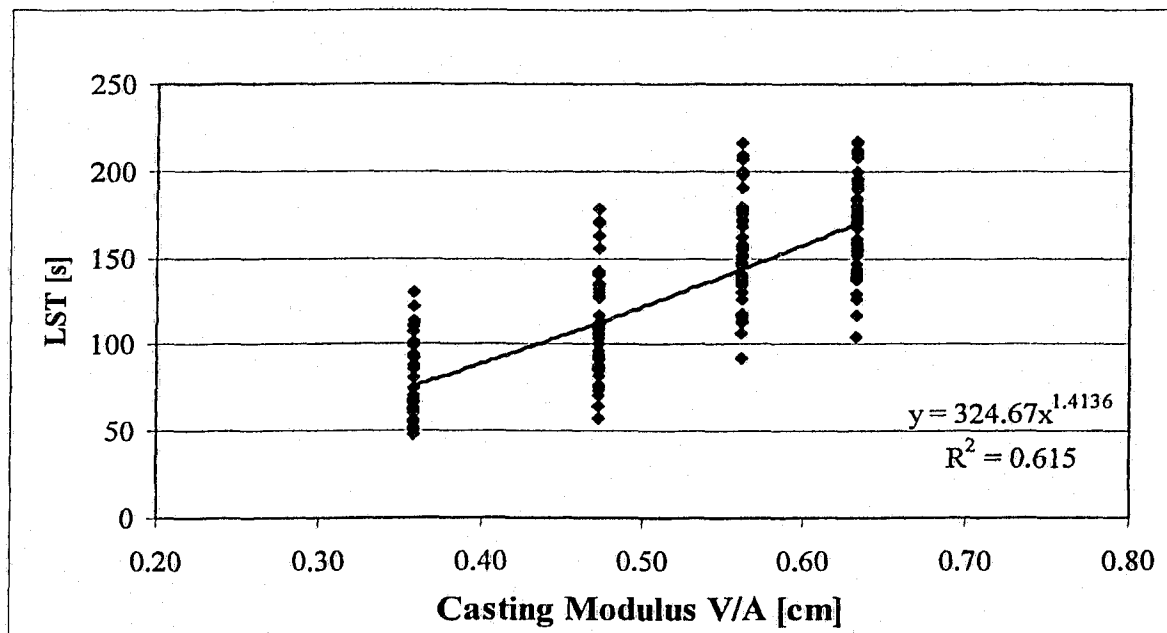
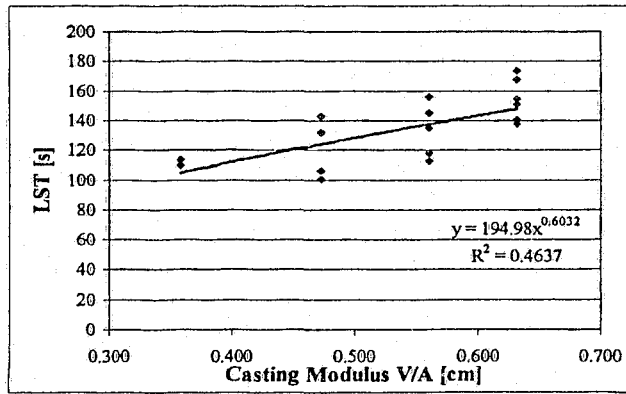
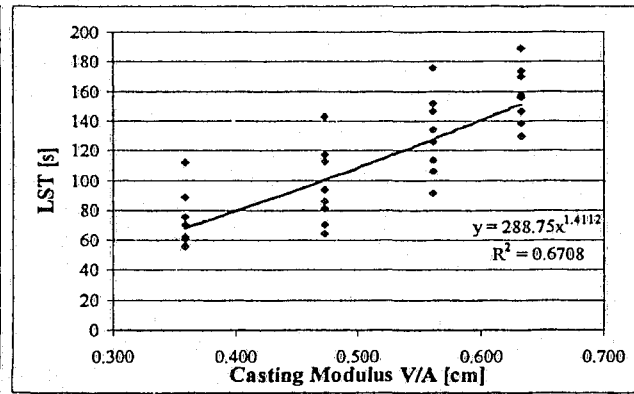


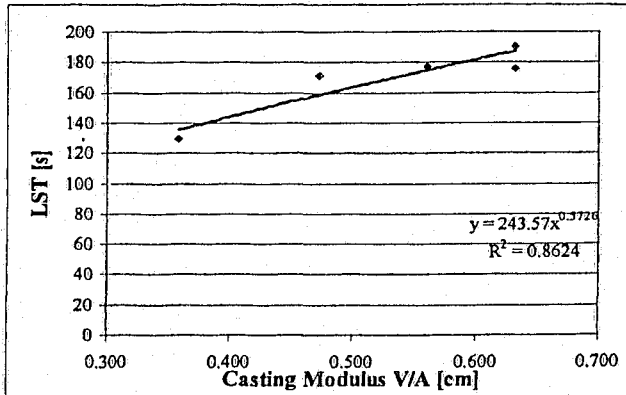
Figure 125: Chvorinov's plot for all casting conditions.



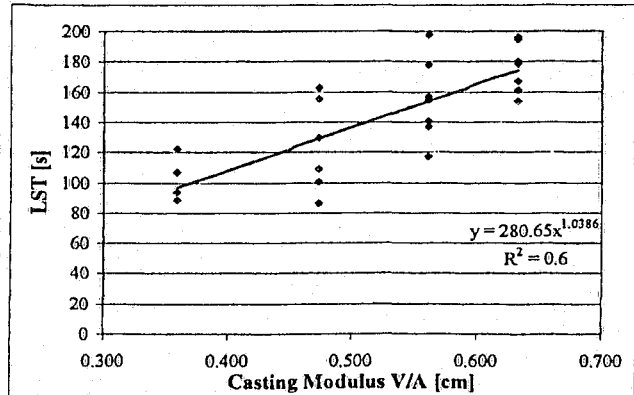
(a) 660 °C, 1.3 pcf, with vacuum



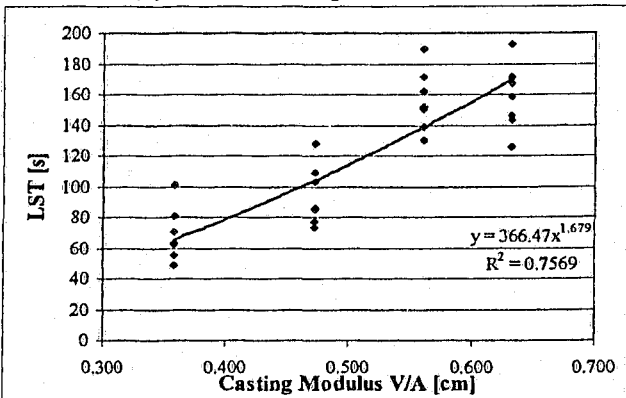
(b) 660 °C, 1.6 pcf, with vacuum



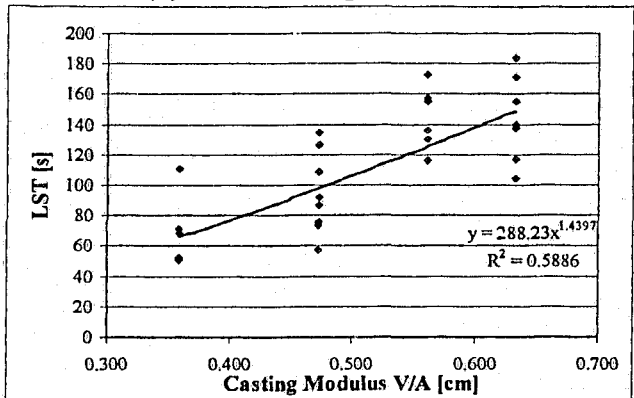
(c) 660 °C, 1.3 pcf, without vacuum



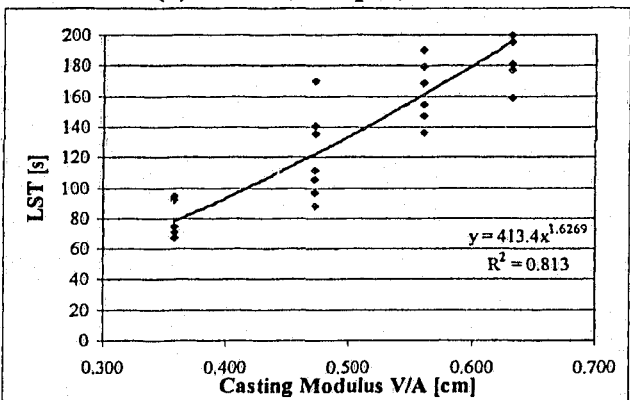
(d) 660 °C, 1.6 pcf, without vacuum



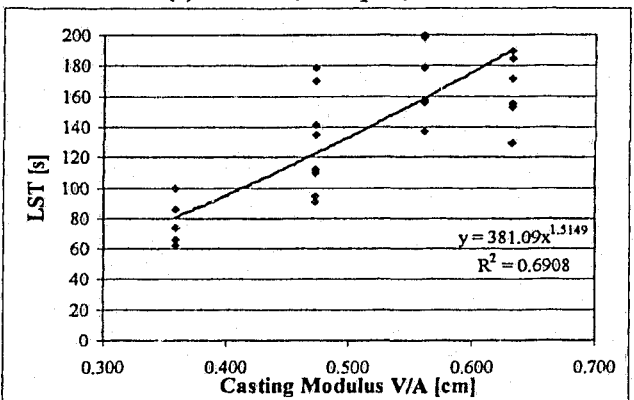
(e) 700 °C, 1.6 pcf, with vacuum



(f) 700 °C, 1.3 pcf, with vacuum



(g) 700 °C, 1.6 pcf, without vacuum



(h) 700 °C, 1.3 pcf, without vacuum

Figure 126: Chvorinov's plots for individual casting conditions.

#### 4.7 Casting temperature distribution

The temperature data collected by the data acquisition system were used to generate temperature distribution plots for the 1.5 cm thick horizontal bars. The temperature distribution profiles were determined for various times after the beginning of solidification (i.e., crossing of the liquidus line).

As Figure 127 shows, castings produced under gravity conditions remained at higher temperatures than vacuum castings, at different stages of solidification. This observation is in agreement with Section 4.6, where higher cooling rates were observed in vacuum castings. Table 17 presents the average temperatures for the 1.5 cm thick horizontal bars for different times after crossing of the liquidus temperature.

*Table 17: Average casting temperatures for different times after beginning of solidification.*

Casting Condition	Time after beginning of solidification [s]			
	15	30	60	120
660 °C / 1.3 pcf / with vacuum	550.4	519.0	472.3	424.3
660 °C / 1.6 pcf / with vacuum	536.9	503.4	454.9	403.2
660 °C / 1.3 pcf / without vacuum	554.9	531.6	496.6	448.1
660 °C / 1.6 pcf / without vacuum	558.4	530.1	480.7	424.3
700 °C / 1.6 pcf / with vacuum	546.0	511.2	461.7	408.2
700 °C / 1.3 pcf / with vacuum	548.3	516.9	469.0	414.1
700 °C / 1.6 pcf / without vacuum	565.4	534.5	485.3	429.7
700 °C / 1.3 pcf / without vacuum	563.3	534.1	486.2	432.0

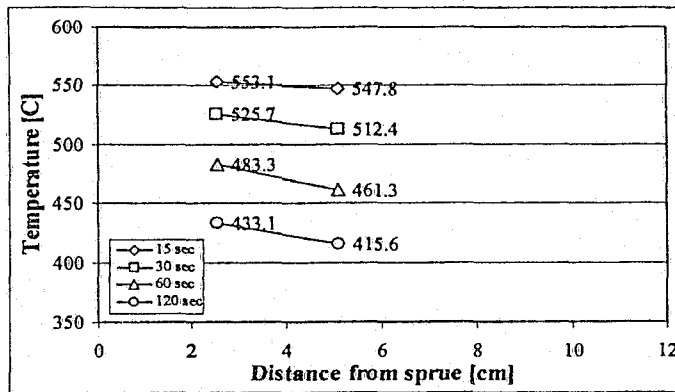
From Table 17 it was determined that the average temperature difference between the vacuum and gravity castings was 16.5 °C for the 1.3 pcf foam trials and 22.9 °C for the 1.6 pcf foam trials.

Inspecting Figure 127, it was further noted that the 40 °C temperature difference in the pouring temperature did not correspond to a 40 °C increase in the casting temperature. In general, the 40 °C increase of superheat caused a 3 – 18 °C increase in the casting temperature.

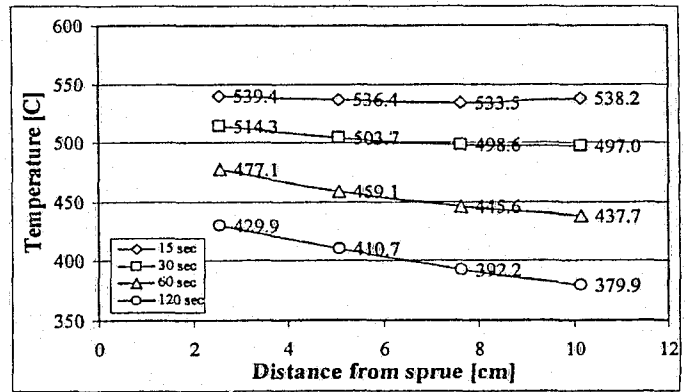
The temperature profiles in Figure 127 correspond with the profiles of the local solidification times (Figure 120 and Figure 124), where the proximity effect of the sprue on the individual casting bars was observed. The temperature profiles in Figure 127 near the sprue also departed from the otherwise linear

monotonic trend. The increase in the casting temperature near the sprue as a result of the sprue proximity effect was typically 5 – 10 °C.

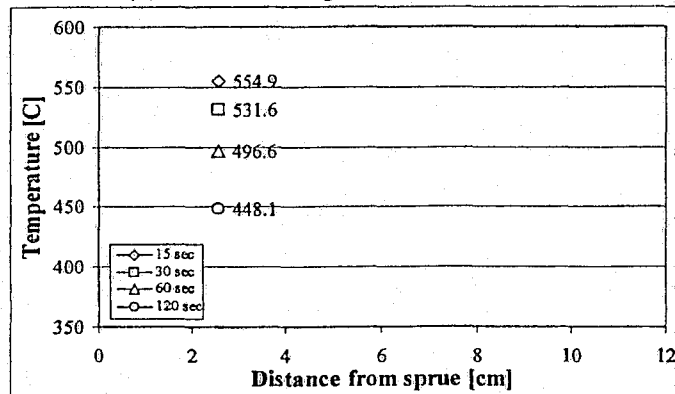
Figure 127 also demonstrates that the casting temperatures in the 1.6 pcf foam castings were, in general, lower than in the case of the 1.3 pcf castings. This observation validates the earlier claim that, during the foam degradation process, the 1.6 pcf foam indeed extracted more thermal energy from the molten metal than the 1.3 pcf foam.



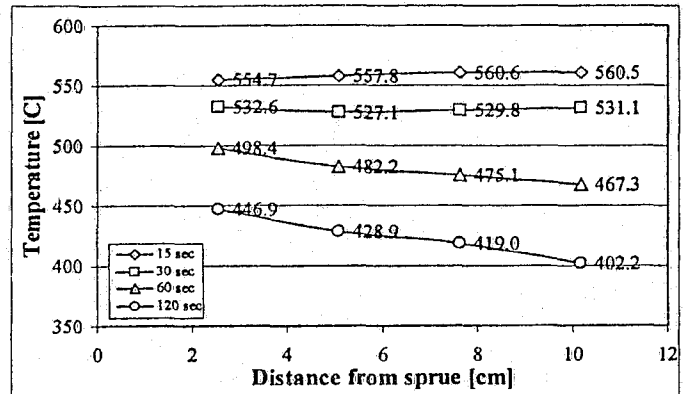
(a) 660 °C, 1.3 pcf, with vacuum



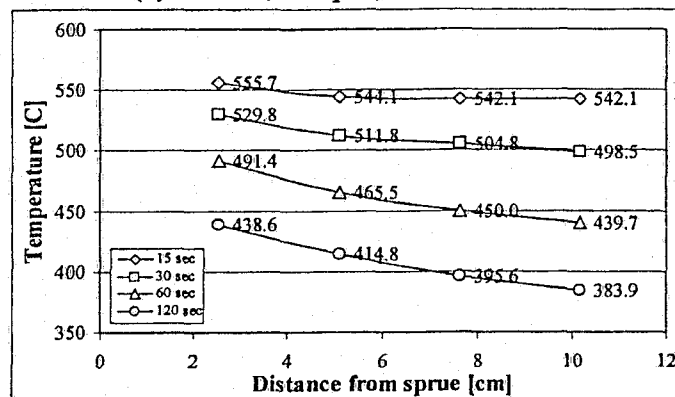
(b) 660 °C, 1.6 pcf, with vacuum



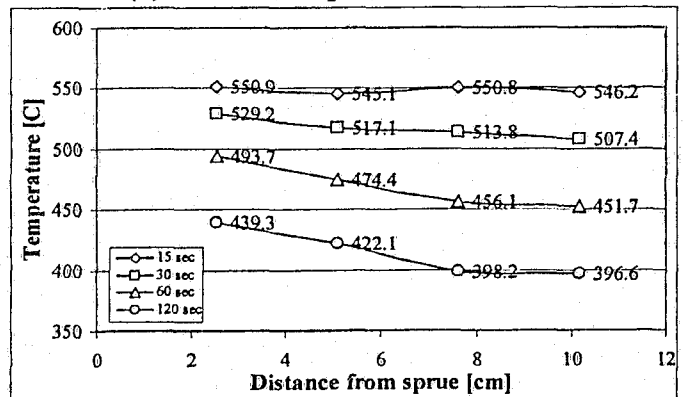
(c) 660 °C, 1.3 pcf, without vacuum



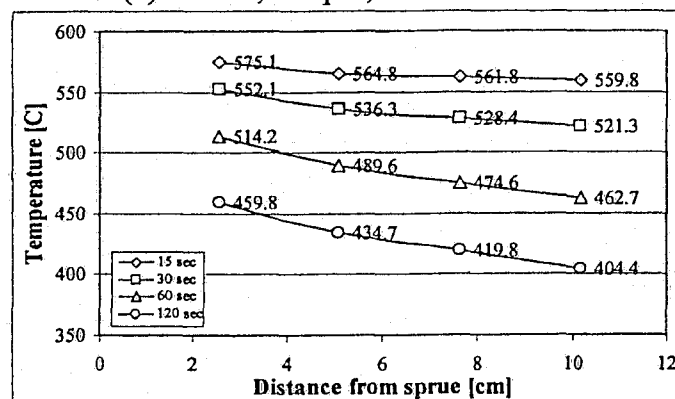
(d) 660 °C, 1.6 pcf, without vacuum



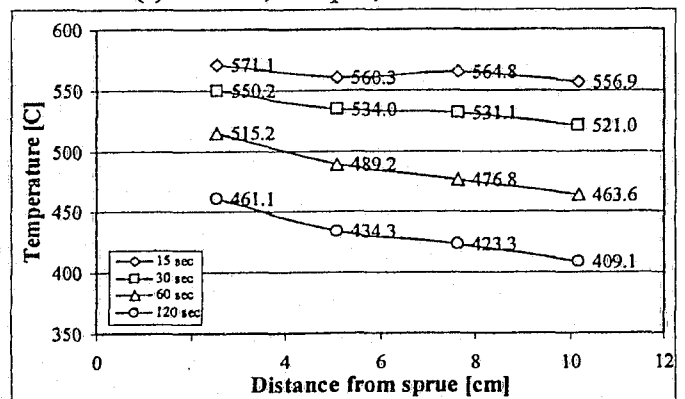
(e) 700 °C, 1.6 pcf, with vacuum



(f) 700 °C, 1.3 pcf, with vacuum



(g) 700 °C, 1.6 pcf, without vacuum



(h) 700 °C, 1.3 pcf, without vacuum

Figure 127: Temperature profiles in the 1.5 cm thick bar after 15, 30, 60 and 120 seconds.

#### 4.8 Casting temperature gradient

The temperature gradient at the 5 cm distance from the sprue was calculated when the temperature at the horizontal bar mid-section reached the non-equilibrium solidus temperature. This allowed the assessment of the presence of directional solidification prior to the completion of casting solidification. A positive temperature gradient suggested that the metal down the stream (i.e., near the frozen metal front) was at a lower temperature than the metal near the sprue. Similarly, a negative temperature gradient would indicate a heat-wave passing through the horizontal bar from the sprue towards the metal front, potentially re-melting the casting.

As observed in Figure 128, the temperature gradients decreased with increasing section thickness. This suggests that the thicker horizontal bars had a more uniform temperature distribution along the length of the bar, relative to the thinner casting sections. In addition, this trend corresponded with the higher cooling rates observed in the thinner casting sections. Thus, the temperature gradient calculations support Adam's Riser Equation predictions.

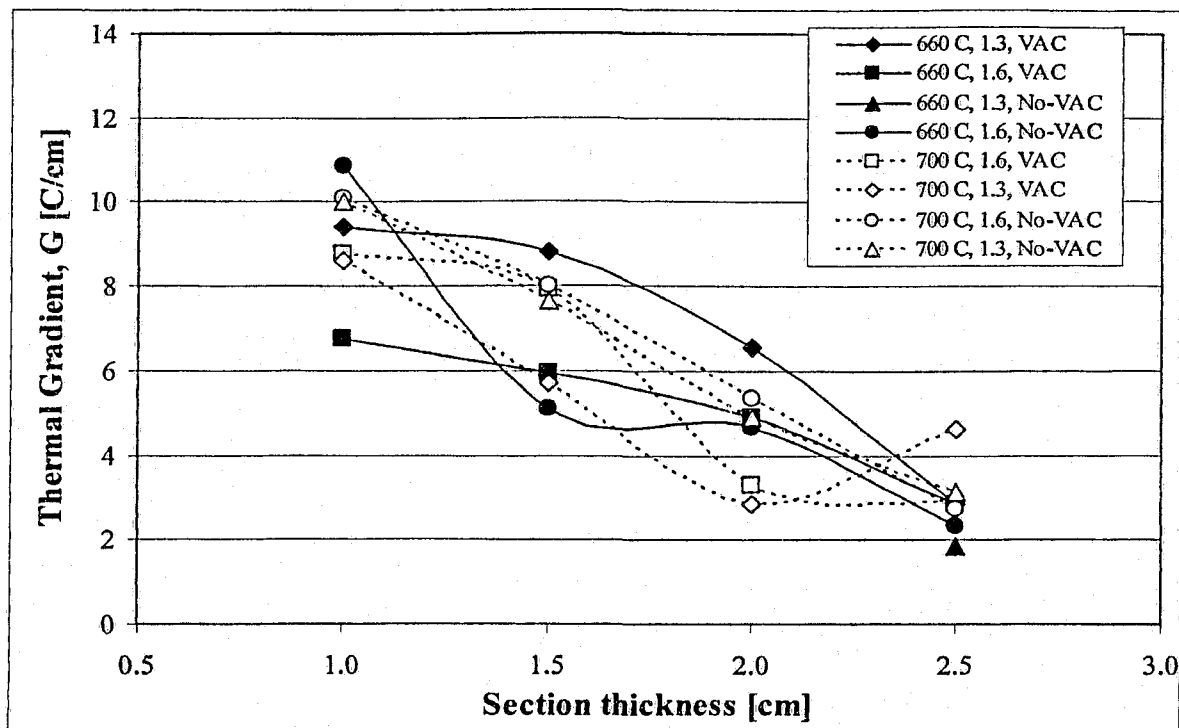


Figure 128: Thermal gradients in the 1.5 cm thick bars at 5 cm distance from the sprue.

There seems to be a general trend of smaller temperature gradients in the vacuum trials, as compared to the gravity casting trials. This suggests the possibility that during the vacuum mold filling process, the molten metal was quickly drawn into the horizontal bar by the vacuum. As a result, the temperature gradients along the horizontal bars decreased and the casting solidified with a more uniform temperature distribution.

The temperature gradients established in the 1.0 cm thick sections were nearly double those in the 2.5 cm thick sections. In general, it appears that there was a monotonic trend of decreasing temperature gradient with increasing section thickness. However, some casting trails exhibited fluctuations in the gradient profile for different section thicknesses.

Further, as observed in Figure 128, it seems that an increase in pouring temperature did not appreciably affect the temperature gradients in the individual horizontal bars. This claim was verified with the ANOVA analysis carried out for the pouring temperature and the section thickness as the two factors studied. The results of the ANOVA analysis are presented in Table 18. Detailed results of the ANOVA analysis are presented in Appendix B.5.

*Table 18: Effect of pouring temperature and section thickness on the thermal gradient, ANOVA analysis.*

Source of Variation	F-statistic	$P_{\alpha-\max}$ [%]	Hypothesis
Pouring temperature	0.461	53.10	Accept
Section thickness	7.207	93.50	Reject

Therefore, the ANOVA results suggest that the pouring temperature did not affect the thermal gradients established in the different casting bars. The casting section thickness indeed affected the thermal gradients in the horizontal bars. These conclusions correlate well with the negligible effect of the melt superheat on the LST and CR values, as discussed in preceding sections.

The temperature gradients seemed to affect the degree of thermal undercooling present in the castings. As Figure 129 illustrates, the thermal undercooling changed along the distance of the 1.5 cm thick horizontal bar. Locations near the sprue (2.5 cm) did not experience any undercooling, while locations near the frozen metal front (10 cm) show undercooling near the non-equilibrium eutectic temperature of 425 °C. These trends would in turn affect the formation of dendrites and consequent solute segregation in along the length of the bar (see Section 4.10).

Since the size of the solute-rich region ahead of the solid-liquid interface is affected by the thermal gradient, then the primary and secondary dendrite arm growth would be likely affected by the thermal gradient as well. Consequently, the as-cast microstructure of the horizontal bars was affected by the temperature gradients. This phenomenon is discussed later in Section 4.10.

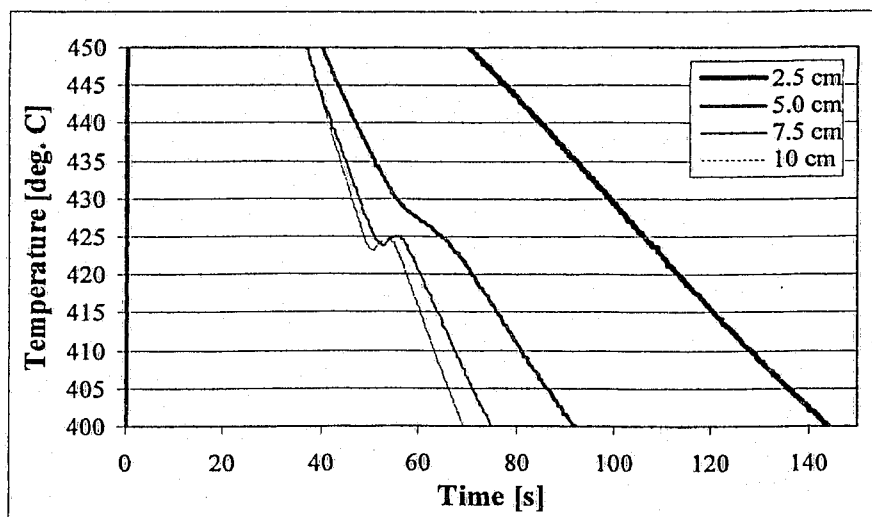


Figure 129: Cooling curves for trial: 660 °C / 1.6 pcf / with vacuum.



## 4.9 Casting porosity and the criterion functions

Microscopic analysis of the metallographic specimens revealed only rare formation of gas porosity. Therefore, it is likely that due to the effective use of the  $\text{CO}_2 + \text{SF}_6$  protective atmosphere, Hydrogen and other gases were not absorbed by the molten metal. As a result, the majority of the observed casting porosity was the result of solidification shrinkage and entrapment of the EPS pyrolysis products.

Formation of solidification shrinkage occurred preferentially in the inter-dendritic regions of the microstructure. These regions were prone to form shrinkage cavities possibly due to the inadequate feeding of liquid metal during the last stages of solidification (as a result of dendrite arm interlocking).

Solidification shrinkage pores often spanned several dendrites, thus forming interdendritic networks. In particular, regions near the mold walls contained extensive networks originating in the casting interior and extending to the casting surface. Due to the increased nucleation rate of the primary Mg dendrites in these locations, the possibility of dendrite arm interlocking increased. In addition, it is likely that the rapid cooling near the mold walls prevented interdendritic eutectic flow, which further accentuated the interdendritic porosity.

The effect of foam density on the casting porosity was readily observed. As suggested earlier in Sections 4.2 and 4.5, the 1.3 pcf foam possibly generated higher volume fractions of the liquid-EPS products than the 1.6 pcf foam. As a result, the probability of entrapping the liquid-EPS residue in the casting increased for the 1.3 pcf foam castings. The measured porosity levels in the 1.3 pcf castings confirmed this prediction.

On the macroscopic level, entrapped liquid-EPS formed voids of several millimeters in width (Figure 93). Unfortunately, inspection of the micrographs did not reveal a characteristic microcavity (porosity) which could be solely attributed to the presence of the liquid-EPS residue.

The casting porosity was seen to be influenced by the pouring temperature. This was attributed to the effect of the metal temperature on the physical properties of the liquid-EPS products.

#### 4.9.1 Pouring temperature: 660 °C

The measured porosity values for the 660 °C pouring temperature castings suggest two distinct trends with respect to the casting section thickness. As Figure 130 indicates, in vacuum castings, the porosity decreased with increasing section thickness. In gravity castings, the porosity increased with increasing section thickness.

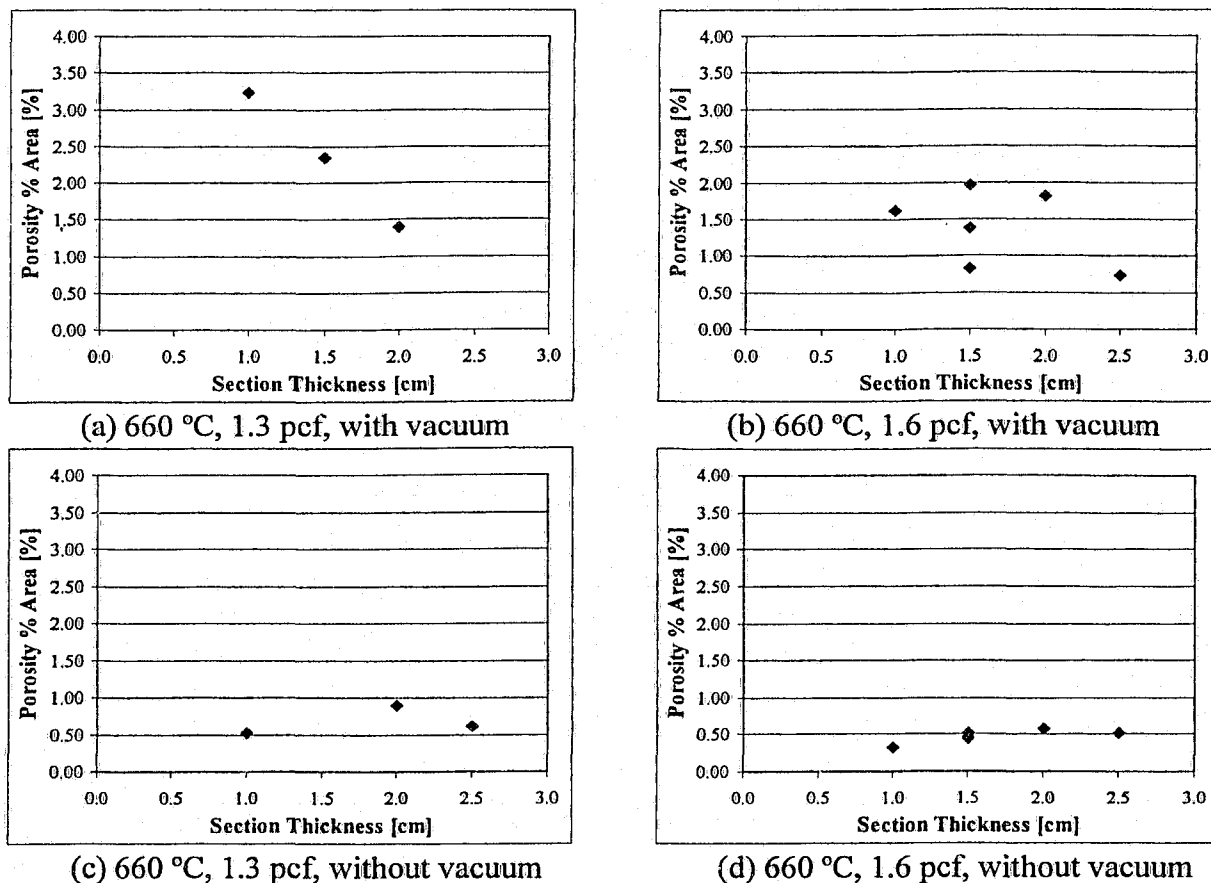


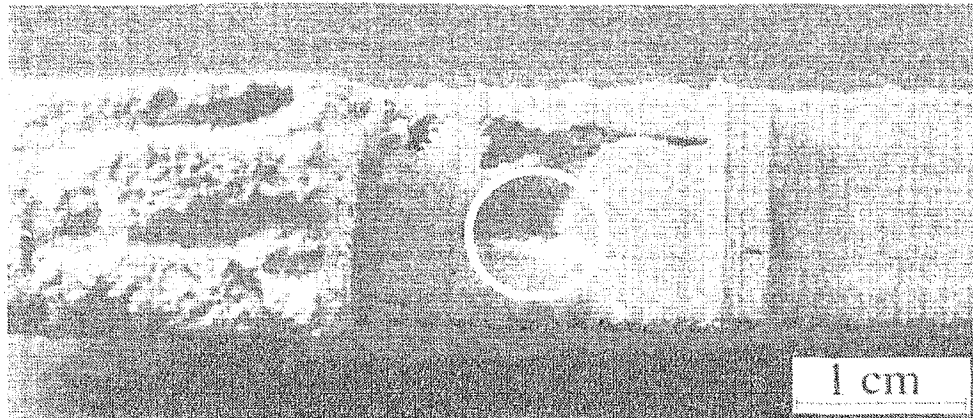
Figure 130: Optical porosity results for the 660 °C pouring temperature trials.

In vacuum casting trials, the relationship between the casting porosity and the section thickness was seen to associate with the relative ease of the liquid-EPS products removal from the casting cavity. The surface area of the 2.5 cm thick horizontal bar was 40% greater than that of the 1.0 cm thick bar. Due to the greater surface area of the 2.5 cm thick bar, lower mass fraction of the EPS pyrolysis products passed through a unit area of the ceramic coating. As a result, the possibility of ceramic coating clogging was reduced in the thicker horizontal bars. To this end, the application of vacuum was beneficial. However, the effect of vacuum on the overall casting porosity was detrimental. As observed in Table 19, the average casting porosity increased in vacuum castings, relative to the gravity castings.

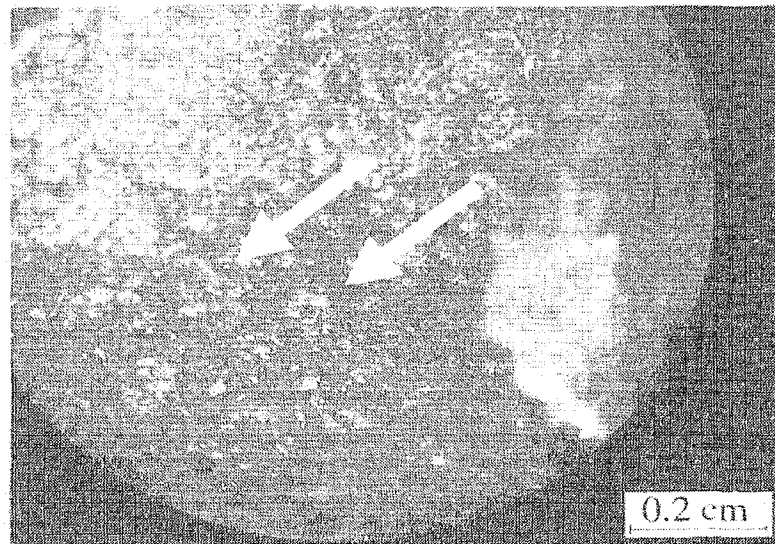
*Table 19: Average casting porosity for the 660 °C pouring temperature casting trials.*

Casting Condition	Average Casting Porosity [% Area]	Porosity Variance [% Area]
1.3 pcf. with vacuum	2.33	0.84
1.6 pcf. with vacuum	1.51	0.47
1.3 pcf. without vacuum	0.67	0.04
1.6 pcf. without vacuum	0.48	0.01

This trend was possibly the result of the partially solidified metal chunks hindering the removal of the liquid-EPS residue from the casting cavity. Figure 131 shows the 1.5 cm thick bar from the 660 °C / 1.6 pcf / with vacuum casting trial. The region of the internal cavity near the solidified metal chunk, enlarged in Figure 132, contained traces of the EPS residue. It is possible, that during the mold filling process, additional residue remained within the horizontal bar interior, thus increasing the casting porosity.



*Figure 131: Entrapped liquid-EPS residue near partially solidified chunks in the casting bar.*



*Figure 132: Traces of liquid-EPS residue near a metal chunk.*

In addition, the concave metal front profile associated with the application of vacuum possibly further contributed to the entrapment of the liquid-EPS products. Since the metal front advanced preferentially along the mold walls, the liquid-EPS products were possibly unable to escape to the upper and lower surfaces of the horizontal bars. As a result, the liquid-EPS products agglomerated in the center regions of the flow channel (viz., Figure 131). As the mold filling process continued, some of the liquid-EPS products were discharged to the sides of the horizontal bar and saturated the ceramic coating pores. Consequently, additional transport of the liquid-EPS or any gaseous-EPS products was impaired, thus increasing casting porosity. In the case of gravity castings, the porosity levels increased with the increasing section thickness. This trend was correlated with the increased volume fraction of the liquid-EPS residue generated in the thicker horizontal bars.

Table 19 also indicates that the foam characteristics affected the casting porosity. Typically, the porosity levels are expected to increase with increasing foam density, due to the increased mass of EPS present in the casting. However, the results of this research suggest that the average casting porosity was higher in the 1.3 pcf foam castings, when compared to the 1.6 pcf foam castings. This observation again supports the suggestion that due to the poor bead fusion, the 1.3 pcf foam generated large quantities of the liquid-EPS products (due to the premature collapse of the solid-EPS foam ahead of the molten metal front), which increased the casting porosity.

Locations near the metal-mold interface often exhibited interdendritic shrinkage porosity networks, as shown in Figure 133 and Figure 134. These porosity networks often extended towards the surface of the casting.

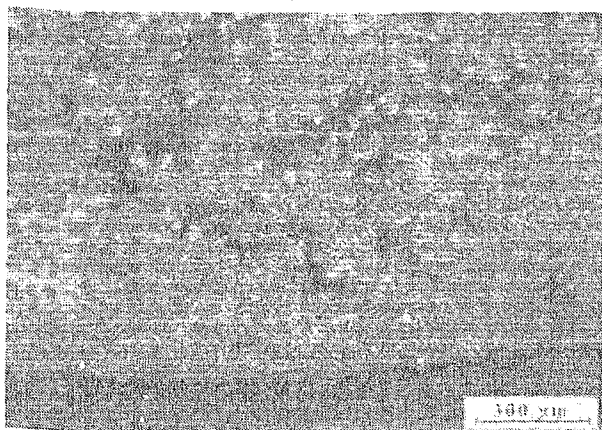


Figure 133: Shrinkage network in the 2.0 cm thick bar at 5 cm distance from the sprue, 660 °C / 1.3 pcf / with vacuum trial.

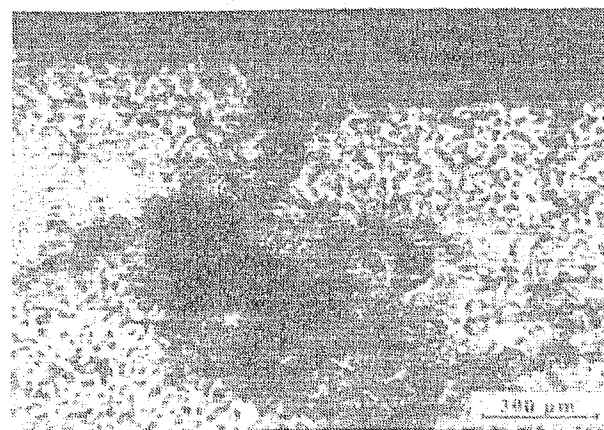
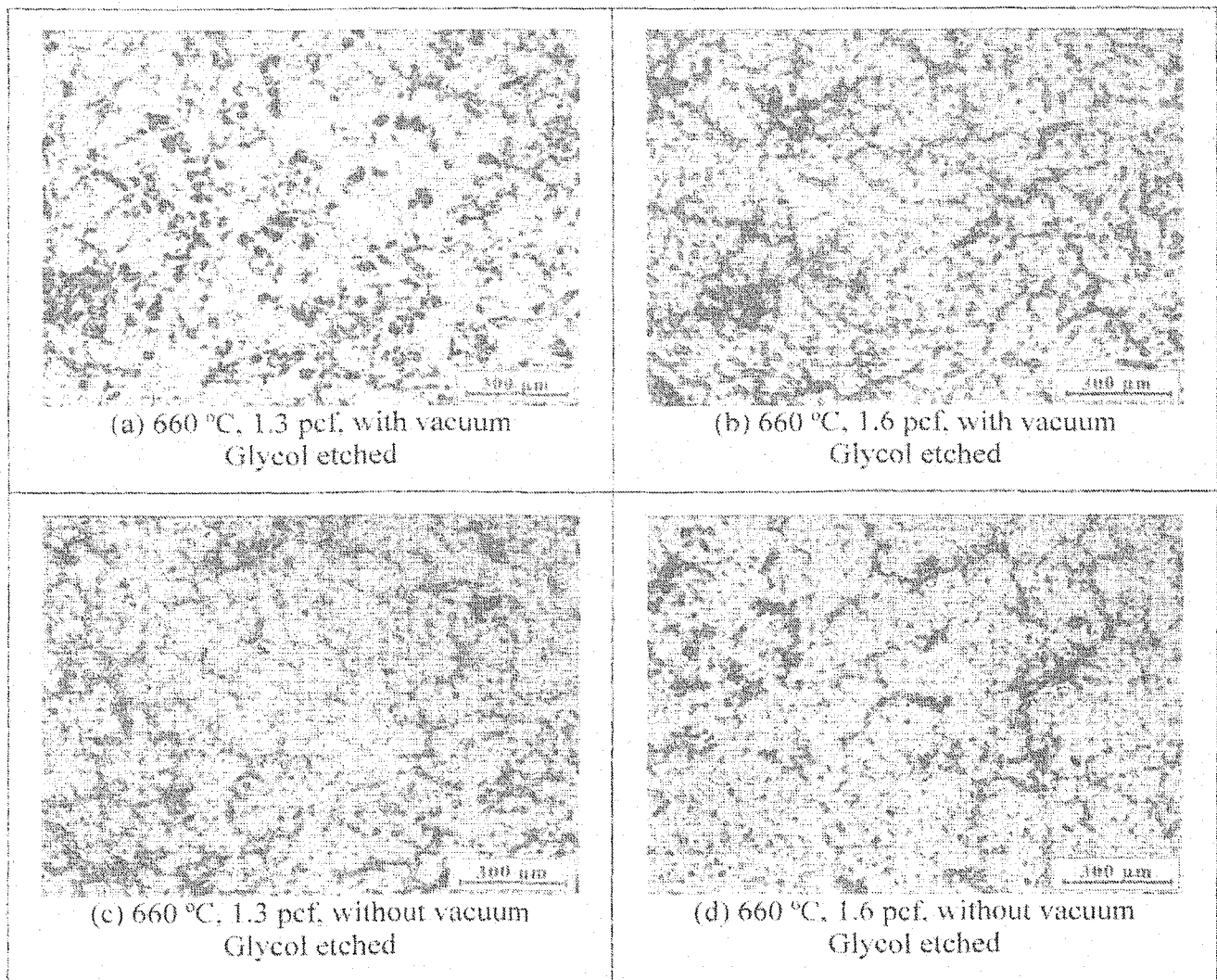


Figure 134: Surface extensions of shrinkage pores in the 660 °C / 1.6 pcf / with vacuum trial.

The casting locations near the horizontal bar center rarely exhibited shrinkage porosity networks. Instead, only distinct pockets with shrinkage pores formed, as observed in Figure 135.



*Figure 135: Microstructure of the 2.5 cm thick bar center location at 5 cm distance from the sprue.*

#### 4.9.2 Pouring temperature: 700 °C

Casting trials with the 700 °C pouring temperature exhibited similar trends of porosity development (as the 660 °C pouring temperature trials) with respect to the increasing section thickness. As Figure 136 suggests, for vacuum castings, the porosity decreased with the increasing section thickness, while for gravity castings, the porosity increased with increasing section thickness. Explanation of these trends was presented in Section 4.9.1.

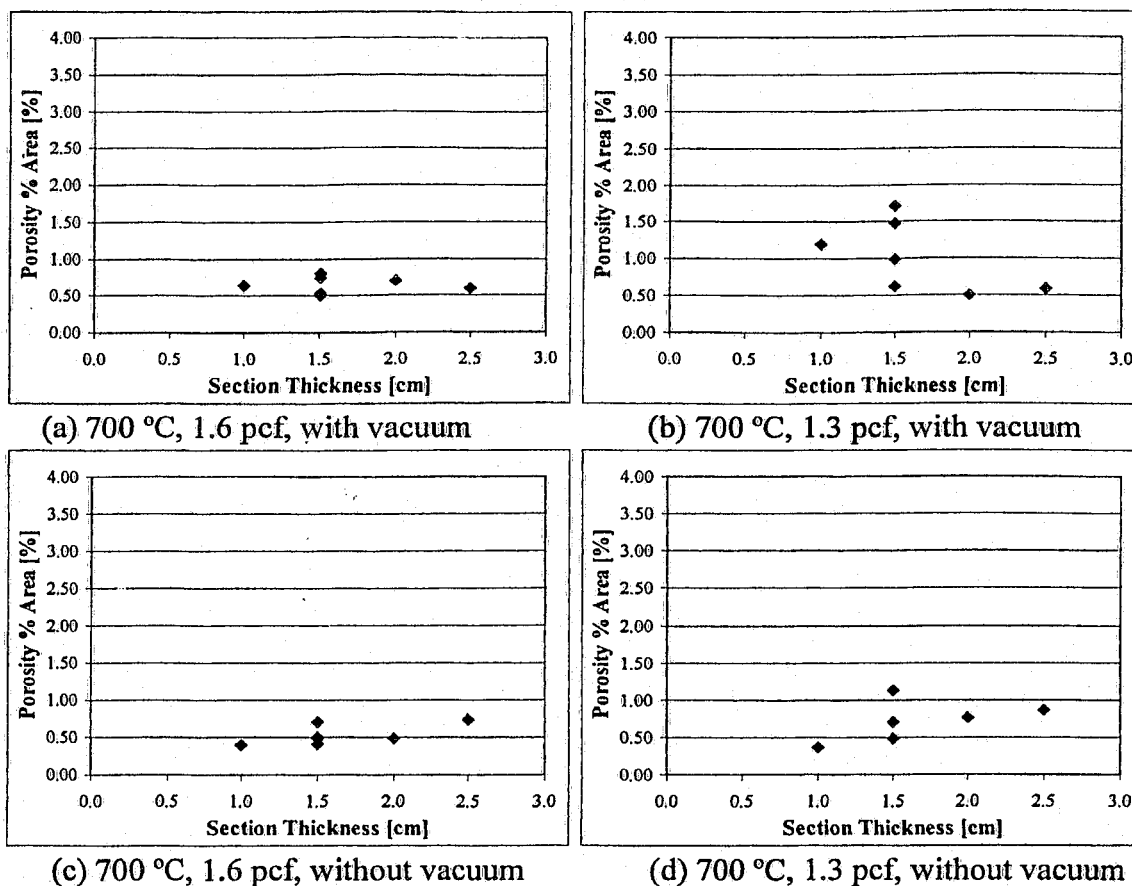


Figure 136: Optical porosity results for the 700 °C pouring temperature trials.

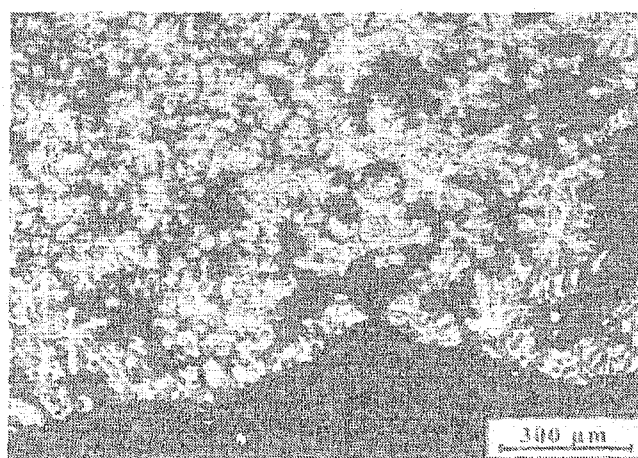
Comparison of entries of Table 19 and Table 20 suggests that in the case of the vacuum casting trials, the increased pouring temperature caused a decrease in the casting porosity. This effect was again correlated with the extraction of the liquid-EPS residue from the casting cavity. At higher pouring temperatures and with application of vacuum, the wetting, wicking and transport of the liquid-EPS residue through the ceramic coating into the surrounding sand was accelerated, with attendant decrease of casting porosity.

Data in Table 19 and Table 20 further indicate similar trends (as in the case of 660 °C pouring temperature) with respect to the effect of vacuum and the foam density on the casting porosity. The 1.3 pcf foam castings exhibited higher porosity levels than the 1.6 pcf castings due to the possible entrapment of the generated pyrolysis products.

*Table 20: Average casting porosity for the 700 °C pouring temperature casting trials.*

Casting Condition	Average Casting Porosity [% Area]	Porosity Variance [% Area]
1.3 pcf, with vacuum	1.01	0.22
1.6 pcf, with vacuum	0.64	0.01
1.3 pcf, without vacuum	0.69	0.07
1.6 pcf, without vacuum	0.53	0.02

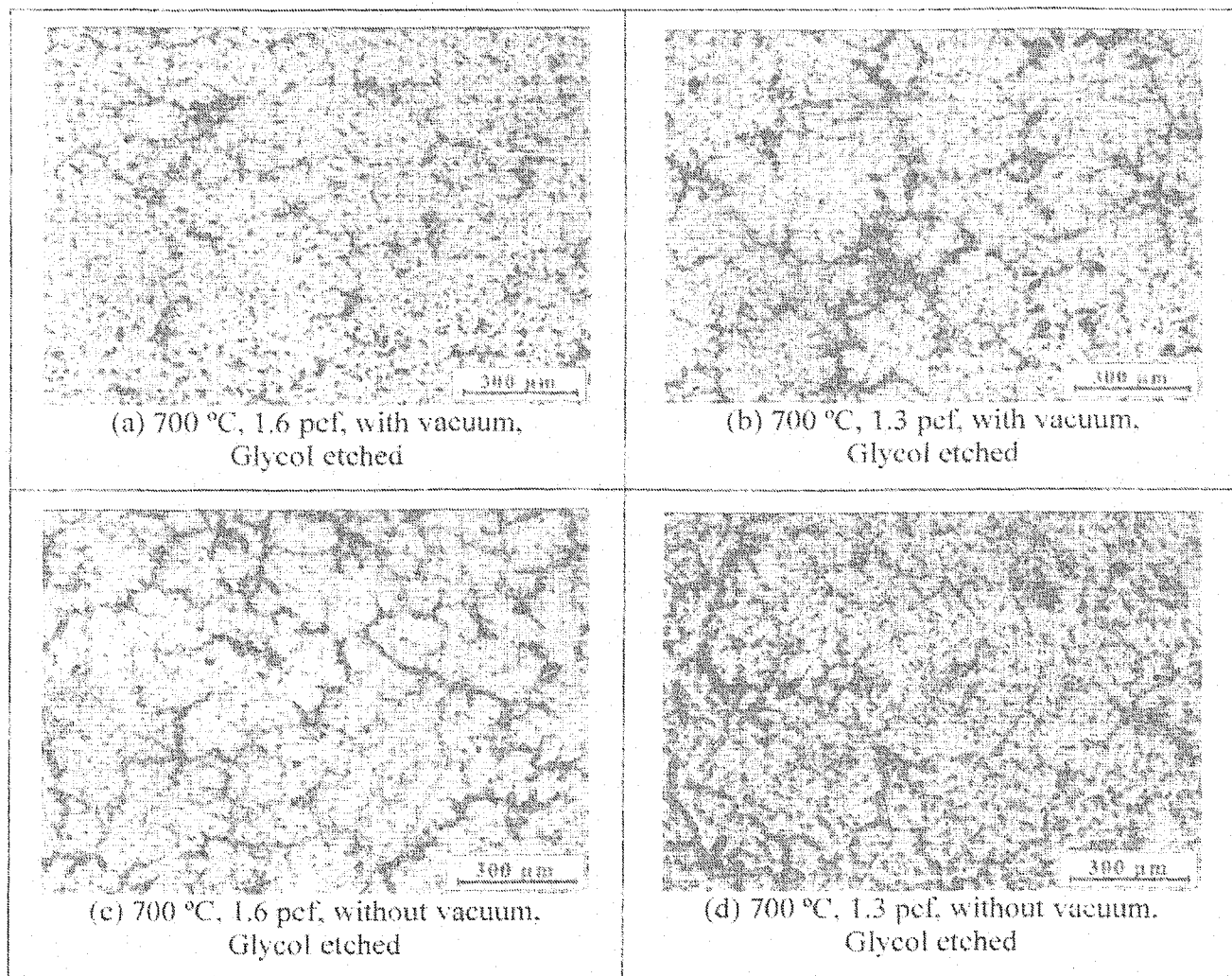
Extensive solidification shrinkage networks were observed in casting locations near the metal-mold interface. Typical network with a partial deformation of the casting surface was seen in Figure 137.



*Figure 137: Shrinkage porosity in the 2.5 cm thick bar at a 5 cm distance from the sprue, 700 °C / 1.6 pcf / with vacuum trial.*

Similarly, as in the case of the 660 °C pouring temperature trials, shrinkage porosity networks were not observed in the center-regions of the casting bars. Instead, only isolated patches of the shrinkage cavities formed, as seen in Figure 138.





*Figure 138: Microstructure of the 2.5 cm thick bar center location at 5 cm distance from the sprue.*

In the casting trial with 700 °C pouring temperature, 1.3 pcf foam and applied vacuum, a unique casting defect was discovered. A spherical cavity was found near the casting surface, as seen in Figure 139. Based on its shape, this defect should be classified as gas-induced porosity. However, close inspection of the walls of the cavity revealed the presence of hardened liquid-EPS residue. Therefore, it appears that the liquid-EPS products did not reach the metal-mold interface and solidified in the casting, with a nearly spherical shape. The arrow in Figure 139 indicates the traces of the liquid-EPS residue.



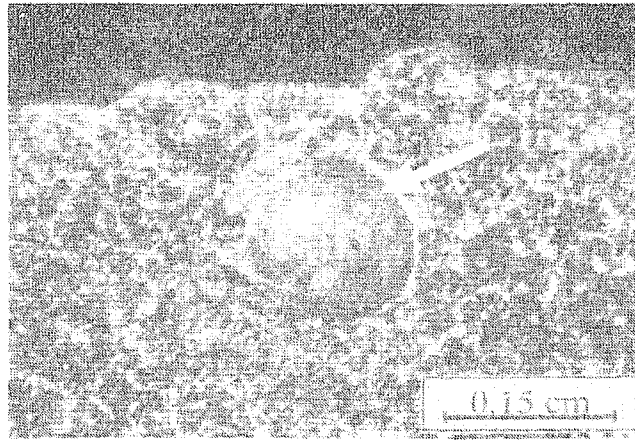


Figure 139: Liquid-EPS bubble near the casting surface.

It was of interest to determine, whether the molten metal front velocity affected the porosity in the casting. Research shows <sup>62,63</sup> that molten metal flow with Reynold's number (Re) less than 2000 is typically laminar. At higher Re values, the flow may become turbulent, with attendant entrapment of gasses by the metal front, thus causing increased porosity levels.

The Reynold's number is defined <sup>64</sup> as:

$$Re = \frac{\rho V L}{\mu} \quad (13)$$

Where:

$\rho$  = Alloy density

$V$  = Metal front velocity

$L$  = Characteristic length

$\mu$  = Alloy viscosity

In this research, the highest possible Re number was achieved in the 1.5 cm thick horizontal bar cast at 660 °C pouring temperature with 1.6 pcf foam pattern under vacuum conditions. The Reynold's number in this case was:

$$Re = \frac{\rho V L}{\mu} = \frac{1740(kg/m^3) * 0.0613(m/s) * 1.5 \times 10^{-2}(m)}{2 \times 10^{-3}(kg/m.s)} = 1507 \quad (14)$$

This calculation suggests, that for the combinations of the LFC parameters investigated, the metal flow remained laminar.

Figure 140 is a plot of the measured optical porosity as a function of the metal velocity. These data pertain to the 1.5 cm thick horizontal bar of different casting conditions at a distance of 5 cm from the sprue.

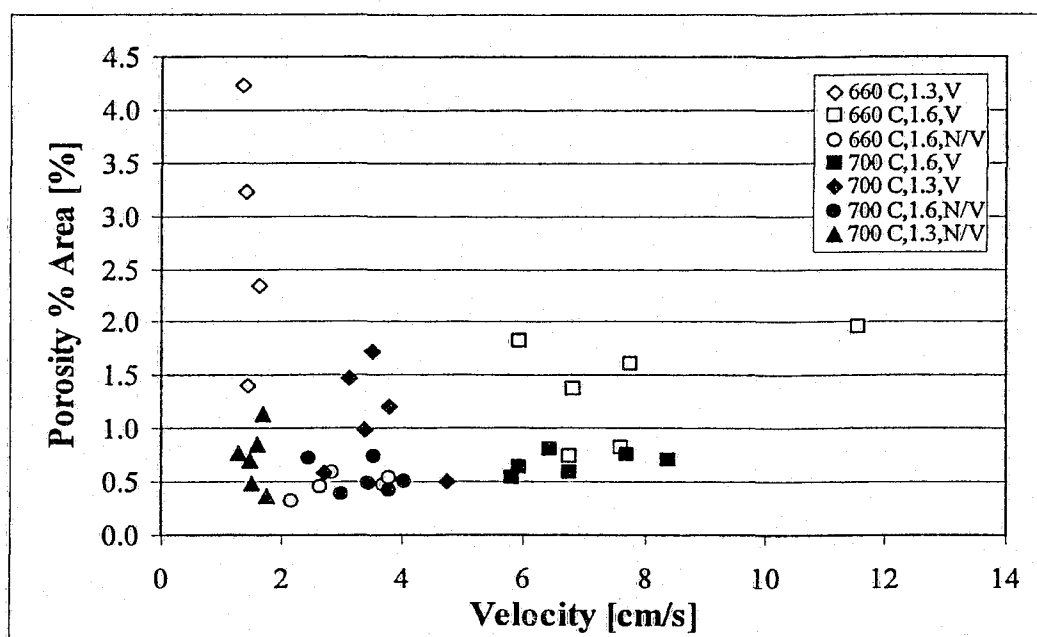


Figure 140: Porosity percent area vs. metal velocity.

It appears from Figure 140 that, with increasing metal velocity, the casting porosity levels decreased. Considering the fact that the metal flow was laminar for all casting trials, then the increased porosity levels in slow-metal velocity cases could be correlated with the difficulty of removing liquid-EPS products from the casting cavity. For a slow moving metal front, the partially solidified chunks obstructed the paths along which the pyrolysis products could escape, thus possibly causing an increase of the casting porosity.

#### **4.9.3 Criterion functions**

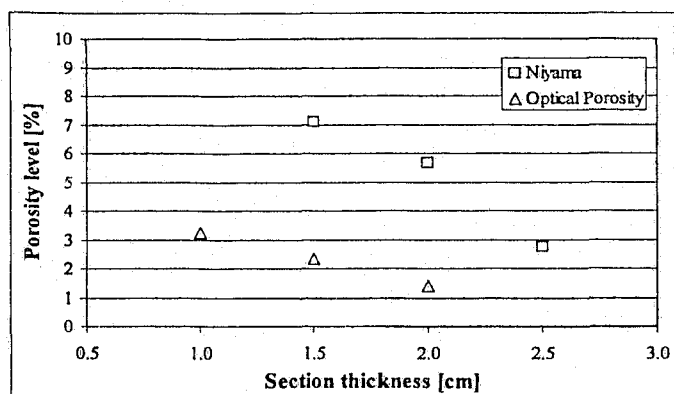
The criterion functions presented in Section 2.7 were evaluated to estimate the average casting porosity in the horizontal bars. Past research <sup>65</sup> indicates that these criterion functions may require modification for a particular casting process and alloy to increase prediction accuracy. Currently, there is no published literature on the validity of these models for the LFC of magnesium alloys.

The criterion functions were evaluated at casting locations where optical porosity values were measured. This allowed ranking of the criterion functions based on their accuracy to predict casting porosity.

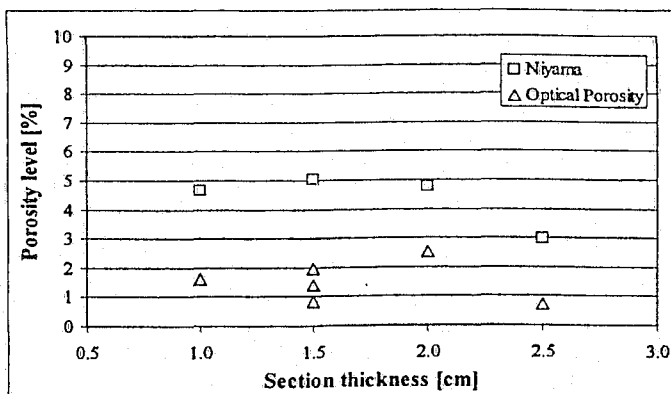
It was observed, that the Freezing Index (FI) and the LCC functions were overestimating the porosity values by two orders of magnitude. The Gradient Acceleration Parameter (GAP) underestimated the porosity values by one order of magnitude. Such trends were observed for the majority of the casting locations. Therefore, these functions were not adequate for the prediction of porosity levels in LFC of magnesium alloys.

As Figure 141 indicates, the Niyama function predicted porosity values within the same order of magnitude as measured by the optical image analysis.

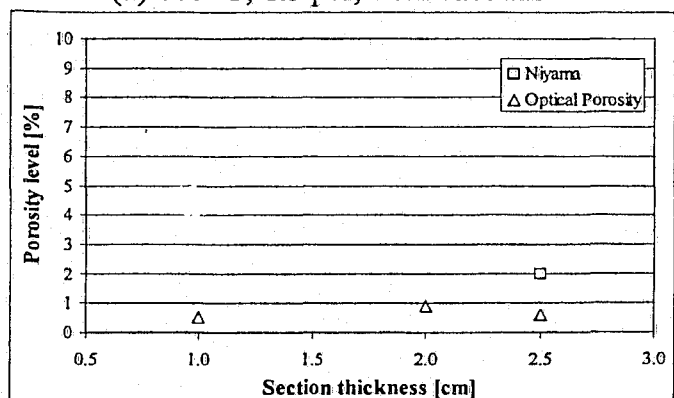
The Niyama function, which is based on the thermal gradient and the cooling rate of the solidifying casting, was seen to relate to the development of shrinkage porosity in the casting. The presence and the volume fraction of the generated liquid-EPS products was not accounted for in the Niyama criterion function. As Section 4.4 shows, formation of the liquid-EPS residue seemed to affect the casting density, soundness and porosity to a great extent. Incorporation of this information into the criterion function is a complex problem dealing with thermo-physical phenomena associated with the LFC process. Lack of accurate information regarding the liquid-EPS generation made the use of the criterion function inaccurate. Aspects such as: foam density, level of bead fusion, metal front profile, alloy superheat and freezing range would have to be quantitatively assessed to improve the prediction model accuracy.



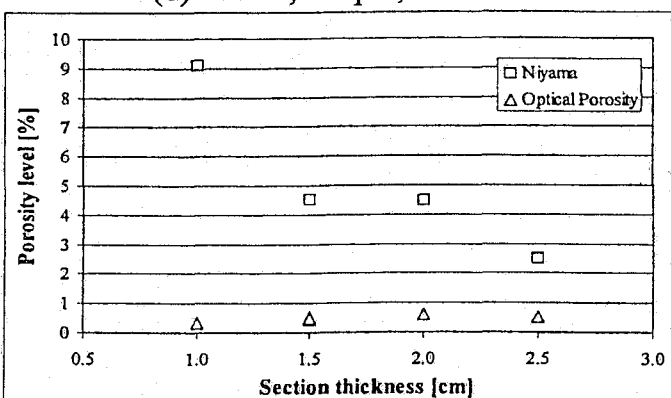
(a) 660 °C, 1.3 pcf, with vacuum



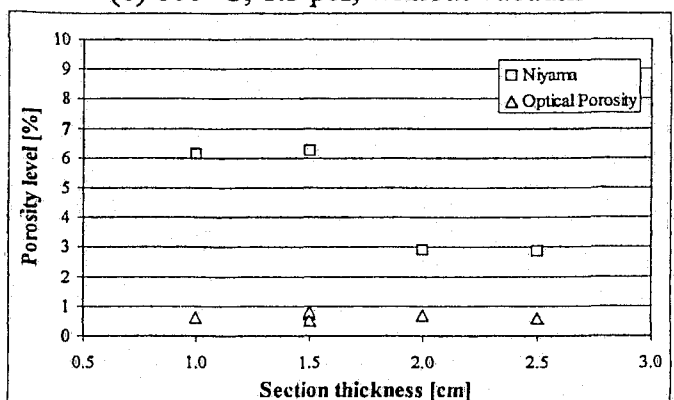
(b) 660 °C, 1.6 pcf, with vacuum



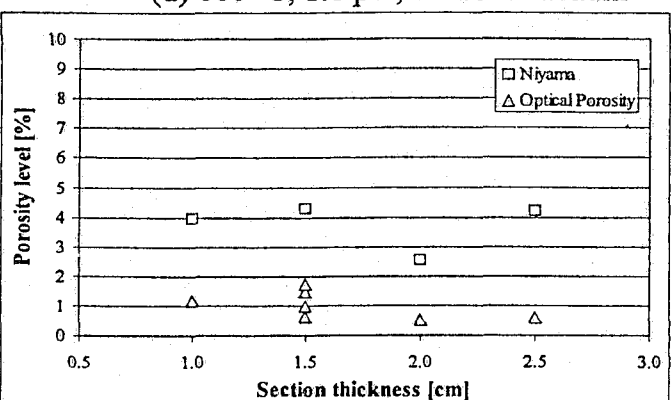
(c) 660 °C, 1.3 pcf, without vacuum



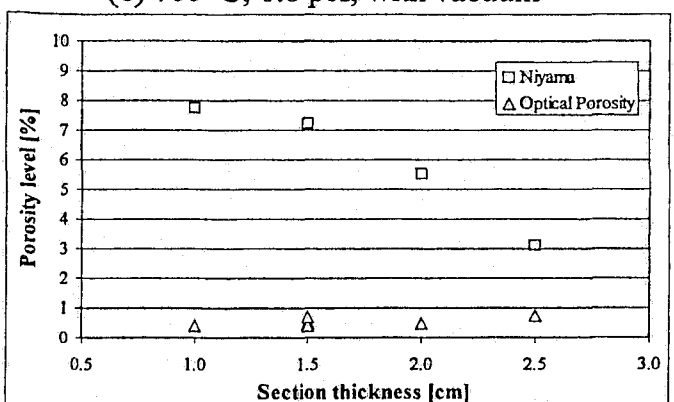
(d) 660 °C, 1.6 pcf, without vacuum



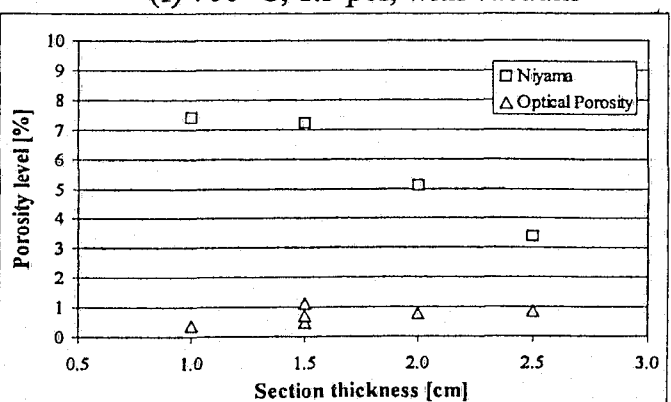
(e) 700 °C, 1.6 pcf, with vacuum



(f) 700 °C, 1.3 pcf, with vacuum



(g) 700 °C, 1.6 pcf, without vacuum



(h) 700 °C, 1.3 pcf, without vacuum

Figure 141: Niyama criterion function and optical porosity.

#### *4.9.4 Section summary*

The porosity levels in all castings were relatively low due to the effective use of the protective atmosphere during melting operations.

The porosity results suggest that application of vacuum caused entrapment of the liquid-EPS products in the casting cavity. As a result, the porosity was seen to be higher in vacuum castings than in the gravity castings. Further, the variance of the porosity data was also seen to increase as a result of the applied vacuum.

The foam density and bead fusion were seen to affect the casting porosity. Poorly fused low-density foam possibly generated more liquid-EPS products which were later entrapped in the casting cavity, thus increasing casting porosity.

Shrinkage porosity networks were observed to form near the casting mold walls. These networks were seen to extend to the surface of the casting, potentially creating surface pores.

Criterion functions were evaluated and compared to the experimental data. With the exception of the Niyama function, the general porosity prediction models were inadequate for LFC of magnesium alloys. The Niyama function seemed to correctly predict the trends of shrinkage porosity development along the length of the bar.

#### 4.10 Microstructure of the casting

The microstructure of the cast specimens was analyzed by the optical microscopy techniques. Image analysis software was used to determine the grain structure and the morphology of the  $\text{Mg}_{17}\text{Al}_{12}$  precipitate.

In general, it was observed that in locations where slow cooling rates prevailed, the shape of the  $\text{Mg}_{17}\text{Al}_{12}$  phase resembled the equilibrium-like (spherical morphology) precipitate. In these cases, the  $\text{Mg}_{17}\text{Al}_{12}$  phase formed from the supersaturated Mg-Al solid solution while it was heterogeneously dispersed throughout the primary magnesium grains.

However, due to the relatively high cooling rates associated with the LFC process, the majority of the cast specimens contained the lamellar (eutectic)  $\text{Mg}_{17}\text{Al}_{12}$  precipitate. This precipitate preferentially formed on the grain boundaries and in the interdendritic regions of the primary magnesium dendrites. Thus, the distribution was also heterogeneous.

In several instances, formation of both types of the precipitate was observed within the same casting. This suggests a localized heterogeneity in solidification conditions within the casting.

Development of the non-equilibrium precipitate was correlated with the thermal analysis data. Thermal undercooling, which occurs during non-equilibrium solidification, was registered by the cooling curve analysis. In addition, constitutional undercooling was established as a result of non-equilibrium solidification (with associated compositional changes). Consequently, solute was rejected by the solid phase into the liquid phase, which resulted in solute segregation, as evidenced by the microstructure.

The image analysis results suggest a correlation between the casting density and the percent area of the eutectic precipitate.

#### 4.10.1 Constitutional undercooling in the AZ91E alloy

Inspection of the metallographic specimens revealed the presence of the lamellar non-equilibrium  $Mg_{17}Al_{12}$  precipitate. Under equilibrium cooling conditions, the AZ91E alloys do not generate this kind of the precipitate. However, the relatively high cooling rates associated with the casting process caused constitutional undercooling.

Based on the equilibrium phase diagram, Figure 7, it is likely that as the solidification front advanced, solute (aluminum) was redistributed at the solid-liquid interface. In particular, the solute was possibly rejected by the solid phase into the liquid phase. The reason for and the mechanism of solute rejection by the solid phase is discussed in the following paragraph. Table 21 demonstrates the development of solute levels in the solid and liquid phases during casting solidification.

Table 21: Solute redistribution in the AZ91E alloy.

Temperature [°C]	Solute Concentration [wt%]		Weight fraction of liquid [%]
	Solid phase	Liquid phase	
600	3.0	9.0	~100
587	3.8	11.6	66
575	4.3	13.8	49
550	5.9	17.5	26
500	8.8	25.5	1.5
450	12.0	33.0	N/A
437	12.7	34.9	N/A

During the solute rejection process, a solute-rich region ahead of the solid-liquid (S-L) interface develops. The concentration profile of this region is schematically illustrated in Figure 142. This curve corresponds to the solute concentration profile in the eutectic liquid ahead of the solid-liquid interface at the eutectic temperature.

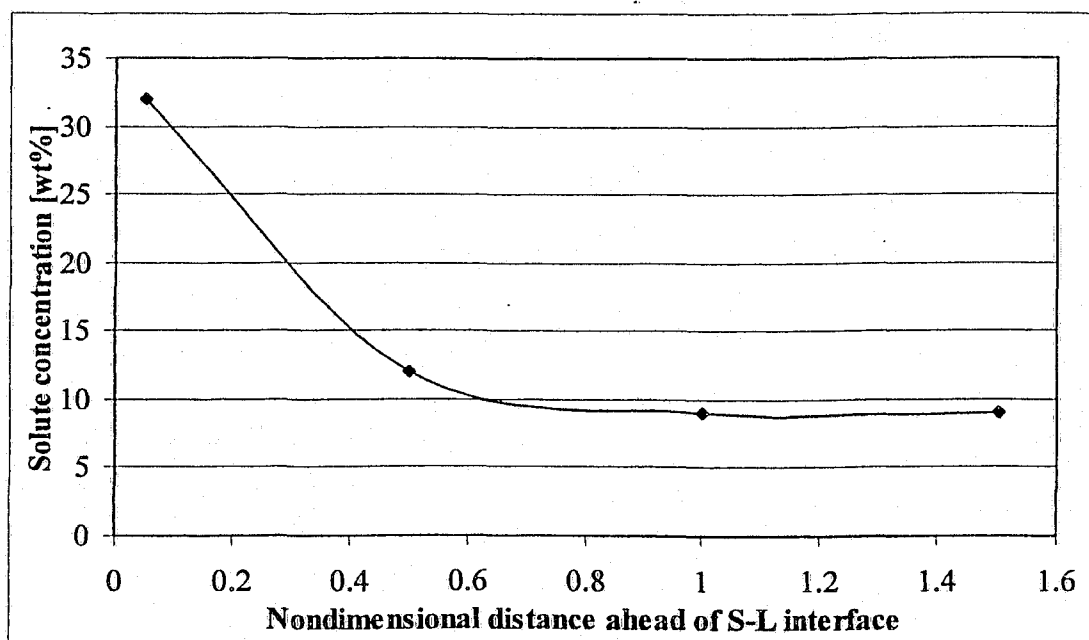


Figure 142: Schematic representation of the solute enriched region ahead of the S-L interface.

An important consequence of the solute accumulation was the possible breakdown of the planar solid-liquid interface into a more random interface.<sup>68</sup> As a result, the grain structure changed from the columnar type, to a mix of cellular and dendritic grain structure. This change occurred because of the liquid well ahead of the solid-liquid interface had a lower solute concentration and hence a higher equilibrium freezing temperature than the liquid at the solid-liquid interface. As a result, any perturbation at the solid-liquid interface would promote growth of the primary dendrite stalks into the constitutionally (chemically) undercooled liquid. Such growth would occur even if the liquid far ahead of the solid-liquid interface was in fact hotter than the liquid near the solid-liquid interface. Therefore, constitutional undercooling was considered as a possible mechanism affecting the growth of dendrites in the castings.

The magnitude of constitutional undercooling was governed by the temperature gradients present ahead of the solid-liquid interface. A schematic illustration of the effect of the thermal gradient on the extent of the constitutional undercooling is presented in Figure 143.



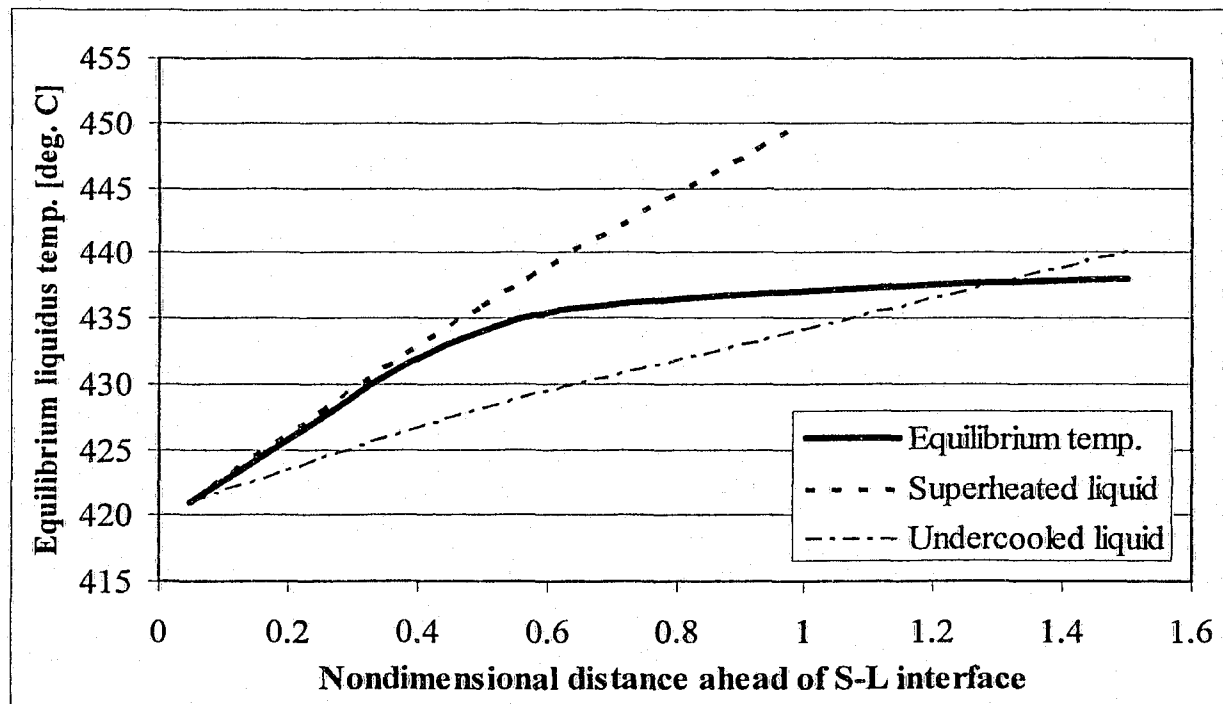


Figure 143: Schematic temperature profiles.

The thermal gradient, which was defined as the slope of the temperature profile ahead of the solid-liquid interface, possibly governed the size of the region where constitutional undercooling occurred. High thermal gradients decreased the thickness of the constitutionally undercooled region and vice versa.

As a result of the solute gradients ahead of the solid-liquid interface, the concentration of the solid magnesium grains was not uniform. The magnesium dendrites / grains formed in solid layers of possibly varying solute concentration. The dendrite center possibly had the lowest concentration (3.3 wt%Al), while the outermost edge of the dendrite solidified with approximately 12.7 wt%Al. The interdendritic region, containing eutectic liquid, solidified with the eutectic composition of ~ 33 wt%Al. Figure 144 shows the estimated solute concentration profile for the magnesium dendrites and the interdendritic region at the eutectic temperature. The extremities of the plot, i.e., interdendritic distances of 0 and 1, correspond to the centers of adjacent dendrite stalks. The solute content between these two stalks varied according to the solute redistribution criteria imposed by the Mg – Mg<sub>17</sub>Al<sub>12</sub> phase diagram.

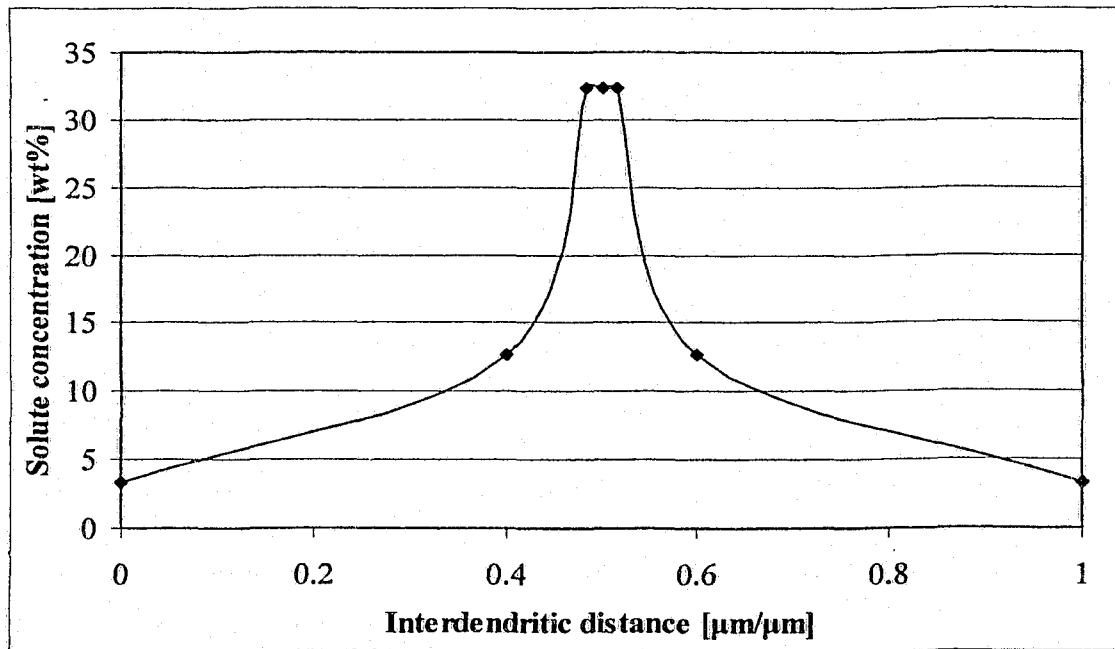


Figure 144: Schematic solute gradient profile for the primary Mg phase.

The presence of solute gradients within the magnesium grains / dendrites resulted in a cored microstructure. This cored microstructure was observed in all castings. An example of this microstructure is seen in Figure 145. In this micrograph, different shades of gray represent different solute concentrations. This figure also clearly shows, that the inter-dendritic regions solidified with the lamellar eutectic phase (dark gray), while the primary magnesium grains contained only limited amount of dissolved aluminum (light gray).

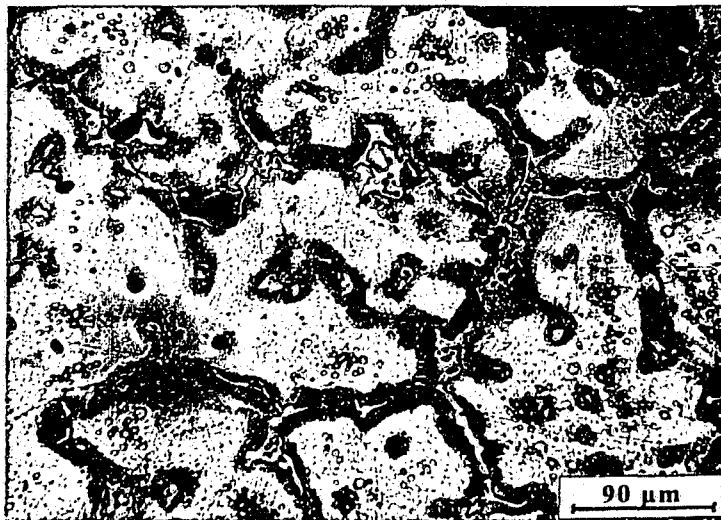


Figure 145: Microstructure of the 2.0 cm thick bar at the 7.6 cm distance from the sprue, 700 °C / 1.6 pcf / with vacuum trial.

#### 4.10.2 Effect of cooling rate on the $Mg_{17}Al_{12}$ precipitate

In general, the casting microstructure consisted of the primary magnesium grains surrounded by the eutectic microconstituent  $Mg_{17}Al_{12}$ . The mass fraction and the exact location of the precipitated  $Mg_{17}Al_{12}$  phase varied throughout the casting and seemed to depend on the localized cooling conditions.

In investigating the effect of the cooling rate on the as-cast alloy microstructure and the  $Mg_{17}Al_{12}$  precipitate, attention was given to the magnitude of the thermal gradients in the horizontal bars. The presence of the thermal gradients affected the solute redistribution kinetics at the solid-liquid interface (Section 4.10.1). The effect of the thermal gradients on the casting microstructure was explained using the constitutional undercooling criterion function.

In the case of the binary eutectic alloys, it is possible to define a partition coefficient,  $k_p$ , which is the ratio of the composition of the solid and the liquid phases at the solid-liquid interface,  $C_s$  and  $C_L$ , respectively:

$$k_p = C_s / C_L \quad (15)$$

Since the solidus and liquidus lines of the Mg- $Mg_{17}Al_{12}$  phase diagram are straight, the value of  $k_p$  was approximately constant for the solidifying AZ91E system.

Theory suggests,<sup>66</sup> that the nature of the solute build-up ahead of the solid-liquid interface is a function of the solid phase growth velocity,  $V_{S-L}$ , the partition coefficient,  $k_p$ , the diffusivity of the solute in the liquid,  $D_L$ , and the slope of the liquidus line,  $m$ . Therefore, these solidification variables were related to the thermal gradient to develop a criterion for the occurrence of constitutional undercooling.

The thermal gradient ( $G$ ) is proportional to the rate of change of the solute ahead of the solid-liquid interface ( $dC_L/dx'$ ) and the slope of the liquidus line ( $m$ ).<sup>67</sup> Hence, the general constitutional undercooling criterion is given by:

$$G < -m \frac{dC_L^*}{dx'} \bigg|_{x'=0} \quad (16)$$

The characteristic distance for this relationship,  $x'$ , is given by  $D_L / V_{S-L}$ , which can also be identified as the solute boundary layer thickness,  $\delta$ .

For most alloy systems, the steady state concentration boundary layer profile,  $C_L^*$ , is estimated as:<sup>68</sup>

$$C_L^* = C_O + \frac{C_O(1 - k_p)V_{S-L}}{k} e^{\left(\frac{x'}{D_L}\right)} \quad (17)$$

Where:

$C_O$  = Bulk solute concentration

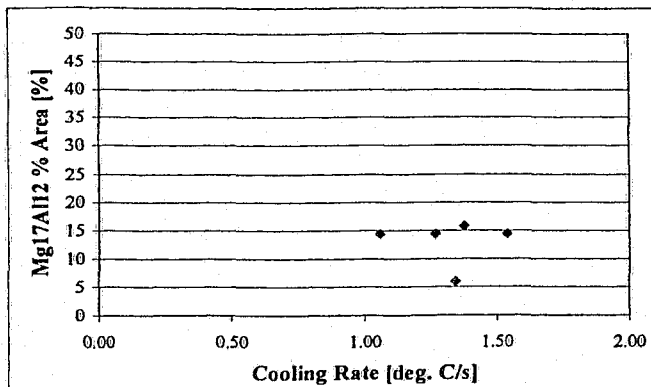
Substituting this expression into Equation 16 and differentiating, the constitutional undercooling criterion is obtained:

$$G < -m \frac{C_O(1 - k_p)V_{S-L}}{kD_L} \quad (18)$$

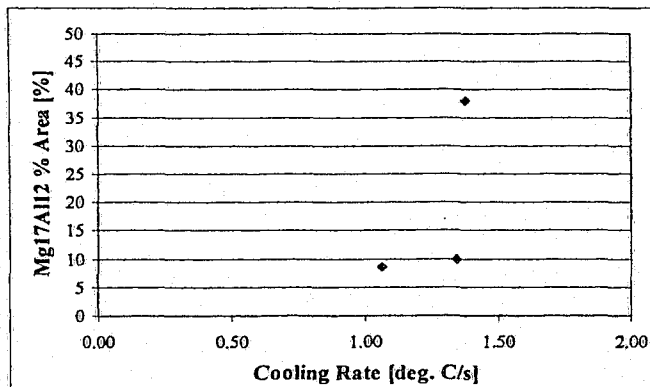
Therefore, as Equation 18 suggests, higher cooling rates (which generate high thermal gradients) decrease the solute boundary layer thickness.

In this research, the  $Mg_{17}Al_{12}$  percent area data obtained from the image analysis software did not show a definite correlation with the cooling rate, as observed in Figure 146. Therefore, it is possible that the range and the magnitude of the cooling rates investigated in this research were not sufficient to appreciably change the  $Mg_{17}Al_{12}$  percent area.

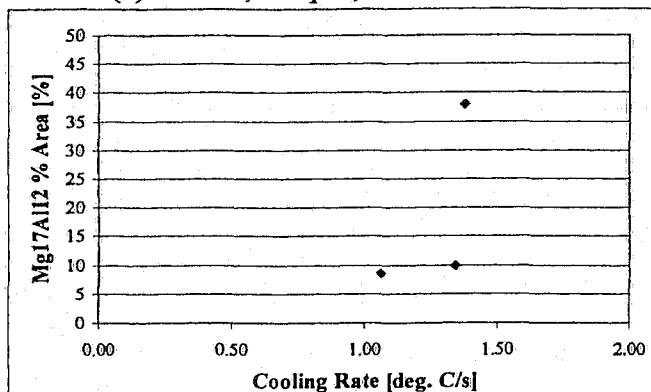
The thermal analysis data suggest, however, that the cooling rate indeed affected the duration of the eutectic reaction. As Figure 147 suggests, increasing the cooling rate generally seemed to decrease the eutectic reaction time. This result agrees with the fact that higher cooling rates cause rapid casting solidification, thus decreasing time for any transformation to occur.



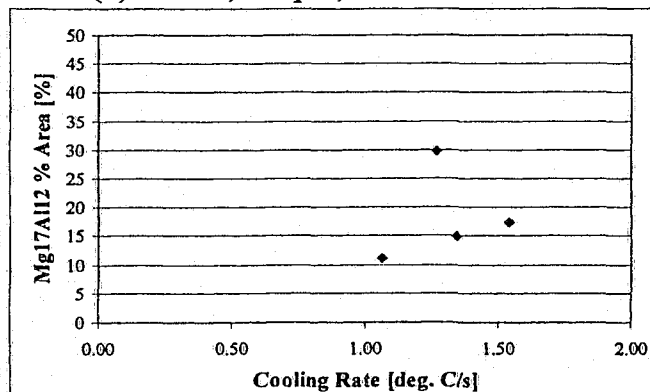
(a) 660 °C, 1.3 pcf, with vacuum



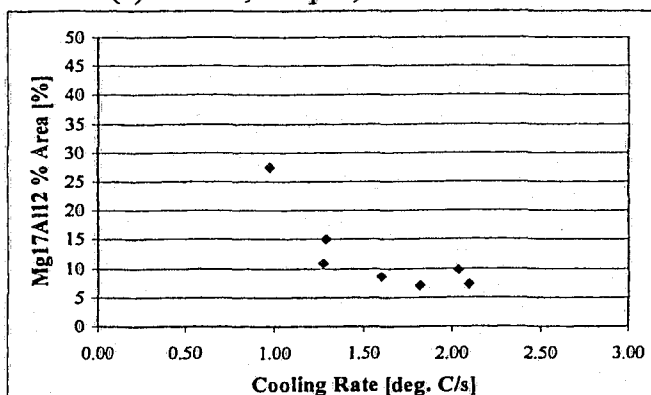
(b) 660 °C, 1.6 pcf, with vacuum



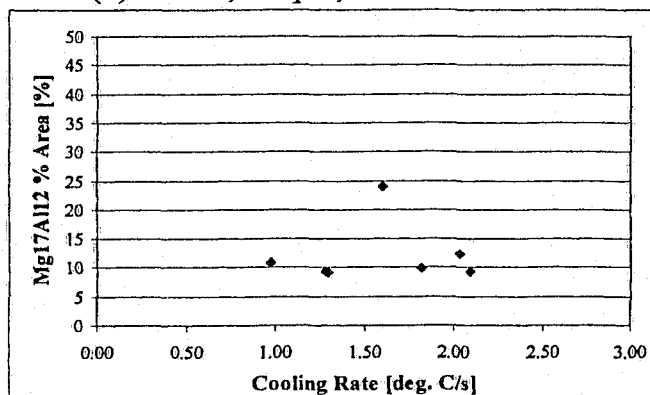
(c) 660 °C, 1.3 pcf, without vacuum



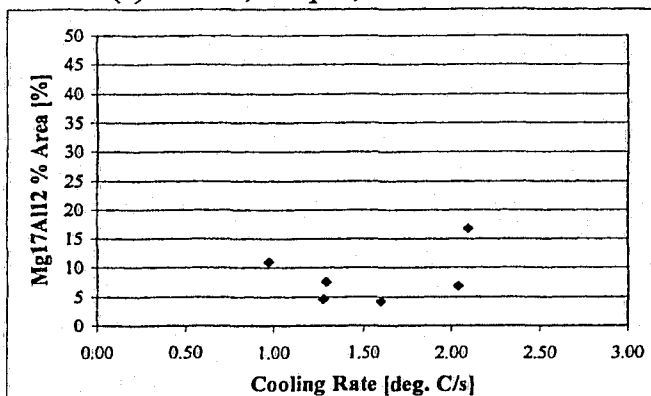
(d) 660 °C, 1.6 pcf, without vacuum



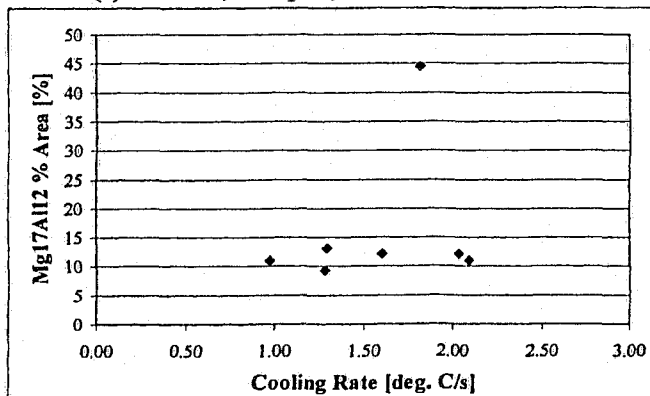
(e) 700 °C, 1.6 pcf, with vacuum



(f) 700 °C, 1.3 pcf, with vacuum

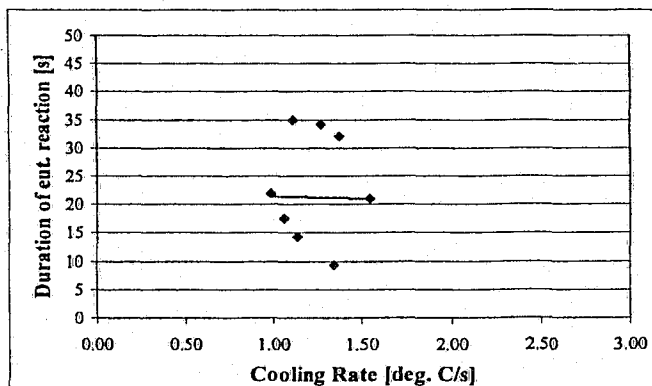


(g) 700 °C, 1.6 pcf, without vacuum

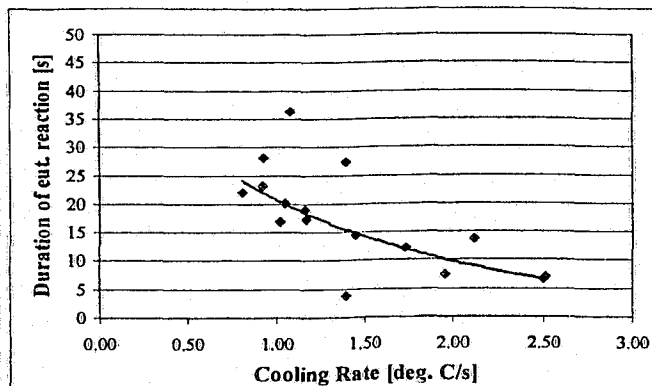


(h) 700 °C, 1.3 pcf, without vacuum

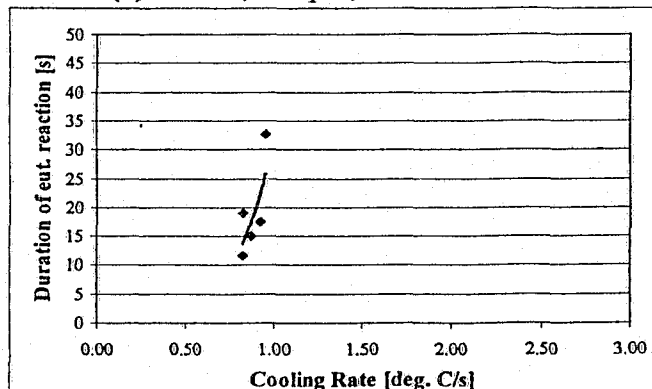
Figure 146: Mg<sub>17</sub>Al<sub>12</sub> percent area vs. cooling rate.



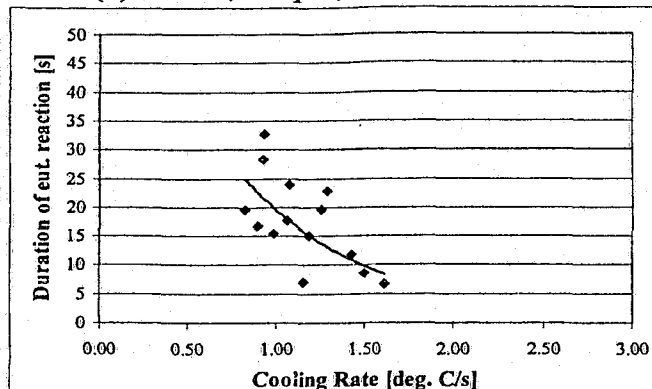
(a) 660 °C, 1.3 pcf, with vacuum



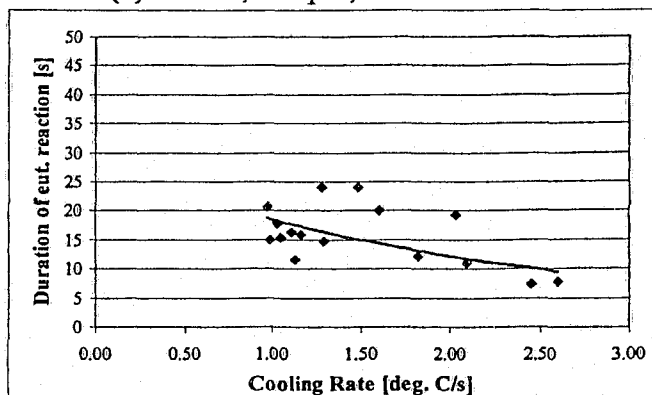
(b) 660 °C, 1.6 pcf, with vacuum



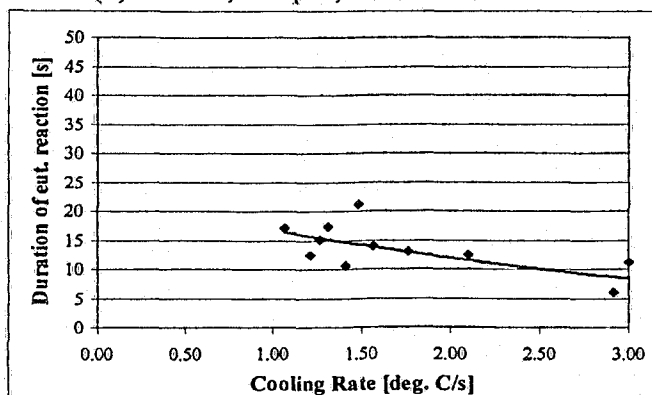
(c) 660 °C, 1.3 pcf, without vacuum



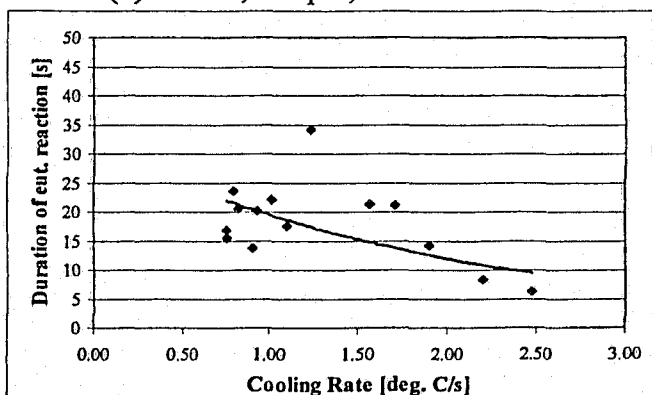
(d) 660 °C, 1.6 pcf, without vacuum



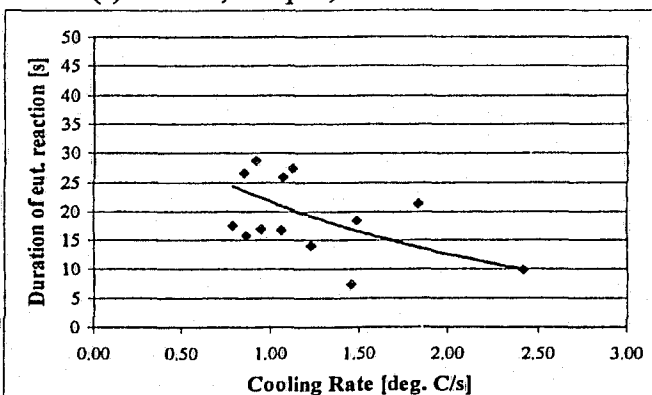
(e) 700 °C, 1.6 pcf, with vacuum



(f) 700 °C, 1.3 pcf, with vacuum



(g) 700 °C, 1.6 pcf, without vacuum

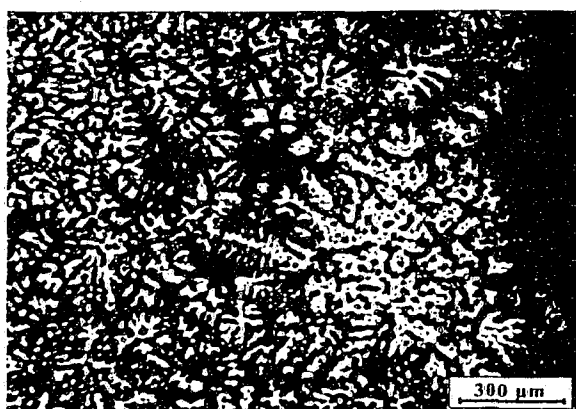


(h) 700 °C, 1.3 pcf, without vacuum

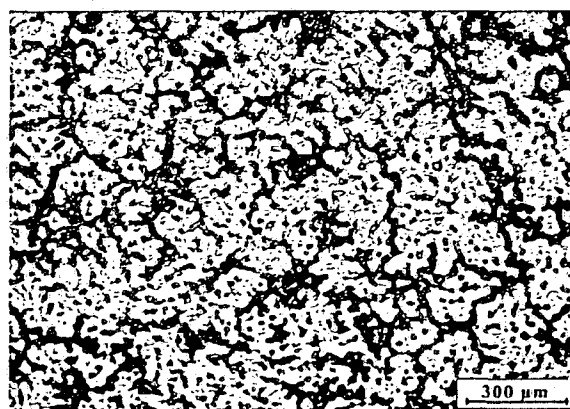
Figure 147: Duration of the eutectic reaction vs. cooling rate.

The microstructure near the mold walls often exhibited dendritic structure. Such a microstructure was attributed to the higher cooling rates resulting from the contact of the molten metal with the relatively cool sand mold, which caused rapid grain nucleation and dendrite growth. Further, the relatively higher cooling rates also promoted branching of the primary dendrite arms, in order to maintain chemical equilibrium of the quickly solidifying Mg-Al system. An example of a highly dendritic microstructure is seen in Figure 148.

The microstructure in the center locations of the casting was not strictly dendritic. Due to the relatively low cooling rates, a microstructure resembling the combination of dendritic and cellular types formed, as observed in Figure 149.



*Figure 148: Dendrites at the mold wall in the 2.0 cm thick bar at 5 cm distance from the sprue, 660 °C / 1.3 pcf / with vacuum trial.*



*Figure 149: Microstructure of the 2.0 cm thick bar midsection at 5 cm distance from the sprue, 660 °C / 1.3 pcf / with vacuum trial.*

The effect of the horizontal bar section thickness on the as-cast microstructure was attributed to the variation of the cooling rate associated with the different horizontal bars. In thinner sections, the cooling rates were higher, therefore facilitating more significant departure from equilibrium solidification conditions. Consequently, the grain nucleation rate, as well as the levels of constitutional undercooling varied. The result was a decrease in grain size and a more pronounced solute segregation. The microstructure of the thicker horizontal bars was representative of the higher LSTs experienced by these bars. In such cases, the magnesium grains were relatively large due to the longer growth times. Further, the degree of solute redistribution was different, since the size of the interdendritic regions depended on the cooling rate. A progressive variation of the microstructure in the 660 °C / 1.6 pcf / without vacuum casting trial is presented in Figure 150. This figure also shows that with the increased grain size, the  $Mg_{17}Al_{12}$  precipitated in discrete regions of the microstructure, whereas in the thinner horizontal bars, the  $Mg_{17}Al_{12}$  phase formed throughout the microstructure.

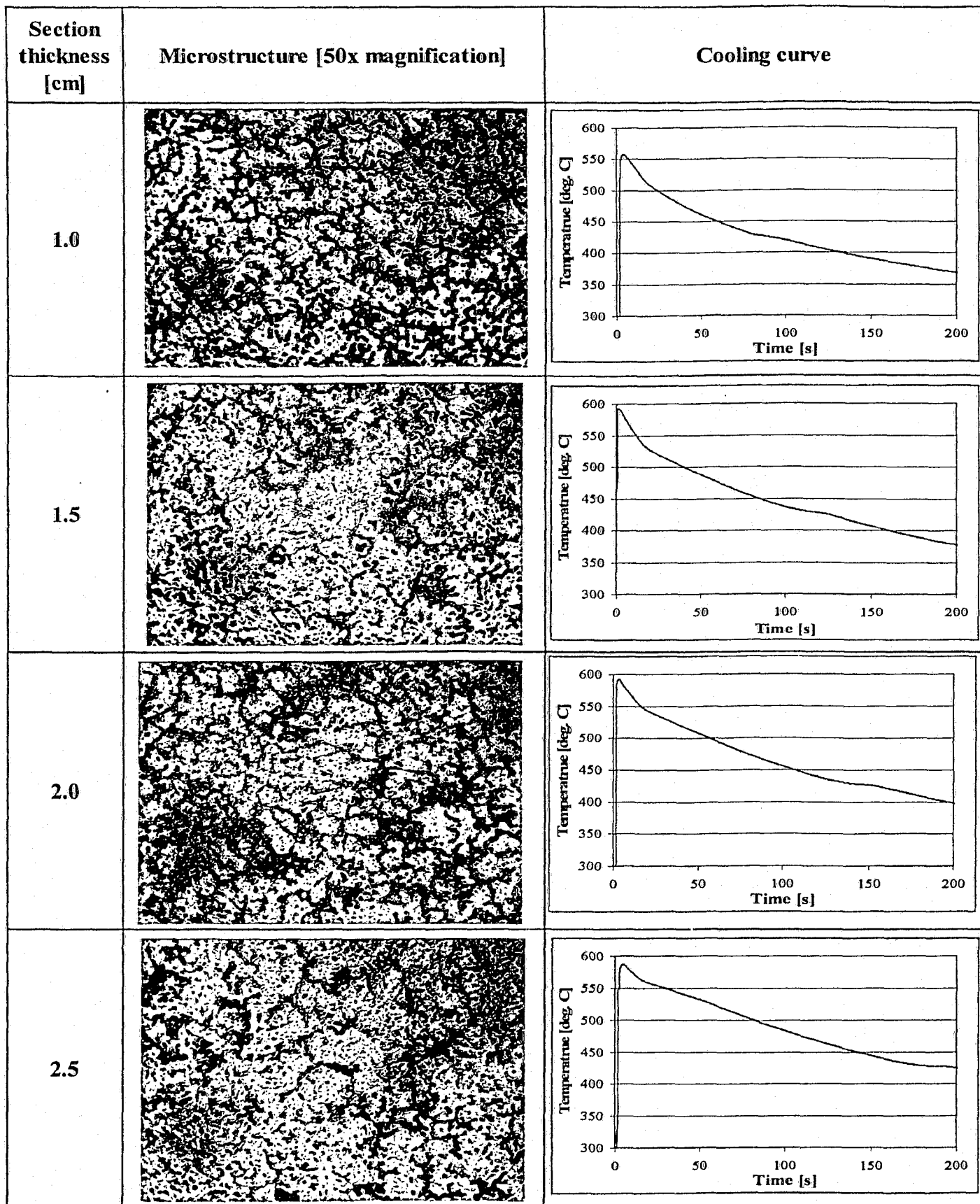


Figure 150: Microstructure development at the 5 cm distance from the sprue.



It appears, that the initial cooling rate (i.e., the cooling rate experienced by the alloy immediately after crossing of the liquidus line) significantly affected the grain morphology of the as-cast microstructure.

For example, in Figure 150, the 2.5 cm thick horizontal bar experienced an initial cooling rate of 0.2 °C/s. As a result of this relatively slow cooling rate, the grain structure does not show the characteristic dendritic microstructure (branching of primary dendrite arms). However, in the case of a casting produced with 700 °C pouring temperature, 1.3 pcf foam, without vacuum, the location at 7.6 cm from the sprue in the 1.5 cm thick bar experienced initial cooling rate of 4.8 °C/s. As a result of the relatively high cooling rate, the casting section was not solidifying under equilibrium conditions and a completely dendritic microstructure formed, as observed in Figure 151. Due to the interlocking of the dendrite arms, it is likely that the interdendritic regions were separated from one another. As a result, geometric constraints were imposed on the growing  $Mg_{17}Al_{12}$  phase. Therefore, the eutectic phase formed uniformly throughout the microstructure.

Formation of the eutectic microconstituent  $Mg_{17}Al_{12}$  appeared to correlate with the thermal gradients established in the horizontal bars. In the case of the 1.5 cm thick horizontal bar of the 700 °C / 1.6 pcf / without vacuum casting trial, the average thermal gradient along the length of the bar was 3.9 °C/cm. However, in the 2.5 cm thick bar of the 700 °C / 1.3 pcf / without vacuum casting trial, the gradient was 1.7 °C/cm. Figure 151 and Figure 152 show the microstructure of the two bars, respectively. Since the gradient in the 1.5 cm thick bar was relatively high, the potential for constitutional undercooling decreased. As a result, formation of the lamellar  $Mg_{17}Al_{12}$  phase decreased and a fibrous  $Mg_{17}Al_{12}$  precipitate formed instead.

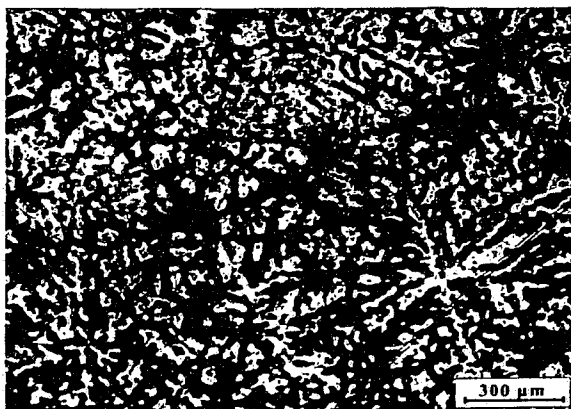


Figure 151: Microstructure of the 1.5 cm bar at 7.6 cm distance from the sprue, 700 °C / 1.3 pcf / without vacuum trial.

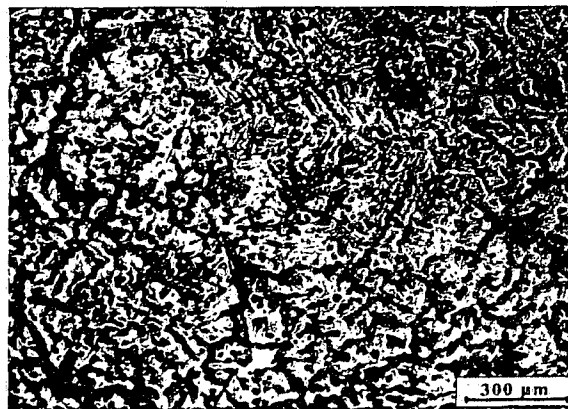


Figure 152: Microstructure of the 2.5 cm bar at 7.6 cm distance from the sprue, 700 °C / 1.3 pcf / without vacuum trial.

It was also observed, that the amount of the precipitated  $Mg_{17}Al_{12}$  phase seemed to vary along the length of the horizontal bars.

Locations near the flow tip, where the cooling rates were relatively high, experienced rapid nucleation of the primary magnesium grains. Consequently, the size of the interdendritic regions decreased and the eutectic liquid was dispersed throughout the entire casting section, as depicted in Figure 153.

Casting sections near the sprue, however, remained hot for longer periods of time, thus potentially allowing flow of the low-melting point eutectic liquid. As a result, the eutectic liquid was pushed by the growing dendrites which allowed the  $Mg_{17}Al_{12}$  phase to precipitate as discrete islands randomly in the microstructure, as shown in Figure 154.

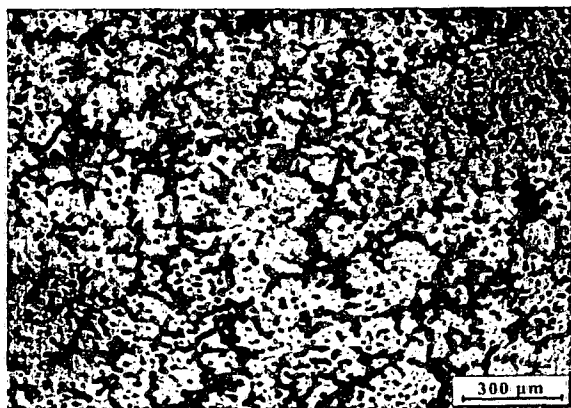


Figure 153: Dispersed  $Mg_{17}Al_{12}$  in the 1.5 cm bar at 7.6 cm distance from the sprue, 700 °C / 1.3 pcf / with vacuum trial.

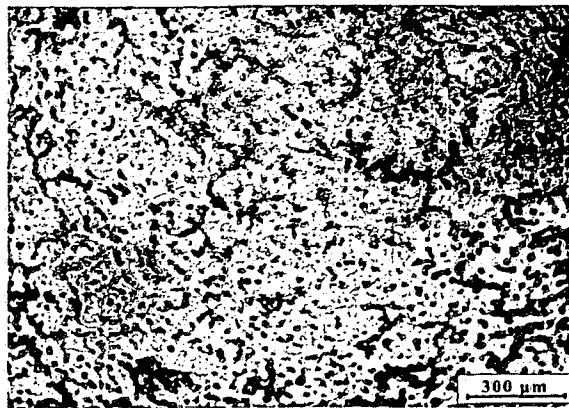


Figure 154:  $Mg_{17}Al_{12}$  phase in the 1.5 cm bar at 2.5 cm distance from the sprue, 700 °C / 1.3 pcf / without vacuum trial.

The unique features of the  $Mg_{17}Al_{12}$  precipitate, such as the formation of lamellae or fibers, depended mainly on the solidification kinetics of the casting. Specifically, it seems that formation of the precipitate was governed by the degree of departure from equilibrium cooling conditions.

#### 4.10.3 Development of the “equilibrium-like” precipitate

The “equilibrium-like”  $\text{Mg}_{17}\text{Al}_{12}$  precipitate had a spherical morphology and was seen to form within the primary magnesium grains, as observed in Figure 155. This micrograph was taken from the 1.5 cm thick bar at 2.5 cm distance from the sprue in the 660 °C / 1.6 pcf / with vacuum trial. It appears, that in this case, only limited fraction of the lamellar precipitate formed on the grain boundaries.

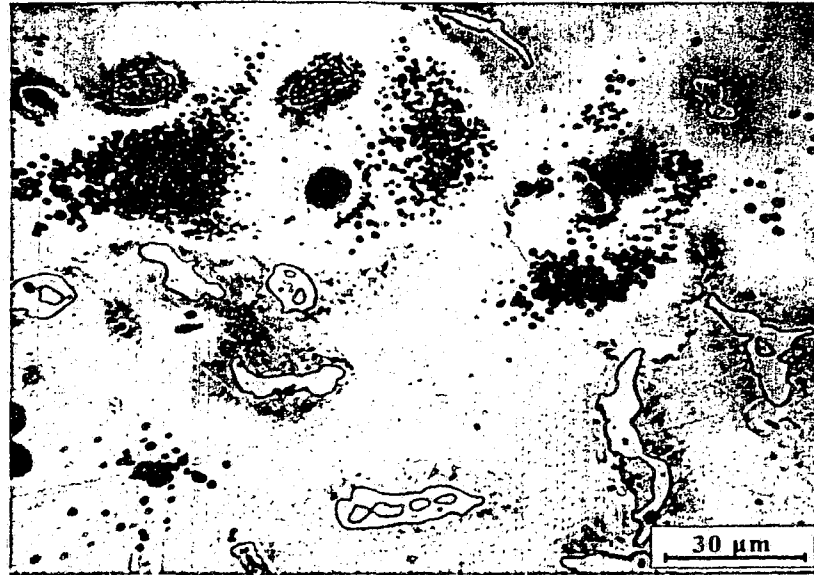


Figure 155:  $\text{Mg}_{17}\text{Al}_{12}$  precipitate within the  $\alpha$ -Mg grains.

Development of the “equilibrium-like” precipitate was associated with the very slow cooling rates experienced by some casting locations. The precipitation mechanics were explained using the Mg-Al equilibrium phase diagram. A schematic portion of a this phase diagram is illustrated in Figure 156. At point “A”, the casting temperature fell below the liquidus temperature and small islands of the primary  $\alpha$ -Mg phase nucleated. The phase development entered the “ $\alpha$  + Liquid” region and with further cooling, the temperature reached the solidus line, at which point all of the liquid was consumed. At point “B”, a solid solution of Mg and Al formed.

Due to the decreasing solid solubility of aluminum in magnesium, further cooling of the alloy caused the  $\text{Mg}_{17}\text{Al}_{12}$  phase to separate from the supersaturated solid solution of  $\alpha$ -Mg and  $\beta$ - $\text{Mg}_{17}\text{Al}_{12}$  phases, point “C”. At this instant, the  $\text{Mg}_{17}\text{Al}_{12}$  particles observed in Figure 155 formed within the magnesium grains.

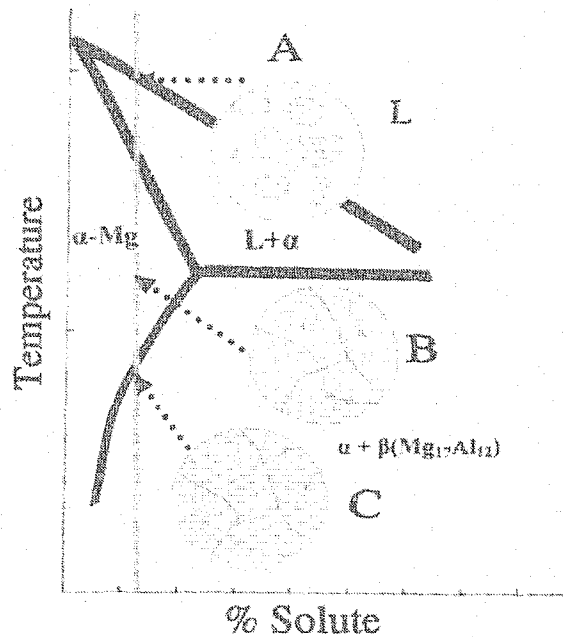


Figure 156: Equilibrium phase generation.

#### 4.10.4 Development of the lamellar “non-equilibrium” precipitate

The lamellar non-equilibrium  $\text{Mg}_{17}\text{Al}_{12}$  precipitate was present in virtually all castings. Formation of this lamellar precipitate was expected, since the cooling rates associated with the LFC process were too high to favor equilibrium precipitation. Further, formation of this precipitate suggested the presence of constitutional undercooling and segregation phenomena.

It is likely, that during solidification, it was difficult for the system to maintain chemical equilibrium. This was caused by the relatively slow atomic diffusion rates in the solid phase, as compared to the diffusion rates in the liquid phase. As a result, solute was rejected by the solid phase into the liquid. Consequently, solute concentration gradients in the liquid ahead of the solid-liquid interface were established.

Due to the much slower diffusion rates in the solid phase, a depression of the solidus line was observed. The solidus line was shifted down-and-left from its original equilibrium position. The degree of the solidus line depression was observed to depend on the cooling rate experienced by the alloy.

In the AZ91E alloy system, the eutectic reaction should occur at 437 °C. In the present study, however, the castings exhibited the eutectic reaction between 424 °C and 428 °C, a 9 – 13 °C depression of the solidus line. This proves that equilibrium conditions were not followed.

It was also observed, that the data collected in the present study suggest that castings produced under near-equilibrium solidification conditions (slow cooling) would indeed exhibit the eutectic reaction at 437 °C, as suggested by Figure 157.

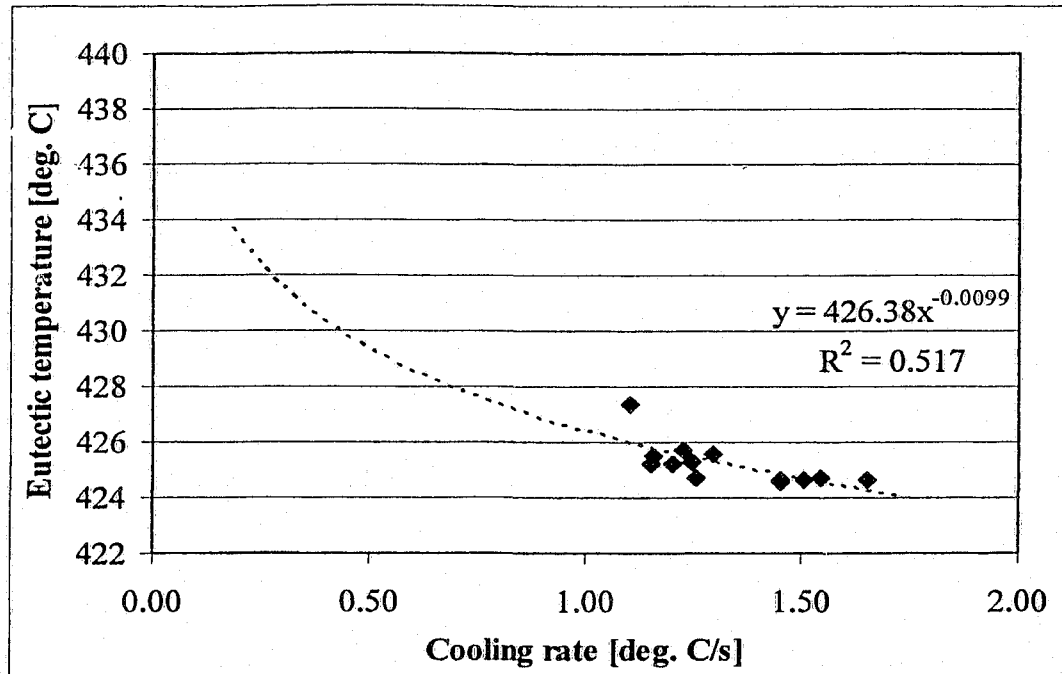


Figure 157: Effect of cooling rate on the eutectic temperature.

The following example explains the mechanism of the solidus line shift:

Figure 158 shows a generic phase diagram. In this hypothetical alloy with 30 wt%B composition, solidification started at  $T_1$ , where a solid solution of composition  $\alpha_1$  formed. At  $T_2$  the liquid was at composition  $L_2$  and the solid solution was of composition  $\alpha_2$ . Since solid diffusion was too slow to occur parallel with the crystal growth, not enough time was allowed to achieve uniformity in the solid (i.e., solute was rejected). Consequently, the solid composition was between  $\alpha_1$  and  $\alpha_2$ , say  $\alpha'_2$ . As the temperature decreased, the average composition departed still further from the equilibrium conditions. At the temperature of  $T_3$ , the average solid solution was of composition  $\alpha'_3$  instead  $\alpha_3$ .

For equilibrium cooling, solidification should be complete at  $T_4$ . However, since the average composition of the solid solution  $\alpha'_4$  did not reach the overall composition of the alloy, some liquid still remained. Solidification therefore continued until  $T_5$  was reached. At this temperature, the composition of the solid solution  $\alpha'_5$  coincided with the alloy composition and the solidification process was complete.

According to this example, the last liquid to solidify had a composition  $L_5$ , and was richer in solute than the last liquid which would solidify under equilibrium conditions. It is apparent then, that the higher the cooling rate, the greater the departure from equilibrium, with attendant wider composition range of the solidified grains.

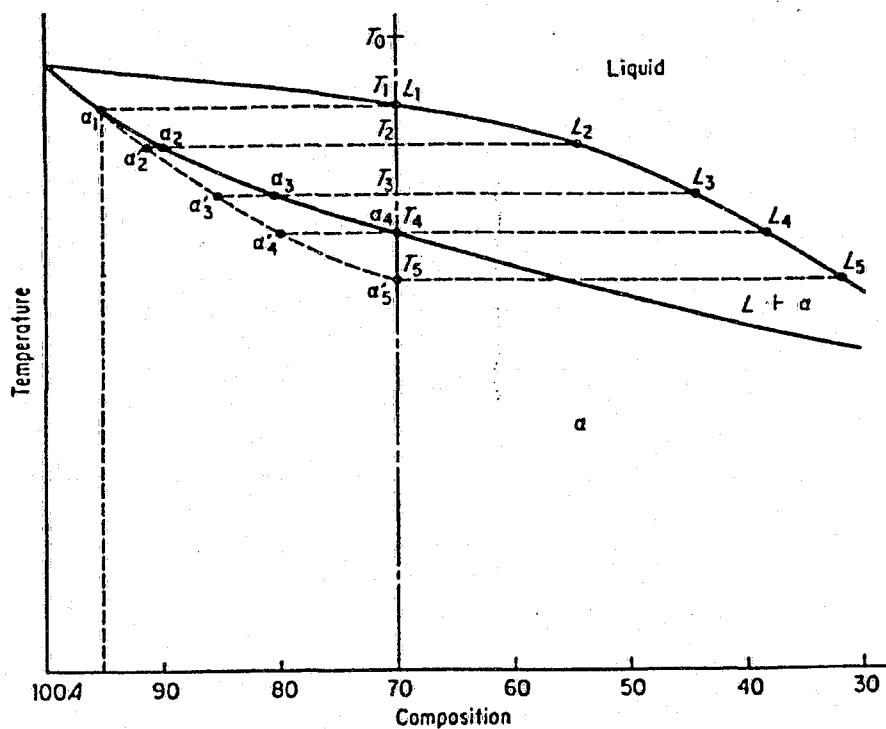


Figure 158: Generic phase diagram.<sup>69</sup>

Due to the shifting of the solidus line, phase development varied from that predicted by the equilibrium phase diagram. The liquid ahead of the solid-liquid interface was enriched in solute up to the level of reaching the eutectic composition (33 wt%Al). Prior to the crossing the eutectic isotherm, the liquid in the interdendritic regions of the casting solidified with the eutectic solute concentration, forming alternating lamellae of magnesium and aluminum. Figure 159 schematically illustrates the phase generation in the non-equilibrium cooling case.

At point "A", the first solid began to form, which was depleted in solute, while the liquid was enriched in solute. Further cooling of the alloy caused growth of the primary  $\alpha$ -Mg grains, point "B". At point "C", the interdendritic liquid solidified with the eutectic lamellar structure of  $\text{Mg}_{17}\text{Al}_{12}$ . A representative microstructure, which was present in all castings, is presented in Figure 160.

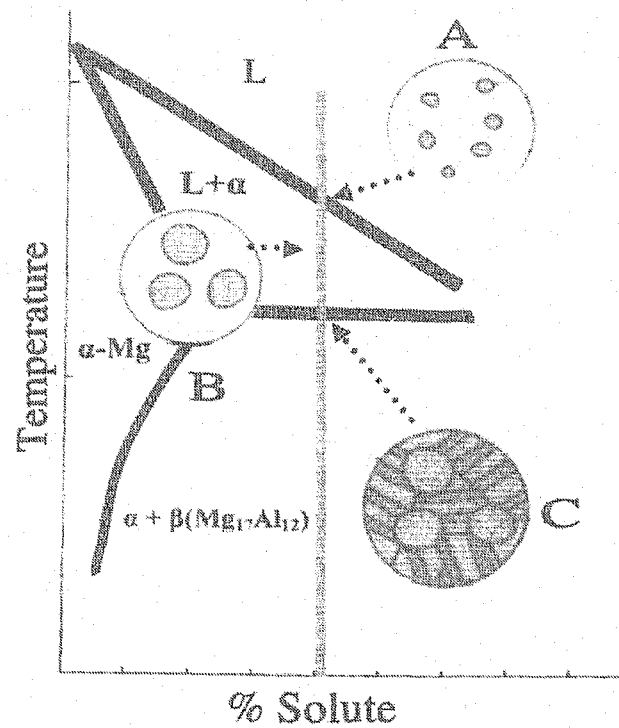


Figure 159: Non-equilibrium phase generation.

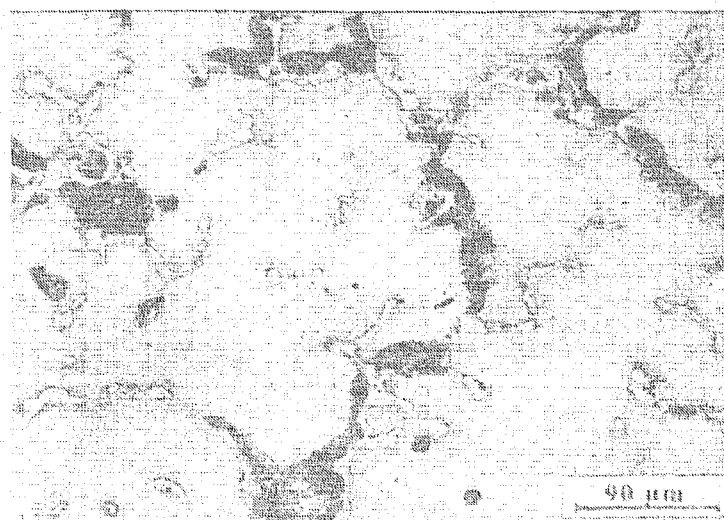


Figure 160: Lamellar  $\text{Mg}_{17}\text{Al}_{12}$  precipitate.

#### **4.10.5 Characterization of the $Mg_{17}Al_{12}$ precipitate**

The majority of the precipitated  $Mg_{17}Al_{12}$  phase was of the lamellar non-equilibrium type. Figure 161 to Figure 168 show representative casting microstructures for the different casting conditions (in cases where metallographic specimens for desired locations were not available, specimens at the nearest adjacent location were prepared to provide indication of the microstructure of the missing specimen).

As expected, the lamellar  $Mg_{17}Al_{12}$  phase formed on the grain boundaries, since the liquid enriched in the solute was continuously pushed by the growing magnesium dendrites to the interdendritic regions. At later stages of solidification, sufficient concentrations of solute and solvent elements were present to allow lateral atomic diffusion. This diffusion mechanism resulted in the formation of alternating lamellae of Mg and Al, with appreciable grain boundary migration, analogous to discontinuous precipitation. This is in agreement with the observations of Nie.<sup>32</sup>






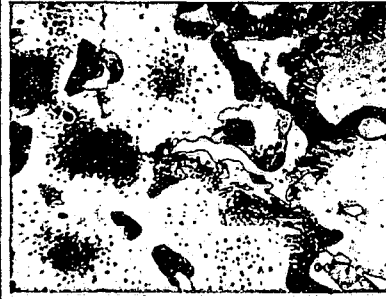
Section Thickness [cm]	Distance from the sprue [cm]			
	2.5	5.0	7.6	10.2
1.0				
1.5				
2.0				
2.5				

Figure 161: Casting microstructure: 660 °C / 1.3 pcf / with vacuum trial (500x).

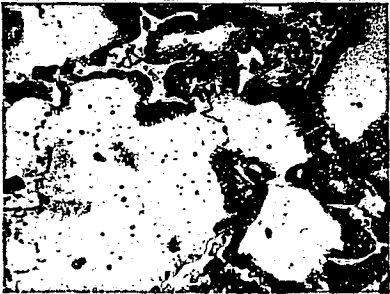
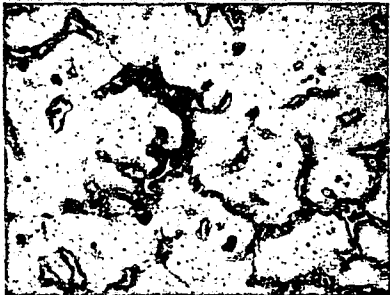

Section Thickness [cm]	Distance from the sprue [cm]			
	2.5	5.0	7.6	10.2
1.0				
1.5				
2.0				
2.5				

Figure 162: Casting microstructure: 660 °C / 1.6 pcf / with vacuum trial (500x).

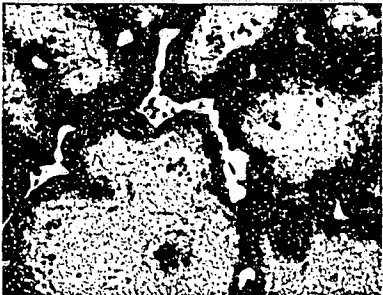
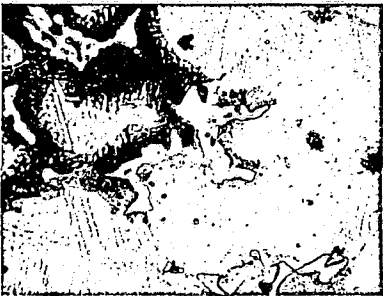

Section Thickness [cm]	Distance from the sprue [cm]			
	2.5	5.0	7.6	10.2
1.0				
1.5				
2.0				
2.5				

Figure 163: Casting microstructure: 660 °C / 1.3 pcf / without vacuum trial (500x).

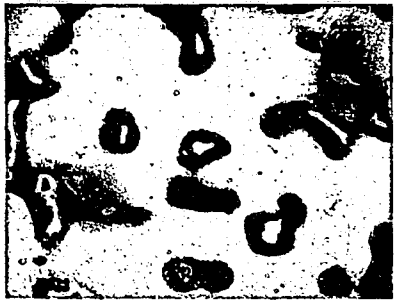

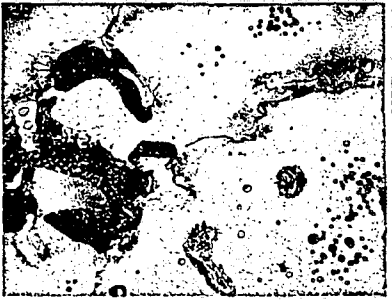



Section Thickness [cm]	Distance from the sprue [cm]			
	2.5	5.0	7.6	10.2
1.0				
1.5				
2.0				
2.5				

Figure 164: Casting microstructure: 660 °C / 1.6 pcf / without vacuum trial (500x).

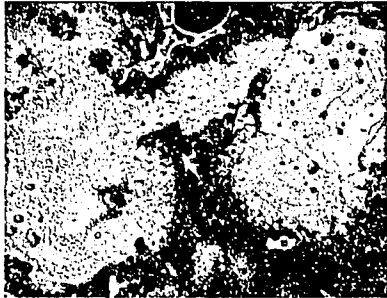
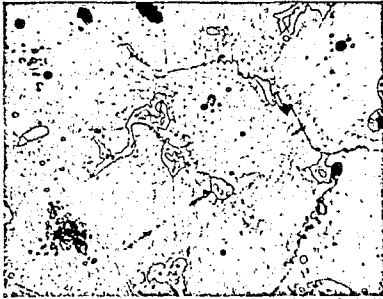


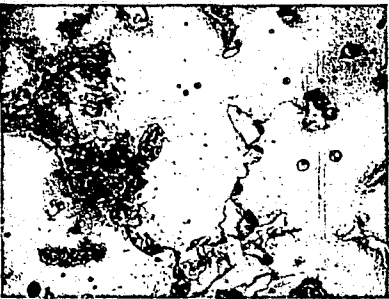


Section Thickness [cm]	Distance from the sprue [cm]			
	2.5	5.0	7.6	10.2
1.0				
1.5				
2.0				
2.5				

Figure 165: Casting microstructure: 700 °C / 1.6 pcf / with vacuum trial (500x).




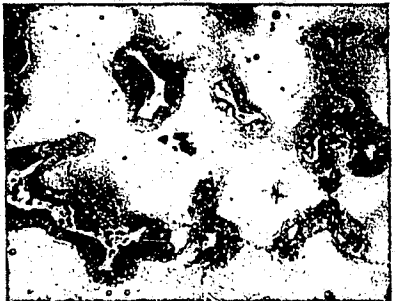


Section Thickness [cm]	Distance from the sprue [cm]			
	2.5	5.0	7.6	10.2
1.0				
1.5				
2.0				
2.5				

Figure 166: Casting microstructure: 700 °C / 1.3 pcf / with vacuum trial (500x).





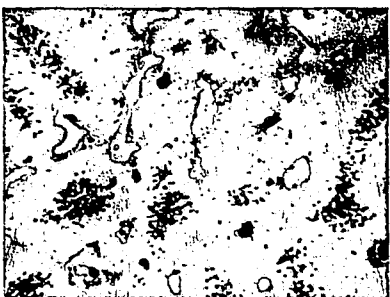


Section Thickness [cm]	Distance from the sprue [cm]			
	2.5	5.0	7.6	10.2
1.0				
1.5				
2.0				
2.5				

Figure 167: Casting microstructure: 700 °C / 1.6 pcf / without vacuum trial (500x).

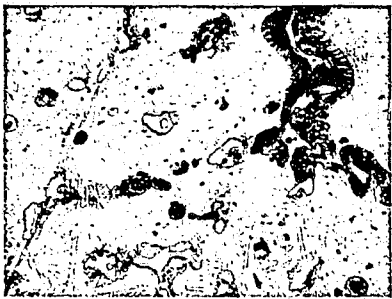


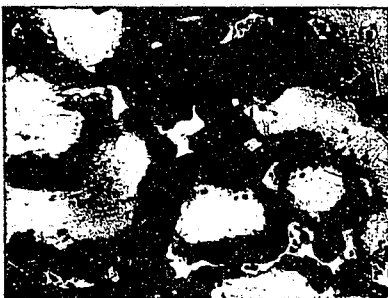
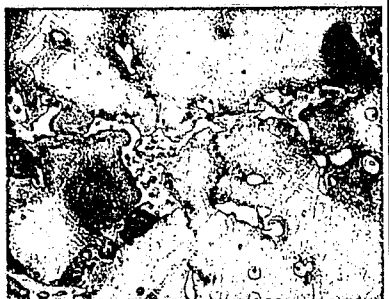


Section Thickness [cm]	Distance from the sprue [cm]			
	2.5	5.0	7.6	10.2
1.0				
1.5				
2.0				
2.5				

Figure 168: Casting microstructure: 700 °C / 1.3 pcf / without vacuum trial (500x).



It was of interest to note, that for some 660 °C pouring temperature casting trials, both types of precipitate were present (i.e., the “equilibrium-like” (A) and non-equilibrium lamellar precipitate (B)) within the same casting, as observed in Figure 169.

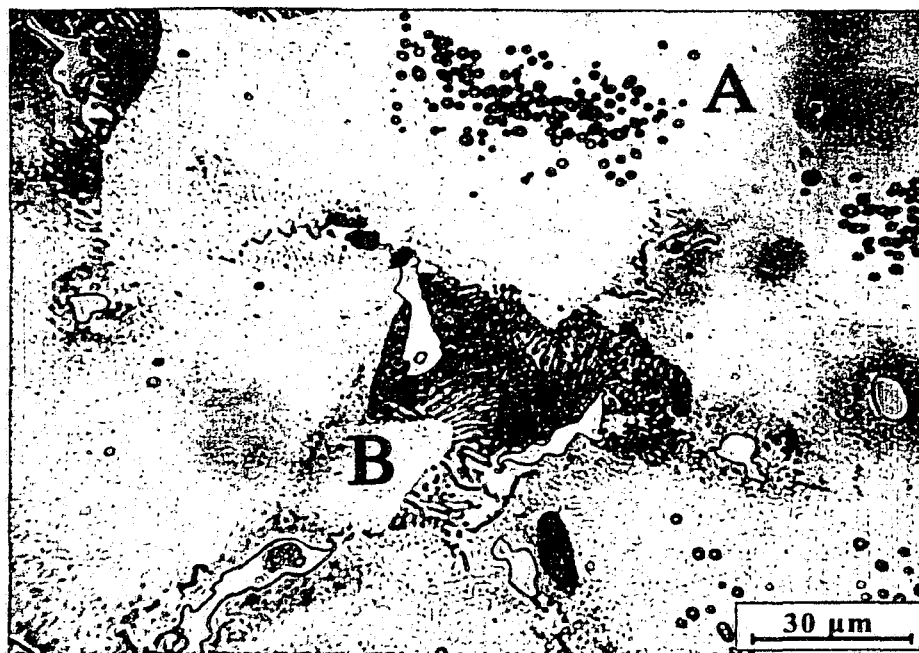


Figure 169: Precipitate in the 2.5 cm bar at 5 cm distance from the sprue, 700 °C / 1.6 pcf / with vacuum trial.

In regions where the “equilibrium-like”  $\text{Mg}_{17}\text{Al}_{12}$  phase formed, the eutectic was fully divorced, as seen in Figure 170. However, in castings where the non-equilibrium lamellar precipitate formed, the partially divorced eutectic was present with islands of Mg phase in the inter-dendritic regions, as observed in Figure 171. These results correspond with the relative grain sizes, as suggested by Nave et. al.<sup>28</sup>



Figure 170: Fully divorced eutectic in the 2.5 cm bar at 5 cm distance from the sprue, 660 °C / 1.3 pcf / with vacuum trial

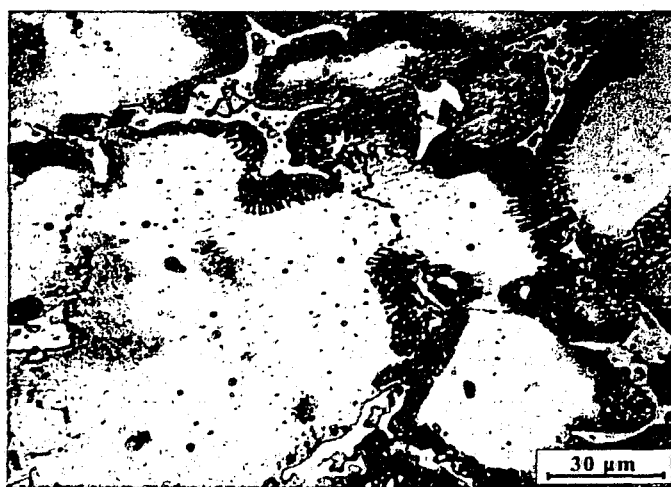


Figure 171: Partially divorced eutectic in the 1.0 cm bar at 5 cm distance from the sprue, 660 °C / 1.6 pcf / with vacuum trial.

Past research suggests,<sup>32</sup> that the lamellar precipitate grows on the pyramidal planes of the Mg crystals. Figure 172 shows a highly lamellar structure of a casting specimen from the 660 °C / 1.3 pcf / without vacuum casting trial. The area indicated by the circle was further enlarged in Figure 173 and revealed that the angle between respective lamellae was ~61°, which was near the theoretical 60° growth angle for the Mg hexagonal pyramidal plane.

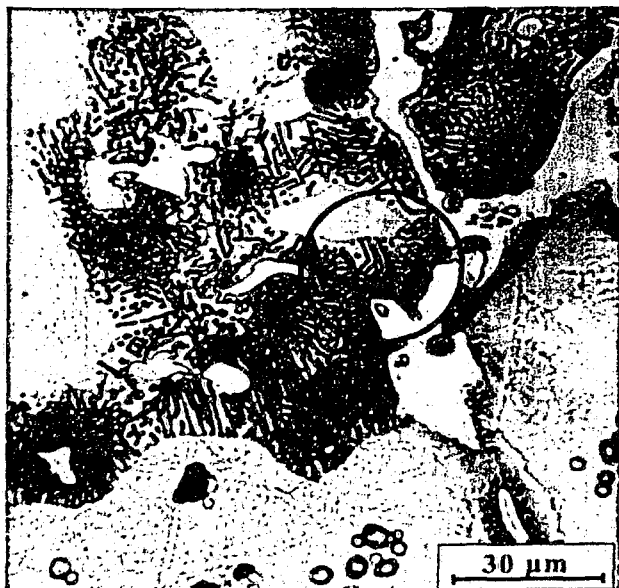
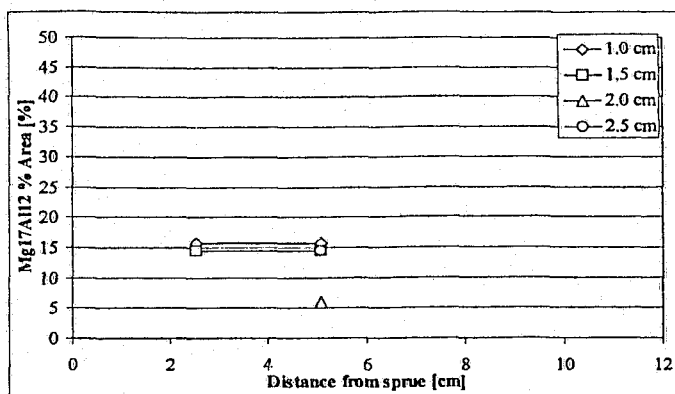


Figure 172: Pyramidal lamellar growth in the 2.5 cm bar at 5 cm distance from the sprue, 660 °C / 1.3 pcf / without vacuum trial.

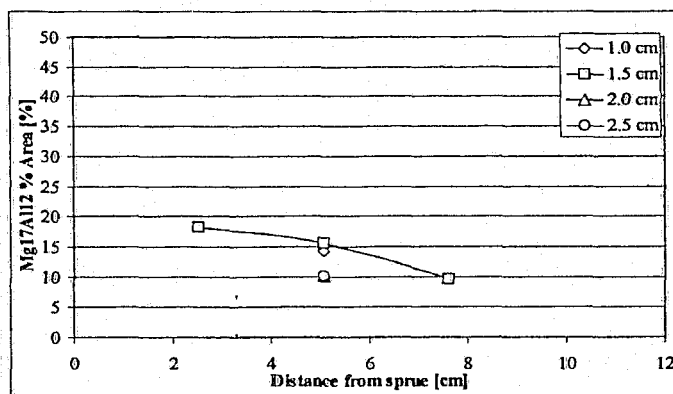


Figure 173: Growth directions of the lamellar  $Mg_{17}Al_{12}$  precipitate

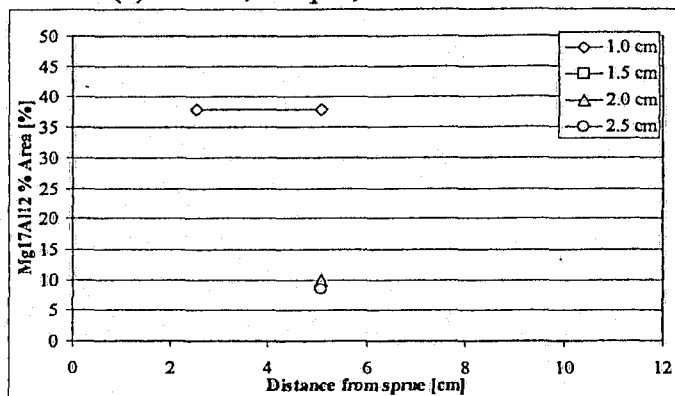
The average  $Mg_{17}Al_{12}$  percent area values for the different casting conditions were obtained from the image analysis software and are presented in Table 22. Plots for individual casting conditions are presented in Figure 174.



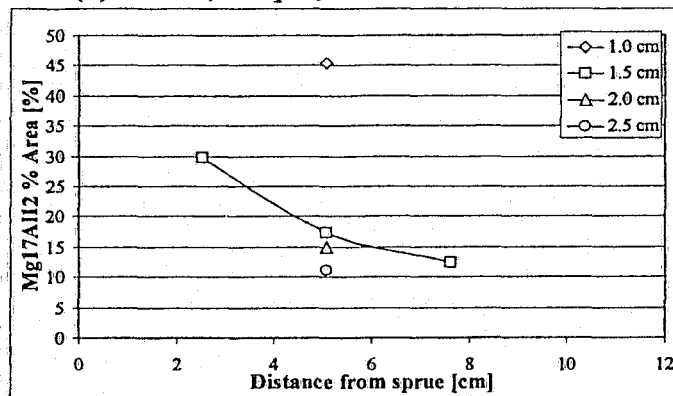
(a) 660 °C, 1.3 pcf, with vacuum



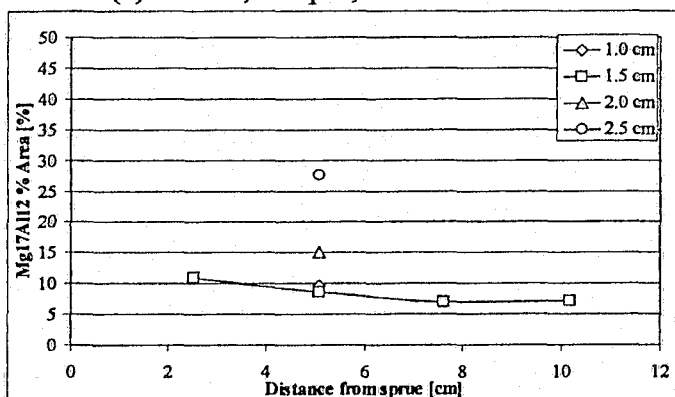
(b) 660 °C, 1.6 pcf, with vacuum



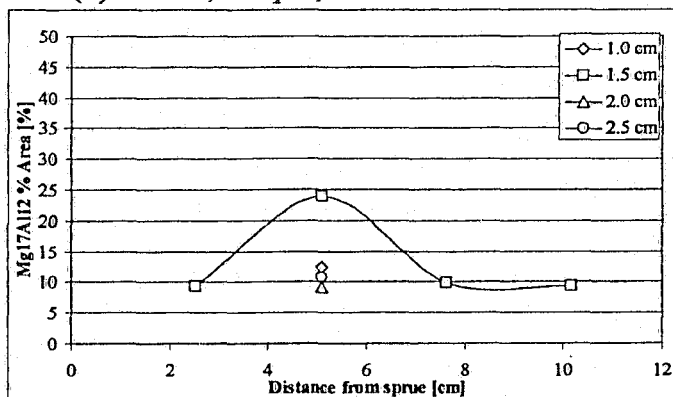
(c) 660 °C, 1.3 pcf, without vacuum



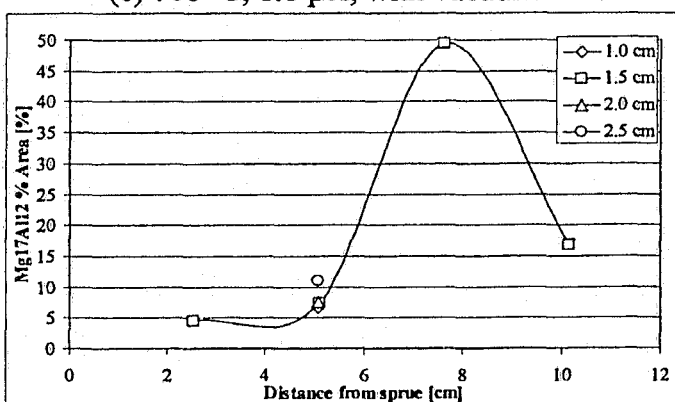
(d) 660 °C, 1.6 pcf, without vacuum



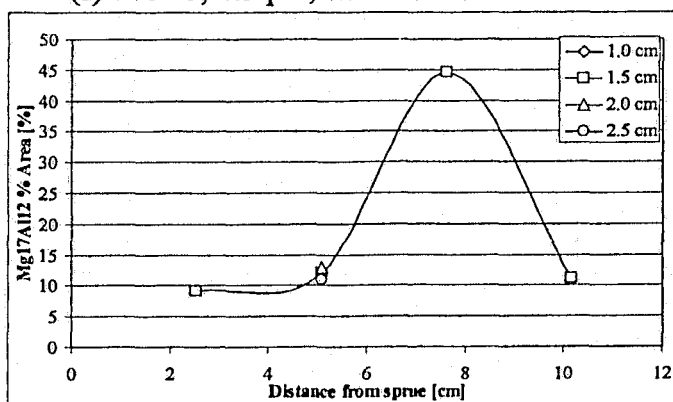
(e) 700 °C, 1.6 pcf, with vacuum



(f) 700 °C, 1.3 pcf, with vacuum



(g) 700 °C, 1.6 pcf, without vacuum



(h) 700 °C, 1.3 pcf, without vacuum

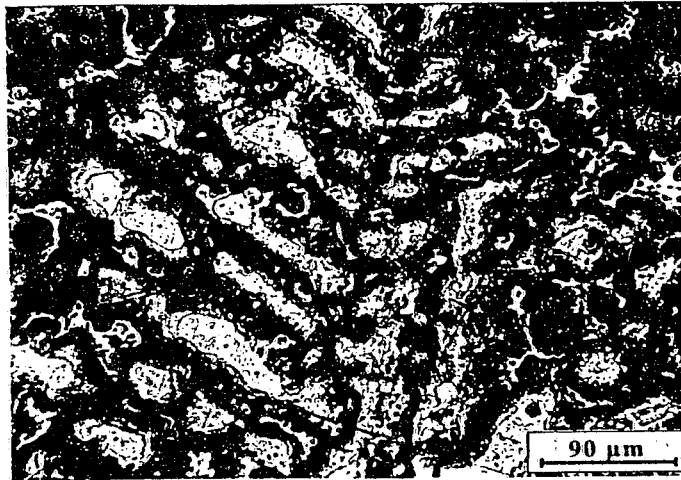
Figure 174:  $Mg_{17}Al_{12}$  percent area vs. distance from the sprue.

Table 22: Average  $Mg_{17}Al_{12}$  percent area for different casting conditions.

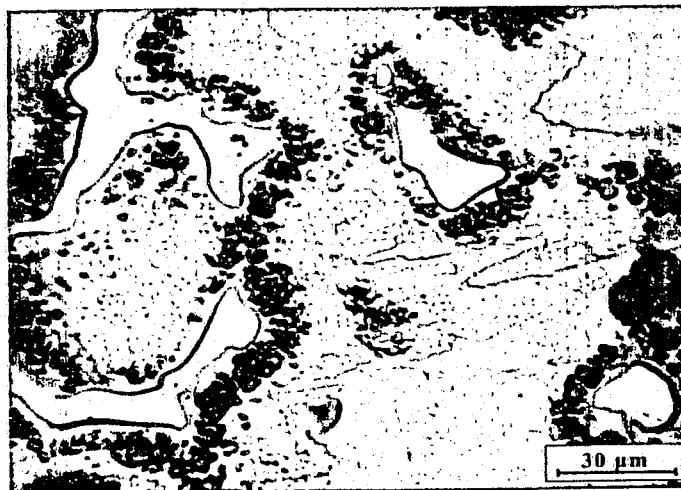
660 °C Pouring temperature	Average $Mg_{17}Al_{12}$ % area [%]	Variance in $Mg_{17}Al_{12}$ % area [%]	700 °C Pouring temperature	Average $Mg_{17}Al_{12}$ % area [%]	Variance in $Mg_{17}Al_{12}$ % area [%]
1.3 pcf, with vacuum	12.6	0.20	1.3 pcf, with vacuum	12.1	0.28
1.6 pcf, with vacuum	13.0	0.13	1.6 pcf, with vacuum	9.8	0.07
1.3 pcf, without vacuum	18.8	2.75	1.3 pcf, without vacuum	16.2	1.58
1.6 pcf, without vacuum	21.8	0.18	1.6 pcf, without vacuum	14.3	2.58

The image analysis results suggest that in the 660°C pouring temperature casting trials, the percent area of the precipitated  $Mg_{17}Al_{12}$  phase was higher when compared to the 700 °C pouring temperature casting trials. This trend was attributed to the lower cooling rates experienced in the 660 °C pouring temperature trials (as verified by Table 13). As a result of the lower cooling rates, the solidifying alloy was allowed more time for the precipitation reaction to occur.

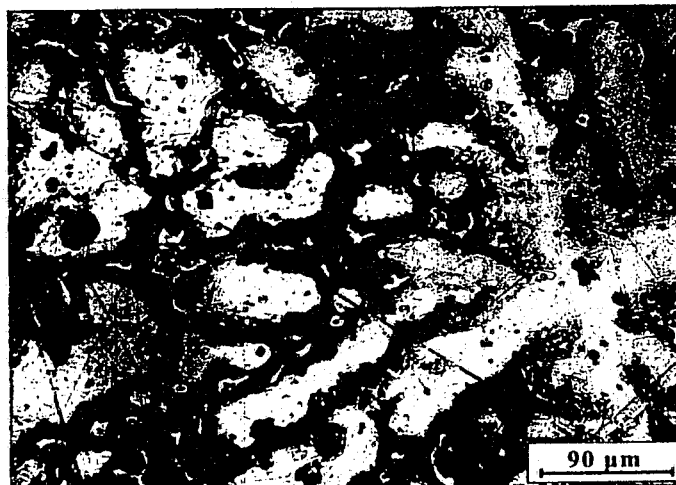
The 1.5 cm thick bars often experienced a sudden increase in the  $Mg_{17}Al_{12}$  percent area near the 8 cm distance from the sprue (Figure 174, (g) and (h)). The exact cause of this behavior remains unknown. However, it was observed (Figure 175 and Figure 177) that the casting locations where this anomaly occurred exhibited predominantly dendritic microstructure (high cooling rate). In these cases, the dendrites were seen to grow along the hexagonal directions of the HCP magnesium crystals. The development of the dendritic microstructure suggests presence of high solute gradients in the casting. It is possible that at locations where high solute gradients existed, the precipitation process caused the break down of the lamellar  $Mg_{17}Al_{12}$  precipitate. Thus, fragmented and degenerated fibrous structure was created, as seen in Figure 176.



*Figure 175: Microstructure of the 1.5 cm thick bar at 7.6 cm distance from the sprue, 700 °C / 1.6 pcf / without vacuum trial.*



*Figure 176: Figure 175 enlarged.*



*Figure 177: Microstructure of the 1.5 cm bar at 7.6 cm distance from the sprue, 700 °C / 1.3 pcf / without vacuum trial*

#### 4.10.6 Effect of the $Mg_{17}Al_{12}$ precipitate on the casting density

Past research suggests,<sup>20</sup> that presence of the low-melting point eutectics, such as the  $Mg_{17}Al_{12}$  phase, may allow eutectic flow before casting solidification is complete. Such eutectic flow may decrease the volume fraction of shrinkage porosity, thus improving the level of casting density.

The  $Mg_{17}Al_{12}$  percent area data plotted in Figure 178 indeed suggest that formation of the precipitate possibly affected the casting density, by allowing eutectic liquid flow, thereby eliminating some of the shrinkage porosity.

Moreover, extending the trend line to the left, which corresponds to an alloy composition with minimal amount of the  $Mg_{17}Al_{12}$  phase, suggests a casting density of  $1.81 \text{ g/cm}^3$ .

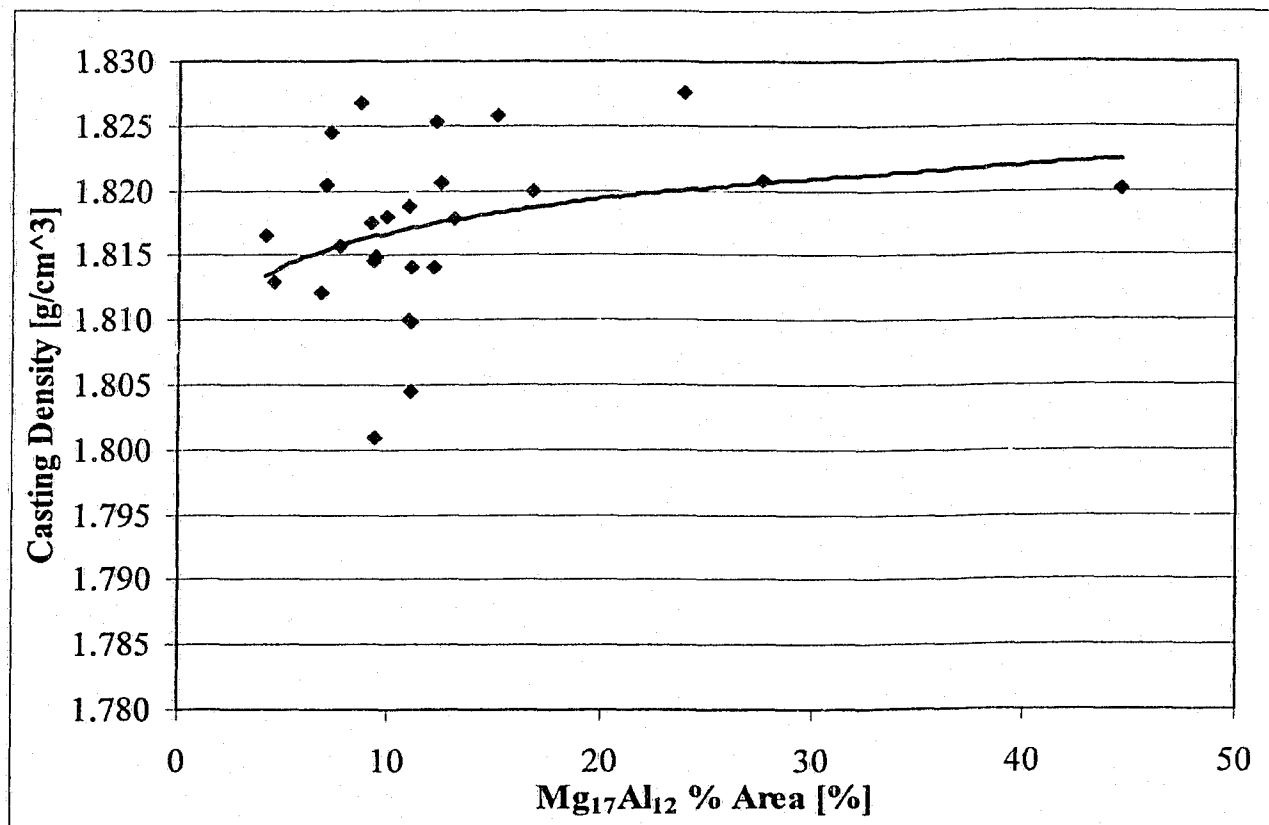


Figure 178: Effect of the  $Mg_{17}Al_{12}$  percent area on the casting density.

#### 4.10.7 Lamellar spacing of the $Mg_{17}Al_{12}$ precipitate

Image analysis software was used to determine the lamellar spacing between the centers of two adjacent parallel lamellae. The lamellar spacing of the  $Mg_{17}Al_{12}$  phase is regarded as an important characteristic of the precipitate, since it affects the mechanical properties of the alloy.

The growth of the lamellar eutectic was rationalized in terms of the solidification kinetics of the casting process. The fineness of the lamellar precipitate was explained by considering the energy changes associated with the phase development during solidification. Theory suggests,<sup>66</sup> that, for a constitutionally undercooled liquid ahead of the solid-liquid interface, the net Gibbs free energy change is:

$$\Delta G = -\frac{\Delta H_f \Delta T_u}{T_e} + \frac{2\gamma_{\alpha/\beta}}{\lambda} \quad (19)$$

Where

$\Delta G$  = Change in Gibbs free energy

$\Delta H_f$  = Change in enthalpy

$\Delta T_u$  = Thermal undercooling

$T_e$  = Eutectic (solidus) temperature

$\gamma_{\alpha/\beta}$  = Interfacial energy

$\lambda$  = Lamellar spacing

For a given undercooling there will be a minimum lamellar spacing,  $\lambda_{\min}$ , obtained by setting  $\Delta G$  in Equation 19 to zero. This is given by:

$$\lambda_{\min} = \frac{2\gamma_{\alpha/\beta} T_e}{\Delta H_f \Delta T_u} \quad (20)$$

The value of the interfacial energy,  $\gamma_{\alpha/\beta}$ , for the AZ91E alloy was not found in the literature. Therefore, typical low and high values of this parameter were assessed. The low and the high possible values of the minimal lamellar spacing,  $\lambda_{\min}$ , were calculated with  $\gamma_{\alpha/\beta} = 0.1$  and  $\gamma_{\alpha/\beta} = 1.0$ , respectively. Substituting appropriate values for the AZ91E magnesium alloy into Equation 20 (Appendix C), the minimum lamellar spacing was calculated to range between 0.017  $\mu m$  and 0.17  $\mu m$ .

As Figure 179 indicates, the lamellar spacing decreased towards the grain boundary. Lamellae indicated as "A" were easily resolved by the microscope. However, lamellae indicated as "B" were too fine to be accounted for. Presence of the fine lamellae was noted after the micrograph was digitally enhanced, as seen in Figure 180.



Figure 179: Fine and coarse lamellae of the  $Mg_{17}Al_{12}$  phase.

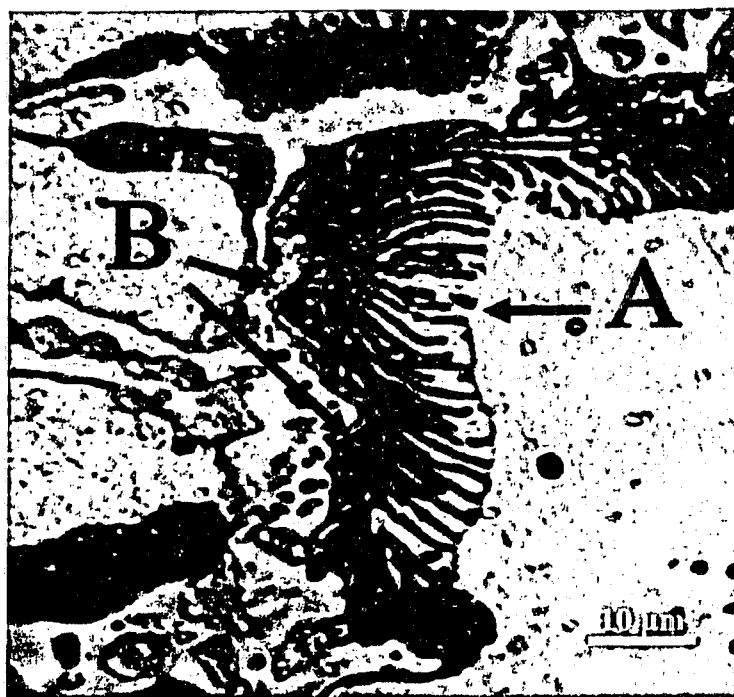
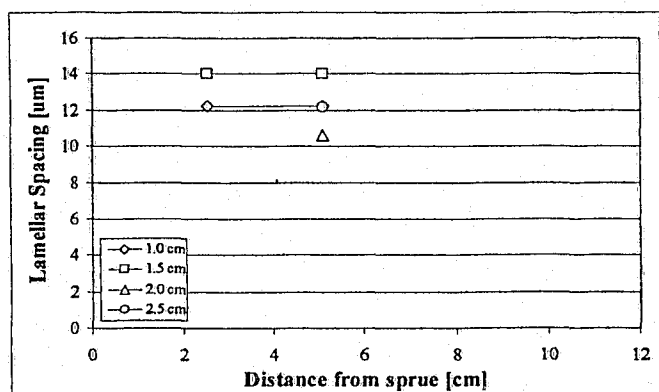


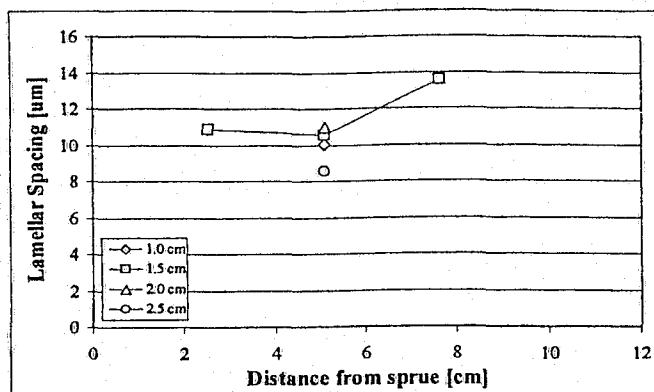
Figure 180: Digitally enhanced Figure 179.



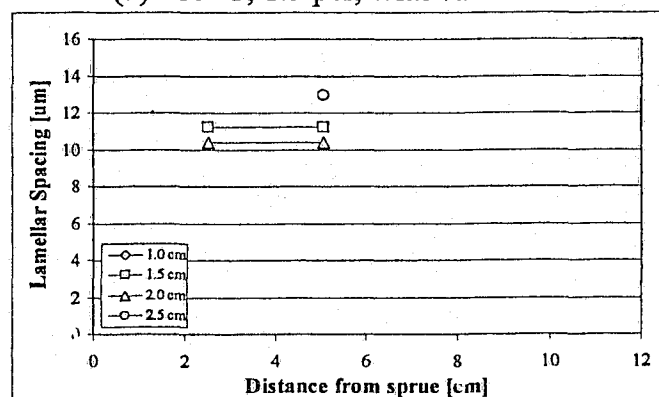
Figure 181 presents the results of the optical image analysis lamellar spacing measurements. It is evident, that the measured lamellar spacing values were significantly higher than the minimal lamellar spacing calculated via Equation 20. One reason for this discrepancy was attributed to the inability of the optical microscope to resolve the very fine lamellae.



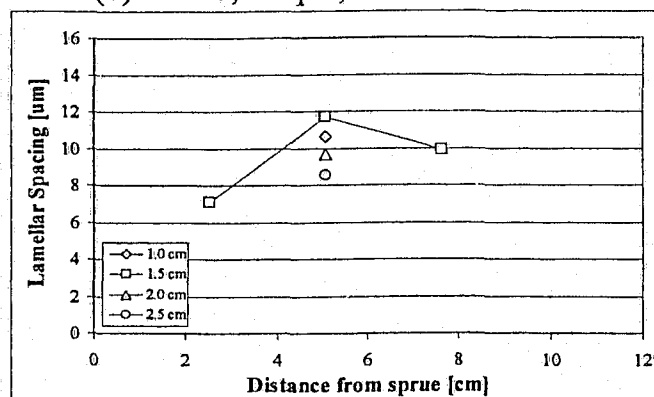
(a) 660 °C, 1.3 pcf, with vacuum



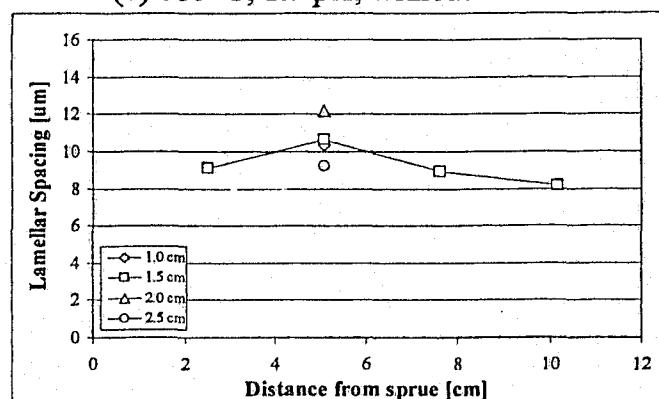
(b) 660 °C, 1.6 pcf, with vacuum



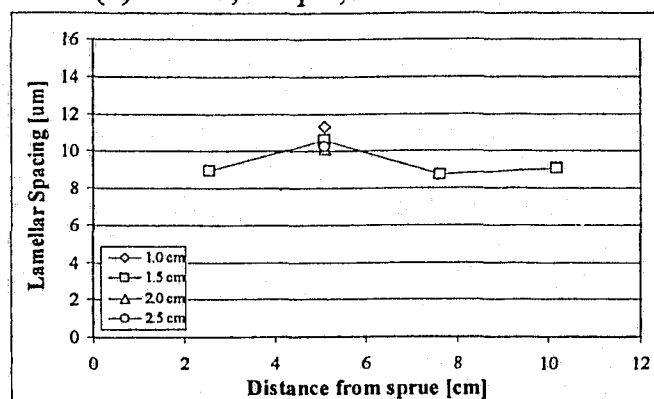
(c) 660 °C, 1.3 pcf, without vacuum



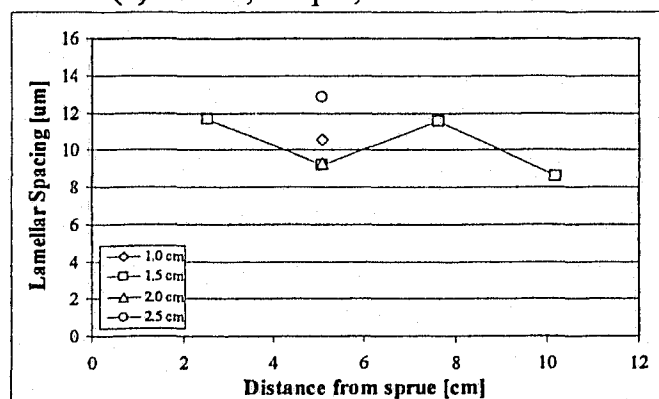
(d) 660 °C, 1.6 pcf, without vacuum



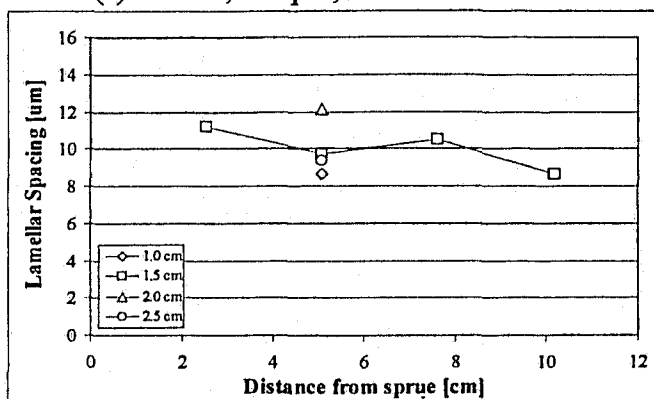
(e) 700 °C, 1.6 pcf, with vacuum



(f) 700 °C, 1.3 pcf, with vacuum



(g) 700 °C, 1.6 pcf, without vacuum



(h) 700 °C, 1.3 pcf, without vacuum

Figure 181:  $Mg_{17}Al_{12}$  lamellar spacing vs. distance from sprue.

#### *4.10.8 Section summary*

The microstructure development was typically observed to follow the non-equilibrium solidification kinetics. Despite the occurrence of the “equilibrium-like”  $\text{Mg}_{17}\text{Al}_{12}$  precipitate forming in some casting bars, the majority of the precipitate was of the lamellar non-equilibrium type.

Constitutional undercooling and development of solute boundary layer was attributed as the driving mechanism of solute segregation. Consequently, the  $\text{Mg}_{17}\text{Al}_{12}$  phase was heterogeneously distributed throughout the casting microstructure.

The casting cooling rate appeared to influence the degree of solute segregation as well as the overall grain morphology. High primary  $\alpha$ -Mg nucleation rates were the result of the high cooling rates, with attendant dispersion of the  $\text{Mg}_{17}\text{Al}_{12}$  phase.

The effect of vacuum, section thickness and pouring temperature on the casting microstructure were all based on their relationship with the alloy cooling rate.

It was observed that the “equilibrium-like” precipitate favored the fully divorced eutectic microstructure, while the lamellar non-equilibrium precipitate formed the partially divorced eutectic microstructure. In the case of the lamellar precipitate, individual lamellae were observed to grow along the pyramidal planes of the HCP magnesium crystals.

The amount of the precipitated  $\text{Mg}_{17}\text{Al}_{12}$  phase suggested correlation with the casting density. This indicates the possibility of eutectic flow prior to complete freezing of the casting.

## Chapter 5 – Conclusions

This research work culminated in a variety of novel observations with respect to the casting quality of magnesium alloy castings and the behavior of the molten AZ91E alloy when cast by the LFC process. These relate to the effect of vacuum, effect of foam characteristics, thermal analysis, casting porosity and the  $Mg_{17}Al_{12}$  intermetallic phase.

### 1. Effect of vacuum

The presence of vacuum caused the molten metal front to change from the conventional convex profile to a concave profile. Further, application of vacuum produced higher metal velocities relative to gravity casting. The effect of vacuum was correlated with the increased extraction rates of the liquid-EPS products from the casting cavity. Due to the effective removal of the liquid-EPS products, the metal flow in vacuum castings resembled that of open-cavity casting processes, where the metal velocity decreased with increasing distance from the sprue. On the contrary, gravity castings exhibited metal velocity oscillations, which suggest that metal flow was governed by the degradation rates of the solid-EPS in the casting cavity.

Statistical analysis revealed that the application of vacuum increased the variance of the metal velocity for different section thicknesses. In addition, the combined results of velocity and the thermal analysis suggest that during vacuum casting trials, the metal flow continued beyond the dendrite coherency point, as evidenced by the partially solidified metal at the frozen metal fronts of the horizontal bars.

### 2. Effect of foam characteristics

Foam density and bead fusion had a distinct impact on the casting fill and metal velocity. Superior mold filling of the 1.6 pcf foam patterns was attributed to the relatively low liquid-EPS residue fraction present in the mold cavity, as compared to the 1.3 pcf foam castings. This anomalous behavior was attributed to the poor bead fusion of the 1.3 pcf foam, which allowed premature degradation of the solid-EPS foam well ahead of the molten metal front. In addition, the metal velocity in the 1.6 pcf foam casting trials was seen to be higher than in the 1.3 pcf foam casting trials. This behavior was also explained by the presence of the liquid-EPS products in the 1.3 pcf casting trials, which possibly accumulated at the metal-mold interface, thus increasing the frictional forces imparted on the liquid metal flow.

Increasing the pouring temperature improved the casting fillability. This result was attributed to the relatively easier solid-EPS and liquid-EPS removal process. However, increasing the pouring temperature also promoted metal penetration into the surrounding sand, with attendant casting surface defects.

### 3. Thermal analysis

The casting cooling rates were observed to impact the degree of solute segregation, as well as the overall grain morphology. High primary  $\alpha$ -Mg nucleation rates were correlated with the high initial cooling rates, with a decrease in grain size and homogeneous dispersion of the  $Mg_{17}Al_{12}$  phase. Further, the results of the thermal analysis enabled calculation of parameters for Chvorinov's equation. The value of the Chvorinov's constant for LFC of magnesium alloys was calculated to be 324.6 and the value of the Chvorinov's exponent was 1.4.

### 4. Casting porosity

Shrinkage porosity was often observed in the casting bars forming as networks (not-connected), especially near the mold wall surfaces. The center regions of the horizontal bars, however, contained only isolated pockets of interdendritic cavities. The Adam's riser model could be used to predict solidification shrinkage trends in gravity castings. However, use of this model was not possible for vacuum castings.

An attempt was made to apply thermal parameter based criterion functions to predict porosity. The Niyama function was observed to predict the trends of porosity within the same order of magnitude for gravity and vacuum castings. This level of accuracy was not achieved with some other known functions.

The application of vacuum possibly promoted the entrapment of liquid-EPS products in the casting cavity thus increasing casting porosity (macroporosity).

## 5. Development of the $Mg_{17}Al_{12}$ phase

The AZ91E microstructure development, in general, followed the non-equilibrium solidification kinetics. Despite the occurrence of the “equilibrium-like” spherical  $Mg_{17}Al_{12}$  precipitate forming in some casting bars, the majority of the precipitate was of the non-equilibrium lamellar type. The “equilibrium-like” spherical precipitate favored the fully divorced eutectic microstructure, while the lamellar non-equilibrium precipitate associated with the partially divorced eutectic microstructure. In the case of the lamellar precipitate, individual lamellae were observed to grow along the pyramidal planes of the HCP magnesium crystals. Constitutional undercooling and the development of solute boundary layer was identified as the driving mechanism of solute segregation and development of the non-equilibrium lamellar precipitate.

## Chapter 6 – Suggestions for Further Work

1. Development of a quantitative technique to assess bead fusion.
2. Development of a method to estimate the amount of liquid-EPS residue present in the casting cavity.
3. Metal flow visualization with real time X-ray spectroscopy to validate the liquid-EPS development phenomena.
4. Development of new porosity prediction model accounting for the presence of liquid-EPS in the casting cavity.
5. Optimization of the vacuum casting conditions to enable improved mold filling without compromising the internal casting structure and surface finish quality.
6. Optimization of the foam / ceramic slurry / mold media parameters to achieve optimal casting fill while preventing liquid-EPS entrapment.
7. Development of image analysis software to determine the ratio of the equilibrium and non-equilibrium  $\text{Mg}_{17}\text{Al}_{12}$  precipitate in the casting.

## Appendix A – EPS foam decomposition (energy approach)

The energy required to transform 1 cm<sup>3</sup> of 1.6 pcf solid-EPS foam to liquid-EPS is given by:

$$Energy_{foam} = H_f m_f + c_f (\Delta T_f) m_f \quad (21)$$

Where:

$H_f$  = Latent heat = heat required to bring about a change in state

$m_f$  = Mass of solid-EPS

$c_f$  = Specific heat of solid-EPS

$\Delta T_f$  = Temperature difference between the foam liquidus temperature and metal temperature

The sensible energy content of 1 cm<sup>3</sup> of superheated alloy is given by:

$$Energy_{metal} = c_m (\Delta T_m) m_m \quad (22)$$

Where:

$c_m$  = Specific heat of the alloy

$\Delta T_m$  = Alloy superheat

$m_m$  = Mass of metal

Substituting typical values into Equation 21 and Equation 22 above, the following is obtained:

$$Energy_{foam} = 876(J/g) * 0.0256(g) + 1.2(J/g.K) * 693.15(K) * 0.0256(g) = 43J$$

$$40\text{ }^{\circ}\text{C superheated metal: } Energy_{metal} = 1.43(J/g.K) * 333.15(K) * 1.74(g) = 828J$$

$$100\text{ }^{\circ}\text{C superheated metal: } Energy_{metal} = 1.43(J/g.K) * 373.15(K) * 1.74(g) = 930J$$



## Appendix B – Statistical analysis

### B.1 - Effect of pouring temperature and vacuum on the casting density for the 1.6 pcf foam castings

Table 23: Detailed results of the ANOVA analysis of the effect of pouring temperature and vacuum on the casting density.

Source of Variation	Sum of Squares	Degrees of Freedom	Mean Square Value	F-statistic	F critical
Pouring temperature	0.000247	1	0.000247	2.942514	7.708647
Application of vacuum	0.000288	1	0.000288	3.428895	7.708647
Interaction	0.000306	1	0.000306	3.649384	7.708647
Within	0.000336	4	8.39E-05		
Total	0.001176	7			

Note: The value of F-critical in the above table was determined for  $\alpha = 5\%$ .

### B.2 - Effect of foam density and vacuum on the average casting density in the 660 °C pouring temperature casting trials.

Table 24: Detailed results of the ANOVA analysis of the effect of foam density and vacuum on the casting density for the 660 °C pouring temperature trials.

Source of Variation	Sum of Squares	Degrees of Freedom	Mean Square Value	F-statistic	F critical
Foam density	3.36E-05	1	3.36E-05	0.124659	7.708647
Presence of vacuum	0.000987	1	0.000987	3.661551	7.708647
Interaction	9.23E-06	1	9.23E-06	0.034254	7.708647
Within	0.001078	4	0.00027		
Total	0.002108	7			

Note: The value of F-critical in the above table was determined for  $\alpha = 5\%$ .

**B.3 - Effect of foam density and vacuum on the average casting density in the 700 °C pouring temperature casting trials.**

*Table 25: Detailed results of the ANOVA analysis for the effect of foam density and vacuum on the casting density in the 700 °C pouring temperature trials.*

Source of Variation	Sum of Squares	Degrees of Freedom	Mean Square Value	F-statistic	F critical
Foam density	5.3E-05	1	5.3E-05	0.652866	7.708647
Presence of vacuum	3.17E-05	1	3.17E-05	0.390813	7.708647
Interaction	2.6E-05	1	2.6E-05	0.31987	7.708647
Within	0.000325	4	8.12E-05		
Total	0.000435	7			

Note: The value of F-critical in the above table was determined for  $\alpha = 5\%$ .

**B.4 - Effect of section thickness and pouring temperature on the local solidification time (LST) for gravity cast 1.6 pcf foam trials.**

*Table 26: Detailed results of the ANOVA analysis of the effect of section thickness and pouring temperature on the LST.*

Source of Variation	Sum of Squares	Degrees of Freedom	Mean Square Value	F-statistic	F critical
Section thickness	0.3844	1	0.3844	0.003622	5.317655
Pouring temperature	21640.83	3	7213.611	67.96229	4.066181
Interaction	878.9495	3	292.9832	2.760311	4.066181
Within	849.131	8	106.1414		
Total	23369.3	15			

Note: The value of F-critical in the above table was determined for  $\alpha = 5\%$ .

**B.5 - Effect of pouring temperature and section thickness on thermal gradients for vacuum cast 1.6 pcf trials.**

*Table 27: Detailed results of the ANOVA analysis of the effect of pouring temperature and section thickness on the casting thermal gradients.*

Source of Variation	Sum of Squares	Degrees of Freedom	Mean Square Value	F-statistic	F critical
Rows	0.6962	1	0.6962	0.461661	10.12796
Columns	32.6061	3	10.8687	7.207201	9.276628
Error	4.5241	3	1.508033		
Total	37.8264	7			

Note: The value of F-critical in the above table was determined for  $\alpha = 5\%$ .

## Appendix C – Minimal lamellar spacing

Using Equation 19, the minimal lamellar spacing was calculated for the AZ91E alloy. Values of appropriate variables were obtained from Reference 9.

$$\lambda_{\min} = \frac{2\gamma_{\alpha/\beta}T_e}{\Delta H_f \Delta T_u} \quad (19, \text{repeat})$$

$$\Delta T_u = 12.5 \text{ K}$$

$$\Delta H_f = 6.751 \times 10^8 \text{ J/kg}$$

$$T_e = 710.15 \text{ K}$$

Substituting these values to Equation 19, the following expression was obtained:

$$\lambda_{\min} = \frac{2\gamma_{\alpha/\beta} 710.15(K)}{6.751 \times 10^8 (J/kg) * 12.5(K)} = 1.683 \times 10^{-7} \gamma_{\alpha/\beta} \quad (23)$$

For the minimum lamellar spacing,  $\gamma_{\alpha/\beta} = 0.1$ . Therefore:  $\lambda_{\min} = 1.683 \times 10^{-8} \text{ m} = 0.0168 \text{ }\mu\text{m}$ .

For the maximum lamellar spacing,  $\gamma_{\alpha/\beta} = 1.0$ . Therefore:  $\lambda_{\min} = 1.683 \times 10^{-7} \text{ m} = 0.168 \text{ }\mu\text{m}$ .

## References

1. R. Simpson, "The Use of Chills as a Means of Influencing Solidification in Lost Foam Cast Aluminum Alloys", M.E.S.c. Thesis, University of Western Ontario, 1997, p. 1.
2. R. W. Monroe, Expandable Pattern Casting, American Foundrymen's Society Inc., 1992, p. 1.
3. C. S. Roberts, Magnesium and Its Alloys, John Wiley & Sons, Inc., New York, 1960, p. 4.
4. C. S. Roberts, Magnesium and Its Alloys, John Wiley & Sons, Inc., New York, 1960, p. 126.
5. R. Ajdar, C. Ravindran, A. McLean, "Total Solidification Time and Flow Length of A356 Alloy During Lost Foam Casting", Light Metals 2000, Ed. J. Kazadi and J. Masounave, 2000, pp. 615 – 629.
6. E. Aghion, B. Bronfin, "The Correlation Between the Microstructure and Properties of Structural Magnesium Alloys in Ingot Form", Proceeding of the Third International Magnesium Conference, The Institute of Materials, Ed. G. W. Lorimer, 1996, pp. 313 – 325.
7. R. Ajdar, "The Effect of Mold Materials on Solidification, Microstructure and Fluidity of A356 Alloy in Lost Foam Casting", M.A.Sc. Thesis, University of Toronto, 2001, p. 25.
8. S. Lun Sin, D. Dube, "Influence of Process Parameters on Fluidity of investment-cast AZ91D magnesium alloy", Materials Science and Engineering A, Vol. 386, 2004, pp. 34 – 42.
9. M. Avedesian, Magnesium and Manganese Alloys, ASM Specialty Handbook, ASM International, 1999, p. 231.
10. J. R. Davis, Aluminum and Aluminum Alloys, ASM Specialty Handbook, ASM International, 1993, p. 720.
11. S. Mehta, S. Shivkumar, "Fluidity of Al Alloys and Composites in the Lost Foam Process", AFS Transactions, Vol. 103, 1995, pp. 663 – 668.
12. Q. Chen and C. Ravindran, "A preliminary study on feeding behavior of A356 alloy with lost foam process", Light Metals 1999, Ed. M. Bouchard and A. Faucher, 1999, pp. 277 – 289.
13. E. N. Pan and K. Y. Liao, "Study on the Filling Behavior of the Evaporative Pattern Casting (EPC) A356 Alloy", AFS CASTEXPO'99, St. Louis, Missouri, U.S.A., 1999, Preprint No: 99-031.
14. L. Bichler, "Lost Foam Casting of Magnesium Alloys: Process Development", B.Eng Thesis, Ryerson University, 2003, p. 36.
15. S. Shivkumar "Fundamental Characteristics of Metal Flow in the Full-Mold Casting of Aluminum Alloys", Ph.D. Thesis, Stevens Institute of Technology, New Jersey, USA, 1987, p. 12.
16. O.E. Okorafor, "Thermal Aspects of Gasifiable Pattern Molds and Solidification of Al-4.25%Cu-1.03%Si Alloy Castings", Aluminum, No. 62, 1986, pp. 110 – 112.

17. Z. Liu, J. Hu, Q. Wang, W. Ding, Y. Zhu, Y. Lu, W. Chen, "Evaluation of the effect of vacuum on mold filling in the magnesium EPC process", Journal of Materials Processing Technology, Vol. 120, 2002, pp. 94 – 100.
18. C. S. Roberts, Magnesium and Its Alloys, John Wiley & Sons, Inc., New York, 1960, p. 17.
19. C. S. Roberts, Magnesium and Its Alloys, John Wiley & Sons, Inc., New York, 1960, p. 18.
20. K. A. Dahle, Y. C. Lee, M. D. Nave, P. L. Schaffer, D. H. StJohn, "Development of the as-cast microstructure in magnesium-aluminum alloys", Journal of Light Metals 1, 2001, pp. 61 – 72.
21. P. Moreno, T. K. Nandy, J. W. Jones, J. E. Allison and T. M. Pollock, "Microstructural characterization of a die-cast magnesium rare-earth alloy", Scripta Materialia, Vol. 45, 2001, pp. 1423 – 1429.
22. A. Beck, "The Technology of Magnesium and Its Alloys", F. A. Hughes and Co. Ltd., London, 1943, p. 38.
23. L. Backerud, E. Krol, J. Tamminen, "Solidification Characteristics of Aluminum Alloys, Volume 1: Wrought Alloys", Skan Aluminum, 1986, p. 7.
24. Z. Koren, H. Rosenson, E. M. Gutman, Y. B. Unigovski, A. Elizer, "Development of semisolid casting for AZ91 and AM50 magnesium alloys", Journal of Light Metals 2, 2002, pp. 81 – 87.
25. D. H. StJohn, A. K. Dahle, T. Abbott, M. D. Nave and Ma Quian, "Solidification of Cast Magnesium Alloys", Magnesium Technology 2003, Ed. H. I. Kaplan, TMS, 2003, pp. 95 – 100.
26. S. Kleiner, O. Beffort, A. Wahlen, P. J. Uggowitzer, "Microstructure and mechanical properties of squeeze cast and semi-solid cast Mg-Al alloys", Journal of Light Metals 2, 2002, pp. 277 – 280.
27. Q. Han, E. A. Kenik, S. R. Agnew, S. Viswanathan, "Solidification behavior of commercial magnesium alloys", Magnesium Technology 2001, Ed. J. Hryn, TMS, 2001, pp. 81 – 86.
28. M. D. Nave, A. K. Dahle and D. H. StJohn, "Eutectic growth morphologies in magnesium-aluminum alloys", Magnesium Technology 2000, Ed. By H. I. Kaplan, J. Hryn, and B. Clow, TMS, 2000, pp. 233 – 242.
29. E. A. Payzant, S. R. Agnew, Q. Han and S. Viswanathan, "Mg<sub>17</sub>Al<sub>12</sub> Phase Precipitation Kinetics in Die-Casting Alloys AZ91D and AM60B", Magnesium Technology 2001, Ed. J. Hryn, TMS, 2001, pp. 183 – 187.
30. J. F. Nie, X. L. Xiao, C. P. Luo, B. C. Muddle, "Characterisation of precipitate phases in magnesium alloys using electron microdiffraction", Micron, Vol 32, 2001, pp. 857 – 863.
31. W. Bulian and E. Fahrenhorst, "Metallography of Magnesium and Its Alloys", F. A. Hughes & Co. Ltd., Abbey House, London, 1945, pp. 15 – 18.
32. J. F. Nie, "Effects of precipitate shape and orientation on dispersion strengthening in magnesium alloys", Scripta Materialia, Vol. 48, 2003, pp. 1009 – 1015.

33. C. S. Roberts, Magnesium and Its Alloys, John Wiley & Sons, Inc., New York, 1960, p. 21.
34. A. M. Talbot and J. T. Norton, "Age-hardening of Magnesium-Aluminum Alloys", Transactions AIME, Vol. 22, 1936, p. 301.
35. A. Fisher, "A Note on Some Structural Changes Produced in a Magnesium Alloy by Heat Treatment", J. Inst. Of Metals, Vol. 67, 1941, p. 289.
36. F. A. Fox and E. Lardner, "An investigation of the Effects of Precipitation Treatment of Binary Magnesium-Aluminum Alloys", J. Inst. Of Metals, Vol. 49, 1943, p. 373.
37. C. T. Haller and C. S. Barrett, "Precipitation in Magnesium Sheet", ASM Transactions, Vol. 39, 1947, p. 670.
38. A. Carvalho, "<http://www.ub.rug.nl/eldoc/dis/science/p.m.c.c.a.de.carvalho/c1.pdf>", University of Groningen, Holland, Accessed: January 14, 2004.
39. N. A. El-Mahallawy, M. A. Taha, E. Pokora, F. Klein, "On the influence of process variables on the thermal conditions and properties of high pressure die-cast magnesium alloys", Journal of Materials Processing Technology, Vol. 73, 1998, pp. 125 – 138.
40. P. Bakke, C. D. Fuerst, H. Westengen, "Solidification Induced In-Homogenities in Magnesium Aluminum Alloy AZ91 Ingots", Magnesium Technology 2000, Ed. H. I. Kaplan, J. Hryn and B. Clow, TMS, 2000, pp. 201 – 210.
41. C. A. Aliravci, J. E. Gruzleski, F. C. Dimayuga, "Effect of Strontium on the Shrinkage Microporosity in magnesium Sand Castings", AFS Transactions, Vol. 100, 1992, pp. 353 – 362.
42. E. N. Pan, J. F. Hu, "Study on Fluidity of Al-Si Alloys", AFS Transactions, Vol. 105, 1997, pp. 413 – 418.
43. G. Marzano, "Foundry Basics Seminar – Sand Casting Alloy Processing Techniques", Haley Industries Inc., 1999, pp. 1 – 45.
44. J. Campbell, Castings Practice – The 10 Rules of Castings, Elsevier Butterworth Heinemann, 2004, p. 96.
45. A. J. Lindemann, M. Schmidt, T. Todte and T. Zeuner, "Thermal analytical investigations of the magnesium alloys AM60 and AZ91 including the melting range", Thermochimica Acta, Vol. 382, 2002, pp. 269 – 275.
46. Y. W. Riddle and M. M. Makhlof, "Characterizing Solidification by Non-Equilibrium Thermal Analysis", Magnesium Technology 2003, Ed. H. I. Kaplan, TMS, 2003, pp. 101 – 107.
47. J. O. Barlow and D. M. Stefanescu, "Computer-Aided Cooling Curve Analysis Revisited", AFS Transactions, Vol. 105, 1997, pp. 349 - 354.

48. A. Savitzky and M. Golay, "Smoothing and Differentiation of Data by Simplified Least Squares Procedure", Analytical Chemistry, Vol 36, No. 8, 1964, pp. 1627 – 1639.
49. D. Nolan, "Infrared Imaging of the Lost Foam Casting Process", Foseco-Morval Inc., 2004 Paderborn Conference, 2004, pp. 1 – 19.
50. J. P. Holman, Experimental Methods for Engineers, McGraw-Hill Book Co., 4<sup>th</sup> Ed., 1984, pp. 50 – 57.
51. S. Shivkumar and B. Gallois, "Physico-Chemical Aspects of the Full Mold Casting of Aluminum Alloys, Part I: The Degradation of Polystyrene", AFS Transactions, Vol. 95, 1987, pp. 791 – 800.
52. L. Wang, S. Shivkumar and D. Apelian, "Effects of Polymer Degradation of Lost Foam Castings", AFS Transactions, Vol. 98, 1990, pp. 923 – 933.
53. D. R. Hess, B. Durham, C. W. Ramsay and D. R. Askeland, "Observations on the Effect of Pattern and Coating Properties on Metal Flow and Defect Formation in Aluminum Lost Foam Castings", AFS Transactions, Vol. 110, 2002, pp. 1435 – 1448.
54. J. Liu, C. W. Ramsay and D. R. Askeland, "Effect of Foam Density and Density Gradients on Metal Fill in the LFC Process", AFS Transactions, Vol. 105, 1997, pp. 435 – 442.
55. E. H. Niemann, "Expandable Polystyrene Pattern Material for the Lost Foam Process", AFS Transactions, Vol. 96, 1988, pp. 793 – 798.
56. J. Rossacci and S. Shivkumar, "Influence of EPS bead fusion on pattern degradation and casting formation in the lost foam process", Journal of Materials Science, Vol. 38, 2003, pp. 2321 – 2330.
57. M. Cai, J. Siak, B. R. Powell, G. Novaine and S. J. Swarin, "Physical and Chemical Analysis of the Thermal Degradation Products of Expanded Polystyrene Patterns with Short Thermal Exposures", AFS Transactions, Vol. 110, 2002, pp. 1463 – 1481.
58. T. V. Molibog and H. Littleton, "Degradation of Expanded Polystyrene Patterns", AFS Transactions, Vol. 110, 2002, pp. 1483 – 1487.
59. D. M. Levine, T. C. Krehbiel, M. L. Berenson, Business Statistics – A First Course, 2nd Ed., Prentice-Hall, New Jersey, 2000, p. 363.
60. L. Bichler and C. Ravindran, "Observations on Fillability and Metal velocity", AFS Transactions, Vol. 113, 2005, In print.
61. N. Chvorinov, "Theory of Casting Solidification", Geisserei, Vol. 27 (1940), pp. 177 – 186.
62. Campbell, Castings Practice – The 10 Rules of Castings, Elsevier Butterworth Heinemann, 2004, p. 18.
63. J. Campbell, Castings, Butterworth-Heinemann, 1991, p. 19.
64. F. M. White, Fluid Mechanics, 4th Ed., WCB McGraw-Hill, 1999, p. 24.



65. Q. Chen and C. Ravindran, "Effects of Hydrogen Content and Solidification Time on Porosity Formation in LFC's of A356 Alloy – A Semi-Empirical Model", AFS Transactions, Vol. 108, 2000, pp. 297 – 303.
66. B. Tanovic, I. Jones, A. Green and P. Berry, "Materials Science – Solidification", "<http://www.matter.org.uk/solidification/>", University of Liverpool, United Kingdom, Accessed: February 2, 2005.
67. J. Gruzleski, Microstructure Development During Metalcasting, AFS, 2000, p. 105.
68. M. C. Flemings, Solidification Processing, McGraw-Hill, 1974, p. 36.
69. S. H. Avner, Introduction to Physical Metallurgy, McGraw-Hill, 1964, p. 128.